TEXTURE EVOLUTION DURING BETA-QUENCHING OF A ZIRCONIUM ALLOY

A thesis submitted to The University of Manchester for the degree of Doctor of Philosophy in the Faculty of Engineering and Physical Sciences

2010

JAVIER E. ROMERO OSPINA

School of Materials

CONTENTS

51840 Words

LIST OF TABLES

LIST OF FIGURES

ABBREVIATIONS

bcc	Body Centred Cubic
BWR	Boiling Water Reactor
CP	Commercially Pure
DHC	Delayed Hydride Cracking
EBSD	Electron Backscatter Diffraction
EBSP	Electron Backscatter Pattern
EPSC	Elasto-Plastic Self-Consistent
ESRF	European Synchrotron Radiation Facility
ETMT	Electro Thermal Mechanical Tester
FEGSEM	Field Emission Gun Scanning Electron Microscope
FWHM	Full-Width Half-Maximum
hcp	Hexagonal Close-Packed
IF	Interstitial-Free
IPF	Inverse Pole Figure
LXRD	Laboratory X-ray Diffraction
mrd	Multiples of a Random Distribution
ND	Normal Direction
OD	Orientation Distribution
ODF	Orientation Distribution Function
OPS	Oxide Polishing Suspension
PKA	Primary Knock-on Atom
PWR	Pressurized Water Reactor
RD	Rolling Direction
SEM	Scanning Electron Microscope/Microscopy
SIPA	Stress Induced Preferential Absorption
SIPN	Stress Induced Preferred Nucleation
SPP	Second Phase Particle
SXRD	Synchrotron X-ray Diffraction
TD	Transverse Direction
TEM	Transmission Electron Microscope/Microscopy
T_m	Melting Point
TOF	Time of Flight
XRD	X-ray Diffraction

TEXTURE EVOLUTION DURING BETA-QUENCHING OF A ZIRCONIUM ALLOY

Abstract of thesis submitted by Javier E. Romero Ospina to the School of Materials,

The University of Manchester for the Degree of Doctor of Philosophy

2010

Zirconium alloys are widely used by the nuclear industry as fuel cladding and structural materials. Many physical and metallurgical properties of zirconium alloys, that are important for their performance in nuclear reactors, are affected by crystallographic texture due to the strong anisotropy of individual crystals. Irradiation assisted growth is one example. Zirconium crystals deform anisotropically under irradiation, which in the presence of strong textures (like the ones observed in cold-rolled sheet) causes undesirable deformation of components during service. For this reason, the nuclear industry is interested in developing thermomechanical processes that produce random textures, taking advantage of the allotropic phase transformation undergone by zirconium, from the low temperature hcp α-phase to the high temperature bcc β-phase. One of these processes is β-quenching, which has showed certain success in weakening strong rolling textures. However, there is no consensus about the fundamental mechanisms involved.

The aim of this work is to study the evolution of the texture of the zirconium alloy Zircaloy-2 during β-quenching, in order to gain understanding on the mechanisms involved on texture development and evolution during the α→β and β→α phase transformations. Firstly industrially β-quenched samples were characterised using well-known techniques such as laboratory X-ray diffraction (LXRD) and electron backscatter diffraction (EBSD), which revealed a relationship between peak temperature and the inherited α texture. An in-situ synchrotron X-ray diffraction (SXRD) experiment provided, for the first time, information of texture evolution of zirconium during rapid changes and at non-ambient conditions. Different peak temperatures and stress/strain conditions were tested. Detailed post-mortem EBSD characterisation of samples studied in-situ provided insight on the relationship between the microstructure and the texture. Finally, laboratory furnaces were used to β-quench samples at very high temperature. It was found that there is selection of orientation variants during β-quenching of zirconium, but while the selection during the α→β transformation is almost negligible, depending on the texture evolution of the β-phase (affected by grain growth and/or plastic deformation), diverse mechanisms of variant selection act during the β→α phase transformation. The inherited textures observed result from the combination of these mechanisms. Some of the results of this work can be transferred to other systems such as titanium and the α→γ→α phase transformation in steel.

DECLARATION

I declare that no portion of the work referred to in the thesis has been submitted in support of an application for another degree of qualification of this or any other university or other institute of learning.

COPYRIGHT STATEMENT

i. The author of this thesis (including any appendices and/or schedules to this thesis) owns certain copyright or related rights in it (the "Copyright") and he has given The University of Manchester certain rights to use such Copyright, including for administrative purposes.

ii. Copies of this thesis, either in full or in extracts and whether in hard or electronic copy, may be made only in accordance with the Copyright, Designs and Patents Act 1988 (as amended) and regulations issued under it or, where appropriate, in accordance with licence agreements which the University has from time to time. This page must form part of any such copies made.

iii. The ownership of certain Copyright, patents, designs, trade marks and other intellectual property (the "Intellectual Property") and any reproductions of copyright works in the thesis, for example graphs and tables ("Reproductions"), which may be described in this thesis, may not be owned by the author and may be owned by third parties. Such Intellectual Property and Reproductions cannot and must not be made available for use without the prior written permission of the owner(s) of the relevant Intellectual Property and Reproductions.

iv. Further information on the conditions under which disclosure, publication and commercialisation of this thesis, the Copyright and any Intellectual Property and/or Reproductions described in it may take place is available in the University IP Policy (see http://www.campus.manchester.ac.uk/medialibrary/policies/intellectual-property.pdf) in any relevant Thesis restriction declarations deposited in the University Library, The University Library's regulations (see http://www.manchester.ac.uk/library/aboutus/regulations) and in the University's policy of presentation of Theses.

ACKNOWLEDGEMENTS

SUPPORTING PUBLICATIONS

Romero, J., Preuss, M. and Quinta da Fonseca, J. (2009) Capturing the texture changes in a zirconium alloy during the allotropic phase transformation. *Scripta Materialia,* 61, 399-402.

Romero, J., Preuss, M. and Quinta da Fonseca, J. (2009) Texture memory and variant selection during phase transformation of a zirconium alloy. *Acta Materialia*, 57, 5501-5511.

Romero, J., Preuss, M., Quinta da Fonseca, J., Comstock, R. J., Dahlbäck, M. and Hallstadius, L. (2010) Texture Evolution of Zircaloy-2 during Beta-quenching: Effect of Process Variables. *Journal of ASTM International*, 7, 1-13.

This work is dedicated to two people who, even though I would love to, for ironically opposite reasons, I can not embrace today: my brother Mauricio and my yet to be born little treasure.

INTRODUCTION

Understanding and controlling the performance of zirconium alloys is critical for the nuclear industry. Zirconium alloys are widely used as fuel cladding and structural materials in nuclear reactors, thanks to their low neutron-capture cross-section, outstanding corrosion resistance, and good mechanical properties at operating temperatures. In the core of boiling water reactors (BWR) and pressurised water reactors (PWR), thin-walled tubes and structural components are made of zirconium alloys (Davis 1998). In zirconium-based alloys, as it occurs in most polycrystalline materials, the majority of the physical and mechanical properties are affected by the orientation of the crystals, i.e. their crystallographic texture. The aim of this work is to study the evolution of the texture of the zirconium alloy Zircaloy-2 during β-quenching.

The economic viability of nuclear power plants is strongly related to the maximum amount of energy that can be extracted from the fuel. In most cases the limitation is not the fuel itself, but the damage caused both by neutron irradiation and by the environment on cladding and structural materials (Banerjee 2001). Nuclear materials

and irradiation defects have opened new fields of research in materials science, due to uncommon changes undergone by the materials during service. For this reason, research for nuclear applications distinctively couples fundamental and applied materials science. Despite this fact, historically, the majority of the research carried out on zirconium alloys has been concentrated on corrosion performance. A vast amount of work has focused on oxidation behaviour and chemical metallurgy of zirconium and its alloys, i.e. the effect of alloying elements on corrosion resistance and hydrogen uptake, while the physical metallurgy has not been treated with the same depth. The present work constitutes a contribution in this less explored area, dealing with a phenomenon closely related to fundamental science, but finding a straightforward application not only for nuclear materials but also for other applications.

Some materials such as zirconium and titanium alloys are strongly anisotropic, and their behaviour during service is affected by this anisotropy in the presence of strong crystallographic texture. Anisotropic irradiation assisted growth is one example of the multiple phenomena that zirconium crystals undergo during service in nuclear reactors, affecting the performance of components due to the presence of strong textures, which are developed during manufacturing processes. Zirconium crystals deform anisotropically under irradiation, which in turn causes undesirable deformation of components. For this reason, the nuclear industry is interested in developing thermomechanical processes that produce random textures in certain zirconium products, by taking advantage of the allotropic phase transformation undergone by

zirconium, from the low temperature hexagonal close-packed alpha (α) phase to the high temperature body-centred cubic beta (β) phase. One important industrial development is a process called β-quenching, which consists of heating the material above the β-transus followed by rapid cooling. Although this process has exhibited certain success in weakening strong rolling textures (Dahlbäck *et al.* 2005), there is no consensus about the fundamental mechanisms responsible for this, and in general for texture development during β-quenching.

The ultimate goal of the present work was to gain understanding on the mechanisms involved on the texture development and evolution during the $\alpha \rightarrow \beta$ and $\beta \rightarrow \alpha$ phase transformations, and help optimise the processing parameters to enhance in-service performance. For this purpose, different techniques for texture and microstructure characterisation were employed, including laboratory X-ray diffraction (LXRD), electron backscatter diffraction (EBSD) and synchrotron X-ray diffraction (SXRD).

This thesis has been divided into seven chapters. The first two chapters review important concepts necessary to understand the results presented subsequently: Chapter 1 deals with texture and anisotropy in general, while Chapter 2 covers the metallurgy of zirconium and its alloys. The following four chapters correspond to different stages of the work carried out in an approximate chronological sequence, reflecting the reasoning during the project. Each chapter constitutes a self-contained piece of work. Chapter 3 starts with the characterisation of Zircaloy-2 samples that were

β-quenched industrially, which led to the subject of Chapter 4: an experiment designed to measure the texture evolution of cold-rolled Zircaloy-2 during β-quenching in-situ using SXRD. SXRD is an innovative approach to study texture, useful in cases where rapid changes occur and/or certain phases are not retained at room temperature, e.g. the β phase in Zircaloy-2. Chapter 4 describes in detail the experimental setup and the data post-processing. Chapter 5 is an extension of the in-situ SXRD experiment, where advanced analyses of posterior EBSD characterisation of the samples tested in-situ are presented. Chapter 6 reports results obtained from β-quenching samples in laboratory furnaces, which were made firstly to mimic the conditions of the industrial process and secondly to expand the range of variables employed with respect to that used in the SXRD experiment, specifically the peak temperature.

Finally, Chapter 7 presents a comprehensive discussion on variant selection, correlating the different results presented in the previous chapters with the relevant literature, and relating the findings of this project to those on other systems such as titanium alloys and steel. This final chapter and the ensuing conclusions summarise the knowledge gained with this project. It is hoped that these conclusions will not only contribute to the understanding of the fundamental mechanisms governing texture evolution during phase transformations, but that the new understanding will also be of benefit for the technological development of thermomechanical processes for zirconium and titanium alloys in the nuclear and aerospace industry.

CHAPTER 1

TEXTURE AND ANISOTROPY

Zirconium alloys, like most engineering metals, are polycrystalline. They consist of an aggregate of grains or crystals, each defined by a crystallographic orientation. The distribution of crystallographic orientations within a polycrystal in most cases is not random and is called texture. This preferential crystallographic orientation affects the mechanical and physical properties of the material, because of the anisotropy of properties of the individual crystals. Most materials develop texture during solidification from a melt, and later during thermomechanical processing (Randle 2001, Wenk and Van Houtte 2004). In this chapter, the main concepts of texture analysis will be revised to establish a platform from which the results in the following chapters can be understood.

1.1 TEXTURE REPRESENTATION

The orientation of crystals can be described and represented in several ways, representations that are used to quantify and visualise texture for systematic study. In

the following sections the basic and most commonly used methods for orientation

representation will be discussed.

1.1.1   DESCRIPTORS OF ORIENTATION

Crystal orientation is defined as the position of the crystal coordinate system with

respect to the specimen coordinate system. At least three independent quantities are

required to describe it. These can be expressed in different ways, creating the different

orientation descriptors (Kelly *et al.* 2000). In this project several orientation descriptors

were employed. Different definitions of Euler angles were used to represent

observed/ideal orientations and to analyse orientation maps. Orientation matrices and

quaternions were used for calculation of orientations during phase transformations and

within reconstruction algorithms, while axis/angle descriptions were occasionally used

in discussions involving misorientation. The following paragraphs describe each of

these orientation descriptors separately.

Euler Angles

Euler angles represent three rotations of a crystal with respect to a fixed coordinate

system. By performing these rotations in the correct sequence, the specimen coordinate

system is transformed onto the crystal coordinate system, which specifies completely

the orientation of the crystal. The Euler angles correspond to the following rotations as

defined by Bunge (Bunge 1982), and illustrated in Figure 1.1:

1. φ_1 about the *z* axis.

2. Φ about the rotated *x* axis.

3. φ_2 about the new rotated *z* axis.
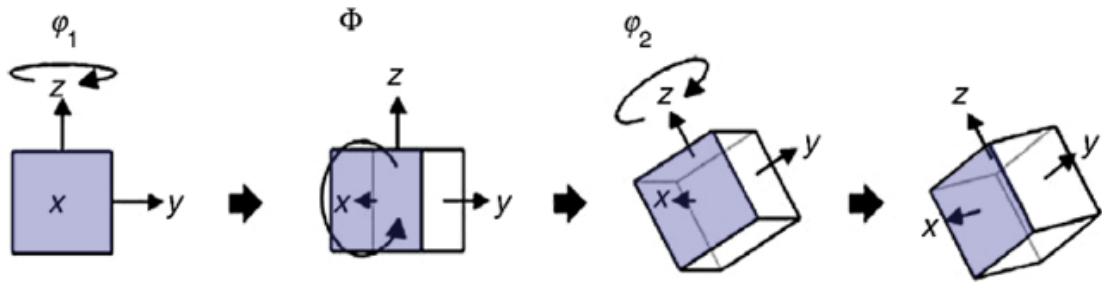
Figure 1.1 Definition of Euler angles (HKL Technology 2006)

An orientation can be then expressed as a point in a three-dimensional coordinate system whose axes are the Euler angles. The volume defined in this way is called Euler space. Euler angles are the most traditional way to represent arbitrary orientations and are strongly related to X-ray diffraction measurements. The main disadvantage of this descriptor is the difficulty to visualise orientation in the 2D representations of the Euler space and the distortions in some of its zones (Randle and Engler 2000, Kocks 1998). There are other definitions of Euler angles, with differences based on the direction of rotation and the choice of rotation axis for the second angle. The most commonly used Euler angle definitions are illustrated in Figure 1.2, and the conversions between them are listed in Table 1.1. Bunge $\left(\varphi_1, \Phi, \varphi_2\right)$ and Roe-Matthies $\left(\alpha, \beta, \gamma\right)$ were the definitions employed in this project.
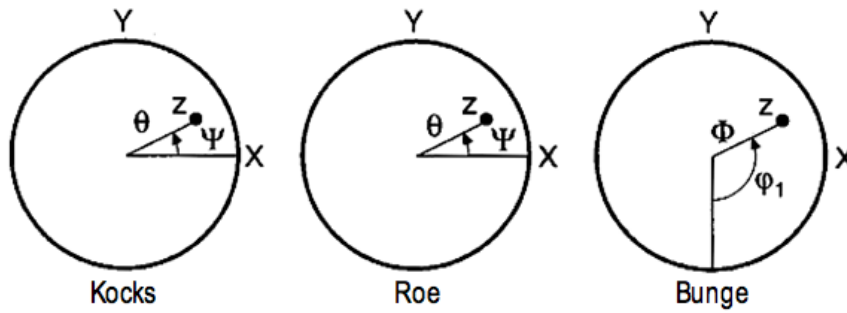
Figure 1.2 Comparison of Euler angles definitions, shown as spherical coordinates in the sample system (Kocks 1998)

Table 1.1 Comparison of Euler angles definitions (Kocks 1998)

Convention	1st	2nd	3rd	2nd angle about axis
Kocks	Ψ	Θ	ϕ	Y
Bunge	$\varphi_1 - \pi/2$	Φ	$\pi/2 - \varphi_2$	X
Roe-Matthies	α	β	$\pi/2 - \gamma$	Y

Orientation Matrix

Another fundamental orientation descriptor is a matrix that represents the rotation of the specimen coordinates on the crystal coordinates (Bunge 1982). The matrix representation is convenient in many practical cases, particularly when computations are required. It is a square matrix of size 3x3. The first row of the matrix is given by the cosines of the angles between the first crystal axis $[100]$ and each of the three specimen axes X, Y and Z, which should be well defined directions in the specimen, preferably associated with its processing. The second row of the matrix corresponds to the cosines of the angles between the second crystal axis $[010]$ and the specimen axes. The third row comprises the cosines of the angles between $[001]$ and X, Y and Z (Randle 2001). The orientation matrix is illustrated in Figure 1.3.

$$\begin{bmatrix} g_{11} & g_{21} & g_{31} \\ g_{21} & g_{22} & g_{23} \\ g_{31} & g_{32} & g_{33} \end{bmatrix} \begin{matrix} [100] \\ [010] \\ [001] \end{matrix}$$

POLE FIGURES

$X = RD \quad Y = TD \quad Z = RD$

INVERSE POLE FIGURES

Figure 1.3 Rows and columns of the orientation matrix (Bunge 1982)

The rotation matrix has interesting and useful mathematical properties. The rotation matrix is orthonormal, i.e. the rows and the columns of the matrix are unit vectors. The inverse of an orthonormal matrix is equal to its transpose. Since only three independent quantities are required to represent the orientation, it is obvious that there are some non-independent terms in the orientation matrix. For example, the cross product of any two rows or columns gives the third. The elements of the orientation matrix in terms of the Euler angles are given by (Randle 2001):

$$g_{11} = \cos\varphi_1 \cos\varphi_2 - \sin\varphi_1 \sin\varphi_2 \cos\Phi \qquad \text{Equation 1.1}$$
$$g_{12} = \sin\varphi_1 \cos\varphi_2 + \cos\varphi_1 \sin\varphi_2 \cos\Phi$$
$$g_{13} = \sin\varphi_2 \sin\Phi$$
$$g_{21} = -\cos\varphi_1 \sin\varphi_2 - \sin\varphi_1 \cos\varphi_2 \cos\Phi$$
$$g_{22} = -\sin\varphi_1 \sin\varphi_2 + \cos\varphi_1 \cos\varphi_2 \cos\Phi$$
$$g_{23} = \cos\varphi_2 \sin\Phi$$
$$g_{31} = \sin\varphi_1 \sin\Phi$$
$$g_{32} = -\cos\varphi_1 \sin\Phi$$
$$g_{33} = \cos\Phi$$

Axis/Angle

Any orientation can be also represented as a rotation of the crystal about a specific axis. This is known as an axis/angle pair. This descriptor is useful when the reference orientation is not necessarily the coordinate system of the specimen, but for example the orientation of a neighbour crystal or grain. In that case the misorientation between the two crystals can be represented easily by a common axis and an angle (Heinz and Neumann 1991).

Rodrigues Vector

Rodrigues vector is an extension of the axis/angle pair. The Rodrigues vector combines the angle θ and the axis of rotation r (with components r_1, r_2, r_3) into one single mathematical term:

$$\mathbf{R} = \tan(\theta/2)\mathbf{r} \qquad \text{Equation 1.2}$$

Using this vector, orientations or misorientations can be displayed in a three-dimensional space known as Rodrigues-Frank (RF) space or simply as Rodrigues space. The axes of the RF space can be either the specimen (to represent orientation) or the crystal axes (to represent misorientation).

The use of both the axis/angle notation and the Rodrigues vector has increased recently, since these descriptors have been found more functional to represent misorientation (Heinz and Neumann 1991).

Quaternions

Quaternions are defined as a four dimensional vector related to the axis/angle representation as follows (Kocks 1998):

$$\mathbf{q} = q(q_1, q_2, q_3, q_4) = q(u\sin\theta/2, v\sin\theta/2, w\sin\theta/2, \cos\theta/2) \quad \text{Equation 1.3}$$

Where $[uvw]$ are the components of the unit vector representing the rotation axis, and θ is the rotation angle.

Quaternions, when used for representation of orientations or rotations, are vectors of unit length, thus, they satisfy the following normalisation condition:

$$\sqrt{\left\{ q_1^{\,2} + q_2^{\,2} + q_3^{\,2} + q_4^{\,2} \right\}} = 1 \quad \text{Equation 1.4}$$

Quaternions have many advantages. For visualisation purposes, they offer a finite space, enclosed in a sphere of unit radius, whereas the Rodrigues space tends to infinity. Perhaps the most important advantage of quaternions is the reduction of calculation work when combining several rotations, either if it is performed numerically or algebraically. Quaternions are the most efficient way of performing computations on

combined rotations, because of the small number of operations required to calculate the product of two rotations (Frank 1988, Altmann 1986). For example, in this project quaternions were used to calculate averages between orientations. Quaternions are widely used for misorientation calculations because they reduce the computing time considerably (Humbert and Gey 2002). Other interesting feature is that quaternions allow distinguishing between positive and negative rotations, although for rotations such as those found in materials, positive and negative rotations are physically indistinguishable. The study of quaternions forms a complete field of mathematics and algebra.

1.1.2   CRYSTAL AND SAMPLE SYMMETRY

The coordinate system of the crystal and the coordinate system of the sample are related with a specific orientation. However, the specification of these coordinate systems is often not unique, and several solutions, i.e. possibilities or representing this relation, can exist depending on the symmetry of both the sample and the crystal. Any rotation that leaves the sample indistinguishable from how it was before must also leaves its properties unchanged (Kocks 1998).

For a cubic crystal, there are 24 crystallographically equivalent solutions. These solutions can be found by multiplying the initial orientation matrix by each one of the so-called 'symmetry matrices'. Other crystals have fewer crystallography-related solutions: hexagonal crystals have twelve and orthorhombic crystals have four.

The selection of a particular symmetry matrix can facilitate the representation and analysis of acquired data using the orientation descriptors mentioned in section 1.1.1. For this reason, crystal and sample symmetry are important to understand the physical meaning of texture data. Additionally, it is known that anisotropy of a macroscopic property is caused by combination of two factors: anisotropy of the particular property in single crystals of the material, and the absence of symmetry in the macroscopic sample (Kocks 1998).

Apart from the symmetries given by the crystal, there can be sample symmetry generated by processing of the material, e.g. wire drawing or sheet rolling. Particular geometries of deformation produce particular symmetries in the crystallographic orientation. A common symmetry found in materials is uniaxial or 'fibre' symmetry. A wire that was initially isotropic and then pulled in tension, or an isotropic sample subjected to compression, will have fibre symmetry in the volume surrounding the load axis, i.e. the properties are transversely isotropic.

Some processes have an orthogonal coordinate system associated with them. Sheet rolling is perhaps the most common of these cases. In ideal sheet rolling there is 'plane-strain compression', i.e. there is a plane of symmetry perpendicular to each of the three directions: the rolling plane normal (ND), the rolling direction (RD) and the transverse direction (TD). This symmetry is called orthotropic, the three axes of orthotropy are given by the intersection of the three mirror planes (Kocks 1998).

Orthotropic sample symmetry was consistently observed in the material studied in this project.

1.1.3   POLE FIGURES AND INVERSE POLE FIGURES

So far, it has been discussed how a single orientation can be described by mathematical entities. These mathematical entities are often represented graphically for analysis purposes. Pole figures are perhaps the most common method of texture representation. To construct a pole figure, poles from the lattice planes are projected in an imaginary reference sphere, often called the unit sphere, surrounding the crystal. A point on the surface of the sphere will then represent the orientation of that particular lattice plane with respect to the reference frame. The position of a pole is given by two angles: α, describing the azimuth of the pole, and β, which represents the rotation of the pole around the polar axis The pole figure corresponds to the two-dimensional projection of the unit sphere on the equatorial plane. Figure 1.4 exemplifies the definition of pole figures using the $\{100\}$ poles of a cubic crystal.
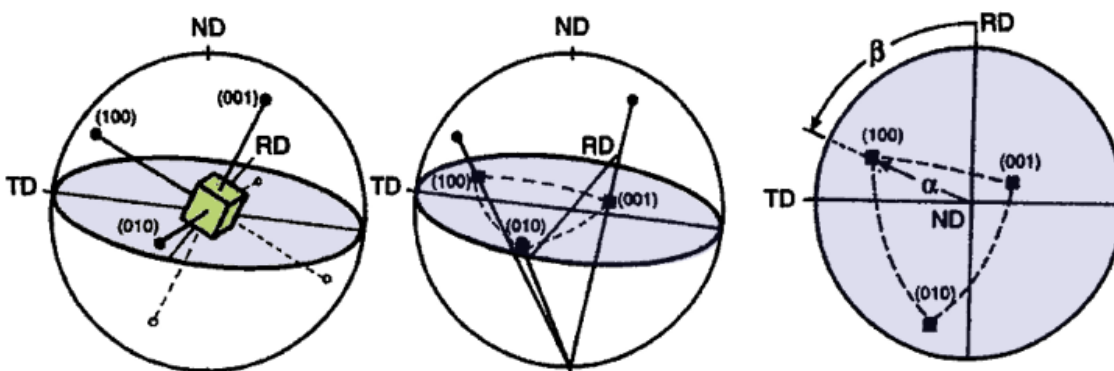
Figure 1.4 Definition of pole figures: (a) the unit sphere surrounding a cubic crystal (b) stereographic projection (c) projection plane (Randle 2001)

In Figure 1.4 the 2D projection is stereographic. However, there is another type of projection called 'equal-area', which was used more extensively in this project, since it is better for visualising orientation distributions because each area in the figure represents correctly the fraction of orientation space covered. Figure 1.5 illustrates this point: a set of points that is randomly distributed on the surface of the sphere appears uniform in the equal-area projection, whereas in the stereographic projection it looks concentrated in the centre and sparse at the periphery. In this project, equal-area projection pole figures were used unless stated otherwise.
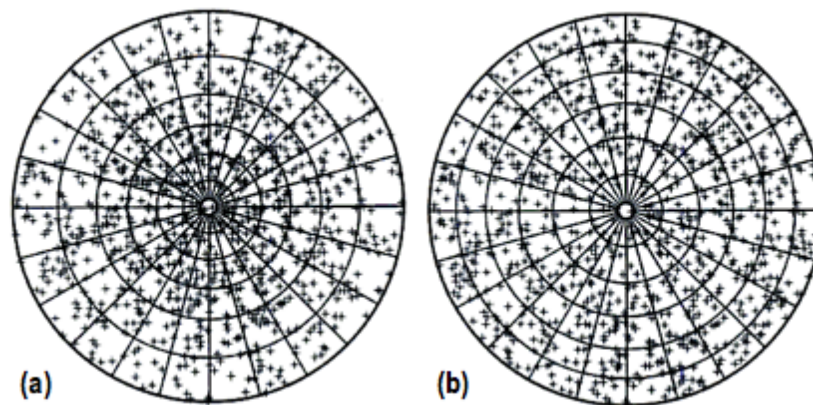
Figure 1.5 Stereographic (a) and equal area (b) projections of a set of random orientations (Kocks 1998)

The orientations of the grains within a polycrystal can be therefore represented as a collection of points in the pole figure. The discrete points do not illustrate the distribution of poles very clearly, so it is common to divide the area of the pole figure in sections, and assign pole intensities according to the number of poles falling in each section. The pole distribution can be then easily visualised if contours or colours of equal level of intensity are drawn in the pole figure.

In order to make pole figures comparable, the pole densities must be normalised to units that are non-dependant on the experimental parameters (Wenk and Kocks 1987). There are two possibilities of normalisation: to a value of one for the average or to a value of one for the integral. A random distribution would correspond ideally to a uniform distribution, so the normalized continuous pole densities in a textured sample are expressed as 'multiples of a random distribution (mrd)', or better 'multiples of uniform intensity' (Kocks 1998).

Inverse pole figures (IPF) are also projections of poles, but in IPFs the orientation of the specimen coordinate system is represented onto the crystal coordinate system. IPFs are often used for axisymmetric specimens. Because of the crystal symmetry, it is not necessary to show the entire pole figure, but one single triangle is enough to represent the distribution of poles.

1.1.4   ORIENTATION DISTRIBUTION FUNCTIONS

A single pole figure is only capable of displaying two-dimensional information. Therefore, since a complete description of an orientation requires three independent quantities, it is necessary to show at least two pole figures to completely characterise the orientation distribution. In polycrystals, the crystallographic orientation becomes a probability distribution, which is described by an orientation distribution function (ODF). ODFs are usually shown in Euler space, where the data are represented directly as density distributions.

In order to obtain full texture data expressed as an ODF, a calculation that uses several pole figures as input must be performed. Such calculation is known as pole figure inversion (Kallend 1998). There are physical and mathematical relations between ODFs and pole figures. Several approaches have been developed to derive ODFs from experimental pole figures, which can be classified into two groups: those in which the computations are performed in Fourier space (harmonic methods), and those in which the computations are performed directly in orientation space (direct or discrete methods).

Harmonic Method

The harmonic method is based on the principle of fitting a series expansion to the ODF and pole figure data. Spherical harmonic functions are the most appropriate series expansion for spherical coordinate systems, which is the case of orientation data from experimental pole figures. A complete scheme on the use of spherical harmonics for texture analysis was proposed and extensively described by Bunge (Bunge 1982), the basics of which is outlined below.

The ODF is represented by a series expansion of generalised spherical harmonic functions:

$$f(\varphi_1, \Phi, \varphi_2) = \sum_{l=0}^{\infty} \sum_{\mu=1}^{M(l)} \sum_{\nu=1}^{N(l)} C_l^{\mu\nu} T_l^{\mu\nu}(\varphi_1, \Phi, \varphi_2) \qquad \text{Equation 1.5}$$

Where $T_l^{\mu\nu}(\varphi_1,\Phi,\varphi_2)$ are the spherical harmonic functions and $C_l^{\mu\nu}$ the coefficients that

completely describe the series expansion. The pole figures can also be expanded in a

series expansion:

$$p(\alpha,\beta) = \sum_{l=0}^{\infty}\sum_{\nu=1}^{N(l)} F_l^n k_l^n(\alpha,\beta) \qquad \text{Equation 1.6}$$

Where F_l^n are the pole figure coefficients, and $k_l^n(\alpha,\beta)$ are symmetrised spherical

harmonic functions. The two-dimensional series expansion coefficients F_l^n are related

to the ODF coefficients through:

$$F_l^n = \frac{4\pi}{2l+1}\sum_{\mu=1}^{M(l)} C_l^{\mu\nu} k_l^{*\mu}(\xi,\eta) \qquad \text{Equation 1.7}$$

Where $*$ denotes complex conjugate, and ξ and η are the polar coordinates of the (hkl)

pole in the crystal coordinate system. This equation forms a system of linear equations,

which can be solved to determine the coefficients $C_l^{\mu\nu}$. For this calculation, the missing

data from incomplete experimental pole figures can sometimes be obtained by

extrapolation using a third-order polynomial. In general, the number of pole figures

necessary to obtain a solution is 3-4 and 5-6 for cubic and hexagonal crystals

respectively (Kallend 1998).

The advantages of the harmonic method are that it is economical, it does not consume

considerable computer memory, and it can be used to estimate the experimental error of

the ODF. The truncation of the series expansion at a certain value l (typically 22) has

the effect of applying a noise filter, assuming that the ODF is a smooth function and this truncation will not affect the solution. The major disadvantage of the harmonic method is the so-called ghosts, which are basically false maxima and minima. Negative values appear occasionally. Additional procedures are required to correct for ghosts when the harmonic method is used (Kallend 1998).

Discrete Methods

The discrete methods are essentially iterative algorithms executed in orientation space to determine the ODF. Both the ODF and the pole figures are represented by discrete values, dividing their domains into regular grids, normally with a spacing of 2.5°, 5° or 10°. A pole $p(\alpha,\beta)$ in a pole figure corresponds to a region in the three dimensional ODF $f(\varphi_1,\Phi,\varphi_2)$ which contains all possible rotations γ about this direction in the pole figure. Mathematically:

$$p(\alpha,\beta) = \frac{1}{2\pi} \int\limits_{0}^{2\pi} f(\varphi_1,\Phi,\varphi_2)d\gamma \qquad \text{Equation 1.8}$$

If the ODF and the pole figures are discretised then the integral becomes a finite summation for each pole figure cell, where only the orientation cells that contribute to intensity in the pole figure are taking into account. This equation defines a set of linear equations, which under appropriate conditions can be solved to obtain the ODF.

The approach of most direct methods is to make an initial estimation of the ODF and then calculate the pole figures that would result from it. The calculated pole figures are compared with the experimental data cell by cell. This procedure is repeated until certain convergence requirements are achieved. The so-called WIMV (Williams-Imhof-Matthies-Vinel) method (Matthies and Vinel 1982) is perhaps the best and most widely used example of discrete methods. In the WIMV method the initial $f_0(\mathbf{g})$ values of each ODF cell are estimated by the geometric mean of the values in the corresponding cells of the contributing experimental pole figures:

$$f_0(\mathbf{g}) = N_0 \prod_{j=1}^{I} \prod_{m_i=1}^{M_i} p_{h_i}^{\exp}(\mathbf{y}_{m_i})^{\frac{1}{IM_i}} \qquad \text{Equation 1.9}$$

Where $p^{\exp}$ denotes the experimental pole figure and $\mathbf{y}$ represents a point on the pole figure (α, β). I is the number of measured pole figures, M_i is the multiplicity of the ith pole and N_0 is the normalisation. Vector $\mathbf{g}$ corresponds to the three Euler angles $(\varphi_1, \Phi, \varphi_2)$.

The ODF is refined subsequently by 'inner iterations' as follows. If p^n represents the recalculated pole figure after the nth iteration step, the correction factor of each OD cell is the ratio of the geometric mean of the corresponding experimental pole figure cells to the mean of the corresponding recalculated pole figure cells. The algorithm converges rapidly, after 10-12 cycles a satisfactory solution is normally achieved.

$$f_{n+1}(\mathbf{g}) = N_n f_n(\mathbf{g}) \frac{f_0(\mathbf{g})}{\prod\limits_{i=1}^{I} \prod\limits_{m_i=1}^{M_i} p_{h_i}^n \left(\mathbf{y}_{m_i}\right)^{\frac{1}{IM_i}}} \qquad \text{Equation 1.10}$$

The WIMV and other direct methods have the advantage that they cannot generate

negative values for $f(\mathbf{g})$, and any zero in a pole figure will give zeros in the ODF.

These physical constraints are not very well met by the harmonic method, which

together with the absence of ghosts are the main advantages of the discrete algorithms.

One of the important disadvantages of the direct methods is the susceptibility to noise if

additional filtering is not applied (Kallend 1998).

The selection of any of the described pole figure inversion methods depends on the data

collected and the aim of the measurement. For instance, if the goal is to calculate simple

averages in high symmetry materials, then the classical harmonic method offers almost

no disadvantages. If only incomplete pole figures are available, the classical harmonic

method has limitations and direct algorithms should be considered. In general, the direct

methods require fewer pole figures than the harmonic method to obtain a satisfactory

solution. There are many free and commercial software tools to calculate ODFs from

pole figures. Some examples are MAUD (Lutterotti *et al.* 1997), BEARTEX (Wenk *et al.* 1998) and POPLA (Kallend *et al.* 1991).

1.1.5   NUMERICAL REPRESENTATIONS

Inverse/direct pole figures and graphical representations of ODFs are useful only for

qualitative analysis, which has motivated different attempts to express the global texture

strength of a polycrystal numerically, specially when the details of the orientation components present are not of interest.

Texture Index

A very convenient numerical representation of texture is the so-called texture index, which is the mean square value of the ODF, normalised to multiples of a random distribution. This value is easily computable from ODF data or from harmonic coefficients (Bunge 1982). An absolute random texture will give a texture index of 1. Higher texture indices correspond to stronger textures.

Kearns Factor

Other numerical parameters have been developed, such as the Kearns factor (Kearns 2001) and the Källström F-parameter, although their usefulness and reliability is still under discussion within the crystallography community (Linga-Murty and Charit 2006). However, within the zirconium community, the Kearns factor has become widely used and accepted. The Kearns factor describes the effective fraction of hexagonal crystals with the basal pole aligned along a particular sample axes. The value is given by (Anderson *et al.* 1999):

$$f_1 = \frac{1}{N} \int_0^{\pi/2} \int_0^{2\pi} I(\alpha,\beta)\sin^3(\alpha)\cos^2(\beta)d\beta d\alpha \qquad \text{Equation 1.11}$$

Where f_1 is the Kearns factor along a given direction, e.g. the rolling direction f_{RD}. $I(\alpha,\beta)$ is the X-ray intensity for a basal pole figure at a certain combination of polar and azimuthal angles from that direction. The normalization constant is:

$$N = \int_0^\pi \int_0^{2\pi} I(\alpha,\beta)\sin(\alpha)d\beta d\alpha \qquad \text{Equation 1.12}$$

The Kearns factors can be easily related with the orientation distribution coefficients defined by Roe (Roe 1965), which are analogous to those defined by Bunge (Bunge 1982) and discussed above. For an aggregate of hexagonal crystals with orthotropic symmetry the Kearns factors are defined by the following equations (Anderson *et al.* 1999):

$$\begin{aligned} f_1 &= f_{RD} = K_1 W_{000} - K_2 W_{200} + K_3 W_{220} \\ f_2 &= f_{TD} = K_1 W_{000} - K_2 W_{200} - K_3 W_{220} \qquad \text{Equation 1.13} \\ f_2 &= f_{ND} = K_1 W_{000} + K_3 W_{220} \end{aligned}$$

Where W_{lmn} represent Roe orientation distribution coefficients. The constants are defined as follows:

$$K_1 = \frac{4\pi^2\sqrt{2}}{3} \quad K_2 = \frac{4\pi^2\sqrt{10}}{15} \quad K_3 = \frac{8\pi^2\sqrt{15}}{15} \qquad \text{Equation 1.14}$$

Therefore, if the orientation distribution coefficients are known, the calculation of the Kearns factors is relatively straightforward. In this project, both the Kearns factor and

the texture index were used occasionally to compare general texture strength in different specimens.

1.2   TEXTURE MEASUREMENT

The majority of the techniques for texture measurement are based on diffraction of X-rays, electrons or neutrons. The suitability of each technique depends strongly on the wavelength of the radiation source employed, which in turn is proportional to its energy. The volume of material irradiated, from which orientation information is obtained, determines the difference between macrotexture and microtexture measurements (Randle 2001).

The main texture measurement techniques currently in use are X-ray diffraction, neutron diffraction and Electron Backscatter Diffraction (EBSD). Other techniques exist, such as selected area channelling in an SEM and TEM, but they are not as developed as the former. TEM techniques are applied in specific cases, especially if high deformations are involved or if dislocation structures are to be studied to evaluate deformation mechanisms and relate them to the texture. Other indirect and qualitative texture measurement methods such as ultrasonic, magnetic, acoustic or optical, are occasionally used (Randle and Engler 2000).

In this project, the measurement techniques employed were EBSD and X-ray diffraction. X-ray diffraction was employed in two forms: SXRD and conventional

LXRD using a goniometer. In the following paragraphs, the techniques used will be described in detail.

1.2.1   LABORATORY X-RAY DIFFRACTION (LXRD)

LXRD is a well-established technique for macrotexture measurement, which provides an averaged texture for the volume of material irradiated. For this reason it is very efficient to obtain an overview of the texture in a polycrystal.

The basic principle for X-ray diffraction is Bragg's law:

$$n\lambda = 2d\sin\theta \qquad \text{Equation 1.15}$$

Where n is the order of the reflection, λ is the wavelength of the radiation, d is the interplanar lattice spacing and θ is the angle of reflection. This law establishes that for a given lattice spacing and wavelength, any incident radiation will only be diffracted if the lattice planes are at a specific angle with respect to the incident beam.

Figure 1.6 (Wenk et al. 2004) depicts the typical geometry of a LXRD measurement. By placing the sample in a goniometer where the diffraction angle (2θ) can be changed and the sample can be rotated (φ) and tilted (ψ), the orientation of different sets of planes with respect to a reference frame can be determined. The material is irradiated with a monochromatic (fixed wavelength) beam at the proper diffraction angle to reflect from certain specific lattice planes, and the X-ray detector is set at the angle 2θ with respect

to the incident beam. A reflected intensity is detected only if the corresponding lattice planes are oriented in such a way that their normal bisects the angle between the incident and the reflected beam (Wenk 1998).
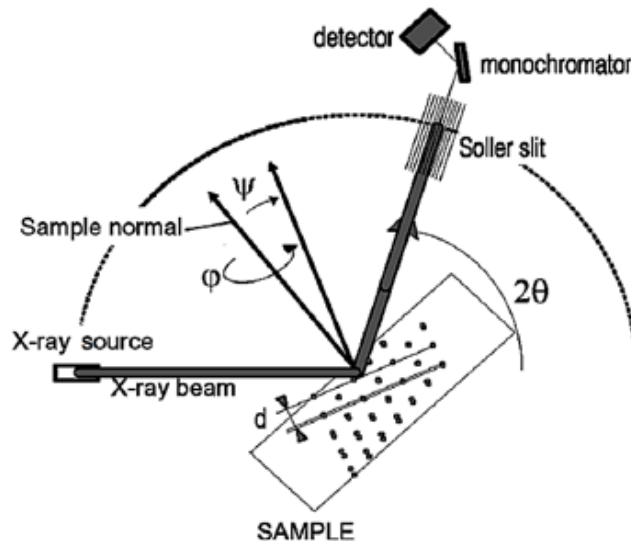
Figure 1.6 LXRD pole figure measurement geometry (Wenk et al. 2004)

In a pole figure measurement, the diffraction angle is kept constant and the sample is systematically rotated and tilted, while the intensities are recorded as a function of the rotation/tilting angles. The intensity recorded at a certain sample orientation is proportional to the volume fraction of grains in diffraction condition (Wenk and Van Houtte 2004, Randle 2001).

One single incomplete pole figure is normally not enough to describe the orientation of the crystals of the material. Normally more than one pole figure is measured, i.e. the diffraction angle is changed to angles corresponding to characteristic crystallographic

planes of the material, and the sample is rotated and tilted again to acquire a new pole figure.

Due to defocusing effects as the sample is tilted, as well as variations in the irradiated volume and absorption, intensity and background corrections are necessary, especially if the reflection geometry is employed. In reflection geometry only incomplete pole figures can be measured, usually to a pole distance of 80-85° from the normal of the sample surface, i.e. the tilting angle ψ normally does not exceed 85°. Defocusing can either be measured, using a non-textured sample of the material to be analysed (e.g. a powder), or calculated if the shape of the diffraction peaks is known. Background intensities are measured and subtracted from the diffraction signal (Randle and Engler 2000). The set of corrected pole figures is eventually combined for the calculation of a complete ODF, as described in section 1.1.4. Once the ODF is obtained, complete pole figures can be calculated from it.

1.2.2   SYNCHROTRON X-RAY DIFFRACTION (SXRD)

The recent availability of extremely high-energy (above 60 keV) X-ray sources allows exploiting them for texture measurement. Laboratory X-ray beams generated by conventional tubes are normally broad and have low intensity. High-energy synchrotron X-rays do not have these two problems, making synchrotron a promising technique for texture measurement. In a synchrotron, a focused, high intensity, white or monochromatic, beam can be used. The main advantages offered by synchrotron

radiation are high intensity, small beam size and wide choice of wavelength. High-energy synchrotron radiation yields a much greater penetration depth, up to the order of centimetres depending on the absorption of the material, compared to values of about 100μm in conventional LXRD (Wenk and Van Houtte 2004, Randle and Engler 2000).
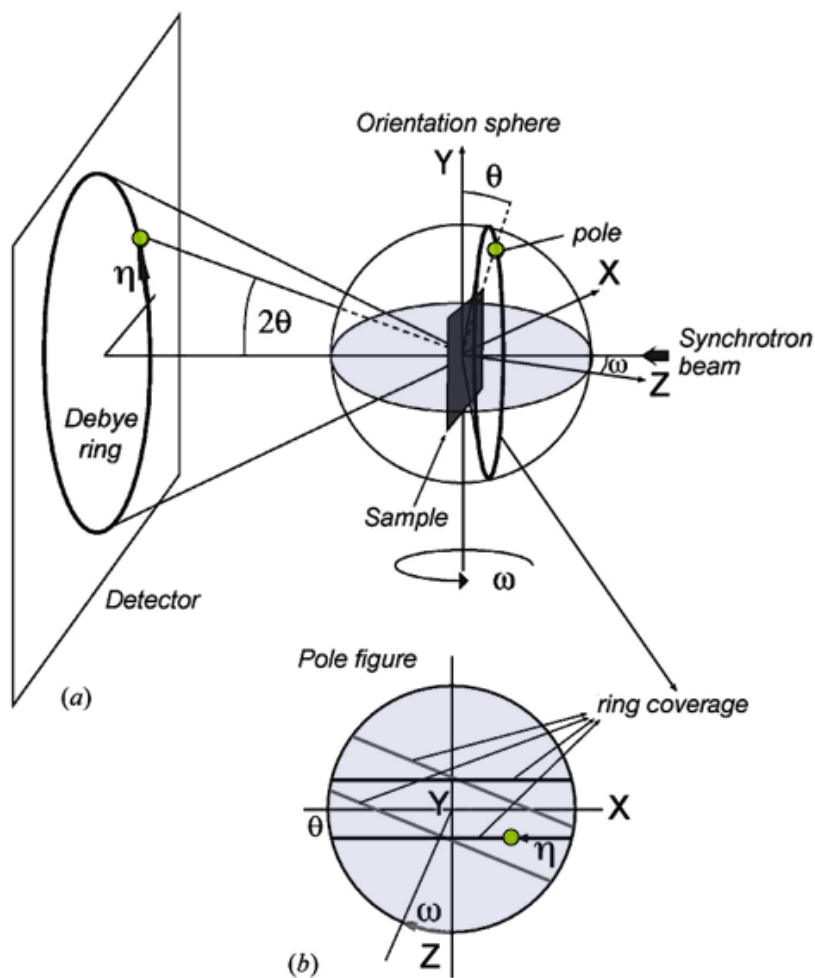
Figure 1.7 SXRD for texture measurement: (a) geometry and (b) pole figure coverage (Lonardelli *et al.* 2005)

The diffraction geometry used in a high-energy SXRD experiment for texture measurement can be seen in Figure 1.7(a) (Lonardelli *et al.* 2005). A beam is focused

on the sample and transmission diffraction images are recorded with a two-dimensional detector or a CCD camera placed perpendicular to the beam. These images display instantaneously the presence of texture as systematic variations of intensity along Debye-Scherrer rings with an opening angle 4θ. Only lattice planes *hkl* that are inclined at an angle of 90°- θ with respect to the incident beam will satisfy the diffraction condition, and the corresponding reciprocal lattice vectors lie on a cone with an opening angle of 180° - 2θ. This cone intersects the orientation unit sphere in a small circle with a radius or pole distance equal to 90°- θ. The polar angle η on the Debye-Scherrer ring corresponds to the pole sphere azimuth when viewed along the incident beam. Because of central symmetry, there is an equivalent circle on the opposite hemisphere.

Pole Figure Coverage

One of the main issues arising when measuring texture with any diffraction technique is pole figure coverage, which is the availability of experimental data to fill the cells of the orientation space (Wenk and Grigull 2003). For the case of transmission X-ray diffraction geometry, each diffraction ring will provide experimental intensities along two circles in the unit sphere, i.e. two lines in the corresponding pole figure, as illustrated in Figure 1.7(b) viewing along the axis Y. The separation between these two lines is 2θ. In the figure the lines are drawn schematically as straight lines, in reality they are curved, if seen in equal area projection. The intensity variation along the ring, as a function of the polar angle η, is directly proportional to the pole intensities along

the lines. By rotating the sample about the Y axis, i.e. changing ω, the pole intensity lines in the pole figures are rotated by the same angle. Images with different rotation angles can be combined to improve pole figure coverage (Lonardelli *et al.* 2005).

Fitting Synchrotron Diffraction Data

Although qualitative assessment of the presence of texture is straightforward, extensive and elaborated data processing is required to determine texture components quantitatively. The procedure of pole figure inversion is efficient if enough pole figures are used and the intensities are well separated with respect to the background. Such analysis becomes difficult when multiphase materials are studied or when the amount of texture information for the calculation is not high, i.e. when too few pole figures or too few sample orientations are used. If that is the case, a more careful fitting of the diffraction data should be performed.

Rietveld analysis (Rietveld 1969) is a method to obtain crystallographic information from continuous powder diffraction patterns, which has been expanded for texture analysis. If a sample has random texture, e.g. a powder, the relative intensities between reflections for all the sample orientations are the same. In a textured material, the intensities change systematically. Such changes can be related to the crystal structure by the structure factor, and can be used to calculate an ODF. The ODF can be implemented in the Rietveld method, either using harmonic or direct methods, and can be refined with a non-linear least square procedure similar to that used to refine crystallographic

parameters. Texture analysis using the Rietveld method has been implemented in several software packages such as GSAS (Von Dreele 1997) and MAUD (Lutterotti *et al.* 1997).

Some initial results have been reported in a range of materials (Heidelbach *et al.* 1999, Wenk and Grigull 2003, Ischia *et al.* 2005, Lonardelli *et al.* 2005), in which the Rietveld method and a modified WIMV algorithm were applied to obtain quantitative texture information from the processing of single SXRD images, without rotating the specimen. In order to maximise the potential of this method some important assumptions have to be made during the data post-processing. Nevertheless, some promising results were reported in cases with high crystal symmetry, even when the number of grains sampled is small. Compared to other diffraction techniques, SXRD texture measurement is extremely fast and can achieve very high spatial resolution. It opens a window for interesting studies that may include:

· In-situ texture measurements during thermomechanical processing, including phase transformation and rapid heating/cooling/loading.

· Non-destructive local texture measurements.

· High spatial resolution texture analysis, including investigation of texture gradients.

· Correlation between internal strain and texture.

In this project SXRD was an important tool in the study of texture evolution during the α→β→α phase transformation on a zirconium alloy. Details of the technique employed and the results obtained are discussed in detail in Chapter 4.

1.2.3   NEUTRON DIFFRACTION

Because neutrons have no electric charge, they exhibit usually much larger useful penetration depths than X-rays or electrons. However, the low interaction of neutrons with matter makes long counting times necessary to achieve suitable diffraction intensities.

Neutrons allow texture measurement in much larger specimens compared to SXRD, which provides the opportunity for non-destructive and in-situ experiments without the risk of poor grain statistics. Even with coarse-grained materials or with low volume fractions of certain second phases, the statistics can be good enough to build reliable representations of global texture (Wenk and Van Houtte 2004). Environmental stages (heating, cooling, straining) can be combined with neutron sources for in-situ observation of texture changes, e.g. during phase transformations. Several successful experiments have been carried out on dedicated instruments such as the HIPPO (High Pressure Preferred Orientation) diffractometer at LANSCE (Los Alamos Neutron Science Centre) (Matthies *et al.* 2005), some of them in materials of interest for this project, such as Zircaloy-4 (Wenk *et al.* 2004) and commercially pure (CP) titanium (Lonardelli *et al.* 2007, Bhattacharyya *et al.* 2006).

1.2.4   ELECTRON BACKSCATTER DIFFRACTION (EBSD)

EBSD is a technique based on measurement of local crystallographic orientation. EBSD measures the orientation of very small volumes of material at specific points on the surface of a sample by using electron diffraction in an electron microscope. Since this technique provides orientation information at a sub-micron spatial location, it enables to relate the crystal orientation to the microstructure. The fact that the orientation of a single point in a sample can be distinguished, gives EBSD the possibility of becoming a fast and automated orientation analysis method, in which orientation maps can be constructed with increasing spatial resolution, in most modern systems as small as 0.05μm (Wright 2000, Humphreys 2001).

The specimen for EBSD should be positioned in a SEM in such a way that a small angle is formed between the incident beam and the surface of the sample, typically 20°. This reduces the path of the electrons that are backscattered in the specimen when the electron beam hits the sample, and increases their chances to be detected. The electron backscatter pattern (or so-called Kikuchi pattern) produced in this way is detected by a phosphor screen, and is the fundamental principle of EBSD. The Kikuchi pattern is unique according to the crystal structure and its orientation with respect to a reference frame. Special algorithms have been developed to solve Kikuchi patterns, which allows determining the crystal structure and the orientation of each point. Figure 1.8 (Randle 2001) illustrates the main components of an EBSD acquisition system.
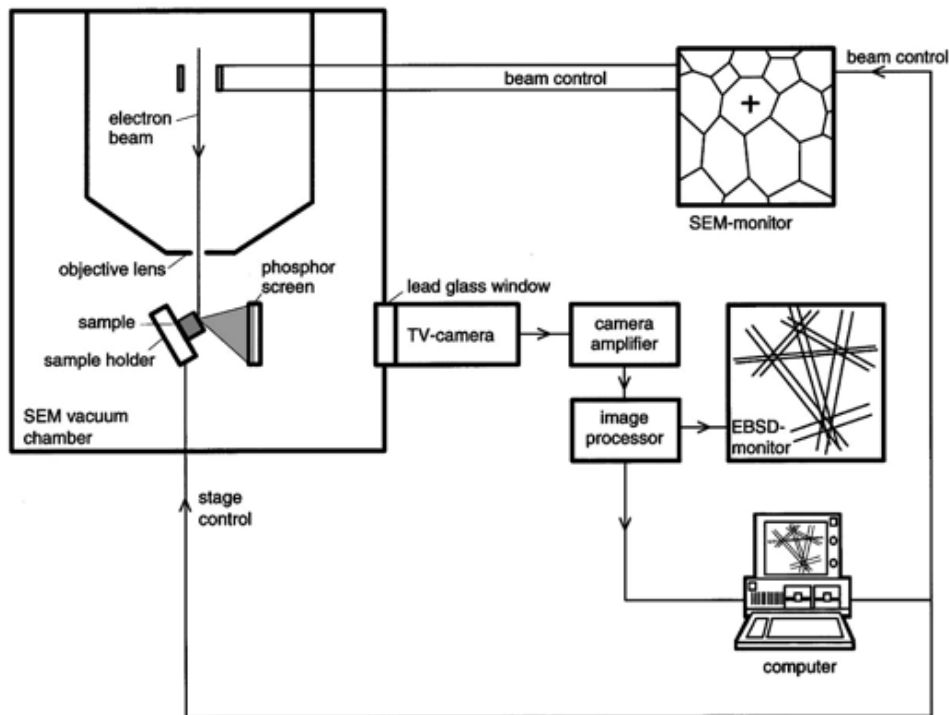
Figure 1.8 Components of an EBSD acquisition system (Randle 2001)

Modern computer systems allow the scanning of millimetre scale areas and automatic storing of the crystallographic orientation of millions of points. In modern systems each point can be stored at a rate as high as $400s^{-1}$, with angular accuracy of ~1°. Speed, spatial resolution and accuracy depend on several factors such as specimen geometry, material, algorithm parameters, microscope voltage/current, and surface preparation (Wright 2000, Randle 2003, Humphreys 2001)

Texture analysis can be divided into two groups: global texture or macrotexture, and local texture or microtexture analysis. Global texture corresponds to the sampling of large areas and/or volumes with multiple orientations, whereas local or microtexture comprises measurements of small areas. The nature of microtexture brings some additional characteristics to the representation of texture. The crystallographic

orientation not only can be related to the microstructure but can also be shown with a clear spatial distribution. Analysis of local misorientation is one of the most important advantages of microtexture and EBSD, and was an important part of this work. An important advantage of EBSD is that the orientation information of each point is obtained directly, normally as a set of three Euler angles. This kind of data can be easily represented, interpreted and mathematically handled. The visualisation of orientation maps is one of the novel and interesting features of EBSD, as well as quantification of other orientation aspects such as misorientation, grain boundaries and global texture statistics (Randle and Engler 2000).

Orientation Distribution Functions

In EBSD measurements, statistical distribution of orientation data is often aimed to quantify the orientation distribution within a specific region of the microstructure. Nevertheless, if the regions mapped are large enough with respect to the grain size, the global texture can be determined, which can be comparable to the results of macrotexture measurements obtained using other methods such as LXRD. However, with EBSD it is important to assess critically the volume of material sampled in order to represent quantitative macrotexture reliably. Some inaccuracies of the conventional pole figure inversion processes discussed above are overcome with EBSD, since grain orientations are measured directly rather than calculated from crystal plane distributions. Provided that enough grains are measured, ODFs obtained from EBSD

measurements produce the true orientation distribution in the sample (Randle and Engler 2000). The question is how many grains should be measured to obtain an acceptable ODF, which is difficult to determine since the answer depends on the texture strength. It has been shown that 100 grains are enough to locate the main features of the ODF, while a minimum of 1000-2000 grains would be required to evaluate the intensity of these main components and reveal secondary features, depending on the sharpness of the texture and the symmetry of the crystal (Bozzolo *et al.* 2007) .

Misindexing and Pseudosymmetry

Occasionally, points in an EBSD orientation map are wrongly indexed, meaning that they are given a wrong value of orientation, or are identified as an incorrect phase. This can occur if the diffraction pattern is symmetrical and/or the quality of the pattern is not good enough. Indexing errors are a particular problem in crystals for which pseudosymmetric Kikuchi patterns exist. A typical case of pseudosymmetry is seen in hexagonal crystals: patterns of crystals having a misorientation of $\pm30°$ about the $\vec{c}$ axis are extremely similar. Consequently, when scanning α zirconium it is common to find points indexed wrongly with this $30°$ rotation. In cubic metals misindexing is very rare, and misindexed points are normally isolated and are highly misoriented with respect to the adjacent points, so they can easily be recognised. This problem can be minimised either by enhancing the quality of the diffraction patterns by means of different sample preparation, increased voltage or probe current, or by improving the indexing

parameters such as calibration or number of bands for pattern solution. Misindexed points can often be systematically removed and extrapolated during post-processing of EBSD data (Humphreys 2001).

Sample Preparation

A disadvantage of EBSD is the difficulty to prepare samples of certain materials, since extensive procedures are sometimes required to achieve just acceptable diffraction patterns. Zirconium alloys are soft and ductile metals, which makes them difficult to prepare by standard methods because of the ease with which they form mechanical twins during cutting and grinding. Some compression-mounting pressures are strong enough to produce twinning, which makes cold resins preferred. Sectioning, mounting, grinding and polishing must be carefully controlled (Vander Voort 1999).

Smearing and flow can easily occur in zirconium alloys during grinding and polishing. Grinding and polishing removal rates must be low. Eliminating all the scratches and deformation can be difficult. Copious water-cooling has to be used with long grinding periods. Only fresh paper should be used. Swab etching between grinding steps is commonly used. If samples are finished mechanically, attack polishing might be necessary (Vander Voort and Van Geertruyden 2006).

Zirconium is quite inert, thus it can be attacked only by hydrofluoric acid (HF) and solutions of nitric (HNO_3) and hydrochloric (HCl) acids. For optical microscopy,

however, zirconium offers an advantage: it normally responds well to polarised light as a result of its anisotropy. Chemical and electrolytic polishing procedures are widely used. Chemically polished or electropolished surfaces normally respond well to polarised light. Most of the chemical polishing solutions contain HF, which attacks the surface, and HNO_3, which prevents staining. Water, hydrogen peroxide, glycerine or lactic acid can be used as solvents. Most are applied vigorously by swabbing, which also facilitates stain removal (Vander Voort 1999). Specific EBSD sample preparation procedures employed in this project are discussed in sections 3.3 and 3.5.

1.3   MODELLING ANISOTROPY OF POLYCRYSTALS

Most of the physical properties of single crystals are anisotropic to certain extent. If the properties of a single crystal and the ODF are known, then the properties of the polycrystal can be calculated. One of the aims of this project is to study the effect of heat treatment on the texture of a zirconium alloy, in order to minimise anisotropy problems such as irradiation growth. Irradiation-assisted growth in single crystals of zirconium-based alloys can be described by a second rank tensor, similar to those used to describe strain and thermal expansion. In the simplest mathematical sense irradiation growth can be treated similarly to elasticity (Tome *et al.* 1996). For a detailed discussion on irradiation growth, refer to section 2.3.1.

Polycrystal elastic properties can be obtained by a summation over all contributing single crystals, taking into account their orientation. Although the calculation of

polycrystal elastic properties must maintain the continuity across grain boundaries when the external stress is applied and minimise local strain concentrations, in practice the local stress/strain distribution is neglected and the summation is done by simple averages. There are two extremes for the grain averages. The upper bound follows the assumption that the total strain is uniform within the aggregate, whereas the lower bound emphasises stress uniformity. There are other intermediate averaging techniques such as the self-consistent average (Tome 1998, Wenk and Van Houtte 2004). In this project the elastoplastic self-consistent (EPSC) model was employed to estimate the effect of different β-quenching heat treatments on the texture, thereby the bulk anisotropy of a zirconium alloy.

In the EPSC model, each grain is considered as an ellipsoidal inclusion embedded in a homogeneous medium, which has the average instantaneous properties of the aggregate. The stress and strain induced in the inclusion by a far-field stress are deduced, assuming that the elastic moduli of the inclusion and of the medium are known. The main characteristic of the self-consistent approach, compared to a classic elastic inclusion problem, is that the matrix and inclusion properties are not defined beforehand. Instead, the boundary conditions on the aggregate and the external stimulus are established in the form of stress or strain increments. Each grain is analysed successively, with the condition that the weighted average response of the grains corresponds to the macroscopic increments imposed on the aggregate. The method is called 'self-consistent' because the medium is adjusted to coincide with the average of the

inclusions. The response in the vicinity of the grain is described by the average moduli of the medium, independently of the actual neighbours of the grain. This makes this approach statistical in essence, since a given orientation represents all the grains with the same orientation, and the medium represents the average neighbourhood. The model can be extended to include the thermal properties, and the thermal expansion is treated as a transformation strain (Tome 1998).

1.4   SUMMARY

Chapter 1 has reviewed the main concepts of texture representation and measurement. In this work, texture representation methods such as pole figures and ODFs were extensively used to represent experimental results obtained using measurement techniques such as LXRD, EBSD and SXRD. Orientation descriptors such as Euler angles, orientation matrices and quaternions were discussed since they were used to analyse and interpret texture components and evolution. Basic polycrystal modelling was introduced in order to later evaluate the effect of the textures obtained on the anisotropy of properties in the materials investigated. This review establishes a baseline to understand the results obtained in this project.

CHAPTER 2
ZIRCONIUM AND ZIRCONIUM ALLOYS

This chapter presents a review of the metallurgical characteristics of zirconium and its alloys, followed by an account of the behaviour of these alloys when exposed to nuclear radiation. The aim is to provide a background on the materials investigated in this project, and introduce their performance requirements for service in a nuclear reactor.

2.1   PHYSICAL METALLURGY OF ZIRCONIUM ALLOYS

2.1.1   ZIRCONIUM ALLOYS

One of the main desired characteristics when designing zirconium alloys for nuclear applications is to retain the low thermal neutron absorption cross-section of pure zirconium. Therefore, only relatively small amounts of alloying elements are added and the level of impurities is very strict, so they are not detrimental for the thermal neutron cross-section of the alloy. Curiously, in the 1950s zirconium was considered inappropriate for use in nuclear applications due to its high thermal neutron absorption. It was later found that the presence of hafnium as a natural occurring impurity was

responsible for this. Table 2.1 compares the thermal neutron cross-section for different

elements and materials.

Table 2.1 Thermal neutron cross-sections (Bolz and Tuve 1973)

	Barns
Magnesium	0.07
Lead	0.17
Zirconium	0.18
Zircaloy-4	0.22
Aluminum	0.23
Hydrogen	0.33
Tin	0.61
Niobium	1.15
Iron	2.56
Chromium	3.1
Austenitic Stainless Steel	3.1
Nickel	4.5
Titanium	6.1
Hafnium	104
Boron	750
Cadmium	2520
Gadolinium	48890

The development of zirconium alloys has primarily been focused on the effects of

alloying elements on the corrosion behaviour in water and steam. However, until recent

times no consensus existed regarding the effect of the different elements. Most conflicts

arose because of differing processing history or corrosion environments. Nevertheless,

some reviews provide factual and useful information, which can be summarised as

follows (Sabol 2005, Davis 1998, Bhattacharyya *et al.* 2003):

·   Tin was added to sponge zirconium to counteract the detrimental action of nitrogen

    on corrosion resistance. If the nitrogen level is kept low, the level of tin may be

    decreased.

·   Small amounts of iron, chromium and nickel are beneficial for the corrosion

    resistance of zirconium-tin alloys due to the formation of intermetallic second phase

particles (SPPs). The size and distribution of the SPPs is strongly correlated to the corrosion resistance.

· Even pure zirconium can have very good corrosion resistance if the level of nitrogen is kept below 30ppm. The effect of tin in such pure zirconium is to reduce the corrosion resistance. However, it is known that oxides formed on zirconium-tin alloys have better adherence to the metal than those on unalloyed zirconium.

· The previous facts are the basis of the composition of the alloy called Zircaloy-2. Zircaloy-4 is a nickel-free variant of Zircaloy-2 with similar oxidation behaviour, but different level of affinity with hydrogen.

· Modifications of Zircaloy-2 appeared at some point. Alloys containing 0.25 to 0.50%wt tin and 0.25 to 0.40%wt iron were tried and named Zircaloy-3, with and without nickel. These alloys generally exhibited unacceptable low strength.

· Although Zircaloy-2 and Zircaloy-4 have been proved successful for many applications, the precise role of iron, chromium, and the SPPs is still unknown. Most of the studies are based on empirical knowledge extracted from extensive experimental programs.

· Other systems such as zirconium-niobium have been developed, showing promising results in long-term corrosion resistance. For this reason new trademark alloys have

been developed, e.g. ZIRLO™[1], E110 (from Russia) and M5™[2], which also have reduced tin content.

Alloying elements in zirconium alloys can be classified into α-stabilisers and β-stabilisers depending on if they raise or lower the phase transformation (β-transus) temperature. Aluminium, antimony, tin, beryllium, lead, hafnium, nitrogen, oxygen and cadmium are the most important α stabilising elements. Phase diagrams for many of the binary alloy systems for α-stabilisers exhibit a peritectic or a peritectoid reaction at the zirconium-rich end (Banerjee and Mukhopadhyay 2007).

β-stabilisers include iron, chromium, nickel, molybdenum, copper, niobium, tantalum, vanadium, thorium, uranium, tungsten, titanium, manganese, cobalt and silver. For binary alloys between zirconium and these elements, there is usually a eutectoid reaction, and often a eutectic reaction at the zirconium-rich end of the phase diagram. A number of β-stabilising elements such as iron, nickel, chromium, and molybdenum have very little solubility in the α phase and they form ordered intermetallic phases which are readily precipitated even in very dilute zirconium alloys, resulting in precipitation hardening (Banerjee 2001).

---

[1] Westinghouse Electric Company

[2] AREVA

Table 2.2 summarises the nominal composition of the most common commercial zirconium alloys. Zircaloy-2 contains the strong α-stabilisers tin and oxygen, plus the β-stabilisers iron, chromium and nickel. Zircaloy-4 does not contain nickel and has a higher and more closely controlled iron content. These compositions result in an extensive α+β field from about 790°C to 1010°C depending on the content of the alloying elements (Bhattacharyya *et al.* 2003).

Table 2.2 Nominal compositions of commercial zirconium alloys

Element (%wt)	Zircaloy-2	Zircaloy-4	Zr-2.5Nb	Zirlo	M5
Tin	1.20-1.70	1.20-1.70	-	0.96-0.98	-
Iron	0.07-0.20	0.18-0.24	-	0.09-0.11	0.01-0.06
Chromium	0.05-0.15	0.07-0.13	-	0.008	-
Nickel	0.03-0.08	-	-	-	-
Niobium	-	-	2.40-2.80	1.02-1.04	0.80-1.20
Oxygen (ppm)	1000-1400	1000-1400	900-1400	900-1200	900-1800

2.1.2   CRYSTAL STRUCTURE

At temperatures below 800°C, zirconium based alloys are stable in the alpha phase (α), with a hexagonal close-packed (hcp) structure, illustrated in Figure 2.1. The unit cell shows the parameters a and c, which typically are ~3.232Å and ~5.147Å respectively. The hexagonal symmetry is commonly illustrated as a hexagonal prism. The main crystallographic planes in this structure are the basal (0002) and two types of prismatic planes: $(10\bar{1}0)$ and $(11\bar{2}0)$. The unit cell aspect ratio of hcp materials changes from metal to metal, in zirconium it is ~1.598, which lies below the ideal sphere packing (c/a=1.633). Although the aspect ratio moves towards the ideal on heating, it remains below ideal at reactor operating temperatures, i.e. between 300 and 400°C (Tenckhoff 2005).
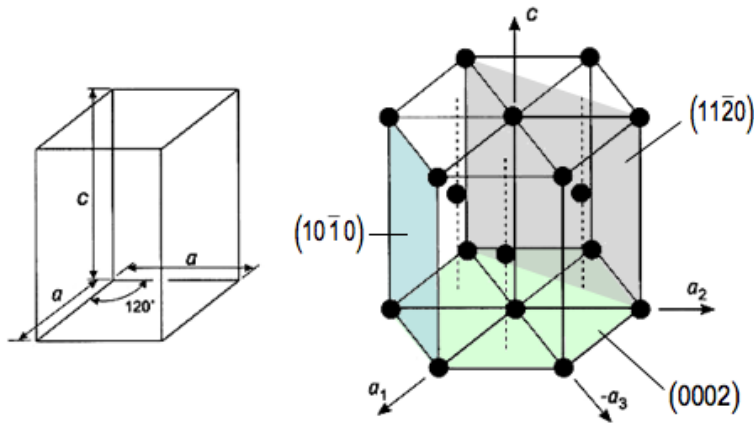
Figure 2.1 Hexagonal close-packed (hcp) crystal structure (Hull and Bacon 2001)

2.1.3 PHASE TRANSFORMATION

At atmospheric pressure, pure zirconium undergoes an allotropic phase transformation at 866°C, from hcp to body-centred cubic (bcc) structure. The cubic structure is denoted as beta (β). The structure of the β phase is shown in Figure 2.2(a). The most close-packed planes in the bcc structure are the (100), (110) and (111) (Banerjee and Mukhopadhyay 2007). The orientation characteristics of this phase transformation are governed by an analogy between the two crystal structures, which is known as the Burgers orientation relationship (Burgers 1934).

$$(0002)\alpha \, || \, (110)\beta \quad \text{and} \quad \langle 11\bar{2}0 \rangle \alpha \, || \, \langle 111 \rangle \beta \qquad \text{Equation 2.1}$$

This orientation relationship states that close-packed or nearly close-packed planes are parallel, and one of the close-packed directions on them have also the same orientation. The Burgers orientation relationship is illustrated in Figure 2.2(b).

In zirconium alloys, the presence of α and β stabilisers and the thermal history determine a temperature range where the two phases coexist, commonly denoted as α+β region (Bhattacharyya *et al.* 2003, Gaunt and Christian 1959). For example for ZIRLO™, the α+β range is 810°C-970°C upon heating and 880°C-755°C upon cooling (Comstock 2006).
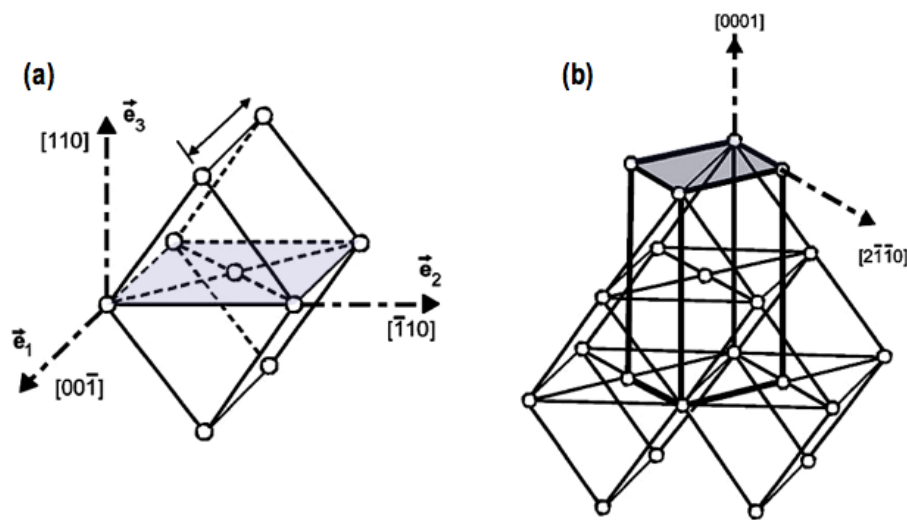
Figure 2.2 Body-centred cubic (β) structure (a) and Burgers orientation relationship (b) (Humbert and Gey 2003)

Transformed Microstructures

On cooling from the β field at a variety of cooling rates, from 2°Cs^{-1} to 200°Cs^{-1}, zirconium alloys develop a Widmanstätten microstructure, with α lamellae developing within prior β grains. Two different morphologies are normally observed: (1) a 'basketweave' structure, resulting from precipitation of relatively short α lamellas on a number of planes within one β grain, and (2) a 'parallel lamellae' structure in which relatively long α lamellas precipitate in the β grain boundaries, and then grow on the

same habit plane (Ökvist and Källström 1970). The two types of microstructure are

illustrated in Figure 2.3.
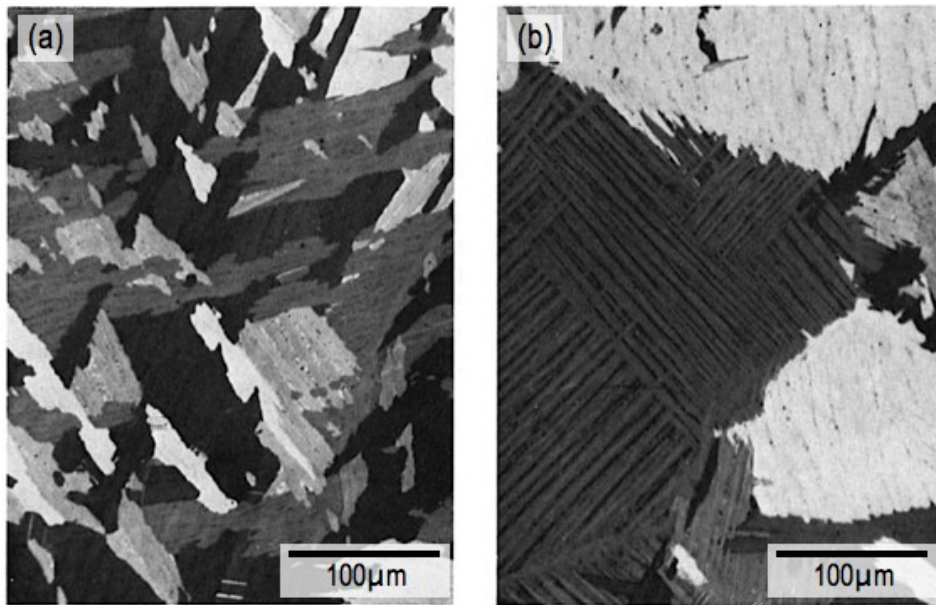
Figure 2.3 Microstructures of Zircaloy-4 after phase transformation from the β field: (a) basketweave
structure (b) parallel plate structure (Holt 1970)

The different transformed microstructures are attributed to nucleation mechanisms, as

opposed to growing mechanisms, more specifically to the number and location of the

nucleation sites. The structure resulting from cooling from the β field depends on the

relative importance between grain boundary nucleation and intergranular nucleation at

non-solved second phase particles. Carbon, silicon and phosphorous are examples of

low-solubility impurities that can act as nucleation sites in the β field. Other impurities

such as chlorine, magnesium, calcium or potassium may be present as inclusions,

stimulating as well a basketweave structure (Massih *et al.* 2003). By increasing the

temperature and/or the time of the β treatment, the growth of β grains reduces the total

grain boundary area available for nucleation, which would stimulate nucleation at

second phase particles within the grains, but at the same time increased temperature/time decreases the particle density. The resultant microstructure is a combination of all these mechanisms (Holt 1970, 1973, Ökvist and Källström 1970). Increased cooling rates produce finer α Widmanstätten lamellas. Classical theories of domain growth, i.e. those assuming that the driving force for the growth is the specific energy of all the boundaries, have been used to fit the dependence of lamella width on cooling rate. At very high cooling rates, above $1000°Cs^{-1}$ martensitic structures can be produced (Massih *et al.* 2003).

2.1.4   STRENGTHENING MECHANISMS

The strengthening of zirconium alloys is achieved mainly by solid solution and precipitation. At operating temperatures, the latter becomes more significant. Pure zirconium, with less than 100 ppm oxygen in annealed condition has very low yield strength (~150MPa). Oxygen in the range of 900 to 1500 ppm for solid solution strengthening is recommended in most of the reactor grade zirconium alloys. Solute strengthening decreases with rising temperature and is negligible at reactor operation temperatures (Davis 1998).

Substitutional elements like iron and chromium have very low solid solubility and for the same level of content, the strengthening effects of these solutes are much larger than that of tin. Mechanical and corrosion properties of Zircaloy-2 and Zircaloy-4 are strongly influenced by the size and distribution of the ordered iron and chromium

intermetallic SPP. Particularly in Zircaloy-2 two distinct types of intermetallic SPP are observed, namely $Zr_2(Fe,Ni)$ and $Zr(Cr,Fe)_2$. Particles at the grain boundaries are usually larger (~3um) and of the first type, whereas the intragranular precipitates are smaller (<1um) and of both types (Banerjee 2001).

2.1.5 DEFORMATION MECHANISMS

In hexagonal metals, the interaction between slip systems is more limited than in cubic metals due to the lower symmetry, thus twinning plays a very important role during deformation. Twinning obeys strict crystallographic orientation relationships. The lack of slip systems combines with twinning to generate strong textures on deformation (Tenckhoff 1988).

The active deformation systems in hcp metals have been found to strongly depend on the c/a ratio. If the c/a ratio is below $\sqrt{3}$ the prismatic slip system dominates, whereas for values above that threshold the basal slip normally becomes more important (Tenckhoff 2005). Consequently, the deformation and texture behaviour should be studied separately for each hcp metal. Zirconium and titanium have a very similar c/a ratio, thus some similarities can be inferred. Titanium also undergoes the same allotropic transformation as zirconium (from hcp to bcc) at ~880°C (Lütjering and Williams 2003). This is the reason why the findings of studies related to deformation mechanisms and texture are often transferred between titanium and zirconium.

Slip occurs normally most easily along close-packed directions on close-packed planes

(Hull and Bacon 2001). In α-zirconium and titanium, up to about 500°C, slip usually

occurs on the first order prismatic planes $\{10\bar{1}0\}$ along the three $\langle 11\bar{2}0 \rangle$ or $\langle a \rangle$

directions. Slip also takes place on the basal plane (0002) in the same directions. In

high stressed regions such as grain boundaries slip along the $\langle a \rangle$ directions appears in

the pyramidal plane $\{10\bar{1}1\}$ (Balasubrahmanyam and Prasad 2002). When these

materials are constrained and deformed at high temperatures an additional slip system

including a component in the $\langle c \rangle$ direction appears. This slip mode normally occurs in

first or second order pyramidal planes $\{10\bar{1}1\}$ or $\{11\bar{2}2\}$ in the $\langle c + a \rangle$ directions

$\langle 11\bar{2}3 \rangle$ (Yoo 1981, Tenckhoff 2005). Figure 2.4 summarises the slip systems in

α-zirconium.

Basal $\langle a \rangle$	Prismatic $\langle a \rangle$	Pyramidal $\langle a \rangle$	1st Pyramidal $\langle c + a \rangle$	2nd Pyramidal $\langle c + a \rangle$
$(0002)\langle 11\bar{2}0 \rangle$	$\{10\bar{1}0\}\langle 11\bar{2}0 \rangle$	$\{10\bar{1}1\}\langle 11\bar{2}0 \rangle$	$\{10\bar{1}1\}\langle 11\bar{2}3 \rangle$	$\{11\bar{2}2\}\langle 11\bar{2}3 \rangle$
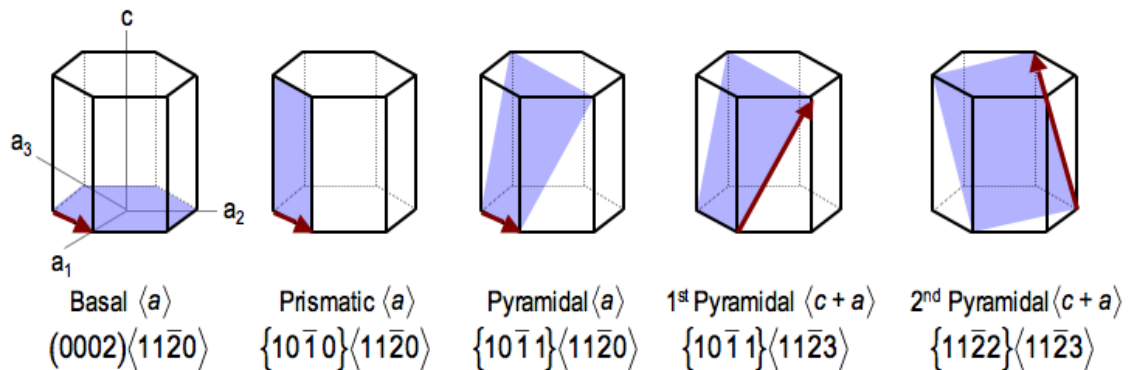
Figure 2.4 Slip systems in α-zirconium

Other deformations with $\langle c \rangle$ components have been explained by twinning on first and

second order pyramidal planes (Kaschner et al. 2006, Kaschner et al. 2007). Twinning is

important since it helps to reorientate lattice regions initially unfavourable for slip,

thereby increasing the possibility of further slip and larger strains. Twinning activates

new slip systems in regions of local stress concentration such as twin boundaries or by interaction with slip. This occurs especially for slip systems including the $\langle c \rangle$ direction. Figure 2.5 (Tenckhoff 1988) illustrates the main twinning systems observed in α-zirconium when subjected to tension or compression along the $\langle c \rangle$ direction.
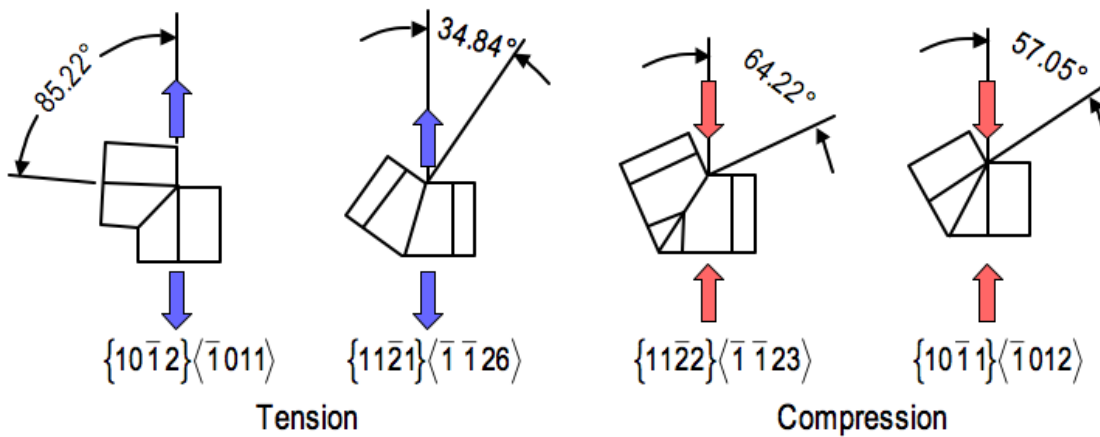
Figure 2.5 Twinning systems in α-zirconium (Tenckhoff 1988)

2.1.6   MECHANICAL PROPERTIES

The mechanical behaviour of zirconium alloys under uniaxial tension has been investigated at a diverse range of temperatures (Garde *et al.* 1978). The differences in mechanical properties between the α and β phases are significant. The β phase is extremely soft and ductile because the equilibrium oxygen concentration is considerable less, and the bcc crystal has a larger number of slip systems when compared to the α phase. As an example, Figure 2.6 (Garde 2010) shows significantly lower yield stress and ultimate tensile strength of Zircaloy-2 in the β-phase (above 950°C), than in the α-phase (700-800°C).
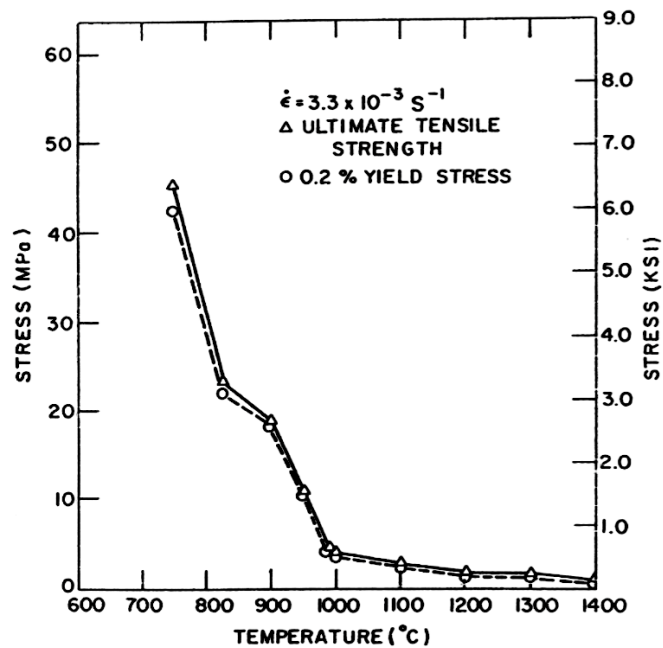
Figure 2.6 Effect of temperature on yield stress and ultimate tensile strength of Zircaloy-2 (Garde 2010)

Steady-state creep of zirconium alloys under uniaxial load has been studied for a range of temperatures, including α phase, the mixed α+β region and pure β phase (Rosinger *et al.* 1979). The constants to describe the creep rates by a power law have been determined, and it was reported that for both the α and the β phases, the activation energies for creep are in agreement with those of self-diffusion, whereas for the α+β region, the creep rate is controlled by grain boundary sliding at the α/(α+β) grain boundaries. The plots of creep rate versus applied stress in Figure 2.7 (Rosinger *et al.* 1979) illustrate the differences between α and β phase. The level of stress necessary for a given steady-state creep rate is practically an order of magnitude lower in the β phase than in the α-phase, mainly due to higher diffusion rates.
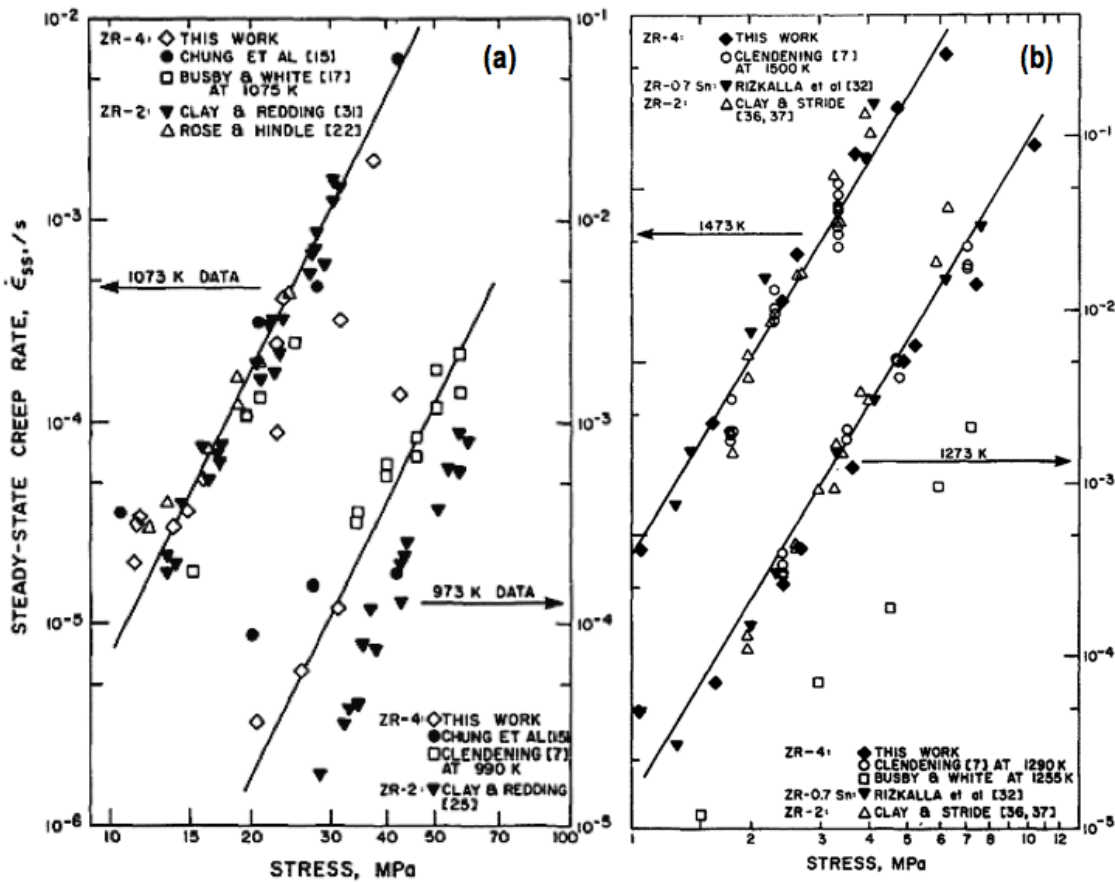
Figure 2.7 Steady-state creep rate versus applied stress for tests conducted in the α(a) and β(b) phase (Rosinger *et al.* 1979)

2.1.7   THERMOMECHANICAL PROCESSING

In addition to the developments in alloy composition mentioned in section 2.1.1, zirconium alloys have also evolved in terms of processing and heat treatment. The following paragraphs describe the main thermomechanical treatments carried out on zirconium alloys during manufacturing of components for nuclear reactors.

Before any cold forming for manufacturing zirconium alloy components such as tubes or sheets, the material is homogenised above the β-transus followed by quenching. This quenching produces a high amount of soluble elements in supersaturation. During

subsequent deformation intermediate annealing steps are required to improve workability and to ensure precipitation of SPPs for optimum corrosion resistance (Northwood 1985, Sabol 2005).

Some experimental studies (Dahlbäck *et al.* 2005) have demonstrated that by β-quenching tubes at their finished size, the irradiation growth rates can be lower than those of components manufactured without a final β-quenching. Annealing after the final β-quenching is required to match corrosion properties of standard materials (Dahlbäck *et al.* 2005, Carpenter *et al.* 1988). Mechanical properties of Zircaloy-4 specimens with different heat treatment conditions have been reported (Ciurchea *et al.* 1996), see Table 2.3. A softening caused by recrystallization and a slight increase in strength by β heat treatment are the most relevant findings.

Table 2.3 Mechanical properties of Zircaloy-4 in different conditions (Ciurchea *et al.* 1996)

	$\sigma_{0.2}$ (MPa)	UTS (MPa)	ε_u (%)	ε_T (%)
Cold worked	552	683	3.2	12.3
Recrystallized	351	466	10.2	24.6
Stress relieved, β transformed	365	473	7.0	15.2
Cold worked, β transformed	375	465	6.8	14.5
Recrystallized, β transformed	395	481	5.6	14.3
Stress relieved, double β heat treatment	410	503	5.3	10.2

2.2   TEXTURE DEVELOPMENT IN ZIRCONIUM ALLOYS

Hexagonal close-packed metals such as zirconium, titanium, magnesium, zinc and their alloys exhibit inherent anisotropic mechanical behaviour due to the limited number of slip systems, which facilitates the development of strong textures during manufacturing processes. Texture is very important for two reasons: during manufacturing, because it

influences the formability; and in service, because it affects properties such as yield strength, thermal/irradiation creep strength, fatigue, stress corrosion cracking resistance, hydride orientation and irradiation growth (Banerjee 2001).

Texture development may be influenced by many factors, which can be classified into two major groups: material and process variables. Amongst material variables are crystal structure, solute content, second phase particles and grain size. Process variables include amount of deformation, strain rate, stress/strain states, annealing conditions, and heating/cooling rates. Many mechanisms can produce texture, but the most important are dislocation glide, twinning and recrystallization (Tenckhoff 1988).

Most of the texture measurements in hcp materials are represented by the basal pole distribution, since the orientation of the $\vec{c}$ axis plays a very important role in the anisotropic behaviour. Few studies have focused on the orientation of prismatic or pyramidal planes, since they are less important than the basal plane regarding mechanical behaviour. However, these planes are indicators of the degree of annealing/recrystallization in the material (Tenckhoff 2005).

2.2.1   DEFORMATION TEXTURES

When a polycrystal is deformed, the stress applied is transmitted to each individual grain. This constitutes a very complex and heterogeneous process: dislocations move on slip systems and interact causing hardening, grains change shape/orientation and interact with neighbours creating stresses. All these phenomena combined make the

understanding and modelling of texture development a cumbersome task. In zirconium, the deformation mechanisms and texture are topical fields of research. The work carried out by Tenckhoff (Tenckhoff 1970, 1988, 2005), has reviewed some of the details involved, a summary of which will be presented in the following paragraphs.

When hcp metals are cold formed, the final orientation of the basal pole (0002) is parallel to the direction of compression, which has been attributed to rapid reorientation of the basal poles due to twinning. There are however, some slight deviations from this general behaviour, which depend on specific metal parameters, mainly the c/a ratio. For this reason, the deformation textures of hcp metals are often classified into three categories according to the c/a ratio and the operative deformation systems. These systems are illustrated in Figure 2.8 (Tenckhoff 2005), which exemplifies the different textures obtained for a flat rolling geometry:

· Metals with c/a ratio above $\sqrt{3}$, e.g. zinc. The position of the basal poles is tilted ±15°-25° from the normal direction towards the rolling direction. Prismatic planes poles are aligned parallel to the transverse direction.

· Metals with c/a ratio approximately equal to the ideal, e.g. magnesium. Basal poles concentrate around the normal direction. Prismatic planes are randomly distributed around the pole of the basal plane.

· Metals with c/a ratio below $\sqrt{3}$, amongst which are zirconium and titanium. The basal planes are tilted by ±20°-40° from the normal direction towards the transverse direction. Prismatic plane poles are aligned parallel to the rolling direction.
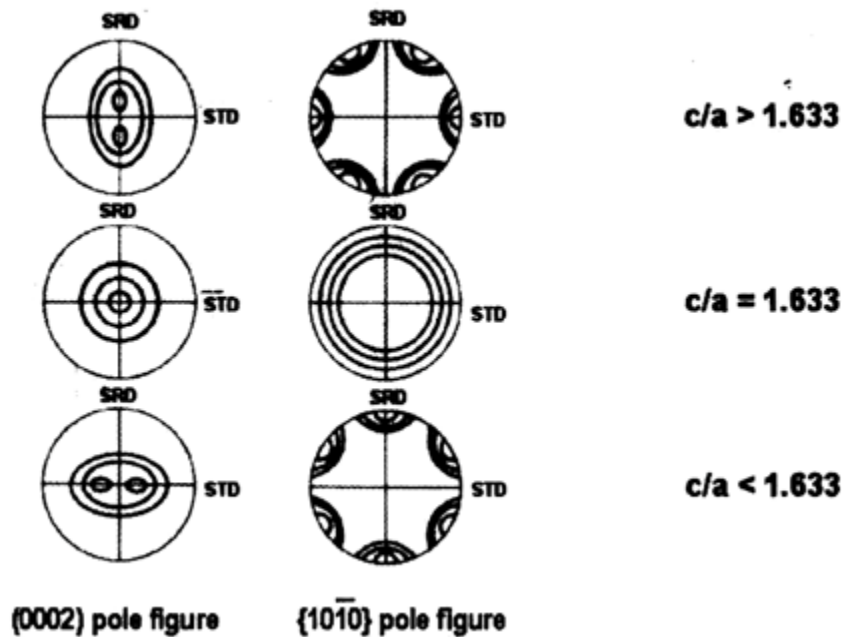
Figure 2.8. Pole figures representing the typical deformation textures of hcp metals with different c/a ratio (Tenckhoff 2005)

Deformation Textures in Tubing

During tube deformation, reduction in cross sectional area is achieved by reduction in diameter (R_D), reduction in wall thickness (R_W) or by a combination of both. In such a manufacturing process, plastic deformations are achieved by the action of compressive forces. If the reduction in wall thickness is more significant than the reduction in diameter, then the compressive forces in radial direction will be stronger, whereas if diameter reduction prevails, the compressive forces in tangential direction will be stronger.

Since in hcp metals the basal poles align parallel to the direction of the effective compressive force, the key factor on the final preferred crystallographic orientation in zirconium alloys tubing is the ratio R_W/R_D. Assuming that a material starts with a random orientation and then is used for tube forming, the resulting texture can be classified into three categories according to the R_W/R_D ratio (Tenckhoff 1988, Rollett and Wright 1998):

· High wall thickness and low diameter reduction ($R_W/R_D > 1$). Material is mainly compressed in the radial direction, whereas forces in tangential direction are comparatively small. The resultant texture shows basal poles preferentially orientated parallel to the radial direction, with some tilting of ±20°-40° towards the tangential direction.

· Wall thickness and diameter reduction approximately equal ($R_W/R_D \approx 1$). In this case compressive forces act with the same strength in both directions. The result is a fibre texture with random distribution of basal planes in the radial-tangential plane.

· Small wall thickness and large diameter reduction ($R_W/R_D > 1$). Compressive forces are larger in tangential direction. Basal poles finish aligned parallel to the tangential direction, with the maxima split by ±20°-40° towards the radial direction.

Deformation Textures in Sheet

During rolling processes, the material is compressed along the sheet normal direction (ND) and lengthened in the rolling direction (RD). Changes in transverse direction have

been found not significant if the ratio of sheet width/sheet thickness is larger than 6. As

expected based on results in tubing, basal poles tend to align parallel to the direction of

compression (ND) spreading by ±20°-40° towards the transverse direction, identical to

that texture found in tubing when $R_W/R_D > 1$. Figure 2.9 summarises the deformation

textures of zirconium for different processes and parameters, including tubing, sheet and

wire (Tenckhoff 2005).
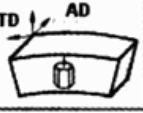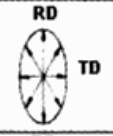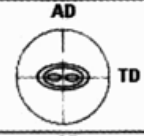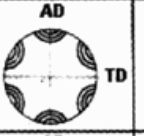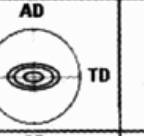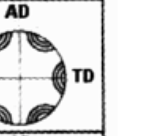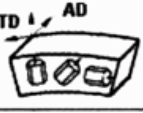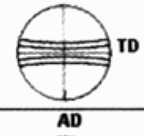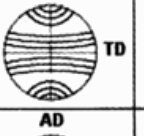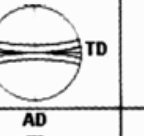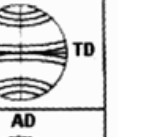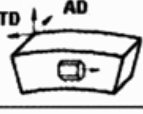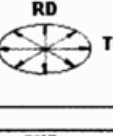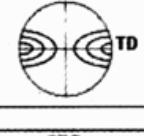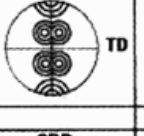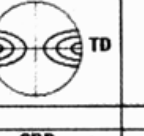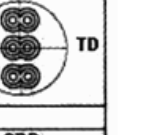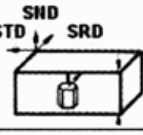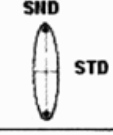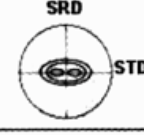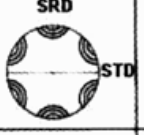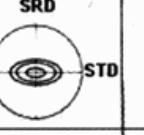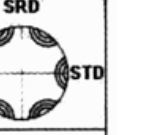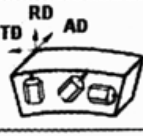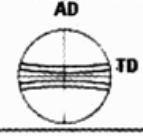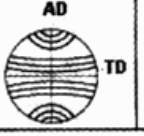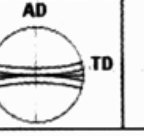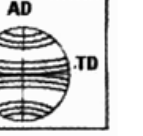
Figure 2.9 Summary of deformation textures in zirconium alloys (Tenckhoff 2005)

2.2.2   ANNEALING TEXTURES

Basal pole figures do not change significantly during annealing for hcp materials. In

some cases it has been seen that the basal poles tend to concentrate in the radial

direction in tubing, or towards ND in sheet. Prismatic plane $\{10\bar{1}0\}$ pole figures appear more influenced by annealing (Tenckhoff 1970).

By increasing the annealing temperature, the basal planes rotate by ±30° around the 'c' axis. Thereby, when the prismatic planes were aligned parallel to the rolling direction, they finish parallel to the axial direction, and vice versa. It is believed that before annealing of hcp metals, some regions are heavily twinned and have high surface energy and heterogeneity. These conditions are ideal for nucleation and the onset of recrystallization (Wenk and Van Houtte 2004).

2.2.3   VARIANT SELECTION

Since the α→β→α phase transformation follows a crystallographic orientation relationship, if the initial material is textured, the new phase will inherit orientation information from the parent phase. By taking into account the Burgers orientation relationship and the symmetries of the two phases, it has been deduced that during heating the transformation of a α grain can give rise to six different β orientations, often called 'variants'. For the reverse transformation, a parent β grain can give rise to twelve α distinct orientation variants (Humbert *et al.* 1994, Humbert 1995). If all the orientation variants were equally activated, the inherited texture would be more random than the parent. However, in many studies on hcp metals strong orientation variant selection has been detected, regardless of whether the transformation is driven by displacive or diffusional mechanisms. The final α texture is significantly stronger than

that calculated on a basis of equal probability of the variants (Jourdan et al. 1991, Gey

et al. 2002a, Gey and Humbert 2002, Gey et al. 2002b, Stanford and Bate 2004).

The mechanisms involved in variant selection have been studied with some detail but

are still poorly understood, even for important phenomena such as the austenite to

ferrite ($\gamma \rightarrow \alpha$) transformation in steel. It has been established that microstructure,

composition and stress have an influence on variant selection. A comprehensive

discussion on variant selection and the factors influencing it will be presented in

Chapter 7.

In zirconium alloys, the high temperature allotropic phase is not normally retained at

room temperature, which makes it difficult to study the selection of variants during the

phase transformations. Nevertheless, the variant selection phenomenon during the $\beta \rightarrow \alpha$

transformation has been studied by processing orientation maps from EBSD data, both

in titanium and in zirconium alloys. Methods to calculate the high temperature β texture

from the inherited α orientation have been developed, which will be discussed in the

following section.

2.2.4   RECONSTRUCTION OF THE HIGH-TEMPERATURE β PHASE

Neutron diffraction and SXRD can provide experimental data of β macrotexture, which

would suffice to discuss variant selection in a global context. However, the

understanding of local variant selection mechanisms requires the knowledge of local β

orientations, which can only be achieved by correlating the β texture with its own

microstructure and the microstructure/texture of the inherited α phase. It has been already mentioned that in many zirconium and titanium alloys, the β phase is not stable at room temperature. As a result, standard EBSD orientation maps only allow direct characterisation of the inherited α phase. However, since the β→α transformation obeys the Burgers orientation relationship, methods of deducing the microtexture of the high temperature β phase from α EBSD orientation maps obtained at room temperature are of great interest, and have been recently developed and applied to titanium and zirconium alloys.

Humbert et al. (Humbert *et al.* 1994, Humbert 1995) demonstrated that taking into account the crystal symmetries of both phases there are six potential β parent orientations for each α orientation variant, and proposed a method to obtain the parent β from a number of inherited α variants in cases where the deviation from the Burgers orientation relationship is small. At that point, the number of α variants required to obtain a unique solution for the parent β grain was for most cases between two and three. The basis established by Humbert et al. was applied subsequently in other approaches for automatic reconstruction of β orientation maps.

Initially the α variants belonging to the same parent β grain had to be identified manually, analysing the transformed microstructure. Sometimes identifying α variants proved to be difficult, making these initial attempts impractical (Moustahfid *et al.* 1997). A later approach (Humbert and Gey 2002) proposed an improved method where

the number of variants used in the evaluation of the parent β grain was no longer limited

to three, and more flexibility from the Burgers orientation relationship was allowed. The

basis of this method is to calculate the six potential parent β orientations for each α

variant and then to deduce the actual parent orientation by finding a common β

orientation between these different sets of solutions. The common orientation is found

averaging the closest orientations from each set of solutions. Figure 2.10 (Humbert and

Gey 2002) illustrates this method. At this point the reconstruction was still limited to

domains containing very few β grains.
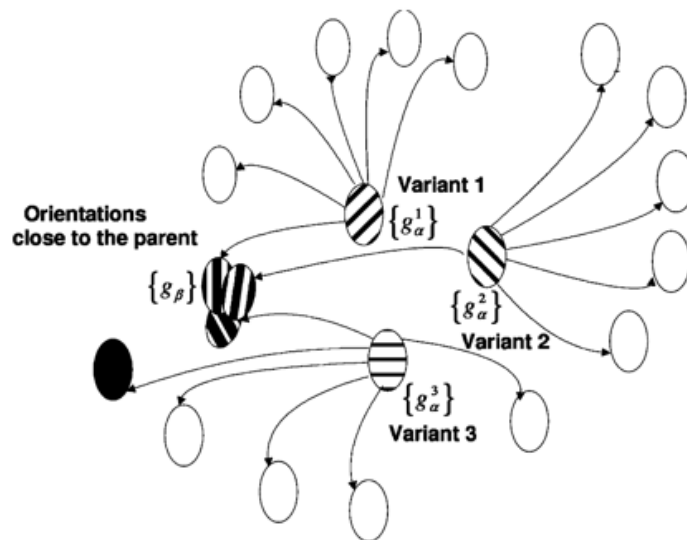
Figure 2.10 Principle of β reconstruction (Humbert and Gey 2002). For each α variant belonging to the same parent β grain, the six potential parent β orientations are determined. Then a common β orientation is found.

The next step in the method proposed by Humbert and Gey (Gey and Humbert 2003)

was the ability to automatically reconstruct larger maps containing many prior β grains.

This was achieved by systematically identifying α variants inherited from the same

parent β grain, considering the misorientation angles and axes between adjacent

measurements. According to the Burgers orientation relationship, inherited α variants belonging to the same β grain have five characteristic misorientations, which are listed in Table 2.4. It is possible to identify traces of prior β grain boundaries, if these characteristic misorientations are displayed in α EBSD maps.

Table 2.4 Specific misorientations between α variants belonging to the same parent β grain

Angle	Axis
10.529°	$\vec{c} = [0001]$
60°	$\vec{a}_2 = [1\,2\,\bar{1}\,0]$
60.832°	$\vec{d}_1$ at 80.97° from $\vec{c}$ in $(\vec{d}_3, \vec{c})$ plane
63.262°	$\vec{d}_2$ at 72.73° from $\vec{c}$ in $(\vec{a}_2, \vec{c})$ plane
90°	$\vec{d}_3$ at 5.26° from $\vec{a}_2$ in basal plane

Based on these characteristic misorientations, automatic algorithms have been developed for reconstruction of β EBSD maps following two basic steps:

1. Identification of α variants: if the misorientation between two adjacent points in an EBSD map is above certain threshold value (usually between 1° and 3°), the points belong to different α variants.

2. Grouping of α variants that probably have the same parent β grain: if the misorientation between two neighbour variants is close (within certain tolerance, between 3° and 5°) to any of the values listed in Table 2.4, then it is very likely that they belong to the same parent β grain, whereas if they do not they surely belong to different parent β grains.

Most automatic β reconstruction algorithms fail in two cases. The first occurs when two prior β grains have a misorientation such as that neighbour inherited α variants belonging to each of them have a misorientation close to those in Table 2.4. The second

occurs when the misorientation between two α variants belonging to different parent β

grains is smaller than the threshold value, thus they are identified as a single variant.

The β reconstruction method was further developed (Germain *et al.* 2007), modifying

the procedure for identifying α variants belonging to the same parent β grain (using

reference α variants), and calculating the probability of finding a unique solution as a

function of the number of variants (see Table 2.5). The evolution of the procedure is

illustrated in Figure 2.11 (Germain *et al.* 2007).

Table 2.5 Probability of finding a unique solution using a β-reconstruction algorithm, as a function of the number of variants (Germain *et al.* 2007)

Number of Variants	Probability (%)
1	0
2	72.72
3	98.18
4 or more	100

After all these improvements, the problem that remains is that using the misorientation

criterion, β boundaries are difficult or impossible to reconstruct where two α variants

have very close orientation (lower than 3°). This has been found to occur on both sides

of a β/β grain boundary, and has been reported as a variant selection mechanism

(Stanford and Bate 2004) . Germain et al. established a list of specific misorientations

where this mechanism occurs, by computing every possible misorientation between all

the six potential parents of an α variant. These specific misorientations are summarised

in Table 2.6 (Germain *et al.* 2007).
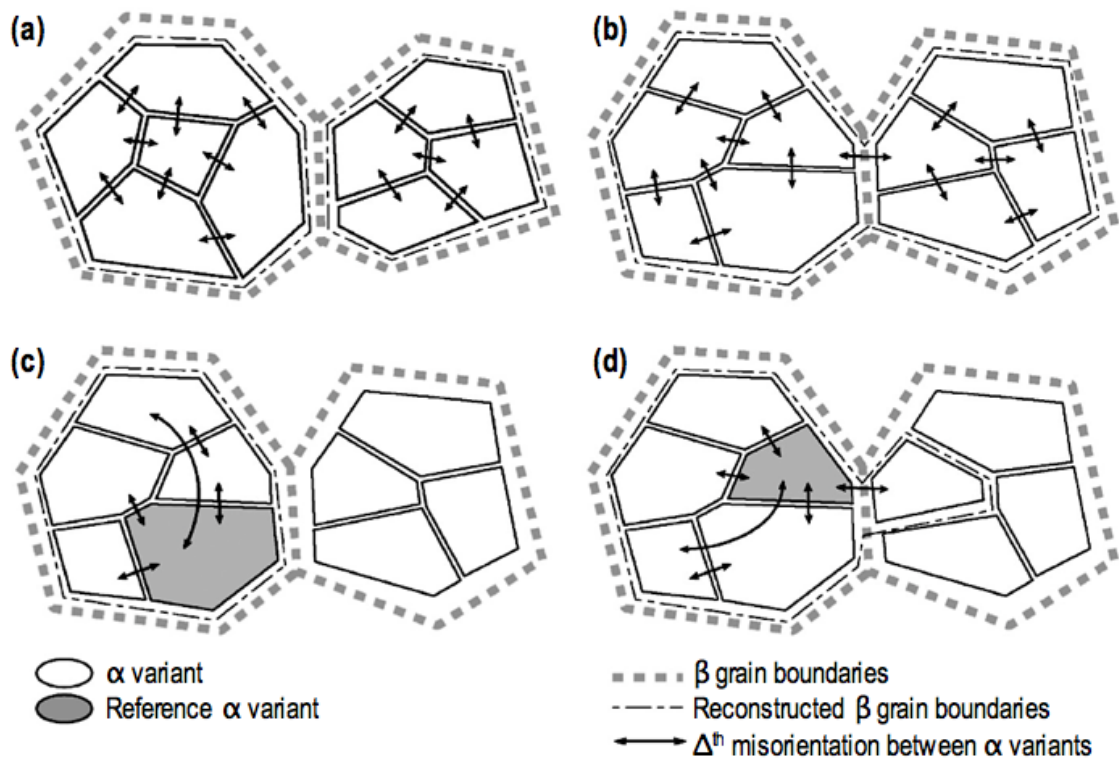
Figure 2.11 Gathering of α variants in different configurations of parent β grains and inherited α variants. (a) α/α misorientations at prior β/β grain boundaries are different from those listed in Table 2.4 (Δ^{th}): the prior β grain boundary is detected by considering the misorientation between neighbour variants only. (b) An α/α misorientation is close to Δ^{th}: the prior β/β grain boundary is not detected by considering the misorientation between orientation variants only. (c) Same as in (b) but the variants are gathered starting from a reference variant. (d) Same as in (c) but starting from a different reference variant, influence of the reference on the variant gathering: the prior β/β grain boundary is not detected (Germain *et al.* 2007)

Table 2.6 Specific misorientations between β grains able to share a common variant (Germain *et al.* 2007)

Angle	Axis
10.5°	$[\bar{1}10]_\beta$
49.5°	$[\bar{1}10]_\beta$
60°	$[\bar{1}10]_\beta$
60°	$[\bar{1}11]_\beta$

The ambiguity of β solutions was independently addressed by Cayron et al. (Cayron *et al.* 2006, Cayron 2007). They also demonstrated that there are special cases when three α variants give rise to two possible β solutions, e.g. when one solution is a twin of the

other through the $(1\bar{1}1)$ mirror plane. This means that four variants are needed to deduce the parent orientation without ambiguities. Cayron et al. evaluated the method proposed by Gey and Humbert (Gey and Humbert 2003). They concluded that β reconstruction methods using the neighbour to neighbour approach work well for titanium alloys, but would struggle in martensitically transformed steels due to the large number of possible variants, and that the martensitic transformation in steel generates high stresses, leading to a more considerable deviation from strict crystallographic relationships. An alternative was proposed, checking all the possible triplets between variants to detect those belonging to the same parent grain. It is claimed that this approach could be applied to a wider range of materials.

Glavicic et al. (Glavicic *et al.* 2003a, b, Glavicic *et al.* 2004) proposed an alternative reconstruction method. This method uses a Monte-Carlo β misorientation minimisation approach, avoiding the manual selection of α colonies. After identifying α variants and determining which of them are adjacent, 'random' pairs of points from adjacent α variants are then selected and the six possible β solutions for each variant are determined. The pair of β solutions with the minimum misorientation between them is selected and assigned a probability number to later evaluate the likelihood that these two variants belong to the same parent β grain. With this technique, the orientations within a β grain are not averaged, making possible to detect orientation gradients within β grains.

The Variant-Based β Reconstruction Technique

Recently a new method to automatically reconstruct β grains from EBSD maps was developed by Davies et al. (Davies *et al.* 2007). The method is based on early fundamental work by Humbert et al. (Humbert *et al.* 1994, Humbert 1995, Humbert *et al.* 1996), where it was determined that each α variant has six potential β parent orientations, and by analysing the misorientation between two α variants it is feasible to reduce the number of possible solutions to three or even less. In most cases, a unique solution can be found. Unlike in the methods described above, in this variant-based β reconstruction technique the inherited α variants do not have to be grouped into their parent β grains, i.e. each α variant is analysed independently using only the misorientation with its neighbours. In order to choose the correct β solution for each α variant, the misorientation between points at the boundaries of a variant and the adjacent points in adjacent variants is evaluated. Compiling the results of this misorientation analysis, the correct β solution should be that which is obtained most often. It is reported that such approach leads to a single solution in most cases. The technique is illustrated in Figure 2.12 (Davies *et al.* 2007).
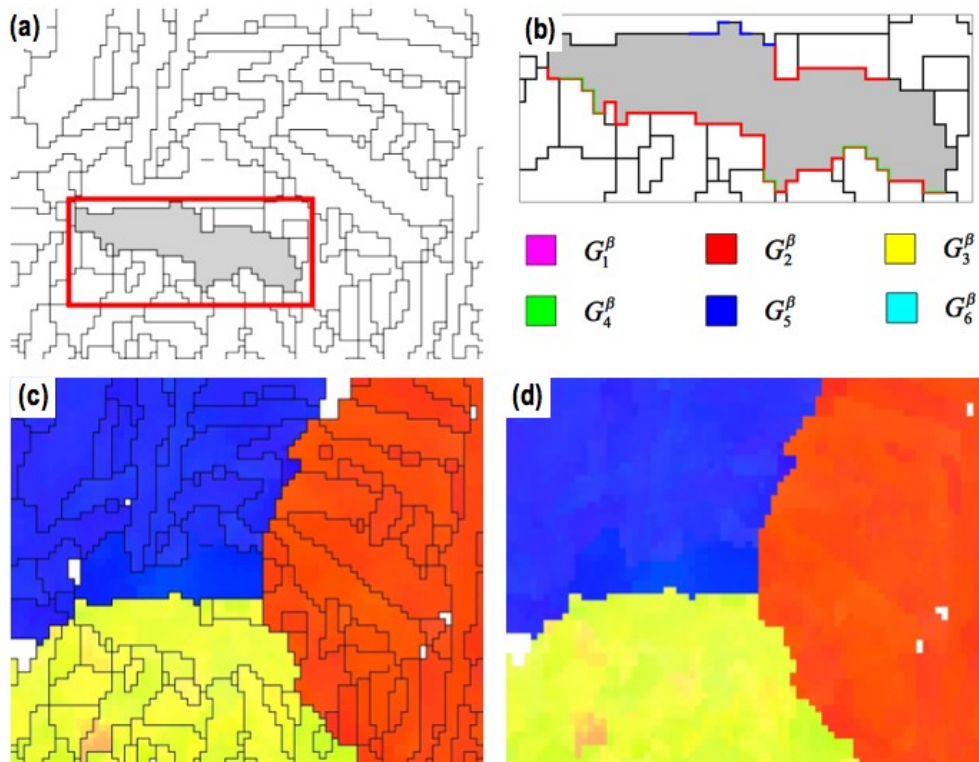
Figure 2.12 The variant-based β reconstruction technique. (a) α variants are identified using a threshold in misorientation, and each variant is analysed independently. (b) The misorientation between the variant and its neighbours is analysed at each point along the α variant boundary, and the potential β solutions G_i^β are found. (c) The most frequent solution is selected for each variant. (d) Missing solutions are found in a secondary reconstruction (Davies *et al.* 2007).

In this method, each α variant is analysed independently, which brings some advantages over the other methods. The main advantage is that it can reconstruct β grains in two particular situations in which other methods struggle: (1) β grains very close orientations, or (2) β grains with misorientations close to those able to generate very similar α variants (listed in Table 2.6). Another advantage is that substructures within the β grains are easily detected, since this method is not based on reconstructing boundaries, but on finding the parent orientation of each α variant independently. One of the disadvantages brought by this approach is that the method will not find a solution if a prior β grain only exhibits one variant, i.e. adjacent variants are necessary.

All the β reconstruction techniques described here have been validated using metastable titanium alloys, where enough volume of β phase is retained at room temperature, which allows measuring parent β orientations directly with EBSD (Gey and Humbert 2003, Glavicic *et al.* 2004). Each method has reported success for specific cases. The difficulty of reconstructing β boundaries between α variants belonging to different parent β grains but with very close orientation is a common denominator for most of the techniques, and it is the interest of this project to asses its significance during β-quenching of Zircaloy-2. In this project the variant-based reconstruction technique (Davies *et al.* 2007) was selected to determine β textures.

2.3   ZIRCONIUM ALLOYS IN NUCLEAR APPLICATIONS

So far, the relevant metallurgical aspects of zirconium alloys have been reviewed. In this section an account of the behaviour of zirconium alloys during service in a nuclear reactor environment will be presented, highlighting the importance of crystallographic texture on the performance of zirconium alloy components during operation.

In the core of BWRs and PWRs most of the components are made of zirconium alloys (Davis 1998). Figure 2.13 shows BWR and PWR fuel assemblies, indicating the main components that are made of zirconium alloys. Thin-walled tubes are used to make cladding for the fuel, as well as PWR structural components (so-called guide tubes). Sheets are used to make PWR grids and BWR channels, while bars of diverse sizes are

used to manufacture endplugs. All these components are subjected to neutron flux during operation, which causes degradation of the material.
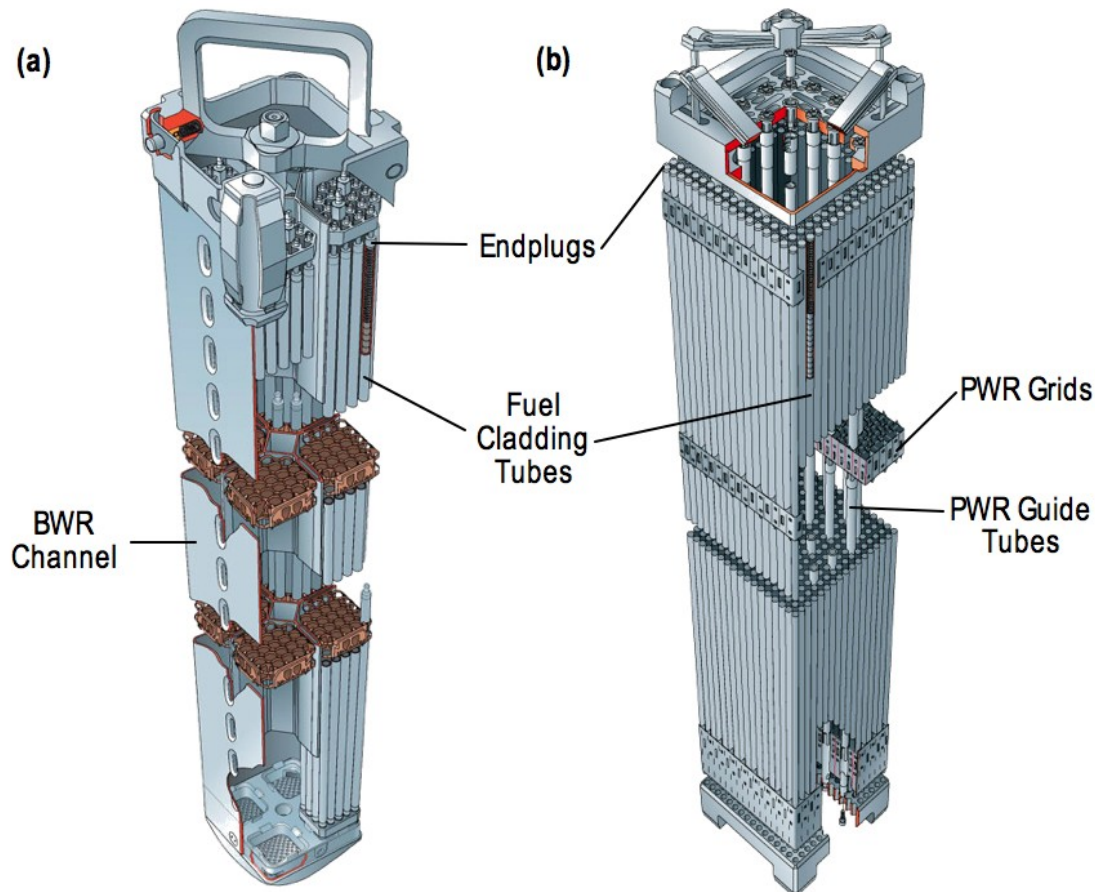
Figure 2.13 BWR (a) and PWR (b) fuel assemblies (courtesy of Westinghouse Electric Sweden AB)

The most important processes that are responsible for the in-reactor degradation of zirconium alloys, and that limit the life of a fuel assembly are: (1) corrosion by coolant water and fission products, (2) hydrogen uptake and consequential effects, and (3) irradiation damages including dimensional changes due to creep and growth (Banerjee 2001). The latter two are highly affected by the texture and will be discussed below with some detail.

When thermal neutrons pass through crystalline solids, they interact with the atoms of the solid losing some energy to them, which can be accompanied by damage to the crystal lattice. Irradiation induced damage can be divided into three types (Rodriguez 2001):

· Production of lattice atoms displaced from their regular lattice positions. Atoms knocked out of their lattice positions result in a vacancy-interstitial pair. The displaced atoms initiate a cascade of displacements that result in the formation of a large number of vacancies and interstitials.

· Changes in the chemical composition by capture of neutrons followed by transmutation.

· Excitation of electrons and ionization of atoms (not permanent in metals).

2.3.1   IRRADIATION GROWTH

Irradiation growth is defined as a shape change with constant volume in the absence of applied stress during irradiation. It occurs due to unequal distribution of interstitial and vacancy loops on different crystallographic planes. Irradiated annealed single crystals of zirconium have been shown to expand in the direction parallel to the $\langle a \rangle$ axis and contract in the direction parallel to the $\langle c \rangle$ axis (Fidleris 1988, Carpenter *et al.* 1988).

Irradiation growth occurs at relatively low temperature ($\sim 0.2 T_m$ where T_m is the melting point), and it is often accompanied by other types of irradiation damage such as

irradiation hardening and embrittlement. In zirconium alloys it has been demonstrated

that during irradiation growth the long term rate of volume change is negligible, which

means that there is an approximate conservation of volume (Holt and Causey 2004).

Most of the information on dimensional change of polycrystalline zirconium comes

from long-term assessment programs on reactor components, which brings a certain

level of uncertainty since the irradiation-induced deformation is typically caused by the

combination of irradiation growth and irradiation creep, interacting with thermal

anisotropy and relaxation of residual stresses caused by the fabrication process. All this

effects occur concurrently, making the analysis and prediction of the material behaviour

extremely difficult (Tome *et al.* 1993)

In early experiments, the expansion along the $\langle a \rangle$ axis was attributed to the formation of

loops of interstitial atoms on prism planes, while the contraction along the $\langle c \rangle$ axis was

attributed to vacancy loops on basal planes. This model has been widely used to derive

growth relationships for polycrystals. The magnitude of the growth strain in any given

direction in a polycrystal can be related to its crystallographic texture and is

proportional to the growth anisotropy factor G_d given by :

$$G_d = 1 - 3f_d^c \quad \text{Equation 2.2}$$

Where f_d^c is the resolved fraction of basal poles in the direction d, i.e. the basal Kearns

factor for that particular direction (see section 1.1.5). Implied in this relationship is that

each grain behaves as an independent single crystal and the volume change is zero

(Fidleris 1988)

The present understanding of irradiation growth is based on the partitioning of

interstitials and vacancies to different sinks such as $\langle a \rangle$, $\langle c \rangle$ and $\langle a+c \rangle$ dislocations

and grain boundaries of different orientations. These sinks are anisotropically

distributed, biased migration of vacancies and interstitials towards these sinks cause

preferential irradiation growth or contraction in different directions (Fidleris 1988). For

a collision between a 1MeV neutron and a zirconium atom, the primary knock-on atom

(PKA) has a maximum energy of 44keV. This PKA causes a cascade of collisions,

which becomes a localised region of high displacement (typically 100-200 atomic

displacements). The vacancies and interstitials generate dislocation loops, which are

mainly associated to the $\langle a \rangle$ type Burgers vector and are arranged in layers parallel to

the basal plane. When the temperature exceeds 300°C it is likely to find $\langle c \rangle$ type

dislocation loops and the irradiation growth increases. The accumulation of defects is

manifested in hardening and growth as a function of irradiation dose. Yield strength and

ultimate tensile strength increase with fluence, and are accompanied by reductions in

ductility and toughness. The effect is less pronounced in cold-worked material than in

recrystallized material (Banerjee 2001).

Irradiation growth is influenced by material characteristics such as texture, internal

stresses, grain size, cold work and alloy content; and irradiation variables such as flux

and temperature (Fidleris 1988). The texture present in zirconium alloy cladding tubes causes the axial length to increase and the cladding diameter and thickness to diminish (Rodriguez 2001). Structural components such as channels made from zirconium alloy sheets elongate and bow (Dahlbäck *et al.* 2005). All these uncontrolled deformations of components during service have an impact on design and safety, to the point where the growth distortions set the operational burnup limits (Banerjee 2001).

2.3.2   IRRADIATION CREEP

Creep is the time-dependent deformation of a material under stress. Irradiation affects thermal creep depending on the temperature, and can also cause macroscopic creep strain that arises due to the presence of point defects (vacancies and interstitials). There are five known fundamental thermal creep mechanisms, some of which are affected by irradiation (Rodriguez 2001):

1.   Glide motion of dislocations, this is the predominant mechanism at temperatures below $0.3T_m$.

2.   Climb of dislocations over localised obstacles occurs at higher temperatures.

3.   At even higher temperatures and low stress, there are other two mechanisms of diffusional flow: Nabarro-Herring creep and Coble creep. They result from the flow of point defects through the grains and around the grain boundaries respectively.

4.   Sliding of grain boundaries.

5.   Twinning

At temperatures below $0.3T_m$, where the dominant creep mechanism is dislocation glide, there will be a reduction of creep rate under irradiation arising from irradiation hardening due to the defect clusters. At higher temperatures, irradiation will increase the creep rate since the excess concentration of vacancies assists the climbing of dislocations. One important effect of the increased concentration of vacancies due to irradiation is the reduction of the temperature range at which dislocation climb can occur. At very high temperatures, above $0.6T_m$, irradiation does not have a significant effect, since the concentration of vacancies produced by irradiation is small compared to the thermal equilibrium concentration of vacancies (Rodriguez 2001).

Besides the conventional thermal creep mechanisms, there are other special mechanisms of irradiation-induced creep: stress induced preferential absorption (SIPA) of point defects by suitable oriented dislocations, and stress induced preferred nucleation (SIPN) of dislocation loops. These two phenomena cause macroscopic creep strain.

In summary, the influence of irradiation on creep processes can be grouped into three categories: irradiation-induced creep, irradiation-enhanced creep, and irradiation-retarded creep. SIPN and SIPA are irradiation-induced creep mechanisms. The influence of microstructural variables in creep rates has not been quantified yet. In general, solutes such as tin, iron, chromium and nickel significantly increase the irradiation creep and thermal creep strength (Rodriguez 2001).

2.3.3   HYDRIDE EMBRITTLEMENT

The reaction between zirconium alloy components and hot water produces hydrogen as H^+ radicals. The solubility of hydrogen in α zirconium is very low, about 60ppm at 300°C, and drops dramatically with temperature. A drop in temperature from 300°C to 30°C results in extensive precipitation of hydrides. Two main types of hydride are encountered in dilute zirconium alloys: the equilibrium δ-hydride and the metastable γ-hydride. The hydride phases tend to assume a plate shape forming along specific habit planes $(10\bar{1}0)$ and $(10\bar{1}7)$ in order to minimise the strain energy associated with the precipitation. Precipitate plates of δ-hydride present macroscopic growth lying in the direction of the maximum tensile stress or in the basal plane if unstressed. Therefore, the crystallographic texture and the stress distribution within a component control the orientation distribution of hydride precipitates (Banerjee, 2001).

This strong temperature dependence of hydrogen solubility and the high diffusivity of hydrogen in the α phase cause continuous redistribution of hydrides as zirconium components undergo temperature variations during operation. Hydrogen diffuses up stress gradients and down thermal gradients, this causes phenomena such as stress-induced reorientation of hydride precipitates, delayed hydride cracking (DHC) and formation of hydride blisters at cold spots (Banerjee 2001).

Zirconium hydrides make components very brittle. If they are unfavourably oriented with respect to the stress state, then the reduction in ductility can be significant. For example, tubular components experiencing hoop stress can fail at very low stress if

hydride plates are oriented in such a manner that their habit planes are predominantly lying along the radial direction. The primary objective for the control of texture of cladding tubes is to orient the basal planes of α grains parallel to the circumferential direction. Such a texture maximises the permissible hoop stress (Banerjee, 2001). Currently the most important application of texture control is achieving favourable orientation distribution of brittle hydride platelets in cladding tubes with strong radial basal texture.

2.4 SUMMARY

Chapter 2 has presented a review of the main metallurgical characteristics of zirconium and zirconium alloys that are relevant to this project. In addition to basic physical information, this review included the effect of alloying elements, strengthening/deformation mechanisms and texture development. The phenomenon of variant selection was introduced, along with a description of β orientation reconstruction techniques. This was followed by an account of the main phenomena occurring to zirconium alloys when they are subjected to radiation during service in a nuclear reactor. The aim was to introduce the main properties of the material studied in this work, and relate these properties to the subject of this investigation: texture evolution, development and control.

CHAPTER 3
INDUSTRIAL SHEET BETA-QUENCHING

Previous chapters have discussed the importance of texture on the performance of zirconium alloys in nuclear reactors, mainly due to anisotropy phenomena such as irradiation creep/growth. Recent efforts by industry, intended to minimise the growth of BWR channels and PWR guide tubes by means of β-processing, have shown positive results (Dahlbäck *et al.* 2005). This chapter reports the characterisation of industrially β-quenched Zircaloy-2 sheets, used for fabrication of fuel channels, by means of optical microscopy, LXRD and EBSD. Besides characterising industrially β-quenched sheets, the aim is to investigate the effect of changing process parameters. The repeatability of results in texture measurements using different techniques is also analysed.

3.1 CONTINUOUS BETA QUENCHING

In recent years, a zirconium sheet manufacturer has developed a system for continuous β-quenching of coils of sheet. The process is based on passing the sheet through consecutive heating and cooling chambers. The uncoiled sheet is initially heated by

means of infrared lamps, and then it is quenched using cooled inert gas. A schematic of the system is shown in Figure 3.1 (Dahlbäck 2007).
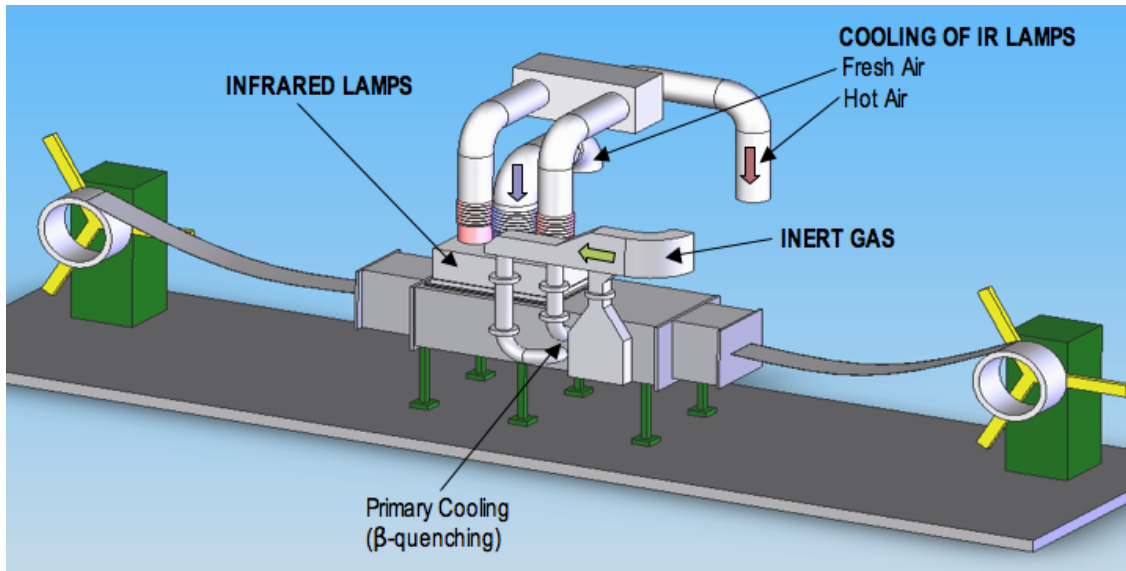
Figure 3.1 Continuous β-quenching system (Dahlbäck 2007)

The process variables that can be controlled in the continuous β-quenching system are temperature and throughput speed. The temperature range available goes from 400°C to 1150°C, while the speed can be varied between 0.1 m/min and 1.5 m/min. The furnace is capable of heating coils 60 to 300 mm wide and 0.88 to 1.44 mm thick. All the heat treatments are carried out in an argon gas atmosphere with a dew point below -54°C and oxygen content below 100ppm.

The temperature in the heating chamber is measured and recorded using an ultraviolet (UV) camera. According to reports of the commissioning of the system, the time that the material remains at the peak temperature depends on the thickness of the sheet and the speed at which it is passed through the chambers, and ranges from 10 to 40 seconds.

A typical temperature profile obtained using a thermocouple attached to the sheet at mid-width is shown in Figure 3.2. The typical heating/cooling rates observed in the system are ~10°Cs^{-1}. In Figure 3.2 the temperature on the surface of the sheet is compared to the temperature measured in the heating chamber by the UV camera (Dahlbäck 2007). When two thermocouples were attached to the edges of the sheet, it was found that there are small differences in the time at the peak temperature, e.g. for a sheet of 1.48 mm thickness and 1100°C peak temperature, the times at peak temperature for the two edges were 34 and 31 seconds.
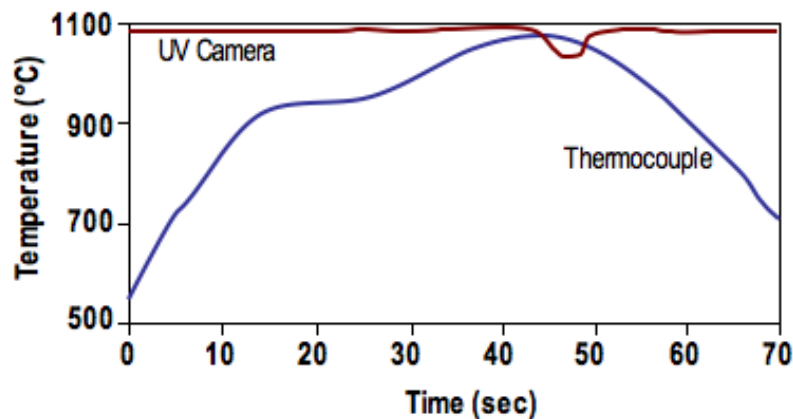
Figure 3.2 Typical temperature profile during continuous β-quenching

3.2 MATERIAL

Six pieces of Zircaloy-2 sheet used for channel manufacturing were received from Westinghouse Electric Sweden AB. One of the pieces was received in as-rolled condition, i.e. cold-rolled to the final thickness (0.9mm), while the other five pieces had been β-quenched after the final cold rolling using the continuous system described in the previous section. All the samples came from the same slab and followed the same

manufacturing route, which minimises differences from chemical composition or other sources different from the final β-quenching. The complete manufacturing process is outlined in Table 3.1.

The peak temperatures for the five β-quenched sheets, as measured using the UV cameras, were: 990ºC, 1020ºC, 1060ºC, 1100ºC and 1110ºC. From the sheets received, numerous specimens of 14 x 14mm^2 size of each β-quenching condition were cut using a conventional guillotine. The specimens were characterised using optical microscopy, LXRD and EBSD, as described in the following sections.

Table 3.1 Manufacturing process of Zircaloy-2 channel sheets

Step	Process	Temperature (°C)	Time (min)	Thickness (mm)
1	Slab			110
2	Hot rolling	930-960	40-120	40
3	Beta quenching	1000-1040	10-20	
4	Hot rolling	770-790	10-20	4.7
5	Brushing and pickling			
6	Annealing	690-710	2-10	
7	Pickling			
8	Cold rolling			3.5
9	Degreasing			
10	Welding			
11	Cold rolling			2
12	Degreasing			
13	Welding			
14	Annealing	690-710	2-10	
15	Surface conditioning			
16	Cold rolling			0.9
17	Degreasing			
18	Beta quenching			
19	Straightening			
20	Annealing	740-760	2-10	

3.3   OPTICAL MICROSCOPY

3.3.1   SAMPLE PREPARATION

Samples for optical microscopy were mounted in Bakelite (30 mm diameter) using a Struers Labopress-3 press. The mounting was carried out using a force of 20kN, with 7 minutes heating at 180°C, followed by 3 minute cooling.

The mounted specimens were ground in five stages, using wet silicon carbide abrasive papers with grit 240, 400, 600, 800 and 1200. On each stage, the samples were ground for 10-20 seconds. After grinding, all the samples were subjected to mechanical polishing with diamond paste on rotating cloths. Rough polishing was carried out using 6μm diamond for 2-3 minutes, followed by fine polishing using 1μm and 0.25μm diamond for 1-2 minutes. Kerosene was used as lubricant and extender during the mechanical polishing process. The final polishing step for optical microscopy consisted of oxide polishing suspension (OPS) for two hours.

3.3.2   MICROGRAPHS

The polished samples were examined using an Olympus BH-2 UMA optical microscope, equipped with capturing software DC-Viewer. Magnifications from 50X to 1000X and polarised light were used for the analysis. Figure 3.3 shows the microstructure in the as-rolled condition, which consists of very fine grains (around 5x10μm in size) elongated in the rolling direction (RD).
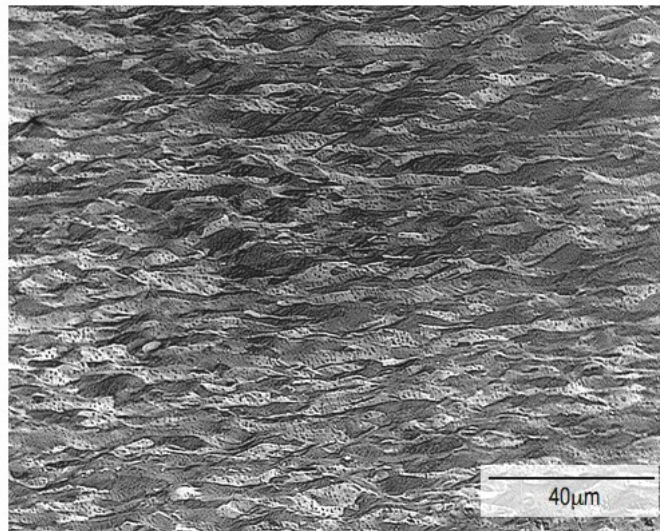
Figure 3.3 Optical micrograph of Zircaloy-2 in as-rolled condition

Figure 3.4 shows typical low magnification micrographs corresponding to the five β-quenched conditions. All the samples exhibit the expected microstructure: colonies of α lamellas decorated by lamellas along the prior β grain boundaries. The prior β grain size was measured using the line intercept method in eight (8) micrographs for each condition. As illustrated by the results shown in Figure 3.6, the prior β grain size increases with the β-quenching temperature, exhibiting significant differences even with small changes in temperature (e.g. 1020°C to 1060°C). The sample β-quenched at 1060°C shows the largest prior β grain size, maybe due to longer time at temperatures above the β-transus, compared to the sample heated to 1100°C.

Figure 3.5 shows higher magnification micrographs that illustrate the behaviour of the α lamella width. The width of the α lamellas initially increases and reaches a maximum at 1060°C, then it decreases as illustrated in Figure 3.7. Lamellas in the sample treated at 1100°C are the thinnest, which suggests that this sample underwent the highest cooling

rate. If the throughput speed and the cooling media are the same for all conditions, sheets at very high temperature would undergo higher cooling rates due to larger temperature differences with respect to the cooling medium. The exact temperature profiles followed by the material studied in this chapter are not known, thus it is not possible to explain these observations completely.

Figure 3.8 illustrates another interesting feature of the β-quenched samples. In some samples, a thin layer with a characteristic microstructure was observed on the rolling surface. This thin layer (~5μm thickness) exhibits a microstructure less lamellar than the bulk, suggesting that the surface was not completely transformed. A possible explanation for this layer is the presence of a small amount of oxygen in the surface, which diffuses into the material at high temperature, and stabilises the α phase at elevated temperature. This layer has been observed during processing of titanium alloys and is know as α-case (Donachie 2000), while very thick α-zirconium layers have been observed in oxidation of zirconium alloys at high temperatures (Urbanic 1977). Incomplete transformations and their effect on the texture after β-quenching will be discussed in detail in section 4.3.
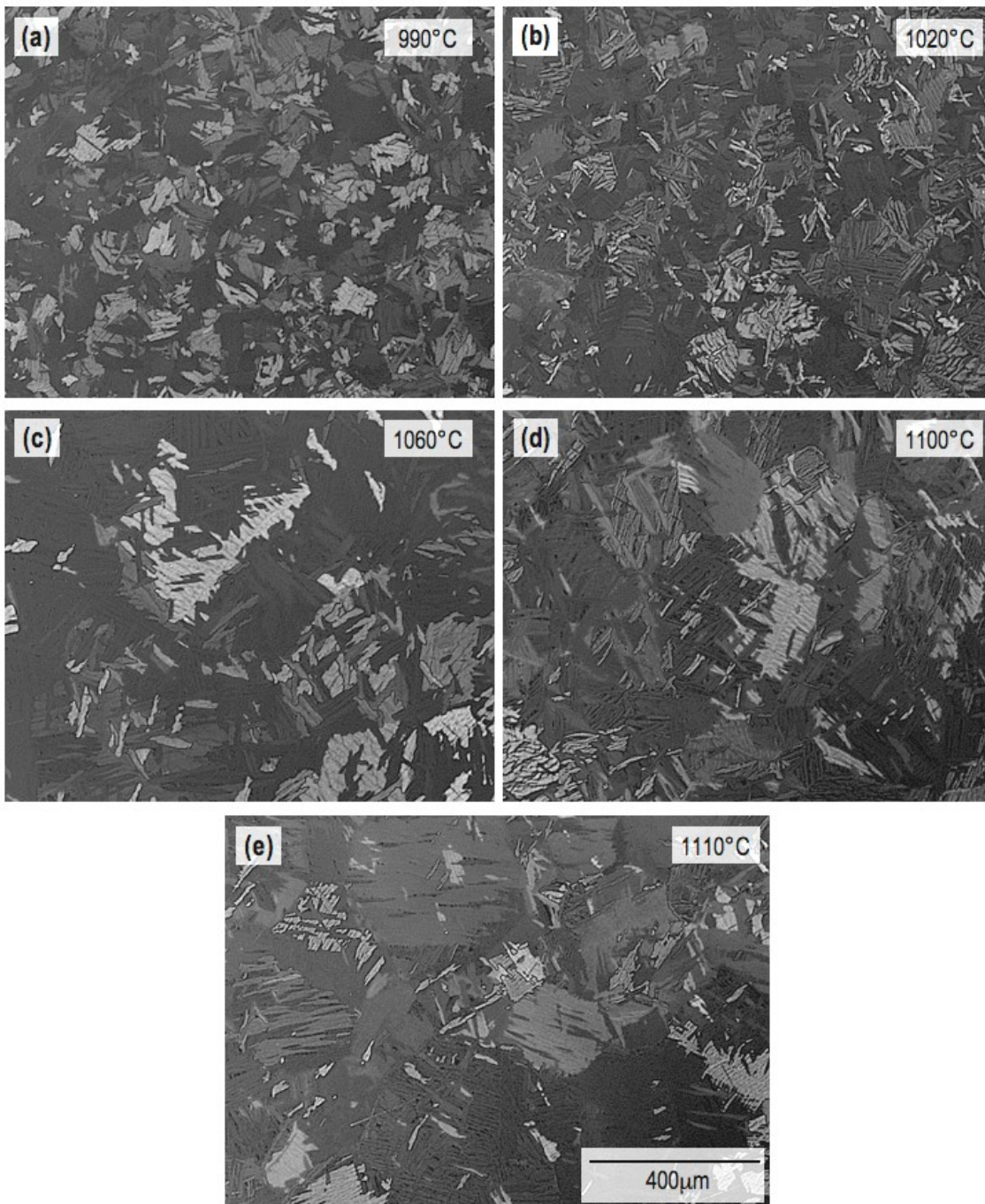
Figure 3.4 Low-magnification optical micrographs of Zircaloy-2 β-quenched industrially using different maximum temperatures
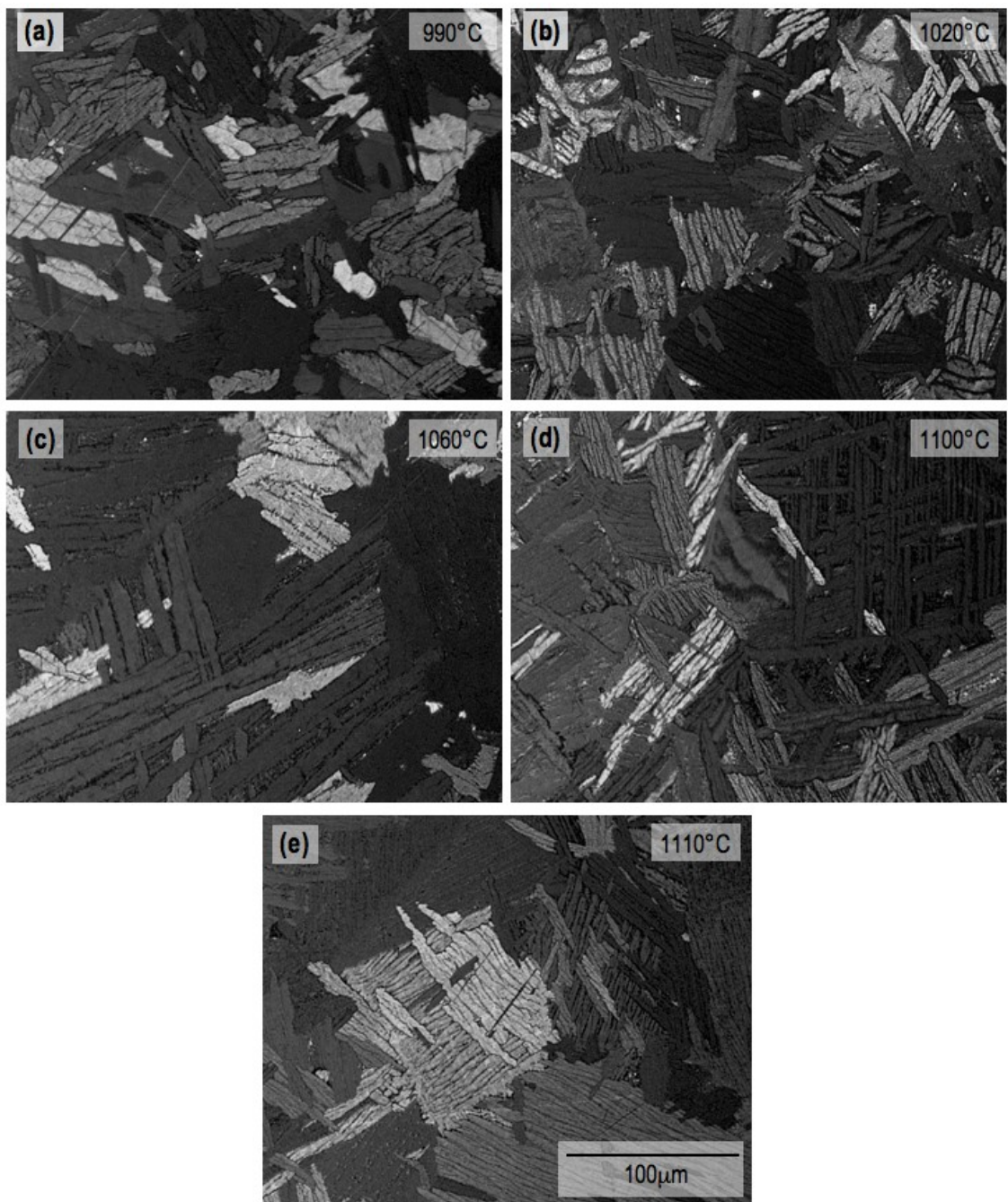
Figure 3.5 High-magnification optical micrographs of Zircaloy-2 β-quenched industrially using different maximum temperatures
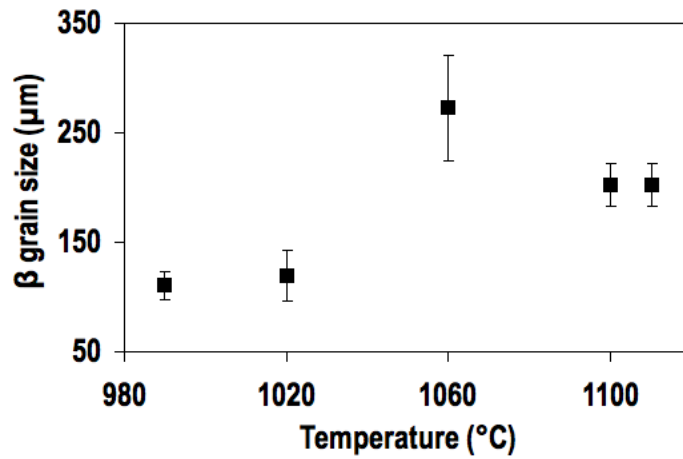
Figure 3.6 Prior β grain size of Zircaloy-2 β-quenched industrially, as a function of the peak temperature
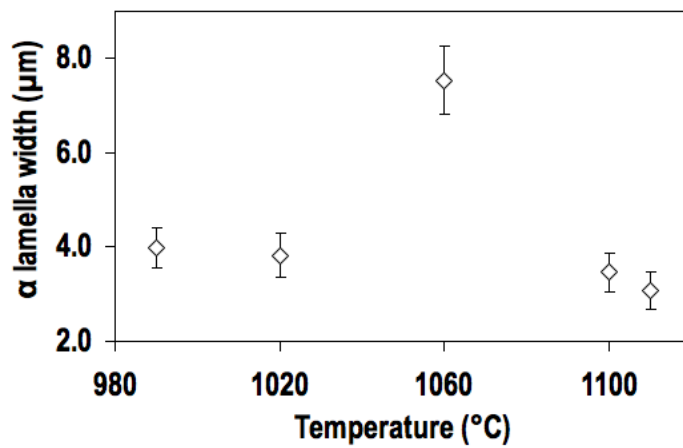
Figure 3.7 α lamella width of Zircaloy-2 β-quenched industrially, as a function of the peak temperature
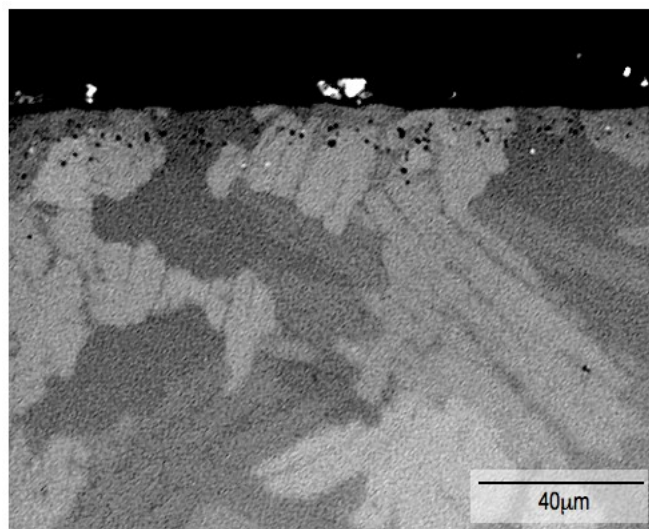
Figure 3.8 Optical micrograph showing the surface of a Zircaloy-2 sheet β-quenched industrially at 990°C

3.4 LABORATORY X-RAY DIFFRACTION

3.4.1 PROCEDURE OF MEASUREMENT AND ANALYSIS

Specimens from each condition were scanned in a laboratory X-ray machine Philips ATC-3, equipped with a cobalt X-ray tube (wavelength 1.79285 Å) and a texture goniometer. Three pole figures were measured for each sample in reflection geometry: (0002), $(10\bar{1}0)$ $(11\bar{2}0)$. A fourth pole figure $(10\bar{1}1)$ was measured in some samples. Figure 3.9 shows the position of the peaks in a diffraction spectrum and Table 3.2 lists some typical parameters. All the pole figures were obtained by varying the rotation angle φ between 0° and 360° and the tilting angle ψ between 0° and 85°, both in steps of 5°. At each position, the X-ray intensity was measured for five seconds. Background intensities were measured for each pole figure. Each measurement took between 6 and 8 hours, depending on the number of pole figures.
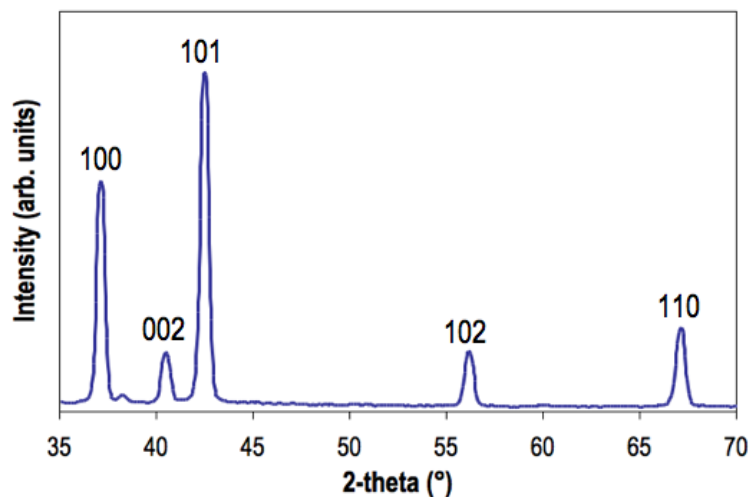
Figure 3.9 Typical LXRD spectrum of a β-quenched Zircaloy-2 sample

Table 3.2 Typical parameters of LXRD peaks for pole figure measurement

hkl	2-theta	FWHM
100	37.17	0.48
002	40.54	0.46
101	42.56	0.47
110	67.17	0.51

The intensities of the raw pole figures were corrected for background and defocusing using the software X'Pert Texture (PANalytical 2005). The background intensities were subtracted. The instrument dimensions and the full width half-maximum (FWHM) of each peak at $\psi=0°$ were used to calculate the defocusing correction factors.

Taking into account the size of the α colonies observed with optical microscopy, difficulties with the grain statistics were expected. This was confirmed when initial pole figure measurements showed sudden variations of intensity caused by very large grain size, with the exception of the as-rolled condition, which showed reasonably smooth pole figures. In order to minimise this problem, a continuous oscillation with an amplitude of 5mm was applied to the samples while measuring the pole figures, which improved considerably the quality of the data.

The corrected pole figures were subsequently used to calculate ODFs using a discrete method as implemented in the software X'Pert Texture. The method is based on minimising a deviation factor denoted as R_p, which is essentially the averaged relative deviation between the measured and the recalculated pole figures. It is defined as follows:

$$R_p = \frac{1}{N} \sum_i \frac{\left| P_i^{obs} - P_i^{cal} \right|}{P_i^{obs}} \qquad \text{Equation 3.1}$$

Where P^{obs} and P^{cal} are respectively the observed and recalculated pole intensities. The summation is over the N measurement points in the i pole figures considered. Table 3.3 lists the parameters used for this calculation. Power refers to the exponent in the equation for the calculation of the sum of differences between measured and calculated pole figures. This value may affect the convergence of the algorithm. The convergence rate limit is the minimum value of the convergence criterion R_p, at which the ODF calculation will be stopped. R_p sensitivity is the minimum value of the changes of the convergence criterion R_p, at which the calculations will be stopped. Eventually (0002), $(10\bar{1}0)$ and $(11\bar{2}0)$ pole figures were recalculated from the ODFs.

Table 3.3 Parameters for ODF calculation from LXRD pole figures

Iterations	50
Power	2
Convergence rate limit	0.5
Rp sensitivity	0.01

All the pole figures provided evidence that the texture in these samples has approximate orthotropic sample symmetry, which is consistent with the rolling geometry. Figure 3.10 shows pole figures of one of the β-quenched samples, recalculated without applying any symmetry to the ODF. Consequently, orthotropic sample symmetry was used to calculate the ODFs.
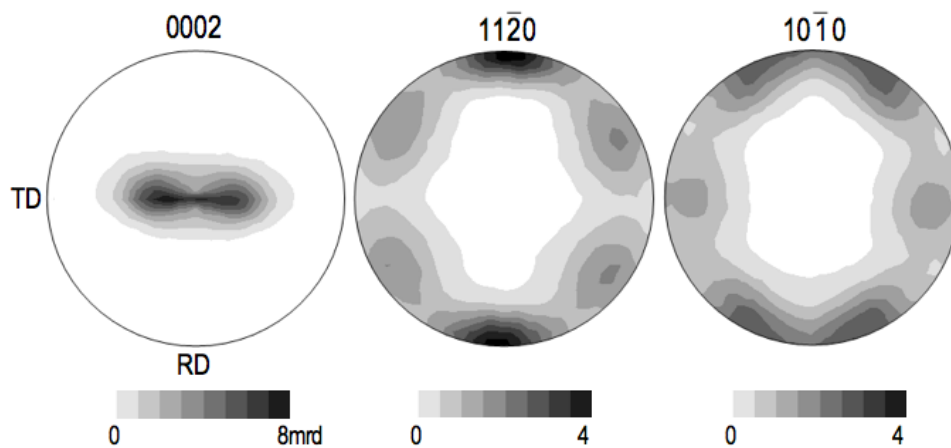
Figure 3.10 Recalculated pole figures of the surface of the sample β-quenched at 990°C. No sample symmetry was applied to the ODF

In order to assess variations of texture across the thickness of the sheet, one set of measurements was carried out without any surface preparation on the samples, while other sets of specimens were ground down to a thickness between 0.40 and 0.45 mm, which is approximately the middle plane of the sample. This grinding was performed in steps up to grit 800, similarly to the procedure used for optical microscopy. After grinding, the samples were electropolished in a solution of 20% perchloric acid and 80% acetic acid. The electrolytic solution was kept at a temperature between 0°C and 5°C using a bath of ice. A voltage of 15V was applied for 60-90 seconds.

3.4.2   RESULTS

The left hand side of Figure 3.11 shows pole figures from the measurements taken on the samples as received, i.e. on the original surface without additional preparation, while the right hand side shows pole figures from measurements on samples after

grinding and electropolishing. Due to the orthorhombic sample symmetry, one quadrant is sufficient to define the pole figure.

It is clear that before β-quenching the material has a strong rolling texture, with basal poles concentrated around ND. At the surface the (0002) poles are split ~30° towards TD, whereas in the middle of the sample they form an oval ring surrounding ND, slightly biased towards TD. The behaviour of the prismatic planes also differs between the surface and the core: the prismatic $(11\bar{2}0)$ poles at the surface are concentrated in RD, whereas at the middle plane they are split ~30° from the same direction. The texture observed in the middle plane has been observed previously in cold-rolled Zircaloy-2 and Zircaloy-4 sheets (Dahlbäck *et al.* 2005, Ciurchea *et al.* 1996).

The pole figures of the five β-quenched samples exhibit considerable differences between the surface and the core of the sheet. At the surface, almost all the specimens show a stronger texture than at the middle of the sample. The dominant features are a split maxima of (0002) poles at ~30° from ND, similar to the as-rolled condition but with slightly more elongated shape; and a (0002) pole maxima parallel to TD appearing in samples treated at 1020°C and above. The $(11\bar{2}0)$ poles at the surface of all the β-quenched samples exhibit a strong maxima parallel to RD, much stronger than that found at the middle plane.
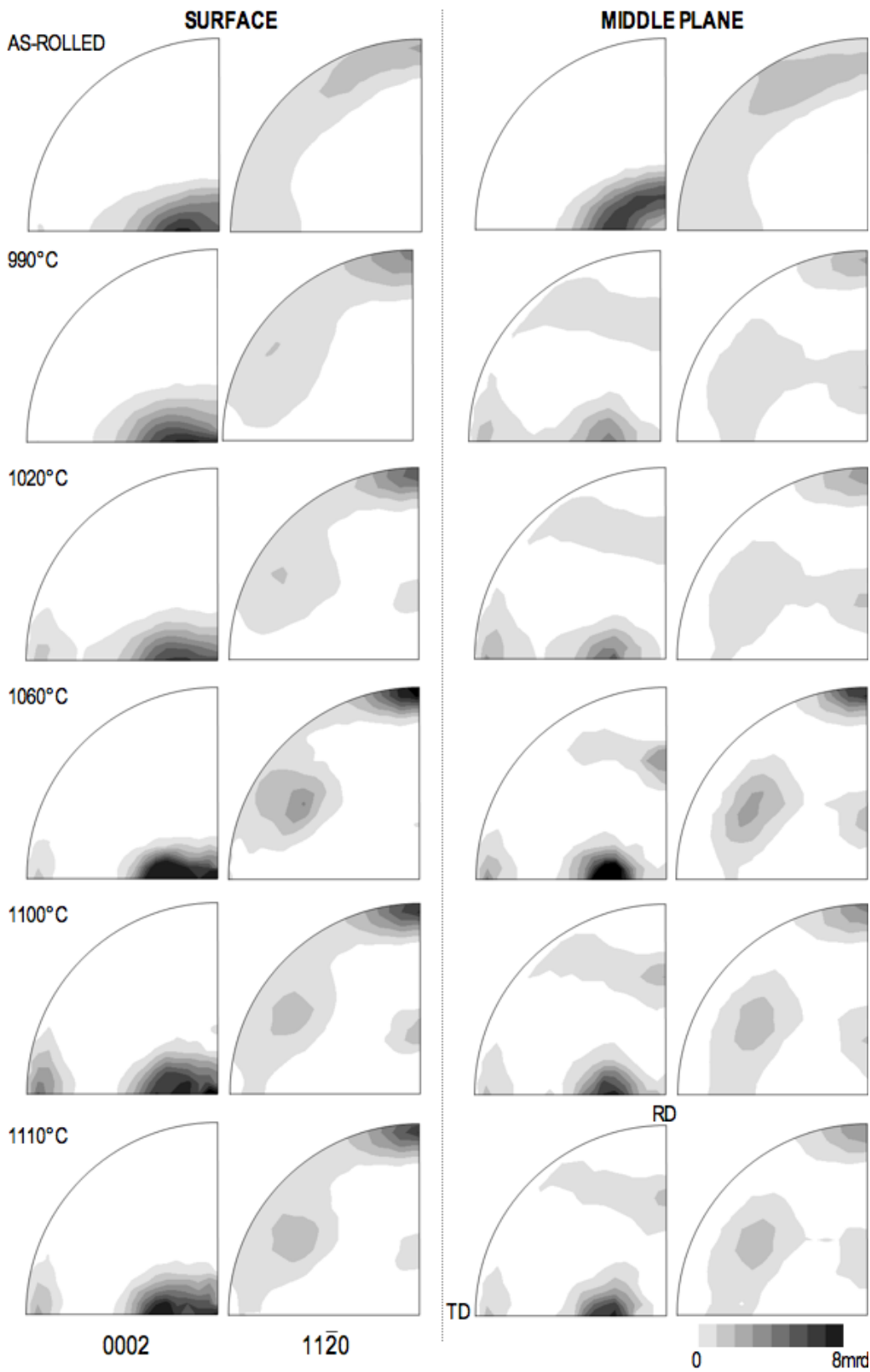
Figure 3.11 LXRD pole figures from samples β-quenched at different temperatures (LXRD-1). Pole figures measured at the rolling surface (left) are compared to those obtained at the middle plane of the sheet after grinding and electropolishing (right).

In the core of all the β-quenched samples, the morphology of the pole figures is considerably different, with additional (0002) pole maxima appearing in addition to the one parallel to TD. There are other maxima surrounding RD at about 30°. The texture in all the β-quenched samples looks considerably weaker than that in the as-rolled condition. The other significant change is that a $(11\bar{2}0)$ maximum parallel to RD dominates the pole figures of the prismatic planes.

The differences between the texture at the surface and the texture at the middle plane may be correlated with the thin layer of material with different microstructure observed with optical microscopy. In the previous section, it was suggested that this thin layer might have been subjected to a slight uptake of oxygen leading to the formation of a so-called α-case, which undergoes increase of the β transformation temperature and could be associated to texture memory. This is more explicit in the sample β-quenched at the lowest temperature (990°C), where the texture at the surface does not even exhibit the new (0002) pole maxima parallel to TD.

If the pole figures of the β-quenched samples in the core of the sheet are compared with each other in detail, it can be noticed that there is strengthening of certain pole intensities as the heat treatment temperature is increased. The split maxima closest to ND are strongest in the sample β-quenched at 1060°C, which incidentally is the sample with the largest prior β grains and the widest α lamellas. The Kearns factors of the basal poles in ND, listed in Table 3.4 (column LXRD-1), also illustrate the strong pole

intensities close to this direction for this particular sample. This evidence suggests a

possible correlation between the prior β grain size, the cooling rate and the strength of

pole components. Figure 3.12 illustrates the direct relationship between prior β grain

size and texture strength, represented by the concentration of basal poles close to ND.

Table 3.4 Kearns factors in the core of industrially β-quenched samples

$f_{0002}{}^{ND}$	LXRD-1	LXRD-2	EBSD
As-rolled	0.744	-	0.653
990°C	0.348	0.334	0.342
1020°C	0.339	0.283	0.299
1060°C	0.443	0.358	0.498
1100°C	0.408	0.327	0.449
1110°C	0.416	0.344	0.459
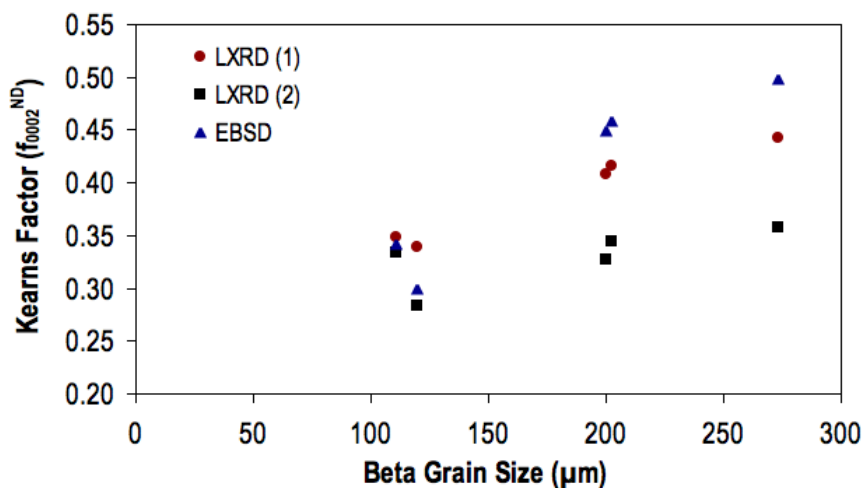
Figure 3.12 Kearns factor as a function of prior β grain size for industrially β-quenched samples

There is the possibility that deteriorated grain statistics with increased peak temperature

could have caused the apparent strengthening of the texture components. For this

reason, a second set of samples was prepared, ground, and their texture measured using

LXRD with the same procedure described above. This time the specimens had a larger

area, 30 x 30 mm^2, and were oscillated in the goniometer using an amplitude of 10 mm,

instead of the 5 mm used for the smaller samples. The pole figures obtained from the second set of samples are shown in Figure 3.13, while the Kearns factors are listed in Table 3.4 (column LXRD-2) and plotted as a function of the prior β grain size in Figure 3.12. Although the absolute values of Kearns factor and the intensities are not identical, these two measurements (LXRD-1 and LXRD-2) show the same trend. This is, the pole maxima observed in the sample treated at 1060°C are still the strongest of the set, while the weakest textures are observed in the samples treated at 990°C and 1020°C. The main differences between the two measurements are the intensities of peripheral pole maxima, e.g. (0002) parallel to TD and $(11\bar{2}0)$ parallel to RD, which in most of the pole figures obtained from larger samples look slightly stronger, with a difference of 1-2mrd with respect to those found on the small samples. The (0002) pole maximum parallel to TD decreases the relative concentration of poles around ND, hence the lower values of Kearns factor observed. Improved calculation of the peripheral pole maxima (which are not measured directly) would be explained by better grain sampling in the larger samples.

Based in all this evidence, it can be concluded that LXRD measurements are reliable up to a temperature of 1110°C and prior β grain sizes of ~500μm, as long as the grain sampling is maximised, and that the correlation between the prior β grain size and strength of pole intensities is evidently not an artefact caused by poor grain statistics. Larger prior β grains are related to stronger texture components.
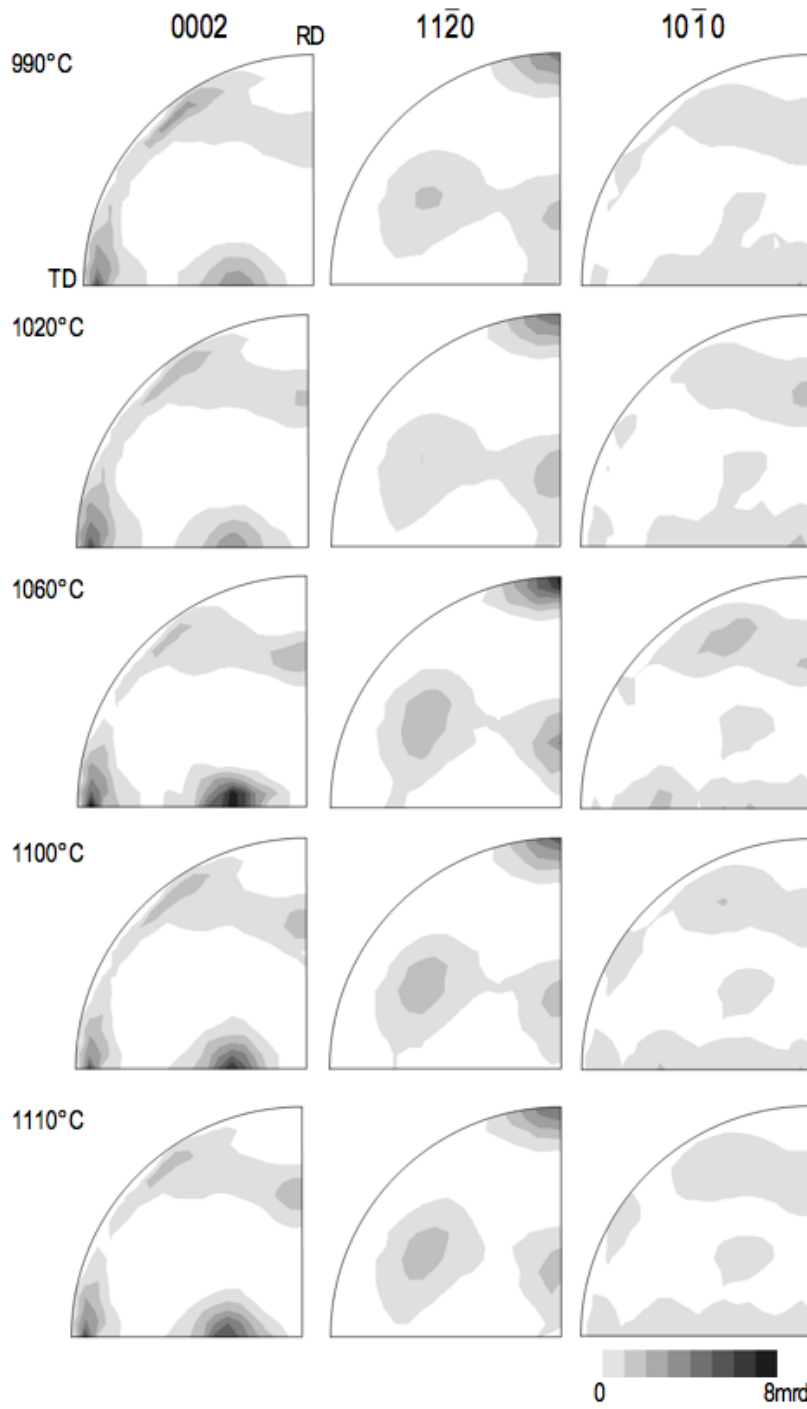
Figure 3.13 LXRD pole figures of large industrially β-quenched samples (LXRD-2)

3.5   ELECTRON BACKSCATTER DIFFRACTION

3.5.1   SAMPLE PREPARATION

In addition to the texture measurements carried out using LXRD, the global texture of the samples in as-rolled and different β-quenching conditions was measured using EBSD. Samples were prepared as if for optical microscopy as described in section 3.3, and subsequently electropolished in a solution of 20% perchloric acid and 80% acetic acid. The electrolytic solution was kept at a temperature between 0°C and 5°C using a bath of ice. A voltage of 15V was applied during 10 seconds. The distance between the anode and the cathode was approximately 5 cm, which resulted in a current density of 0.4-0.7 A/cm^2.

3.5.2   PROCEDURES OF MEASUREMENT

The samples were scanned in a CamScan 2040S FEGSEM equipped with HKL EBSD acquisition systems. HKL Channel 5 software was used to analyse the data. In all the scans, an acceleration voltage of 20kV was employed. In order to measure the global texture, and given the relative large prior β grain size detected in the samples, it was necessary to scan large areas with relatively large step size to collect representative data. The size of the maps collected, the acquisition parameters and the indexing rates obtained are listed in Table 3.5.

Table 3.5 EBSD parameters for industrial samples

Sample	Map Size (mm²)			Step Size (µm)	Indexing (%)
As-rolled	0.4	x	0.3	0.7	69.55
990°C	10.2	x	10.2	200	73.98
1020°C	12.2	x	12.2	200	92.99
1060°C	12.2	x	12.2	200	89.06
1100°C	10.2	x	9.2	200	84.31
1110°C	12.8	x	9.2	200	72.26

3.5.3   RESULTS

The pole figures obtained using EBSD are shown in Figure 3.14, where they are compared to the pole figures obtained using LXRD in the middle plane of small samples (LXRD-1). There is very good agreement between these sets of pole figures, with all the features present and very similar pole intensities. Pole intensities in the periphery of the pole figures are the most important difference between the two techniques, being consistently lower in the LXRD-1 results. The differences are small (<1mrd), which lessens concerns of underestimating these intensities during the recalculation of pole figures from incomplete LXRD raw data. It was demonstrated in the previous section that sampling larger areas helps to reduce this difference. When EBSD and LXRD-2 results are compared the differences are even smaller. This brings confidence to the findings, given the very different nature of the two measurements. The trends observed in the LXRD results are also observed in the EBSD results, mainly the increased intensity of the main pole maxima with β grain growth.
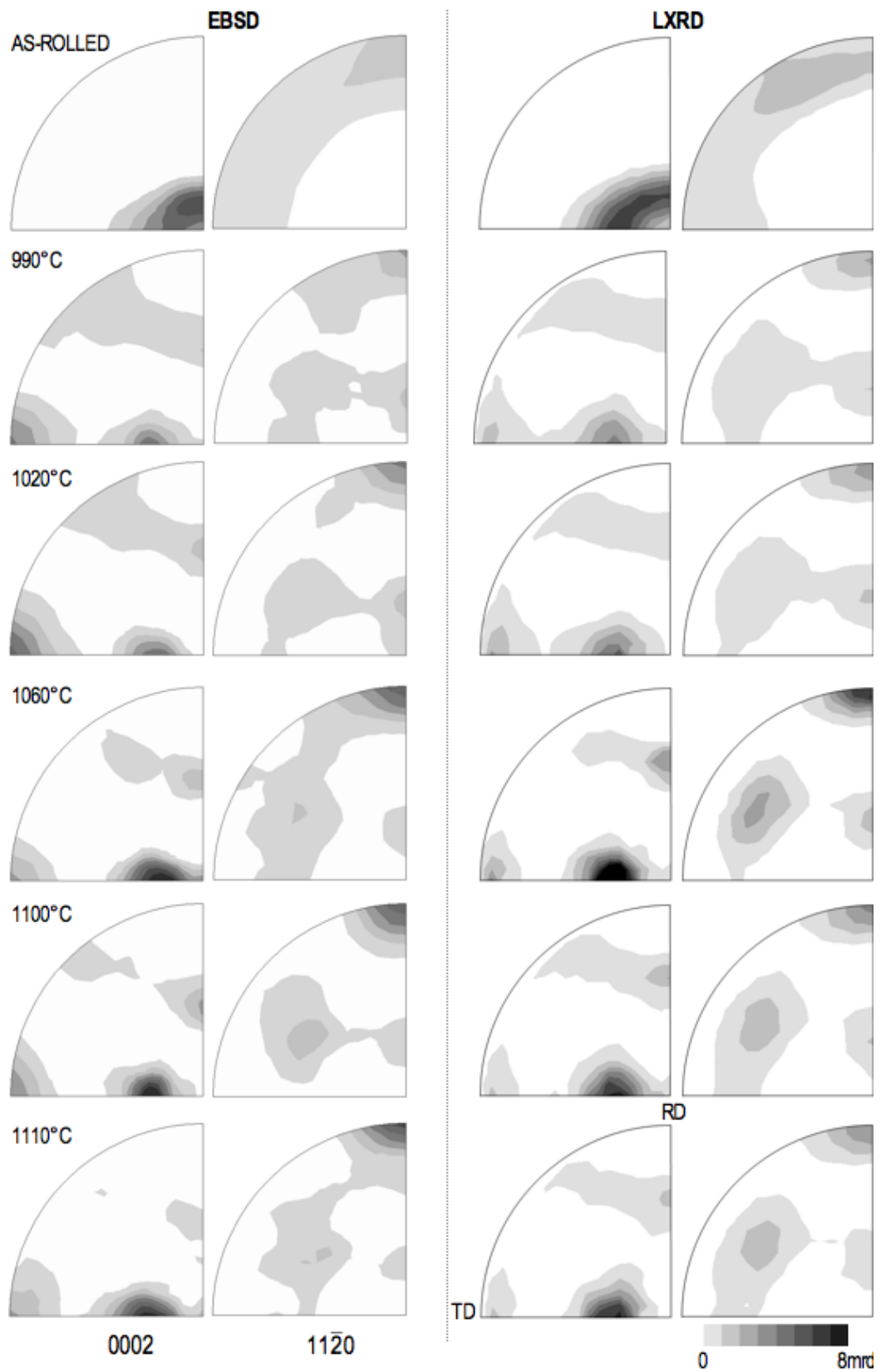
Figure 3.14 Pole figures from samples β-quenched at different temperatures. Pole figures obtained using EBSD (left) are compared to those obtained using LXRD (right).

In the as-rolled condition, there is a notable difference in the $(11\bar{2}0)$ pole figures. In the EBSD results, the poles look more concentrated towards RD than in the LXRD results. This can be attributed to misindexing, given that in this particular sample the amount of deformation is very high, which makes the indexing difficult and exacerbates this kind of effect. This results in an apparent 30° rotation around the $\langle c \rangle$ axis. For all the conditions, the (0002) pole maxima surrounding ND are closer to that direction than those measured using LXRD, which explains the higher Kearns factors listed in Table 3.4 (column EBSD) and plotted in Figure 3.12.

3.6   SUMMARY

This chapter has reported the characterisation of industrially β-quenched Zircaloy-2 sheets. The industrial β-quenching process has been explained, and six samples obtained from it have been studied: one in as-rolled condition and another five β-quenched using peak temperatures ranging between 990°C and 1110°C. Optical microscopy, LXRD and EBSD have been used to characterise these samples, drawing the following conclusions:

· The microstructure in as-rolled condition reveals the strong deformation undergone by the material during the last step of cold rolling.

· All the β-quenched samples exhibit the typical microstructure for this condition: colonies of α lamellas decorated by lamellas along the prior β grain boundaries.

· Despite short times at peak temperature, samples heat treated at higher temperatures exhibit significantly larger prior β grain size.

· The cooling rate is very sensitive to the set peak temperature for this industrial process. According to measurements of α-lamella width, the cooling rate increases if the maximum temperature is above 1060°C.

· The texture of the β-quenched material is significantly weaker than that found in the as-rolled condition.

· A significant surface effect was observed. The texture on the original surface of the sheets is considerably stronger than that at the core. There are indications of a thin layer of material on the surface that may have not undergone a complete transformation, probably due to the presence of oxygen, which stabilises an α-case and increases the β-transus. This may be associated with texture memory.

· Even though peripheral pole intensities are slightly underestimated using LXRD, very good agreement was found between LXRD and EBSD measurements. The agreement between techniques improves when the grain sampling in LXRD is increased.

· There is a correlation between prior β grain size and the strength of the inherited α texture: larger prior β grain size results in sharper pole intensities. This correlation was observed using both LXRD and EBSD.

CHAPTER 4
IN-SITU TEXTURE MEASUREMENT

The characterisation of industrially β-quenched sheet has shown that β-quenching of cold-rolled Zircaloy-2 weakens the initial strong rolling texture, producing new texture components. However, according to the literature, there is no consensus on what are the fundamental mechanisms responsible for the texture change. This lack of knowledge is partially due to the difficulty to obtain direct experimental measurements of texture at high temperature using conventional techniques such as LXRD or EBSD, especially in Zircaloy-2 where no β phase is present at room temperature. In order to evaluate the origins of the final α texture, it is necessary to know the evolution of texture components during the α→β→α phase transformation.

Initial attempts to measure the high temperature β texture in titanium and zirconium alloys have employed in-situ neutron diffraction and EBSD. Neutron time-of-flight measurements have been carried out in Zircaloy-4 (Wenk *et al.* 2004), in commercially pure (CP) titanium, and in Ti-6Al-4V (Lonardelli *et al.* 2007), while in-situ EBSD has been tried in CP titanium (Seward *et al.* 2004). These studies have presented the first

experimental data of high temperature β transformation textures. However, both neutron diffraction and EBSD require keeping the sample at constant conditions for a considerable amount of time in order to complete a texture measurement. For neutron diffraction the time can range from 20 minutes to up to 1 hour, while for EBSD the minimum time is ~1 hour, depending on the resolution and the size of the orientation map. These long counting/scanning times make it impossible to study the texture evolution in-situ during fast heating/cooling/loading conditions. In this project, it is desired to study the texture evolution during thermal cycles similar to those used in the industrial process described in section 3.1, which exhibit relatively fast heating/cooling rates. It is therefore desirable to measure the texture at high temperatures and dynamically, which demands the use of an alternative technique. Synchrotron X-ray diffraction (SXRD) was chosen for this purpose.

4.1 MEASURING TEXTURE IN-SITU USING SXRD

Several researchers have demonstrated that obtaining quantitative texture information from single 2D synchrotron X-ray diffraction images is possible (Wenk and Grigull 2003, Lonardelli *et al.* 2005). Initial in-situ results have been reported during annealing of cold-rolled zirconium at 560°C in a vacuum furnace (Ischia *et al.* 2005). Figure 4.1 and Figure 4.2 show examples of diffraction images and pole figures obtained by Ischia et al., who found agreement between LXRD and SXRD results.
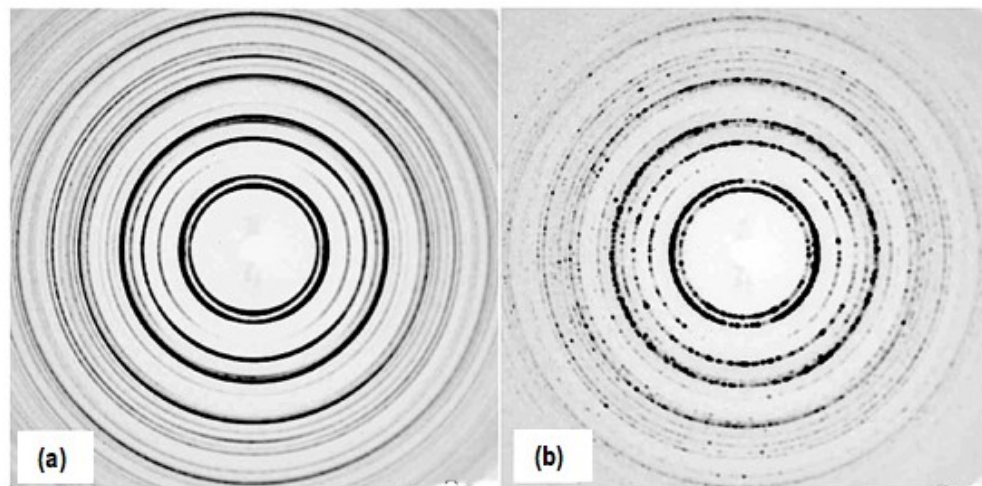
Figure 4.1 Synchrotron diffraction images of cold-rolled zirconium at (a) room temperature and (b) 560°C with advanced grain growth (Ischia *et al.* 2005)
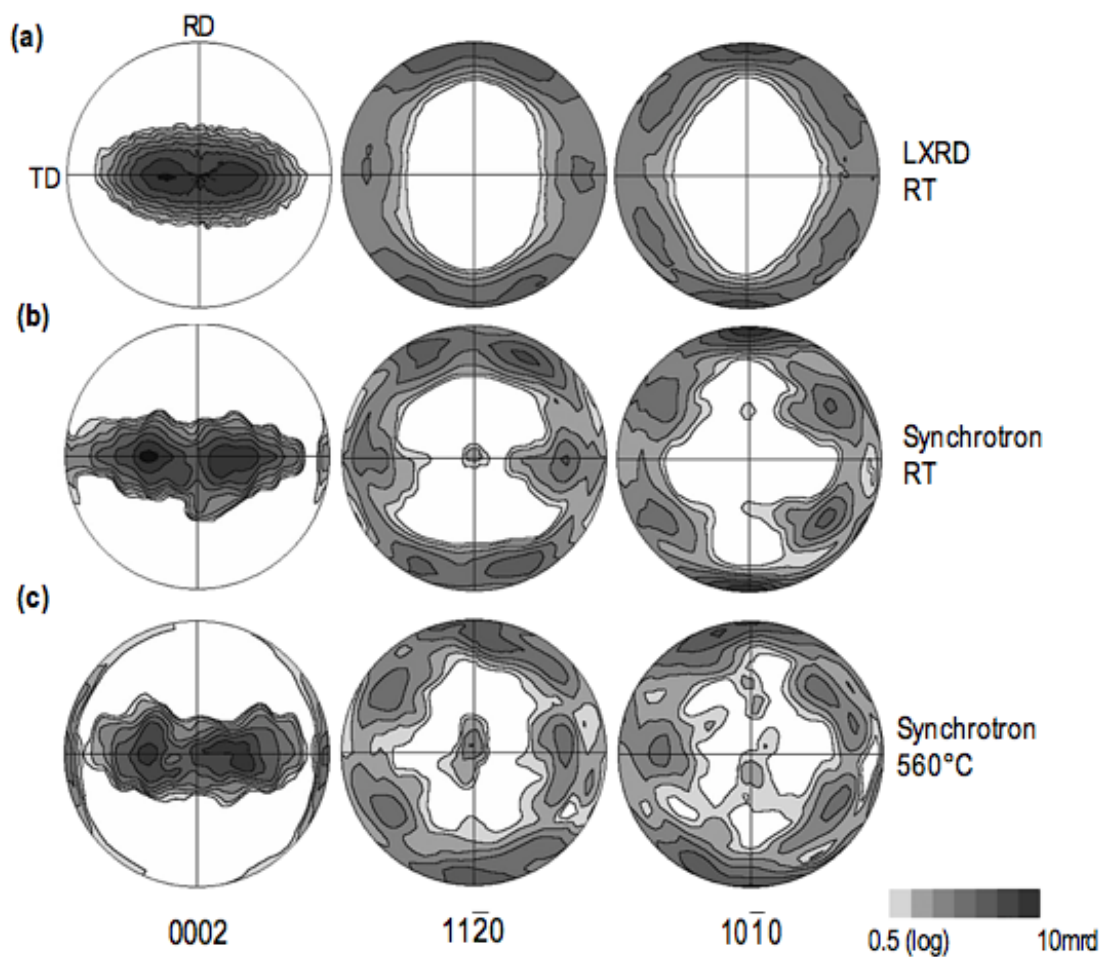
Figure 4.2 Pole figures of cold rolled zirconium (a) measured with a conventional goniometer (LXRD) at room temperature, (b) measured with SXRD at room temperature, and (c) measured with SXRD at 560°C (Ischia *et al.* 2005)

In this project SXRD for texture measurement was taken further. The capabilities and advantages of high-energy X-ray sources were combined with an experimental setup that allowed continuous measurement of the texture during the $\alpha \rightarrow \beta \rightarrow \alpha$ phase transformation.

4.1.1 BEAMLINE SETUP

For the SXRD experiment of this project, matchstick size samples were prepared from a Zircaloy-2 sheet in the as-rolled condition. The thermomechanical history of this material is described in section 3.2. The samples were cut from the sheet using a diamond wheel. The dimensions of the samples were 40mm length and 1 to 2mm width, preserving the original thickness of the sheet (0.9mm).

The experiment was carried out at the beamline ID15B at the European Synchrotron Radiation Facility (ESRF) in Grenoble, France. The complete setup is illustrated in Figure 4.3. The beamline was used in Debye-Scherrer transmission geometry, with a monochromatic beam of 0.1415Å wavelength (88keV) and a size of 200µm x 200µm. This beamline was equipped with a flat panel high-resolution digital detector Pixium 4700 (Trixell 2007). This detector is designed for real-time X-ray imaging, combining an amorphous silicon panel with a caesium iodide scintillator. It has a physical array of 2640 x 1910 pixels with 154µm x 154µm pixel size, which results in a total X-ray sensitive area of 381.9 x 294.1 mm^2.
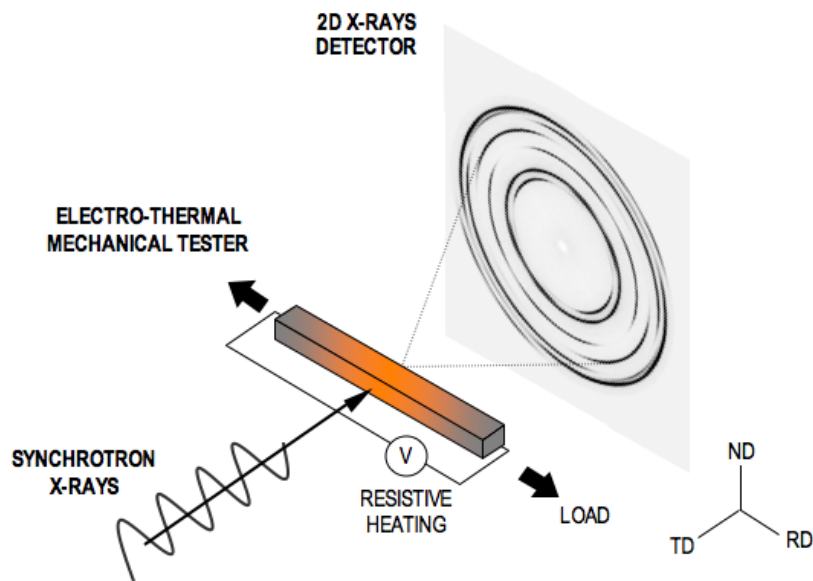
Figure 4.3. ID15B beamline setup

The samples were mounted on an electro-thermomechanical testing rig (ETMT), oriented with RD perpendicular and TD parallel to the X-ray beam. The distance between the sample and the detector was ~700 mm. The ETMT is a versatile stress rig that allows controlled resistive heating in miniature test pieces (Instron Corporation 2007). Sample cooling is achieved by heat dissipation and conduction through water-cooled grips, when the electrical current is decreased. The ETMT has a 3kN load cell and can achieve heating rates of $800°Cs^{-1}$ and cooling rates of $100°Cs^{-1}$, depending on the electrical resistivity and the thermal conductivity of the material. The temperature on the specimens was measured using a R-type thermocouple spot-welded to the middle of the samples, which also provides the feedback for the temperature control. The temperature value measured by the thermocouple was logged during the tests, along with load, position and electrical current data, with an acquisition frequency of 10Hz.

The resistive nature of the heating in the ETMT creates a parabolic temperature distribution along the sample, with the highest temperature halfway between the grips. For this reason, extra care was taken to ensure that the volume of material sampled by the synchrotron X-ray beam was as close as possible to the thermocouple, in order to minimise temperature measurement errors. A gas enclosure was used in order to minimise the presence of oxygen surrounding the sample. An inert atmosphere with argon at low pressure and constant flow was maintained throughout all the tests.

The synchrotron experiment was carried out in two stages. In a first stage one diffraction image was obtained every 1.7 seconds during temperature cycles from room temperature to above the β-transus and back, aiming to study complete thermomechanical cycles. The acquisition frequency in this first stage was limited by the time needed to acquire and save one diffraction image in the acquisition computer. The acquisition time during this first stage allowed saving instantaneous data of load, temperature and position from the ETMT in a log file, meaning that each diffraction image acquired had a temperature stamp.

On the second stage of the experiment, the α→β→α transformation was studied in more detail. One diffraction image was acquired every 0.4 seconds, which was the fastest acquisition time achievable by the system, limited by the time needed to acquire and save a diffraction image in the temporary memory of the detector. This very short acquisition time brought two disadvantages. The first is that only one hundred (100)

images could be saved at a time, which meant that diffraction images could be acquired only during specific phases of the temperature cycles. The second is that with such a short acquisition time it was not possible to match the temperature/load data from the ETMT to each diffraction image directly. The temperature had to be estimated from identical thermal cycles run in the first stage.

4.1.2 THERMOMECHANICAL CYCLES

A wide range of maximum temperatures, heating/cooling rates and dwell times were tested, using numerous specimens. Table 4.1 lists the most representative samples, whose results will be presented in this and the following chapters, and summarise the experimental matrix. Most of the tests were carried out in load control, meaning that free thermal expansion and contraction was allowed without significant changes in the set value of load applied to the sample. One sample (S1) was heat treated under displacement constraint, meaning that the load was generated by thermal expansion/contraction and by the phase transformation.

Table 4.1 Experimental matrix for in-situ synchrotron experiment

SAMPLE	MAX. TEMP. (°C)	HEATING (°Cs^{-1})	DWELL (s)	COOLING (°Cs^{-1})	LOAD (N)
T1	1000	10	10	10	0
T2	1000	2	10	10	0
T3	950	10	3	50	0
T4	950	12	0	12	0
T5	940	12	0	12	0
S1	950	10	0	50	(a)
S2	940	10	3	50	7
S3	950	12	0	12	20

(a): constrained

It is important to recall that the capacity of the load cell of the ETMT is 3kN, and the tensile load that could be applied to the Zircaloy-2 matchstick-like samples without causing failure in the high temperature β phase was very small, between 5 and 10N. Therefore, the stability and accuracy of the load was not as high as was wished. Figure 4.4 exemplifies the oscillation of the load in two of the tests (T3 and S2). The load oscillates ±1N for most of the test, apart from a sudden tensile load caused by thermal contraction during fast cooling.
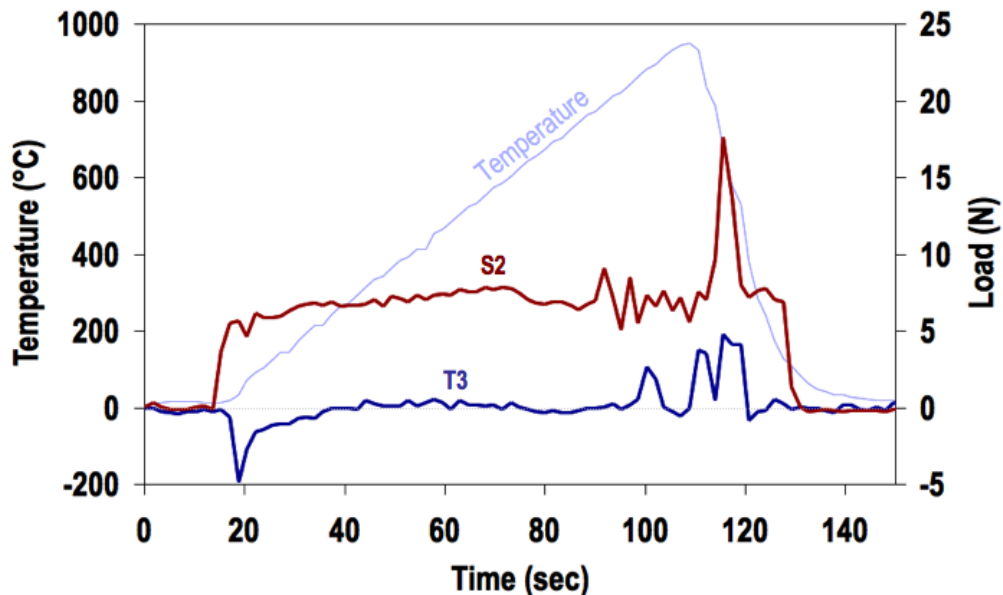
Figure 4.4 Oscillation of load during ETMT tests. Nominal loads 0N (T3) and 7N (S2).

Due to the temperature distribution present during the tests in the ETMT, different peak temperatures are reached at different positions along the sample. Although the exact peak temperature was measured only at one point in the specimen, thanks to the temperature gradient it is possible to qualitatively correlate different peak temperatures with changes in texture. For this purpose, the synchrotron X-ray beam was used to

record diffraction patterns every 0.5 mm along the length of the sample (RD) at the end of most of the tests.

4.1.3   TEMPERATURE MEASUREMENT UNCERTAINTY

Temperature measurement is very important for the evaluation of results of the in-situ SXRD experiment. The aim of this section is to investigate the uncertainty of the temperature value measured by the thermocouples, as well as the uncertainty in the temperature stamps assigned to the diffraction images acquired during the thermomechanical cycles.

The thermocouples for the experiment were made from R-type wires, i.e. pure platinum for one conductor and an alloy of platinum containing 13% rhodium for the other. To make a thermocouple the wires are melted together to produce a bead, which subsequently is spot-welded to the surface of the specimen. Although the thermocouples were fabricated following a standard procedure, they were made manually, which means that there were potential differences in the size of the bead, the quality of the contact between the thermocouple wires and the quality of the contact between the thermocouple bead and the surface of the specimen. All these factors produce uncertainty in the temperature measurement. In addition, the temperature stamps assigned to the SXRD images can have another sources of error, such as the distance between the thermocouple and the X–ray beam, and delay in temperature logging.

The variability in the measured phase transformation temperature was used to evaluate the extent of these uncertainties. If identical Zircaloy-2 samples are heat treated under the same conditions (heating/cooling rate, load), the measured transformation temperature should not differ between samples. The transformation temperatures were evaluated in two different ways: (1) performing resistivity measurements during the α→β phase transformation in similar thermomechanical cycles, and (2) analysing diffraction images acquired during the synchrotron experiment.

Resistivity Measurements

Numerous samples were subjected to thermal cycles without applied load, similar to those applied to sample T1, in order to determine the phase transformation temperatures by means of resistivity measurements. These tests were carried out at The University of Manchester, in an ETMT of similar characteristics to the one at the ESRF, with exception of the absence of inert gas atmosphere, i.e. the surface of the samples was subjected to oxidation. The resistivity measurements were not direct. Two platinum wires were spot-welded to the samples, as close as possible to the thermocouple bead, and the electrical potential difference (voltage) between these two connectors was logged along with the temperature, current, and load. The resistivity was calculated from instantaneous data of current and voltage.

Figure 4.5 shows the resistivity obtained in four different samples during heating. All these samples were thermally cycled starting in the as-rolled condition, and using a

heating rate of $10Cs^{-1}$. The absolute resistivity values differ between samples, due to differences in cross-section and in the distance between the conductors measuring the voltage. The resistivity trace obtained during cooling (at $50Cs^{-1}$) is shown for one of the samples (R1) to illustrate the hysteresis of the phase transformation. All the results exhibit some degree of noise in the signal, which is a major obstacle to determine accurately the transformation temperatures. The noise in the resistivity signals comes from oscillation of the electrical current applied to the sample to control the temperature. Nevertheless, the start and the end of the $\alpha \rightarrow \beta$ phase transformation are evident, marked by changes in the gradient of the resistivity.

In order to approximate the transformation temperatures, the signals shown in Figure 4.5 were normalised and fitted to a Gaussian peak as implemented in (O'Haver 2009). An example of the results is shown in Figure 4.6, and the transformation temperatures for the four samples are shown in Table 4.2. According to these results, the variation in measured transformation temperature ranges between 6 and 9°C.
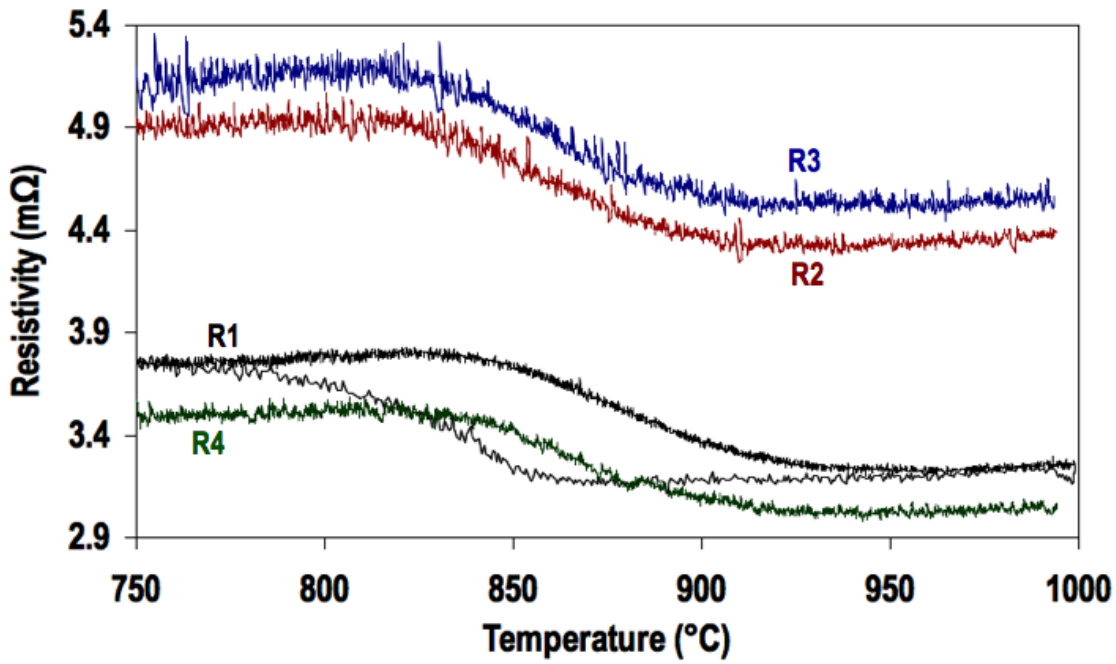
Figure 4.5 Resistivity measurements during thermal cycling of as-rolled samples
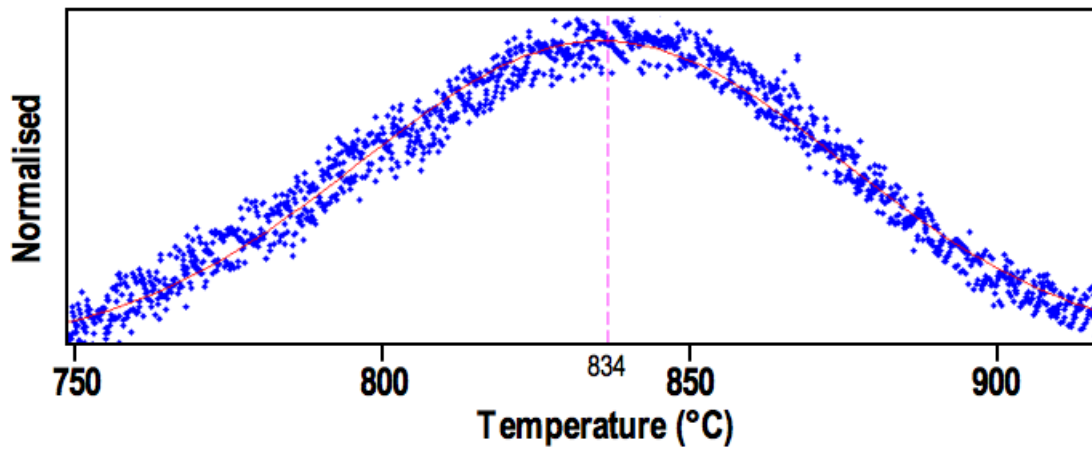
Figure 4.6 Example of peak fitting of resistivity measurements, corresponding to the first transition observed during heating in sample R1.

Table 4.2 Transformation temperatures according to resistivity measurements

SAMPLE	$\alpha \rightarrow \alpha+\beta$ (°C)	$\alpha+\beta \rightarrow \beta$ (°C)
R1	834	919
R2	821	907
R3	821	899
R4	826	910

With the aim of isolating the effect of changing thermocouples, an additional set of tests was carried out. This time one single sample was used, maintaining the wires to measure the voltage, so the effect of cross section and location/attachment of the wires was minimised. The thermal cycle on this sample was applied using a current cycle: the current was increased from 0 to 32A with a rate of $0.25As^{-1}$ and then decreased at a rate of $1.50 As^{-1}$. This cycle emulates one of the temperature-controlled β-quenching cycles, taking the sample to a peak temperature of 1100°C with mean heating and cooling rates of ~$9Cs^{-1}$ and ~$40Cs^{-1}$ respectively. This cycle was repeated five times (RC-1 to RC-5), and then the thermocouple was changed, before repeating the cycle another five times (RC-6 to RC-10). Sections of the temperature profiles obtained are shown in Figure 4.7, while the maximum temperatures measured are listed in Table 4.3.
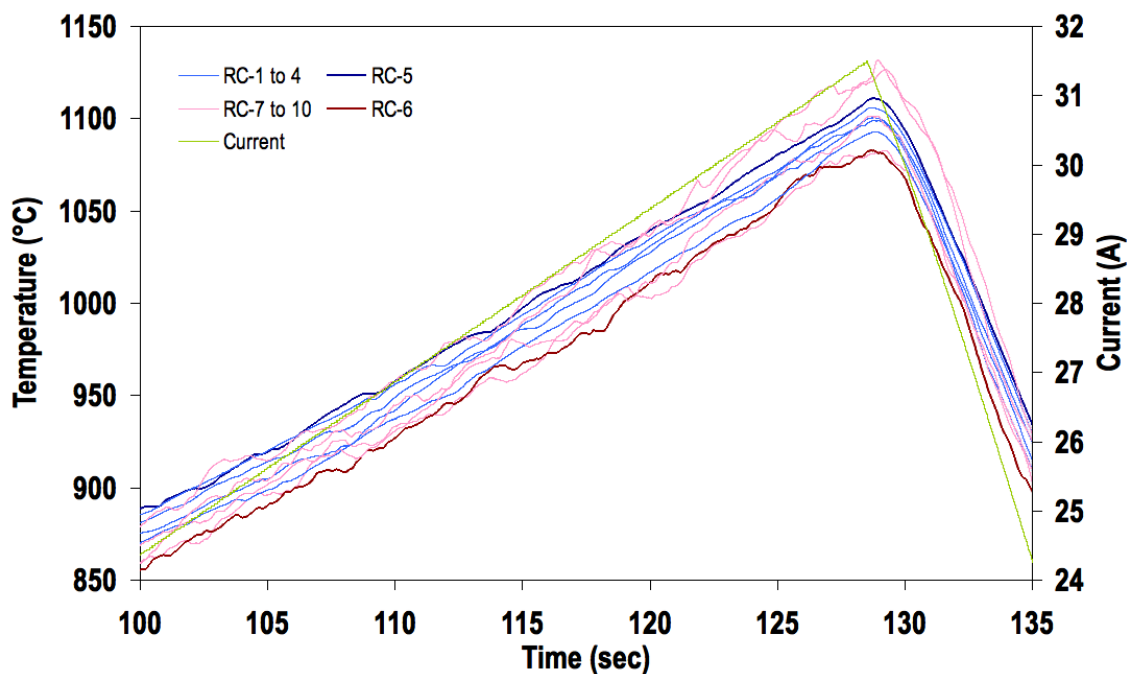
Figure 4.7 Temperature profiles obtained from sample TC in different cycles.

Table 4.3 Maximum temperatures measured in sample RC in different cycles

Cycle	Max. Temperature (°C)
RC-1	1099
RC-2	1092
RC-3	1101
RC-4	1106
RC-5	1110
RC-6	1082
RC-7	1083
RC-8	1101
RC-9	1132
RC-10	1127

For this sample, it is clear that in addition to the effect of the thermocouple, the sample undergoes physical changes, which makes difficult to evaluate temperature uncertainty quantitatively. However, some useful observations can be made:

·   The temperature profile of the first run (RC-1) showed more variability than runs RC-2 to RC-4. This may be explained by stabilisation of the thermocouple and the spot weld. Conversely, the second thermocouple seems to deteriorate, runs RC-7 to RC-10 show significantly less stable temperature profiles than run RC-6.

·   The temperature measured increased from run RC-2 to run RC-5. This would indicate that after β-quenching the first time, the resistivity of the material increases slightly with each new β-quench. This may be related to an accumulated oxidation in the surface with each cycle, given that these samples were heat treated in air.

·   Regarding the effect of the thermocouple, minimising the physical changes in the sample, one can compare the results between run RC-5 and RC-6, i.e. the last run of the first thermocouple and the first run of the second thermocouple. The differences in measured temperature between these two runs, for the same value of current, range between 20 and 40°C with an average of ~33°C. This large difference could

be explained by the difficulty of attaching a second thermocouple in a surface that was already oxidized.

Analysis of Diffraction Images

According to results that will be presented in the next section (4.1.4), there are three main events occurring during heating of cold-rolled Zircaloy-2 samples, which are detectable in the diffraction images: (1) start of recrystallization, (2) start of the $\alpha{\rightarrow}\beta$ phase transformation, and (3) end of the $\alpha{\rightarrow}\beta$ phase transformation (β-transus). During the first stage of the in-situ synchrotron experiment, i.e. where temperature stamps were logged with each individual diffraction image, two pairs of samples were subjected to identical heating to samples T2 and T3 in the experimental matrix, and their diffraction images were acquired using the same parameters (frequency and exposure).

Table 4.4 lists the temperatures at which recrystallization and phase transformation were observed in the diffraction images for these two pairs of samples, according to the corresponding temperature stamps. As a reference, resistivity measurements carried out by Gey et al. in Zircaloy-4 (Gey et al. 2002a) detected the start and the end of the phase transformation at 834°C and 938°C respectively. The differences with respect to these results and to the resistivity measurements may be attributed to a delay in the macroscopic response of the resistivity variations (depending on the size of the sample), and the differences in composition between Zircaloy-2 and Zircaloy-4.

Table 4.4 Transformation temperatures from in-situ experiment

SAMPLE	HEATING ($°Cs^{-1}$)	MAX. TEMP. (°C)	DWELL (s)	LOAD (N)	START RX (°C)	START $\alpha \rightarrow \beta$ (°C)	β-TRANSUS (°C)
T2 (1)	2	1000	10	0	584	797	916
T2 (2)	2	1000	10	0	588	805	920
T3 (1)	10	950	3	0	623	823	934
T3 (2)	10	950	3	0	631	816	930

The results in Table 4.4 suggest that the heating rate has an effect on the measured transition temperatures. The transformation temperatures observed in the two samples heated at $2°Cs^{-1}$ are similar to each other, as are the ones of the group heated at $10°Cs^{-1}$. However, there is a consistent difference between the two groups, with lower transition temperatures obtained in the slow heated samples. This effect could be attributed to a consistent delay between the time at which the diffraction image is saved, and the time at which the temperature is logged. Although the number of data points for this analysis is limited, the data in the table suggests that the temperature uncertainty ranges between 5°C and 8°C, which is close to the results obtained from the resistivity measurements carried out in similar conditions. This uncertainty was taken into account when analysing the results of the following sections.

4.1.4   DIFFRACTION IMAGES OBTAINED IN-SITU

Figure 4.8 shows a series of diffraction images obtained during heating of one of the samples (T3 in Table 4.1), which are typical for most of the tests. All the images acquired exhibited symmetry with respect to the centre of the rings, which suggest already the presence of orthotropic sample symmetry. In the figure, only one quadrant of each image is displayed to facilitate their interpretation.
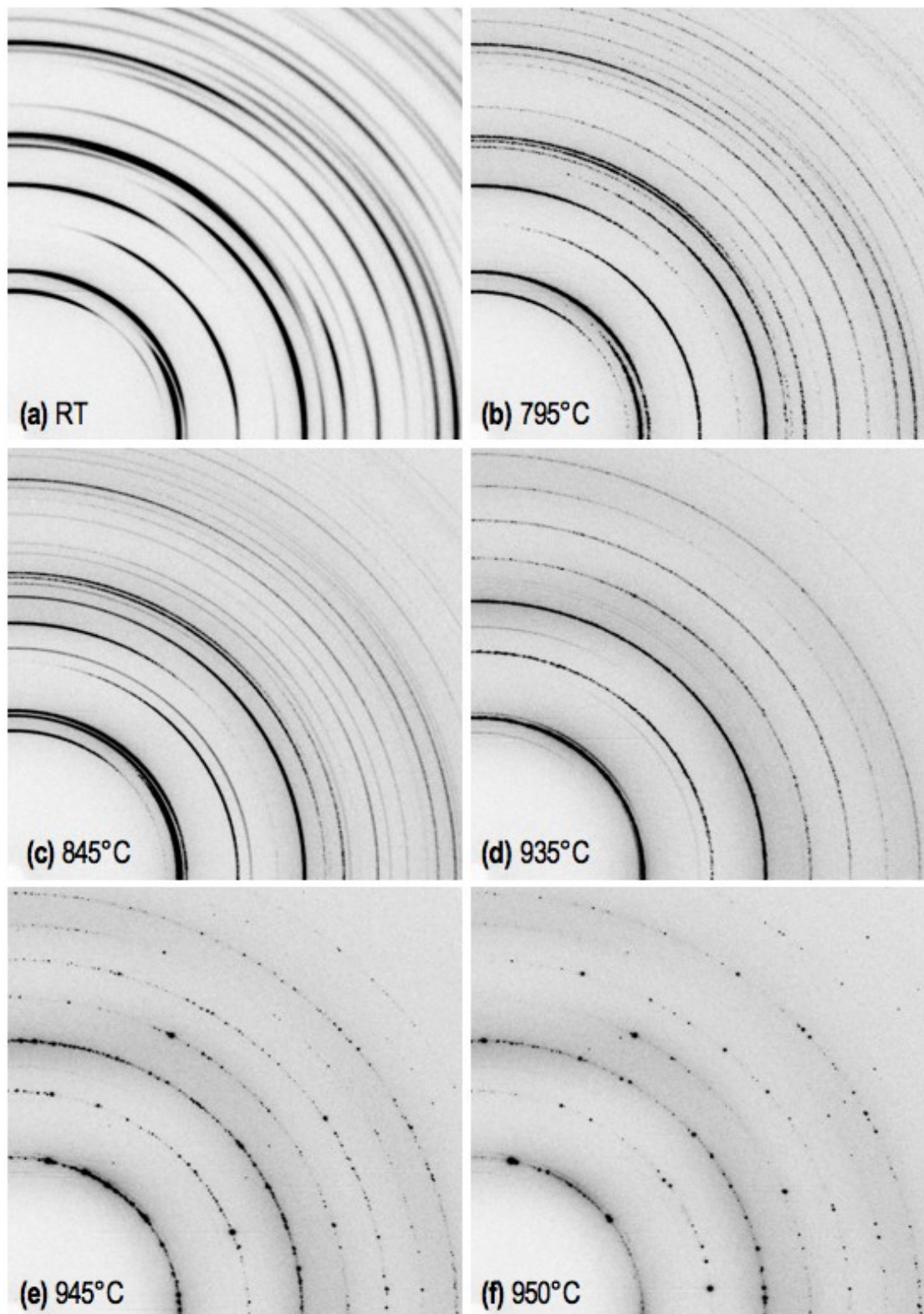
Figure 4.8 SXRD images taken at different temperatures during heating of sample T3. (a) cold-rolled (as-received), (b) before the onset of the α→β transformation, (c) intermediate stage ~55%β, (d) phase transformation almost complete ~98%β, (e-f) 100%β illustrating grain growth

From Figure 4.8(a) it can be inferred that in the as-rolled condition the microstructure is extremely fine and presents a strong texture. The diffraction rings are smooth, suggesting that a large number of grains are being sampled (consisted with a cold worked material). Along each ring there are systematic variations in intensity. Figure 4.8(b) shows how the diffraction images obtained are extremely sensitive to the grain size and the annealing state of the material. At 795°C the intensities along the α diffraction rings are slightly scattered, which evidences microstructural changes, probably recrystallization and/or grain growth.

The presence of the high temperature β phase emerges in the diffraction images at approximately 800°C, with an estimated volume fraction of ~10%. Volume fractions of β below this threshold are difficult to detect. An intermediate stage of the phase transformation is illustrated in Figure 4.8(c), where both phases are present. At 935°C, Figure 4.8(d), the $\alpha\rightarrow\beta$ transformation is practically complete. The diffraction image is dominated by β-phase rings with a tenuous presence of α, estimated to be ~2%. The homogeneous distribution of intensity along the β rings indicates that the β texture at this point is not particularly strong. The next two diffraction patterns acquired, Figure 4.8(e-f), show rapid scattering of the intensities along the β rings, to the point that at 950°C there are only erratic spots around the rings in the image. This evidences a sudden change in the microstructure in a narrow range of temperature, most probably due to highly accelerated β grain growth once the $\alpha\rightarrow\beta$ transformation is complete. When the temperature was increased further, the diffraction images showed only few

spots. This is important because the amount of grains sampled affects the suitability of

these images for texture analysis.
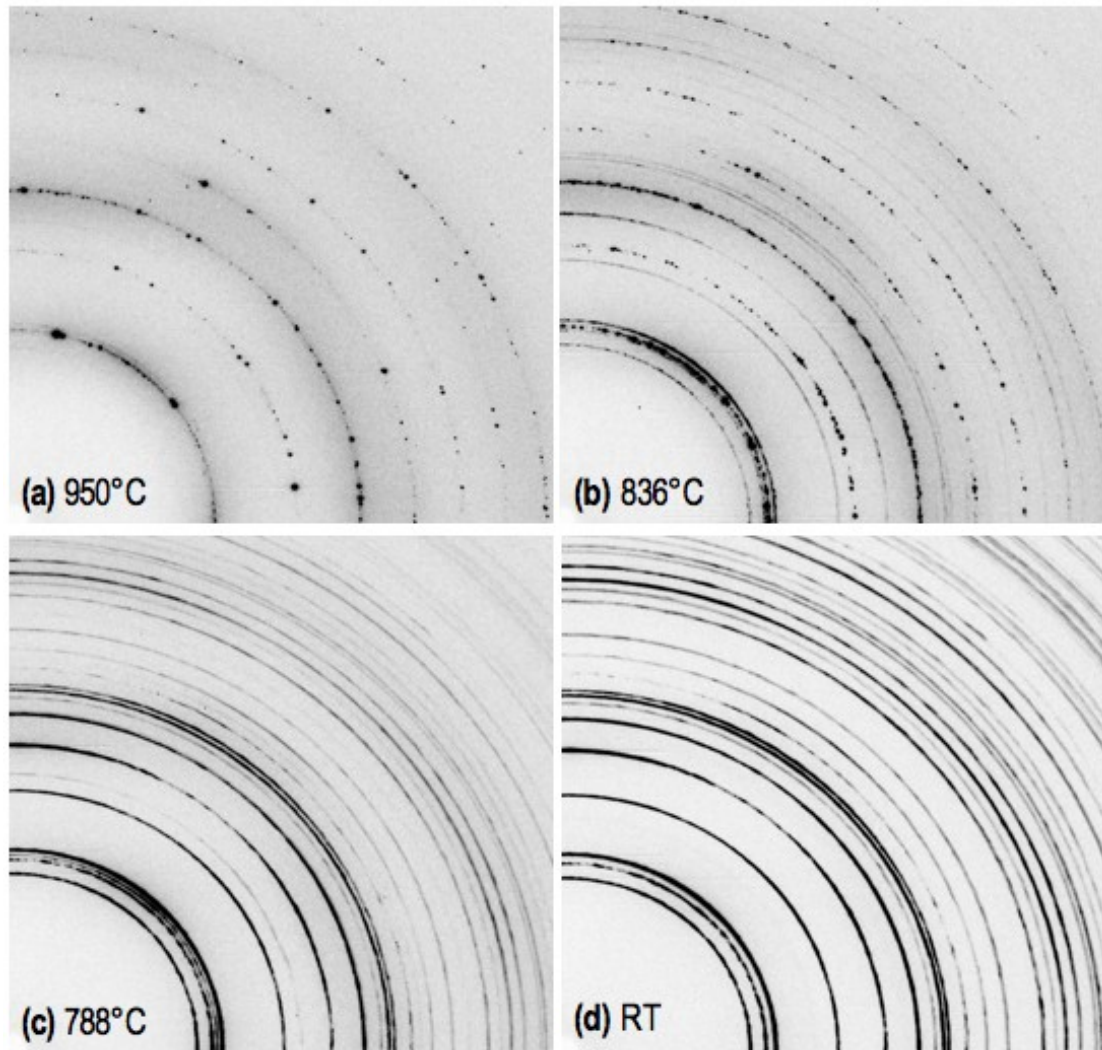
Figure 4.9 SXRD images taken at different temperatures during cooling of sample T3. (a) 100%β, (b) 15%α, (c) 85%α, (d) room temperature β-quenched

Figure 4.9 shows a series of images obtained during cooling of the same sample. These

images are also typical for most of the tests carried out. In the majority of the tests the

samples underwent relatively fast cooling, thus the amount of diffraction images

available is more limited. The α diffraction rings appear very quickly and the

distribution of intensities along them does not change significantly during the process. In Figure 4.9(b), the estimated volume fraction of α is 15% and the rings appear already smoother than in the as-rolled condition, exhibiting less changes in intensity. The intensity distribution along the α rings does not change significantly in Figure 4.9(b-d). This suggests that the crystallographic texture of the inherited α phase is determined during the early stages of the $\beta \rightarrow \alpha$ phase transformation, and subsequently remains relatively unchanged.

4.1.5   DATA PROCESSING

The 2D diffraction images were stored using a standard ESRF file format. Each file contained the array of intensities, together with metadata such as an acquisition time stamp, run number, etc. These diffraction images contain texture information from two sources: the first is a systematic variation of intensity along a single ring corresponding to a given reflection, and the second is the correlation of intensity variations between several reflections from the same image. With area X-ray detectors, multiple incomplete experimental pole figures are sampled simultaneously, since diffraction rings belonging to several sets of planes are captured at once.

Measurements were carried out using radial diffraction geometry, meaning that there were some important instrument parameters to take into account for the refinement of the data. The actual wavelength, the centre of the image, the sample to detector distance, and the tilting of the detector had to be determined. In this particular

experiment, these parameters were kept constant and were calibrated through

measurements on a standard aluminium powder of known lattice parameters at different

sample to detector distances. From the differences between the distances, the absolute

values can be determined. Figure 4.10 compares the diffraction images of the

aluminium standard and a sample of Zircaloy-2 in as-rolled condition. The standard

should not have signs of texture, i.e. the intensity along each ring should be constant.
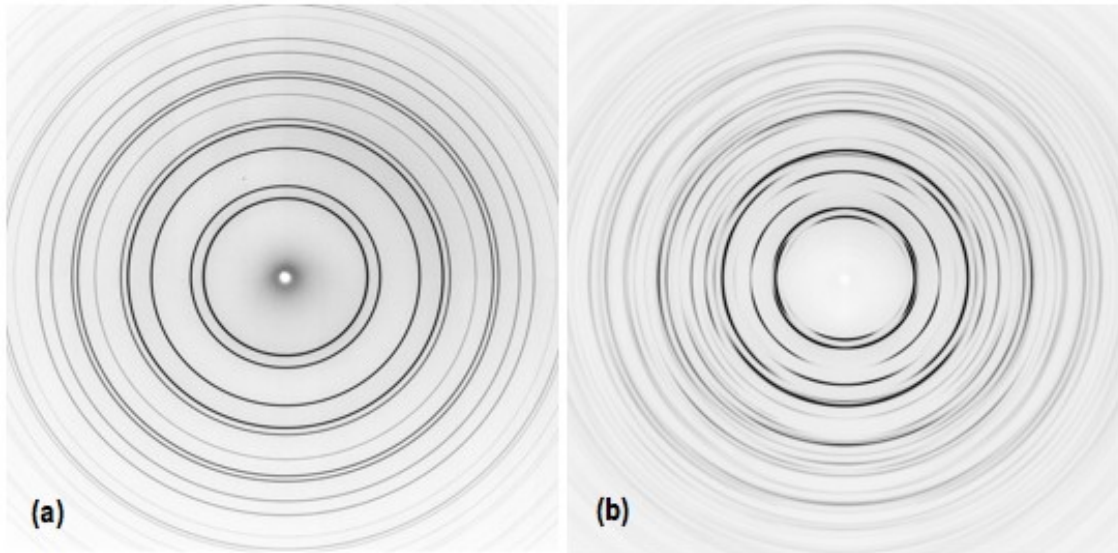
Figure 4.10 Diffraction images from (a) aluminium powder standard and (b) as-rolled Zircaloy-2.

The calibration of geometric parameters was carried out using the software FIT2D

(Hammersley 1998). FIT2D is a general-purpose program for analysis of X-ray

diffraction data in one and two dimensions. It has become a standard in most of the

beamlines of the ESRF and in many other crystallography research groups. Calibration

and correction of detector distortions are precisely amongst the most important uses of

FIT2D. Normally the first step when calibrating a 2D diffraction image is the correction

of dark field, flat field and spatial distortions. With the Pixium detector, the dark-field

correction was performed applying a function built into the detector hardware while there was not incident radiation. The geometrical parameters obtained after analysing the calibration images are listed in Table 4.5.

Table 4.5 Calibration parameters for synchrotron experiment

Wavelength (Å)	0.141582
Image centre (pixels)	x: 1326.558 y: 960.724
Image centre (mm)	x: 204.290 y: 148.106
Detector distance (mm)	697.831
Tilt axis (°)	-48.18
Tilt angle (°)	-0.13

The next step is to determine the diffraction intensities of all the reflections as a function of the polar angle in the Debye ring (normally denoted as η). For this purpose the diffraction image is sliced in polar angular sections, and the intensity within each slice is integrated. When the number of grains sampled is high and the diffraction rings appear smooth, angular sections of 5° are normally used. If the intensity along the rings appears more scattered, then larger angles may be chosen. For this particular experiment, the maximum angular section used was 10°. The integration process converts the diffraction image into a set of 2-theta diffraction spectra at different polar angles (36 or 72 spectra depending on the section size).

For the integration of the diffraction images acquired during the thermal tests, the calibration parameters are critical. Therefore, the calibration must be checked beforehand. This can be done by examining an integrated diffraction image from the calibration standard. Figure 4.11 shows a diffraction image from the aluminium calibration standard after integration. Since the aluminium standard is a powder, neither

texture nor residual stresses should be present. Therefore, the integrated rings should not exhibit shifts in the diffraction angle or changes in intensity along each reflection. In Figure 4.11, the rings appear as straight vertical lines with constant intensity, which evidences a satisfactory calibration.
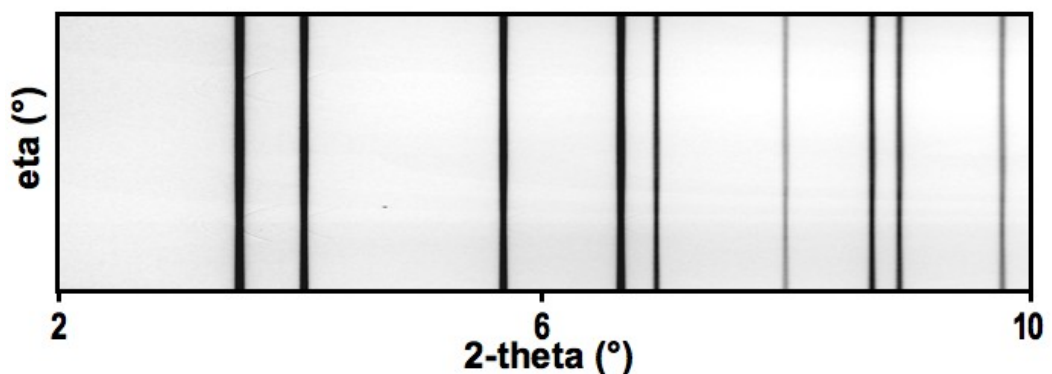
Figure 4.11 Integrated diffraction image from the aluminium standard

The integrated intensities obtained from FIT2D were exported to be analysed using the Rietveld (Rietveld 1969) method as implemented in the software MAUD (Lutterotti *et al.* 1997). MAUD is a general diffraction analysis program that has many advantages for its application in this project. It is very versatile and can analyse multiple spectra, it supports different instruments and techniques and includes many useful functions such as texture and residual stresses calculations. However, being so general, it takes many parameters into account, which makes the fitting process very laborious. In addition, MAUD is closed-source so it is not possible to know exactly what algorithms are used.

The raw files obtained from the beamline were converted into sets of 2-theta spectra and loaded into MAUD. For the aluminium calibration standard, the crystal and all the

geometrical parameters were known. All the other instrument parameters available in MAUD such as peak shape parameters, 2-theta offset, etc. were refined at this point until the calculated diffraction spectra matched the experimental data. This refinement was a laborious process, especially when multiple phases were present and the diffraction peaks overlapped. The parameters were normally refined in the following order: (1) incident intensity and background, (2) cell parameters, crystallite size and microstrain, and (3) volume fraction of phases. At this stage, the background, the peak position and the peak profiles showed a good agreement with the experimental data, and the texture could be introduced to match the changes in intensity. The texture was included in the Rietveld refinement using 10 iterations of the enhanced E-WIMV (Matthies and Vinel 1982) discrete algorithm implemented in MAUD. For the fitting, intensities from the spectra were extracted using the LeBail method (Le Bail *et al.* 1988). An incomplete pole figure was extracted from each diffraction ring and the E-WIMV algorithm was used to calculate ODFs from these pole figures. The resolution of all the ODFs obtained from synchrotron data was set to 10° and no sample symmetry was imposed. Once the refinement of the ODFs was finished for each diffraction image analysed, complete pole figures were recalculated.

For the refinement of actual data, most of the instrument parameters obtained from the standard were used. However, since the incident intensity, the background and the image centre may change during the measurements, they were refined again for each diffraction image. Figure 4.12 shows the results of the Rietveld analysis in MAUD for a

diffraction image from a Zircaloy-2 specimen in as-rolled condition. Thanks to the resolution of the detector and an adequate sample to detector distance, it was possible to capture a reasonable number of Debye-Scherrer rings, which maximised the amount of information available for ODF calculations. Up to 46 and 13 diffraction rings were captured for the α and β phases respectively, within a 2-theta range between 2° and 10°.
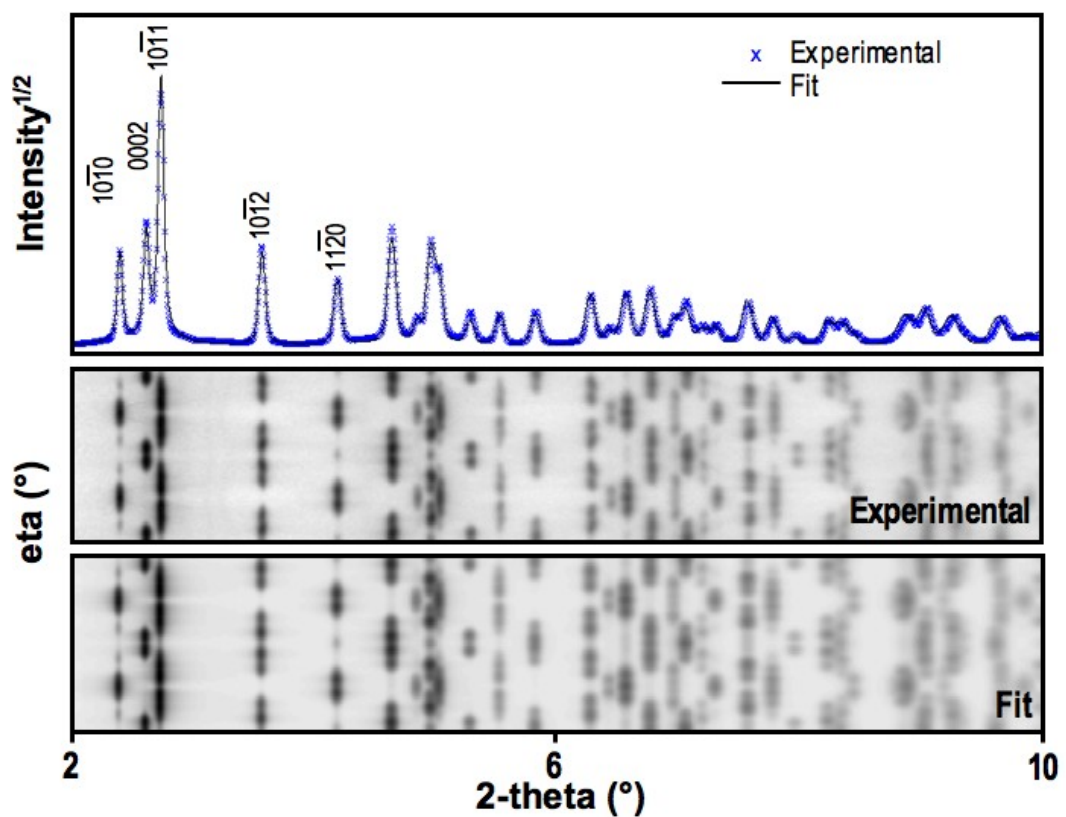
Figure 4.12 Results of fitting a set of synchrotron X-ray spectra, corresponding to the as-rolled condition. Sum of all spectra at the top and comparison of intensity 2D views at the bottom.

4.1.6   SXRD RESULTS COMPARED TO LXRD AND EBSD

As described in section 1.2.2, the pole figure coverage achieved with data from a single synchrotron diffraction image is limited. In the SXRD experiment of this work, no rotations could be applied to the samples during the thermomechanical tests. For this

reason, it is important to compare results obtained using this technique, with other results obtained using better-established methods such as LXRD and EBSD. Figure 4.13 and Figure 4.14 serve for this purpose, displaying comparisons for two different conditions of the material: as-rolled and recrystallized. The comparison of results in as-rolled condition is simple, since identical samples were characterised using the three different techniques. The synchrotron results of the recrystallized condition were obtained at high temperature, thus it is not possible to compare them with results obtained at room temperature using LXRD or EBSD. Two samples that had been fully recrystallized in different conditions are used. For a side-by-side comparison in this case it has to be assumed that the recrystallization texture does not change during cooling, as long as the temperature is below the start of the phase transformation (<800°C). The EBSD data was obtained in a recrystallized region of one of the samples heat treated in the ETMT (S1 in Table 4.1), following procedures that will be discussed in detail in the next chapter, section 5.1.

There is very good agreement between the results obtained with the three techniques for these two conditions. The sets of pole figures obtained with SXRD and LXRD show practically the same features, with a good match in shape and intensity. The EBSD results are in general similar to the other two, but the shape and intensity of the maxima are slightly different, especially for the prismatic planes $(11\bar{2}0)$ and $(10\bar{1}0)$. This is more evident in the as-rolled condition. This can be attributed mainly to the common EBSD misindexing found in hcp metals, that "rotates" the real orientation of the crystal

30° around the $\vec{c}$ axis. Misindexing is more likely in the heavily deformed sample, so it is understandable to find the most significant differences between the EBSD results and the other techniques in the as-rolled condition. The (0002) pole maxima close to ND appear more concentrated around that direction in the EBSD results for both conditions, which was also evidenced in section 3.5.
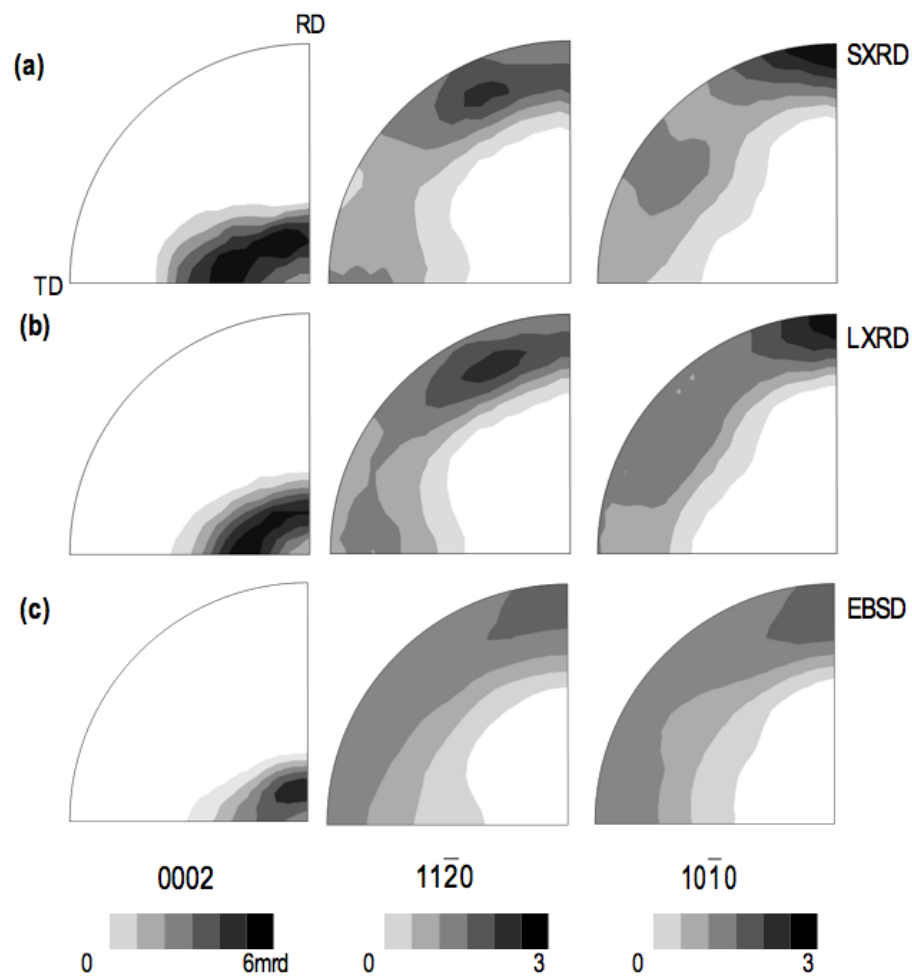
Figure 4.13 Pole figures of Zircaloy-2 in as-rolled condition. Identical samples were characterised using the three different techniques.

The quality of the pole figures obtained in this SXRD experiment, compared to those obtained using LXRD, represents an important improvement with respect to the results

presented by Ischia et al. (Ischia *et al.* 2005) shown in section 4.1. This improvement

can be attributed to the increased number of available reflections and the quality of the

fitting.
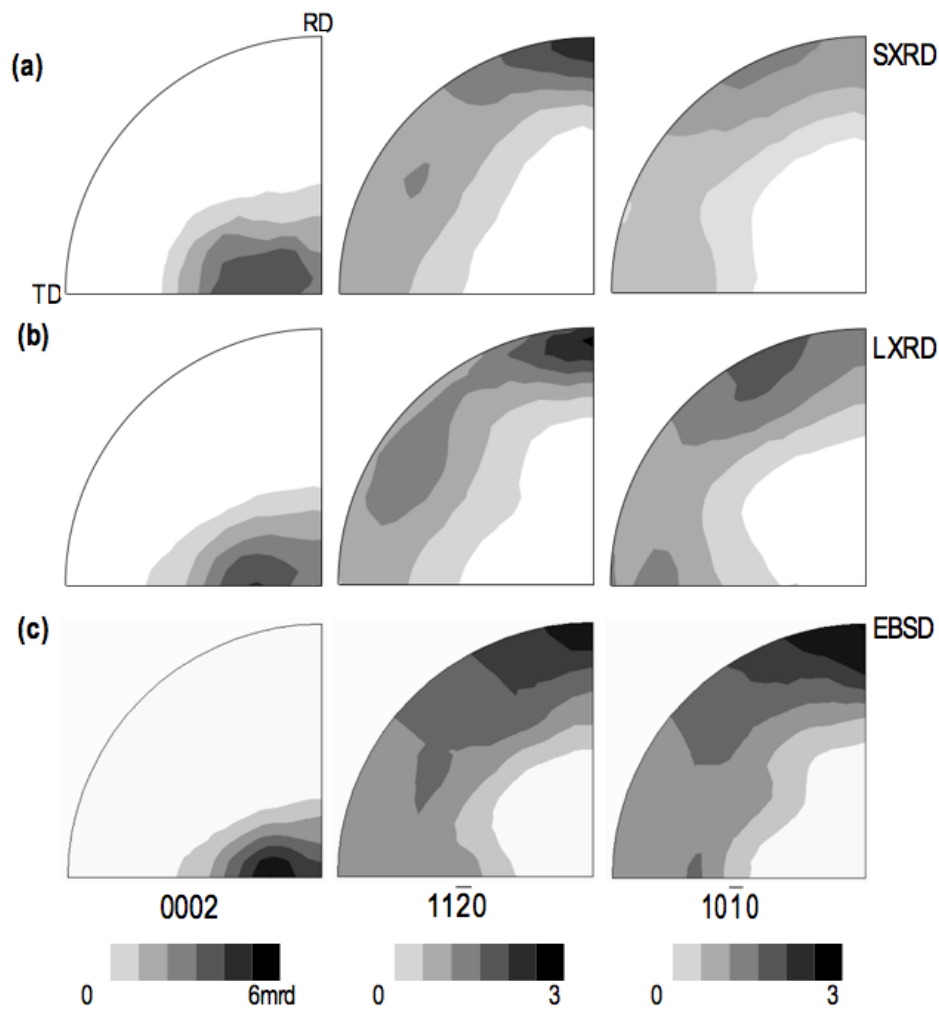
Figure 4.14 Pole figures of Zircaloy-2 in fully recrystallized condition: (a) obtained using SXRD in-situ at 795°C, (b) obtained using LXRD at room temperature in a sample recrystallized in a tube furnace for 5 minutes at ~775°C and cooled in air, (c) obtained using EBSD at room temperature in a recrystallized region of a sample β-quenched in a ETMT (S1), estimated maximum temperature ~790°C.

Figure 4.15 indicates that the agreement between techniques is worse in the β-quenched

condition. Figure 4.15(a) and (c) correspond to the same sample, the former obtained

in-situ using SXRD and the latter obtained during posterior EBSD characterization in

approximately the same region where the sample was irradiated in-situ. The sample

used for LXRD, Figure 4.15(b), was β-quenched differently and should be seen as a

reference only. Two main differences are found: (1) pole maxima obtained using EBSD

are sharper, although they have relatively the same intensity as those obtained using

SXRD, and (2) the (0002) pole figures in the β-quenched condition exhibit a maximum

parallel to TD. This maximum is clearly observed in the LXRD and EBSD results, but it

is significantly underestimated when using synchrotron X-rays. The area scanned using

EBSD to obtain the pole figures shown in Figure 4.15(c) was large enough to ensure

good statistics (see sample T3 in Chapter 5), so it can be assumed that the sharper pole

maxima are real, and not an artefact created by insufficient sampling.

The underestimation of the (0002) pole maxima parallel to TD finds an explanation in

the geometry employed for the measurements. In this experiment, TD was parallel to

the beam. In transmission SXRD, crystallographic planes lying perpendicular to the

X-ray beam do not contribute to the diffracted intensities, thus they cannot be detected

in the diffraction image. Therefore, no pole intensities from (0002) planes

perpendicular to the beam can be measured directly, and have to be reconstructed from

the information given by other reflections when the ODF is calculated. These reflections

lie at high angles and have much lower intensity; therefore it is more difficult to

reconstruct pole intensities parallel to TD accurately. Apparently, the texture observed

in this condition is not sufficiently strong to compensate for the lack of directly

measured experimental data. This is an important limitation of the SXRD results

because, as it will be seen later, this pole belongs to a distinct texture component that is heavily underestimated in the SXRD data.
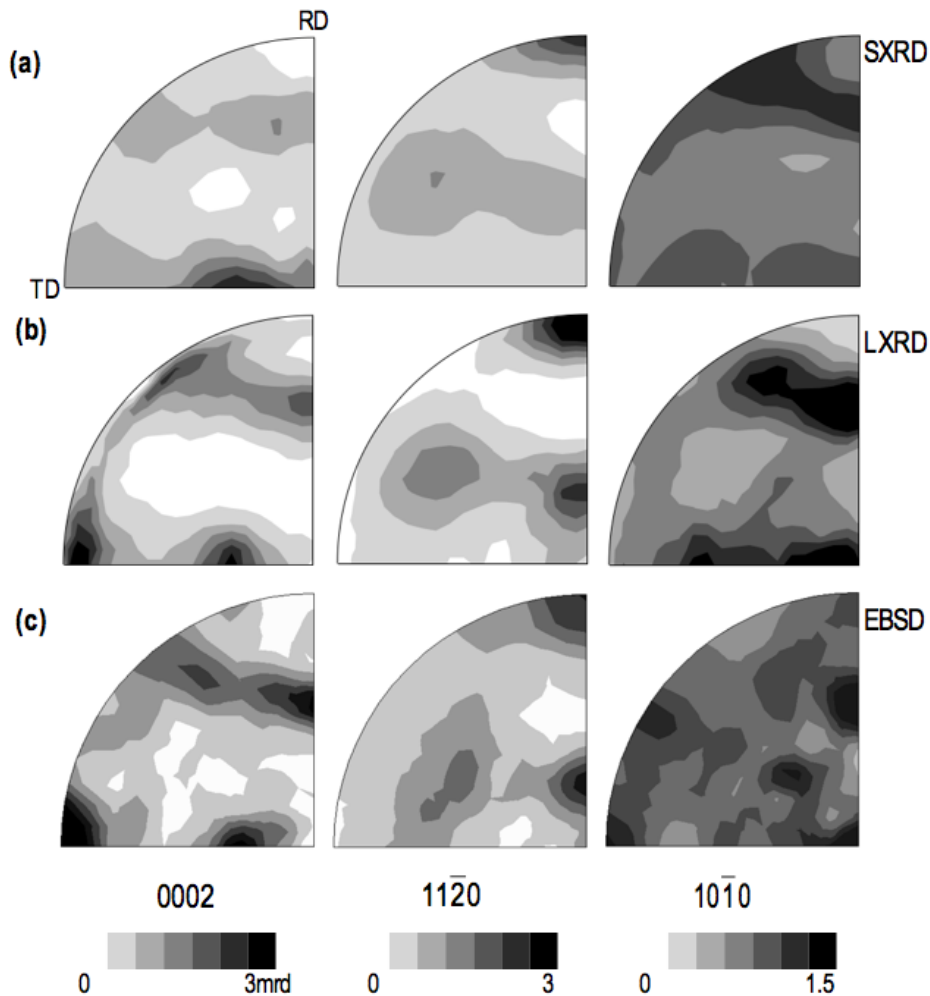
Figure 4.15 Pole figures of Zircaloy-2 in β-quenched condition: (a) obtained in-situ using SXRD at room temperature after β-quenching at 950°C (sample T3), (b) obtained using LXRD on a sample β-quenched in a tube furnace at ~953°C (sample A15 section 6.1 for details), (c) obtained using EBSD in approximately the same region as (a).

In summary, by comparing the results of texture measurements from single synchrotron diffraction images with those obtained using LXRD and EBSD, it was found that they are reliable for most conditions, especially if the texture is relatively strong. Some pole maxima, hence some ODF components, are underestimated in certain cases. These

findings were taken into account when analysing the results in the following sections of this chapter.

4.2   TEXTURE EVOLUTION DURING THE α→β→α PHASE TRANSFORMATION

The series of pole figures in Figure 4.16 illustrates the most significant changes of crystallographic orientation occurring during a complete α→β→α transformation. The pole figures shown are the basal (0002) and the prismatic $(11\bar{2}0)$ for the α-phase, and the (110) and (111) for the β-phase. These sets of pole figures are representative of the texture for each phase, and can be directly associated with the Burgers orientation relationship. The pole figures shown in Figure 4.16 correspond to thermomechanical cycle T3 of the list shown in Table 4.1, and are typical for most of the tests carried out.

4.2.1   RECRYSTALLIZATION

The strong rolling texture observed in the starting material, shown in Figure 4.16(a), remains practically constant from room temperature to approximately 620°C. At this temperature, the diffraction images start to change: the intensities along each ring start to scatter, evidencing alterations in the microstructure. The texture begins to change and stabilises again at approximately 730°C, remaining unchanged until the onset of the α→β phase transformation at ~810°C. Figure 4.16(b) illustrates the texture at 795°C.
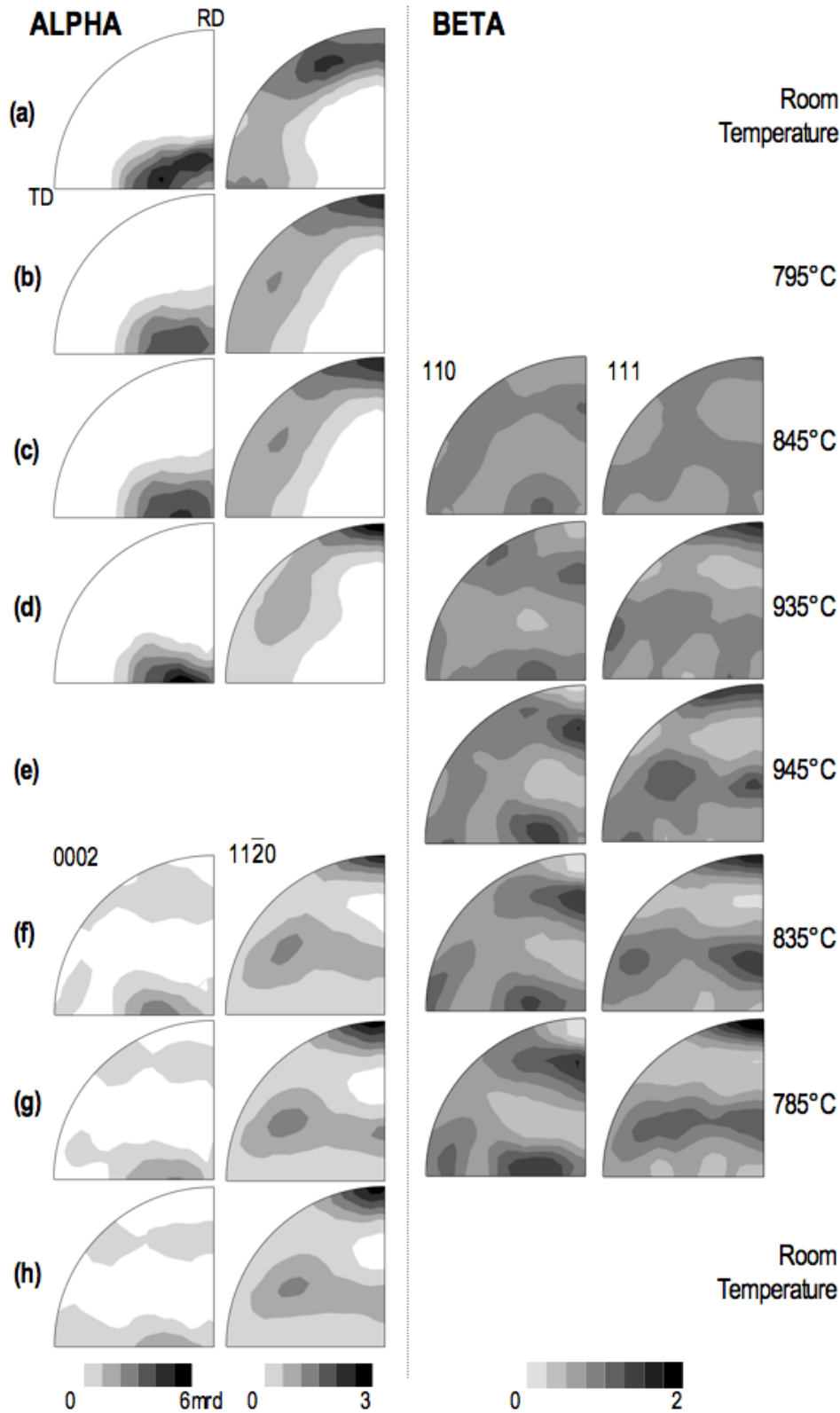
Figure 4.16 α and β pole figures obtained in-situ using SXRD during a complete α→β→α phase transformation: (a) cold-rolled, (b) recrystallized, before the start of the α→β phase transformation, (c) 46% α and 54% β, (d) at the end of the α→β phase transformation ~98% β, (e) 100% β before grain growth, (f) 15% α and 85% β, (g) 85% α and 15% β, (h) after β-quenching

The stored energy in the cold-rolled material stimulates annealing, a combination of recovery and recrystallization. This is evidenced by the increase in spottiness on the diffraction images, and the growth of the $(11\bar{2}0)$ pole component parallel to RD at expense of the rolling component $(10\bar{1}0)$ parallel to RD. These results are similar to those previously reported in other zirconium alloys and in CP titanium (Wenk *et al.* 2004, Lonardelli *et al.* 2007, Tenckhoff 1988, Wagner *et al.* 2002). This characteristic crystallographic rotation has been attributed to primary recrystallization and subsequent grain growth. Some differences have been observed between the present study and previous work, the most important being the behaviour of the basal poles. It has been reported that the (0002) maxima move towards ND during annealing (Tenckhoff 1970), but these results show that the splitting towards TD occurs during annealing.

4.2.2   α→β PHASE TRANSFORMATION

The α→β phase transformation starts at 810°C and finishes at approximately 940°C. Figure 4.16(c) shows pole figures corresponding to an intermediate step of the phase transformation at 845°C, where the volume fraction of α and β is similar. At 935°C, the transformation is almost complete, illustrated by the pole figures in Figure 4.16(d). At this point, the Rietveld analysis estimates 2% volume fraction of α-phase remaining.

Previous work on CP titanium (Lonardelli *et al.* 2007) has shown that, during transformation on heating, the $(11\bar{2}0)$ pole density parallel to RD is significantly reduced, which was attributed to preferential transformation of the recrystallization

texture component. The justification given by Lonardelli et al. is that the grains with this orientation are more prone to twinning, and β nuclei are formed mainly in these highly deformed regions. In the synchrotron experiment presented here, however, the α texture does not change considerably at least during first half of the transformation, Figure 4.16(b-d). The pole intensity of the recrystallization texture component appears to increase slightly only in Figure 4.16(c), when the fraction of α-phase has been reduced to ~15%. This would suggest that if there is preferential transformation, it occurs in α grains that do not belong to the principal texture component. Figure 4.17 illustrates how the α texture index does not vary significantly during most of the α→β transformation.
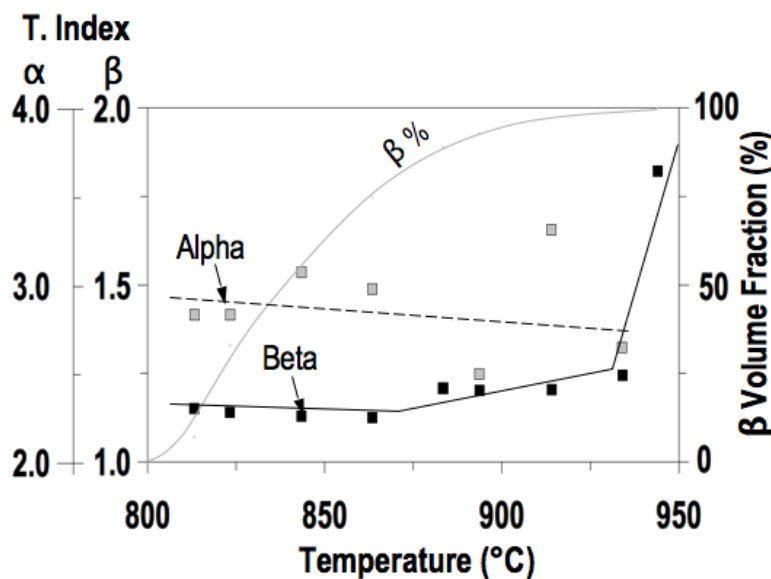
Figure 4.17 Evolution of texture indices during the α→β transformation (Romero *et al.* 2009).

The succession of β pole figures in Figure 4.16(c-e) displays slightly increasing pole intensities with temperature. In Figure 4.17 the β texture index increases when the β

volume fraction exceeds 50%, before dramatically increasing when the α→β phase transformation is close to completion. This evidence indicates strengthening of the β texture during heating. Strengthening of the β texture was seen previously in CP titanium (Lonardelli *et al.* 2007), being associated to competitive growth between β grains. In-situ SEM and EBSD studies in CP titanium rolled sheets (Seward *et al.* 2004) have shown that in the very early stages of the α→β transformation there is simultaneous nucleation of β phase not only at the α grain boundaries as allotriomorphs, but also within the grains as plates. Seward et al. reported that grain boundary β tends to maintain the Burgers orientation relationship with one of the parent α grains, whereas the orientation distribution of intragranular β is more random. They suggest that the final stage of the transformation consists of a competitive growth between these two types of nuclei, being dominated by the grain boundary β, since it has faster moving interfaces. If one assumes that the α→β transformation in cold-rolled sheets of Zircaloy-2 occurs in a similar manner, the slight strengthening of the β texture on heating can be explained by preferential growth of variants that have nucleated in the α grain boundaries.

4.2.3   β TEXTURE

The α→β phase transformation is complete at 945°C, when only β reflections are detected in the diffraction image and a significant microstructural change is evidenced, probably the first stages of β grain growth. The scattered intensities along the diffraction rings at 945°C and 950°C (see Figure 4.8), evidence extremely rapid grain

growth once the β-transus has been exceeded. The β texture observed at the end of the

α→β transformation is not particularly strong, with the pole intensities ranging from 0.5

to 2 times random and a texture index of only 1.85. The texture measured at 950°C

shows sharper pole intensities, but since it comes from a highly scattered diffraction

image, it is difficult to differentiate between genuine texture strengthening and an

insufficient number of sampled grains. The most relevant feature of the high

temperature β texture is a (111) maxima parallel to RD. The (110) pole figure exhibits

four maxima surrounding ND, two tilted ~60° towards RD and two tilted ~30° towards

TD, the latter resembling the split maxima of the (0002) α pole figure of the

recrystallization texture before the transformation.

The β texture observed here is similar to that found during in-situ texture measurements

in zirconium and CP titanium reported in the literature. Wenk et al. (Wenk *et al.* 2004)

carried out in-situ texture measurements during the phase transformation of 6 x 6 x 6

mm^3 cubes of hot-rolled Zircaloy-4, while Lonardelli et al. (Lonardelli *et al.* 2007)

studied 5 x 5 x 5 mm^3 cubes of cold-rolled CP titanium. These experiments were carried

out in a vacuum furnace with heating and cooling rates about 20°C/min, using neutron

diffraction. Their samples were kept at different steps of temperature for about one

hour, while the temperature stabilised and all the rotations for texture measurement

were performed. Figure 4.18 compares the pole figures obtained in the SXRD

experiment in this work, with those obtained by Wenk *et al.* using neutron TOF

diffraction in Zircaloy-4. The β-transus temperature for Zircaloy-4 is approximately

970°C, so in Figure 4.18(a) the transformation is incomplete, while in Figure 4.18(b) the transformation is certainly complete, even with some evidence of β grain growth. The origin of the β texture reported by Wenk et al. and Lonardelli et al. was attributed to preferential transformation of the recrystallization orientations. As mentioned in the previous section, no evidence of preferential transformation was observed during the α→β transformation in this work.
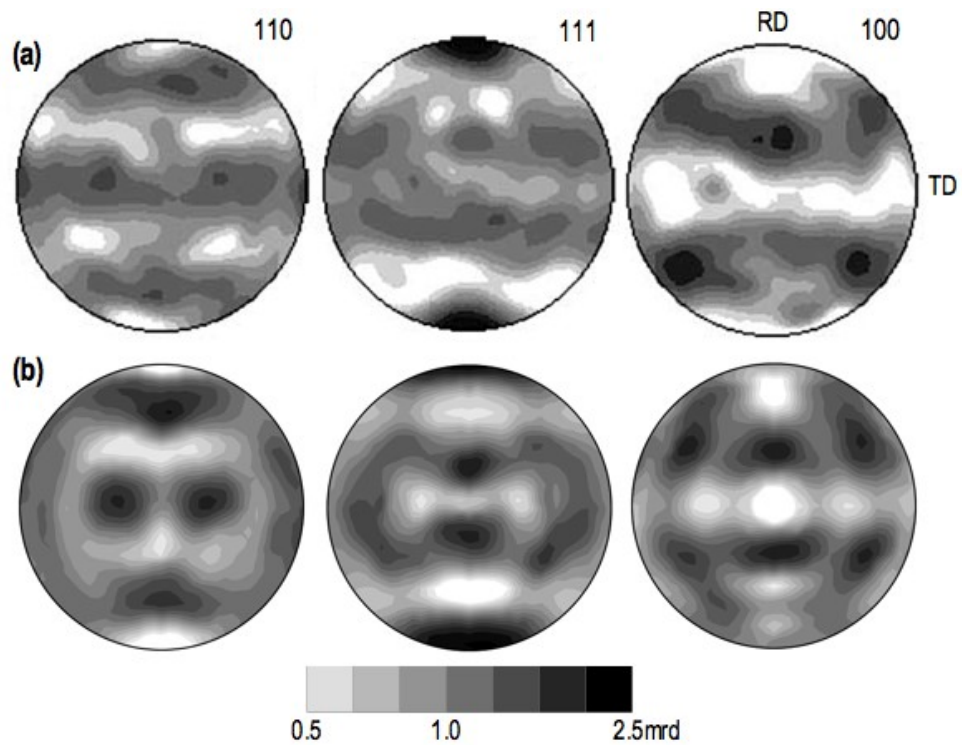
Figure 4.18 Comparison between β pole figures: (a) Zircaloy-4 at 950°C obtained using neutron diffraction (Wenk *et al.* 2004), (b) Zircaloy-2 at 950°C obtained using SXRD in this work. Note the logarithmic scale used.

4.2.4   β→α PHASE TRANSFORMATION

In most of the tests carried out during the synchrotron experiment, the transformation upon cooling occurred very quickly. However, it is clear that even the initial fractions of

α-phase produce pole figures with all the features of the final texture. The succession of α pole figures in Figure 4.16(f-h) does not show significant changes from the initial α volume fraction (~15%), to the final texture at room temperature when the β→α transformation is complete. The initial rolling texture is significantly weakened by the complete β heat treatment. The starting texture index is 4.09. It drops to 2.89 after annealing and to 1.65 once the material has cooled down from above the β-transus.

The main features seen in the pole figures after β-quenching are still the $(11\bar{2}0)$ maxima parallel to RD and the (0002) maxima at 30° from ND towards TD, but with significantly decreased intensities. New pole intensities are observed, that were not present before the transformation. These new texture components and the presence of variant selection will be discussed in detail in Chapter 7. The pole figures in the transformed condition are very similar to those found by Gey et al. from cold-rolled and fully recrystallized CP titanium sheets after a complete α→β→α phase transformation (Gey and Humbert 2002).

4.3   THE EFFECT OF THE PEAK TEMPERATURE ON THE TEXTURE EVOLUTION

In the experimental setup used for the synchrotron experiment, the samples were heat treated by electrical resistance and held by water-cooled grips. As a result, the maximum temperature reached by the material during the thermal cycle varies with position. This makes it possible to correlate the inherited texture with the maximum

temperature reached by using the diffraction images acquired at different positions along the sample at the end of each thermomechanical cycle. Although the temperature in the samples was measured only at one point with a thermocouple, the temperature distribution along each sample can be estimated with some confidence. From the results of the in-situ tests, it is known that recrystallization starts at approximately 620°C. Recrystallization produces a very characteristic texture, which can be used to determine the positions that reached the recrystallization temperature. A parabolic temperature distribution can then be fitted to two points: (1) the position of the thermocouple, and (2) the first position at which the recrystallization texture is observed, from the grip towards the middle of the sample.

Typical results of the post-treatment scans (e.g. sample T3) are summarised in Figure 4.19 and Figure 4.20. Figure 4.20 presents results of calculations of Kearns factor and texture index for different positions along the sample, while Figure 4.19 shows pole figures and SEM micrographs representing some of these positions, indicated with letters (a-e). Two significant changes are observed, at ~620°C and ~940°C. According to the in-situ tests, these two temperatures correspond to the start of recrystallization and the β-transus respectively.
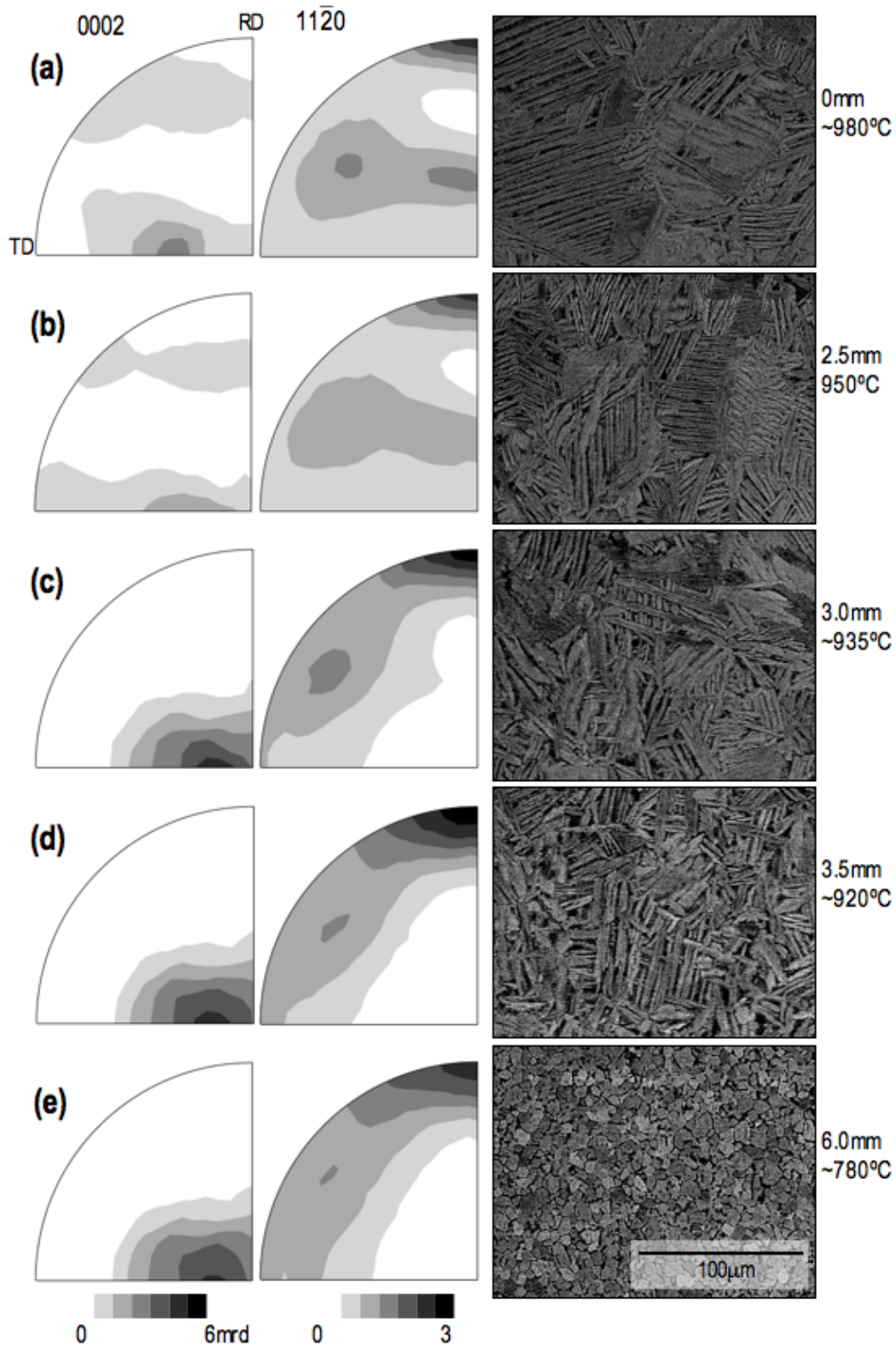
Figure 4.19 Pole figures and backscatter electrons micrographs from different positions along a sample β-quenched in an ETMT (sample T3). Positions (a-e) are indicated in Figure 4.20. (a) corresponds to the centre of the sample.
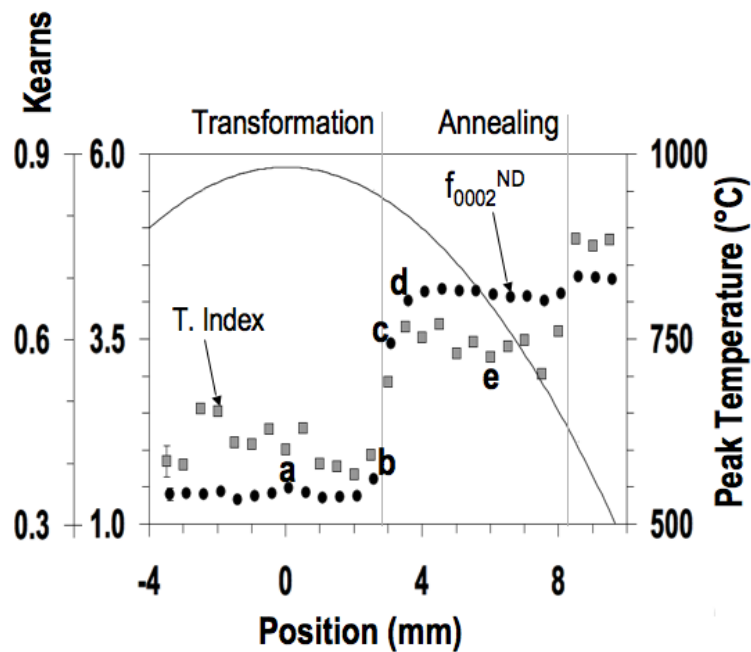
Figure 4.20 α phase texture index and basal Kearns factor along a sample β-quenched in an ETMT (sample T3). Pole figures and micrographs corresponding to positions (a-e) are shown in Figure 4.19.

The peak temperature of 950°C at position (b) was measured directly using the thermocouple, while the peak temperatures at positions (c) and (d) were estimated in 935°C and 920°C respectively. There is a sudden change of texture between these three positions. Interestingly, although position (c) and (d) exhibit a typical recrystallization texture, the microstructure is dramatically different to that where no transformation took place, e.g. position (e). The in-situ tests indicate that between 920°C and 935°C the volume fraction of untransformed α is below 5%. This post-treatment texture distribution along the samples shows that the inherited texture is very sensitive to the maximum temperature when it is near the β-transus. Sections of the sample reaching temperatures below 940°C exhibit exactly the same texture as before the transformation, i.e. the recrystallization texture, even though the microstructure undergoes a significant change. This certainly exemplifies texture memory, i.e. even though most of the

α-phase was transformed to β, after the reverse β→α transformation the texture is practically the same.

4.4 THE EFFECT OF STRESS AND PLASTIC DEFORMATION ON THE TEXTURE EVOLUTION

With the aim of studying the effect of stress on the texture evolution during a complete α→β→α phase transformation, some of the samples in the SXRD experiment were subjected to mechanical loading, applied in different ways:

1. Sample S1 was tested under displacement constraint during the thermal cycle. The thermal cycle was carried out under displacement control in the ETMT, maintaining the grips static. This means that there was a build up of stress in the sample, caused by both thermal expansion/contraction and by the phase transformation.

2. Sample S2 was tested under moderate tensile load. The load applied was the maximum possible without causing excessive plastic deformation and failure. This load was 7N for a sample with an initial cross section of $1.54 \times 0.90 \text{ mm}^2$, i.e. an approximate engineering stress of ~5 MPa.

3. Sample S3 was tested under higher tensile load, 20N for an initial cross section of 2.35×0.90 mm, resulting in an approximate engineering stress of ~9.5MPa and a significant amount of plastic strain (estimated ~20-30% where the sample was being irradiated). Although the sample failed during the thermal cycle, interesting information could be obtained from the diffraction images before the failure. Figure 4.21 shows a picture of sample S3 after the test.
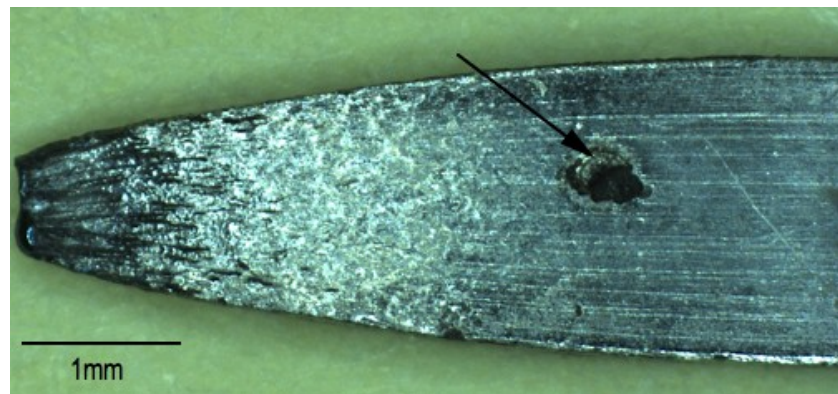
Figure 4.21 Sample S3, the position where the thermocouple was attached (i.e. the approximate position of irradiation) is indicated.

The temperature and load curves for sample S1 and S2 are shown in Figure 4.22. In sample S1 there is an initial compressive load, created when the grips were tightened and that was not removed before the test. The compressive load increases as the sample undergoes thermal expansion from room temperature to approximately 300°C, where it starts to be relieved probably due to softening of the material. Since the β phase is much softer than the α phase, there is no load when the phase transformation occurs. During cooling, a significant tensile load is built up, caused mainly by thermal contraction. The tensile load present during the phase transformation on cooling, i.e. from 950°C to 780°C, is very small compared to the maximum tensile load accumulated, but is in the same order of magnitude as the tensile load that could be applied in sample S2.

The temperature and load curves for sample S3 are shown in Figure 4.23(a). They are accompanied by current and grip position curves of the same sample in Figure 4.23(b). From these graphs, it can be seen that the failure of this sample occurred during cooling, at approximately 882°C, probably due to extra tensile stress caused by rapid thermal

contraction during cooling (the sample started yielding well before that point). There was a significant elongation of the sample before failure, ~4mm according to the change in grip position. The precise moment of failure is determined by the sudden drop in current at ~19sec. The thermocouple did not detach from the sample, thus it was possible to see the cooling profile undergone by the specimen, obtaining a very high cooling rate of ~100Cs^{-1}.
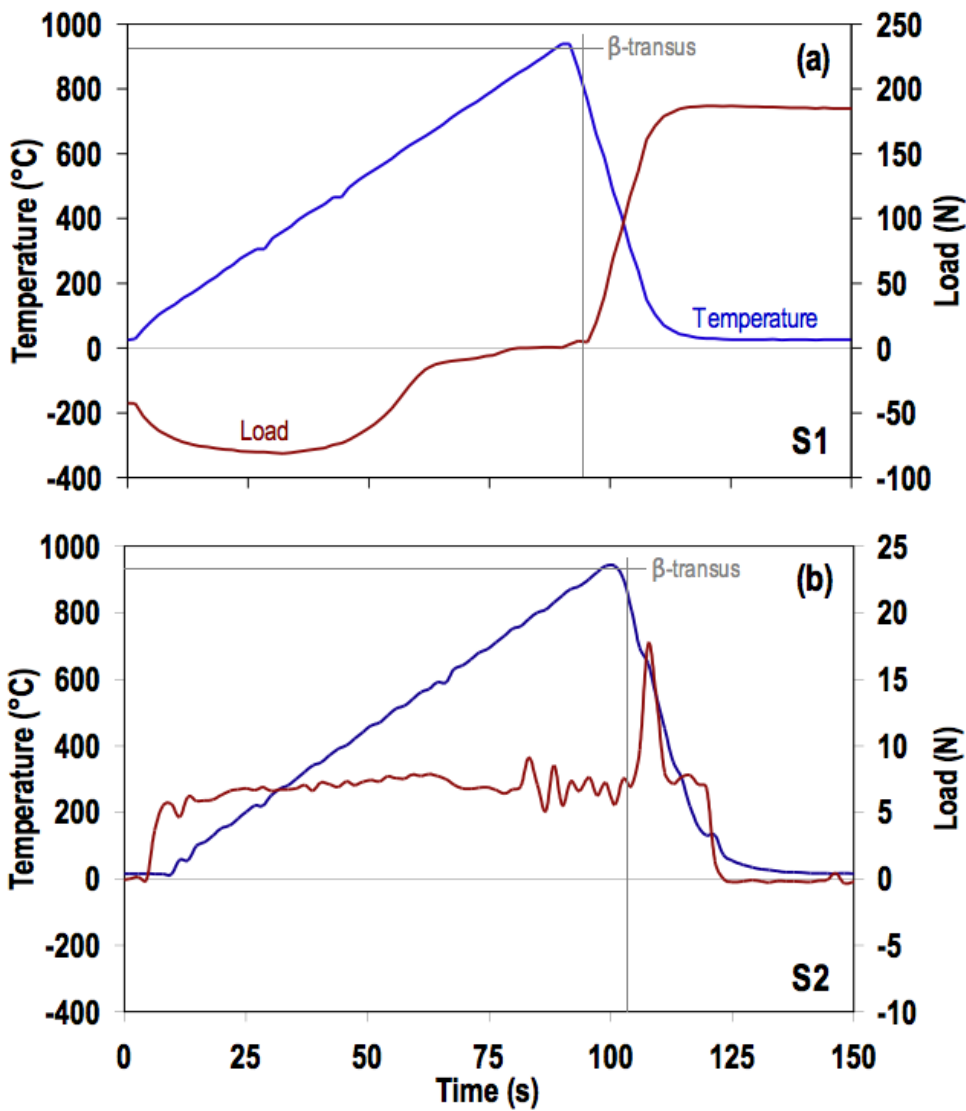
Figure 4.22 Temperature and load: (a) constrained, sample S1, (b) 7N tensile load, sample S2.
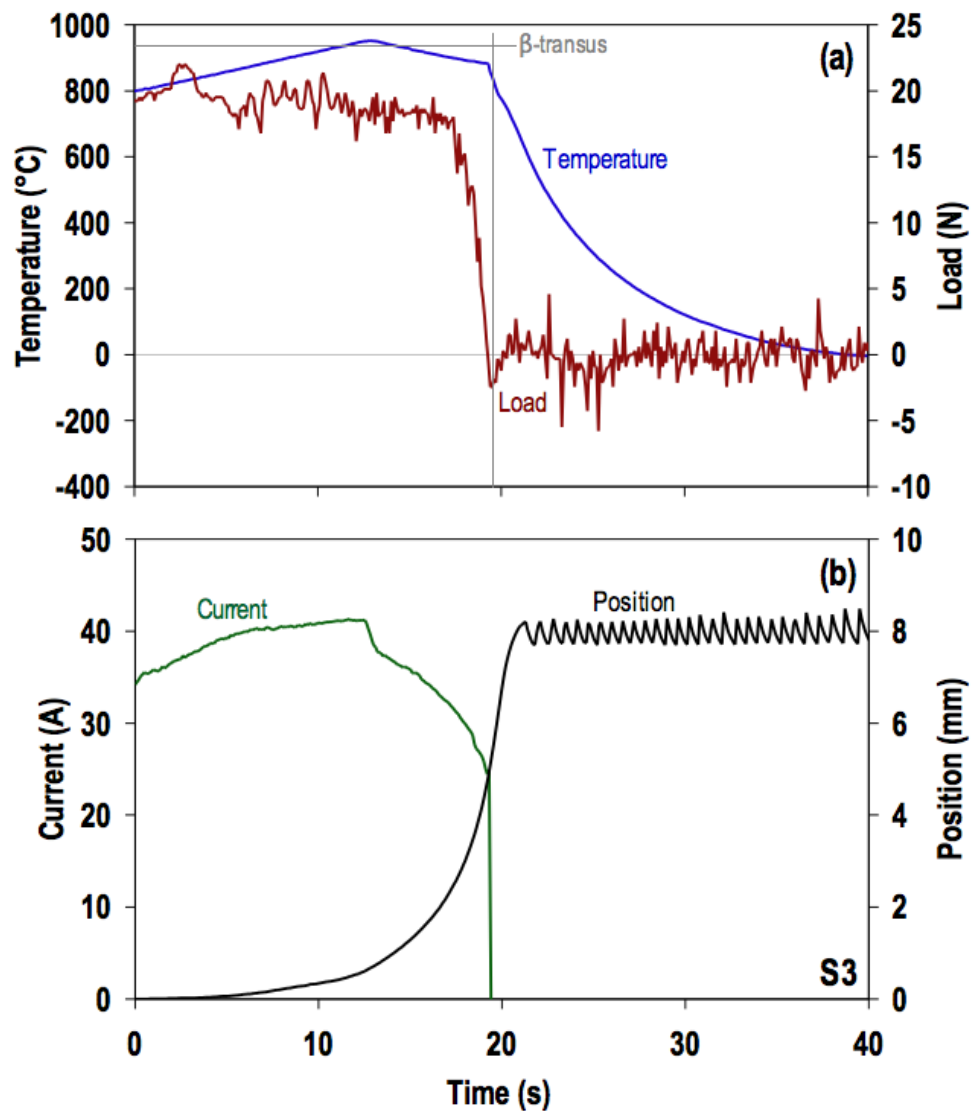
Figure 4.23 Temperature, load, current and grip position for sample S3.

4.4.1 EFFECT OF DISPLACEMENT CONSTRAINT AND MODERATE TENSILE STRESS

Figure 4.24(a-c) compares the pole figures of the inherited α phase of one of the samples β-quenched without applied load (T3), with those of the samples tested under constraint (S1) and moderate tensile stress (S2).
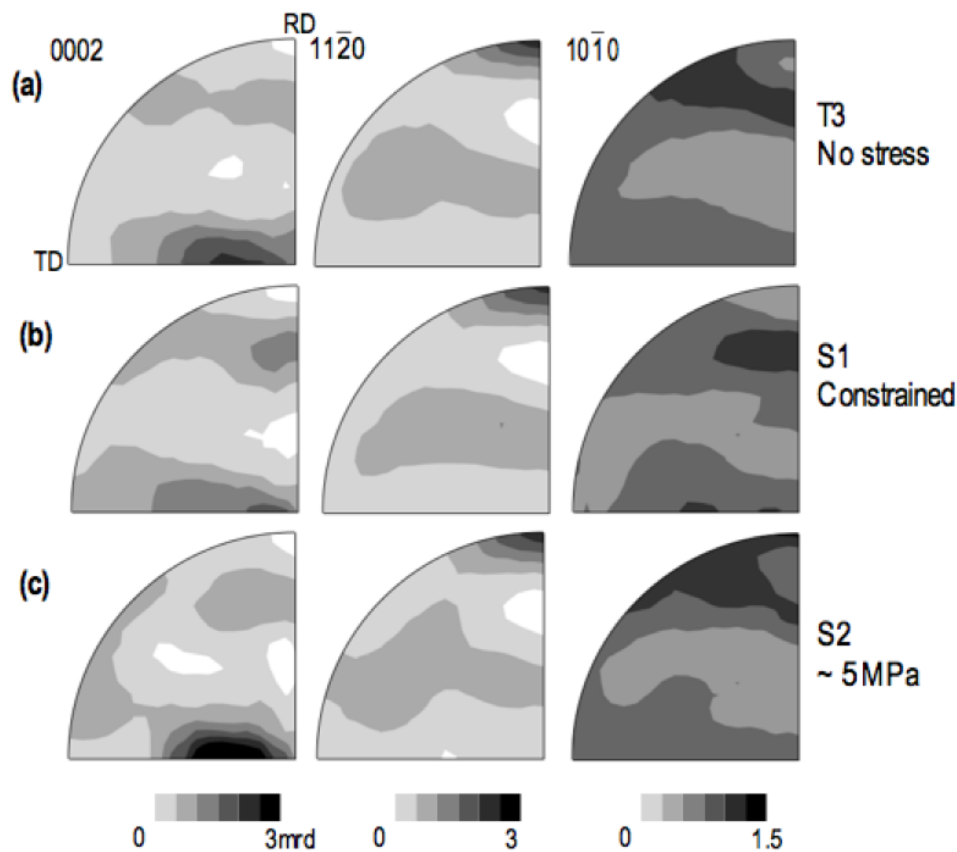
Figure 4.24 Inherited α pole figures of samples β-quenched under different mechanical conditions.

The pole figures are in general terms very similar, exhibiting only subtle differences in morphology and intensity. The sample heat treated under permanent stress exhibits slightly increased intensity of the split (0002) maxima at 30° from ND, whereas in the sample tested under constraint these maxima are slightly weaker. Other small differences are observed in the $(10\bar{1}0)$ pole figures. The stress-free sample exhibits maxima surrounding RD, whereas the sample treated under permanent stress has some intensity at RD. These differences are not conclusive, and are within the estimated error for texture measurements using SXRD. Figure 4.25 compares pole figures of the high-temperature β-phase at the end of the α→β phase transformation for these three

samples. The β pole figures are practically identical. This evidence indicates that the stresses undergone by these samples during the phase transformation on heating is not strong enough to modify either the development of the β texture or the inherited α texture.
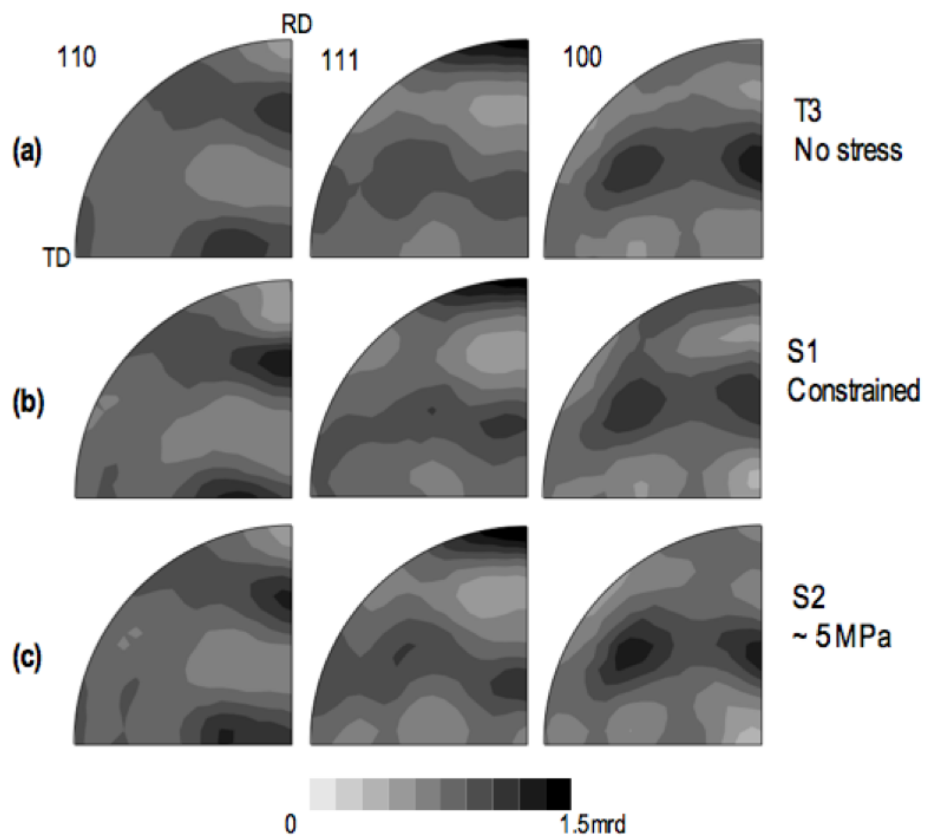
Figure 4.25 High-temperature β pole figures of samples β-quenched under different mechanical conditions, at the end of the α→β phase transformation (935-940°C).

4.4.2   EFFECT OF PLASTIC DEFORMATION

During heating, up to the end of the α→β phase transformation, sample S3 exhibited a similar behaviour to samples T3, S1 and S2. The β texture is not particularly strong and very similar to that observed in the other samples. The β pole figures of this sample at

~935°C during heating are shown in Figure 4.26(a). Although there is a hint of a previously unseen (100) pole maximum parallel to RD and other different maxima, the dominant features are very similar to those found in the samples β-quenched under other stress conditions. The corresponding diffraction image is displayed in Figure 4.27(a).

Once the α→β transformation was complete, an extreme plastic deformation led to failure, as observed above in Figure 4.21 and Figure 4.23. Sample S3 underwent moderated grain growth, as indicated by the scattered intensities in Figure 4.27(b), but the crystal defects created during plastic deformation contributed to produce a diffraction image with smooth rings, shown in Figure 4.27(c), being reliable enough to observe the texture just before failure, which is illustrated by the pole figures in Figure 4.26(b).

The β pole figures obtained before the failure are completely different to those seen in the other samples: instead of the (111) pole maximum that dominates other results, there is a strong (110) maximum parallel to the loading direction (RD). These pole figures display an almost perfect fibre texture, typical of bcc materials after uniaxial tension (Rollett and Wright 1998). As mentioned in section 2.1.6, the β phase is extremely soft and ductile, which combined with the high tensile load applied to the specimen results in a significant amount of plastic strain (~0.25 at the measurement point), causing the development of this typical fibre texture.
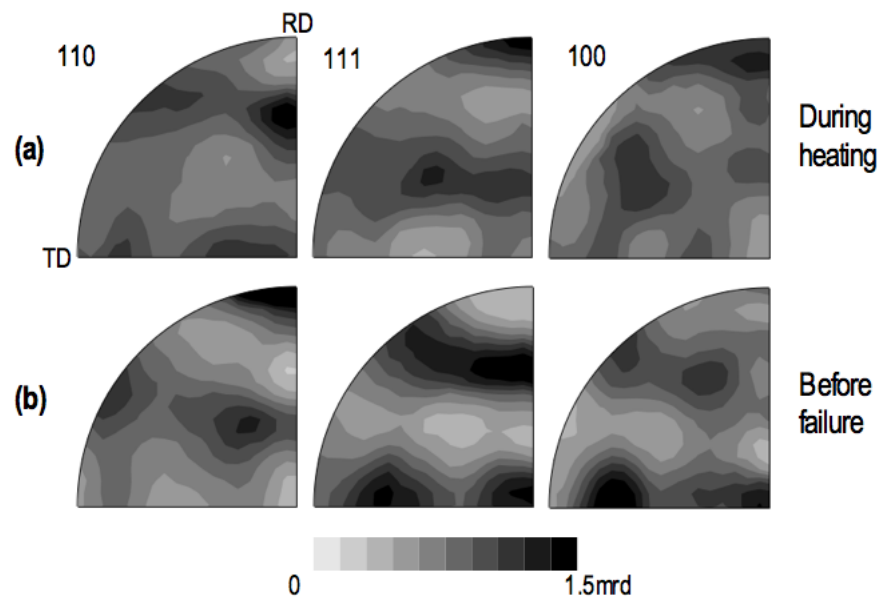
Figure 4.26 High-temperature β pole figures of sample S3: (a) at ~935°C during heating, (b) at ~882°C during cooling just before failure.
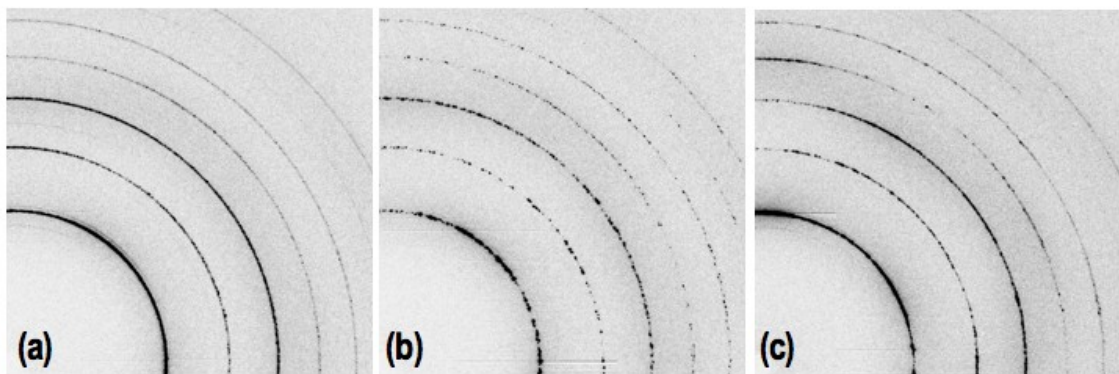
Figure 4.27 Diffraction images of sample S3: (a) at ~935°C during heating, (b) at ~950°C, (c) at ~882°C during cooling just before failure.

4.5 SUMMARY

The development and evolution of texture in cold-rolled Zircaloy-2 during a $\alpha \rightarrow \beta \rightarrow \alpha$ phase transformation has been characterised in-situ and at non-ambient conditions by means of a SXRD experiment. The experimental setup allowed the measurement of texture during fast microstructural changes, at high temperature and with the presence of both phases. Furthermore, the spatial resolution achievable using synchrotron diffraction allowed the correlation between the inherited texture and the maximum temperature reached, both below and above the β-transus. The experimental details and limitations of this technique have been discussed, e.g. an uncertainty in temperature measurements between 5 and 10°C.

The most noticeable finding is that by β-quenching the cold-rolling texture is weakened, producing new texture components. However, this only occurs if the transformation is complete and the β-transus is well exceeded. A range of heating experiments were undertaken, and whenever the material exceeded the β-transus and the transformation was complete, the results demonstrate texture weakening. Neither texture memory, where the texture before the phase transformation is replicated, nor texture strengthening was observed. The α transformation textures observed are weaker but not as random as expected from the orientation relationship, which suggests that some variant selection occurs during the process. Variant selection will be discussed in detail in Chapter 7.

The degree of texture memory during a α→β→α transformation is strongly influenced by the peak temperature. Transformations where the β-transus was not completely exceeded exhibit perfect texture memory. This could be caused by a combination of mechanisms leading to variant selection.

The effect of stress and plastic deformation was also studied, demonstrating that plastic deformation and/or grain growth in the β-phase lead to changes in the β texture and modify the inherited α texture. According to the SXRD results, the texture evolution is not sensitive to levels of stress that do not cause plastic deformation in the β-phase.

4.5.1   SUMMARY OF THE TEXTURE COMPONENTS OBSERVED

In order to gain a better understanding of the results of the SXRD experiment, and establish a basis for analysis of results in the following chapters, the experimental textures observed can be decomposed into texture components. The main texture components for α-phase and β-phase are listed in Table 4.6 and illustrated in the schematic $(0002)_\alpha$ and $(110)_\beta$ pole figures and ODF sections in Figure 4.28.

The experimental results presented have shown that the texture before the α→β→α phase transformation, i.e. the recrystallization texture, is dominated by component g_1^α (~80%). After the phase transformation, the main new texture component developed is g_2^α, accompanied by some additional minor components (g_3^α and g_4^α). The high temperature β texture is relatively simpler, resulting from the combination of g_A^β (~65%) and g_A^β (~35%).

Table 4.6 Main texture components observed during β-quenching of cold-rolled Zircaloy-2

	Euler Angles (°)		
Component	α	β	γ
g_1^α	90	30	30
g_2^α	90	90	30
g_3^α	0	60	0
g_4^α	30	70	20
g_A^β	0	35	135
g_B^β	0	0	0

Figure 4.28 Main texture components observed during β-quenching of cold-rolled Zircaloy-2: (a) α-phase and (b) β-phase.

CHAPTER 5
MICROTEXTURE CHARACTERISATION

The results obtained in the SXRD experiment, discussed in Chapter 4, showed the changes in texture occurring during the α→β→α phase transformation in a macrotexture context. In order to investigate the local mechanisms that generated the global textures observed, some of the samples tested in-situ were subsequently studied using electron backscatter diffraction (EBSD). This analysis aimed to correlate the results acquired in-situ to measurements of local orientation/reorientation, as well as relate the microtexture to the microstructure.

5.1   CHARACTERISING MICROTEXTURE USING EBSD

Different FEGSEMs were employed to collect the results presented in this chapter: a Zeiss SUPRA 40, a CamScan 2040S, a Philips Sirion and a Philips XL30. All of them were equipped with HKL EBSD acquisition systems. The Channel 5 software suite (HKL Technology 2006) was used to post-process and analyse the data.

Selected samples were prepared as described in section 3.5. The typical EBSD

acquisition parameters are listed Table 2.1. With this sample preparation and acquisition

parameters the indexing rate obtained was in most cases above 80%, with some specific

maps with indexing between 70% and 80%. The acquisition rate achieved ranged

between 0.1 and 0.5 seconds per measuring point. Unless stated otherwise, all the maps

were acquired using a relatively small step size, between 0.5 and 2μm, enough to be

able to identify the α variants (colonies) in the microstructure. In some cases, the step

size was small enough to see individual α lamellas in band contrast maps.

Table 5.1 Typical EBSD acquisition parameters

Voltage	20kV
Spot size	6
Working distance	12-25 mm
Magnification	100-300x
Gain	High (10-15)
Pixel binning	4x4
Time per frame	10-50 ms
Frame averaging	3 frames
Band centres or edges	Edges
Min/max number of bands	4/8
Hough resolution	60

All the maps were subjected to a systematic post-processing procedure, aimed to reduce

the noise and eliminate effects such as pseudosymmetry (described in section 1.2.4).

The post-processing procedure is outlined below, and illustrated in Figure 5.1(a-c). In

Figure 5.1(a-c), the non-indexed points are white, and the misorientations corresponding

to systematic misindexing of hexagonal phases, i.e. 30° rotations about the $\vec{c}$ axis, are

delineated in black.
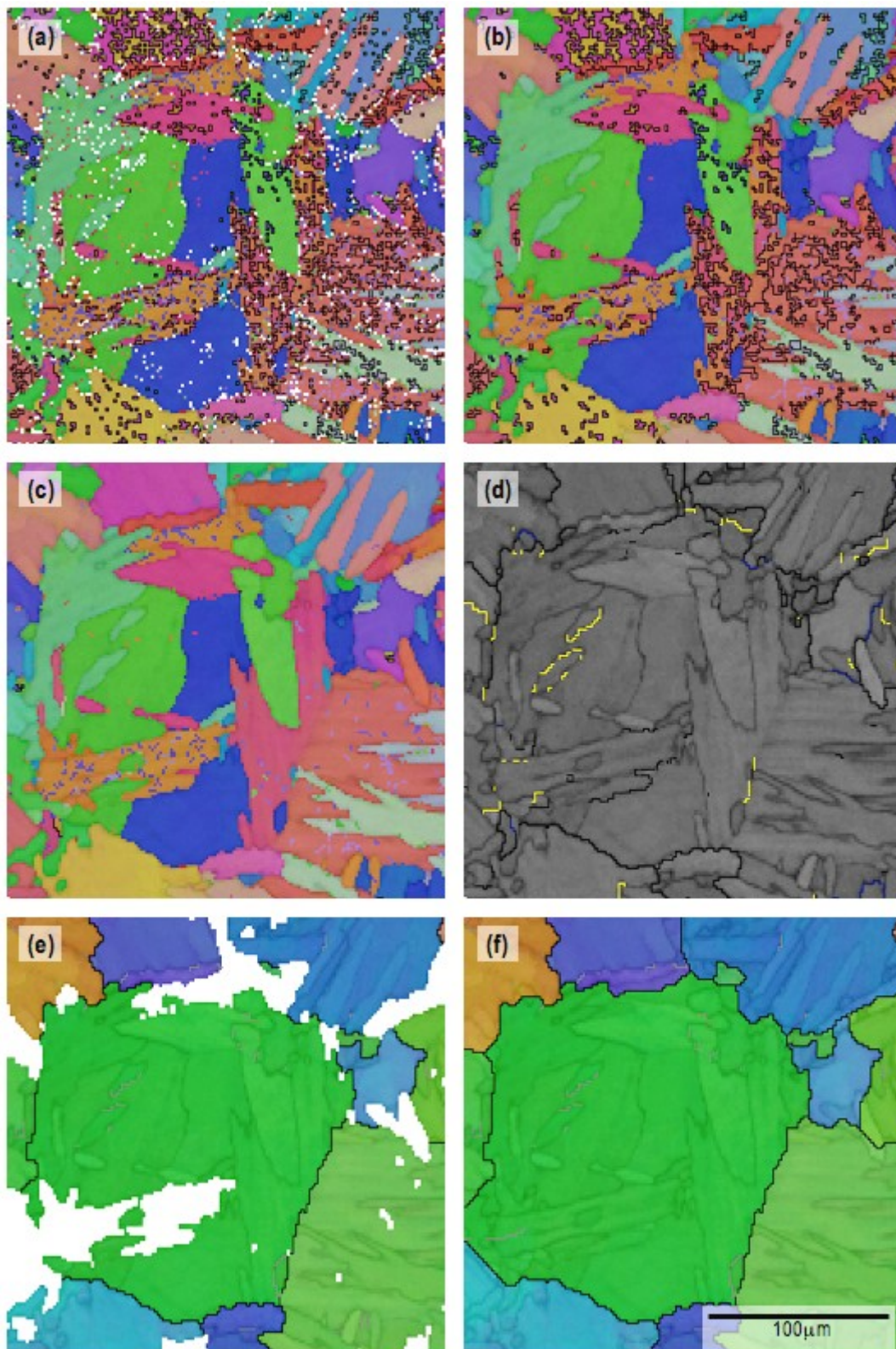
Figure 5.1 EBSD data post-processing: (a) raw data (IPF colouring), (b) after wild spikes correction and extrapolation, (c) after systematic misindexing correction, (d) band contrast map after α data correction showing probable prior β grain boundaries, (e) result of β reconstruction algorithm (IPF colouring), (f) extrapolation of β reconstruction

1. Correction of wild spikes: isolated points are removed.

2. Extrapolation: non-indexed points are assigned a value of orientation, extrapolated from the values of adjacent points. The extrapolation is carried out in steps, using data from 8, 7, 6 and 5 adjacent points successively. After this step for most of the maps, the percentage of non-indexed points was below 2%. A final extrapolation using 4 neighbours was applied if necessary. Extrapolation was used with caution, since large portions of non-indexed points can indicate the presence of unknown phases or contamination on the surface.

3. Remove systematic misindexing: misindexed points caused by pseudosymmetry are corrected, i.e. rotated 30° around the $\vec{c}$ axis.

4. Remove extremely small clusters: clusters of points with areas equal or smaller than four pixels and that are detected as grains, i.e. having a misorientation above 3°, are removed and then assigned a value of orientation by extrapolation.

After reducing the noise, it is possible to have an idea of the prior β grain size and shape by displaying certain misorientations in the α orientation maps. As mentioned in section 2.2.4, α variants belonging to the same parent β grain have characteristic misorientations. Any other misorientation between identified α variants would constitute a prior β grain boundary. In Figure 5.1(d), the misorientations between α colonies that probably constitute prior β grain boundaries are delineated in black, while boundaries between α variants having a misorientation below 3° are delineated in yellow.

In order to know the actual orientation of the prior β grains, the β reconstruction algorithm developed by Davies et al. (Davies *et al.* 2007) (described in detail in section 2.2.4) was used in some α maps. The resultant β orientation maps were corrected

following the steps 1 and 2 of the procedure above. This is exemplified in Figure 5.1(e-f). It is important to notice that the amount of unsolved points in the raw β reconstructed maps sometimes reached 40%, thus in some cases even after extrapolation there were still areas without precise β orientation information.

The results of EBSD mapping and β reconstruction on selected samples will be presented in the following sections. The presentation of the results will consist of several orientation maps and pole figures, described as follows:

1. Inverse pole figure (IPF) map. In this map, the colouring corresponds to the orientation of each measurement point in an inverse pole figure of a selected sample direction. The sample directions selected are shown in the legend of each map.

2. Band-contrast map including probable prior β grain boundaries and misindexing boundaries. In this map, the greyscale represents the quality of the electron backscatter pattern (EBSP) for each point. The lighter the shade of grey, the higher the band contrast and hence the EBSP quality. Band contrast maps reveal microstructural features such as grain boundaries and surface imperfections. The prior β grain boundaries (delineated in black) correspond to boundaries between α variants whose misorientation are above 3°, and are not within 2.5° of the characteristic misorientation of variants belonging to the same parent β grain. Boundaries between α variants with misorientation between 3° and 8 °, are delineated in bright blue. Probable misindexing boundaries are delineated in dark blue.

3. β reconstruction map using IPF colouring and including β grain boundaries. This map is the result of applying the β reconstruction algorithm. The colouring corresponds to an inverse pole figure for a cubic crystal in the selected sample direction. High-angle (black) and low-angle (grey) grain boundaries are included, with limit values of 10° and 1° respectively.

4. Pole figures obtained from the α and β orientation maps. All the EBSD pole figures presented in this chapter correspond to recalculated pole figures, from ODFs calculated using the harmonic method as implemented in TEXTAN III (Bate 1990). Orthotropic sample symmetry was applied. The β pole figures are those obtained directly from reconstructed data, before applying any extrapolation.

For comparison purposes all the EBSD pole figures obtained from the samples studied in this chapter are compiled in Figure 5.2 (α) and Figure 5.3 (β). These figures will be discussed later.

5.2 LOAD-FREE TRANSFORMATIONS. THE EFFECT OF THE PEAK TEMPERATURE ON THE MICROTEXTURE

The first scenario studied during the in-situ experiment was β-quenching without applied stress. Figure 5.4 shows results of EBSD mapping in sample T1, β-quenched at 1000°C during 10 seconds. This map was taken at the location of the thermocouple, which is, approximately, where the synchrotron X-ray beam irradiated the sample during the in-situ experiment. It is important to notice the directions chosen for each IPF map. In Figure 5.4(a), the colouring of the α-phase corresponds to an inverse pole figure of ND, which is aimed to illustrate the deviation of the inherited texture with respect to the initial strong rolling texture. In a map of this type, the initial rolling texture is dominated by red colour since the basal planes are very close to ND. In the map in Figure 5.4(a), the distribution of the colouring does not show any particular trend, indicating that the rolling texture has been weakened.
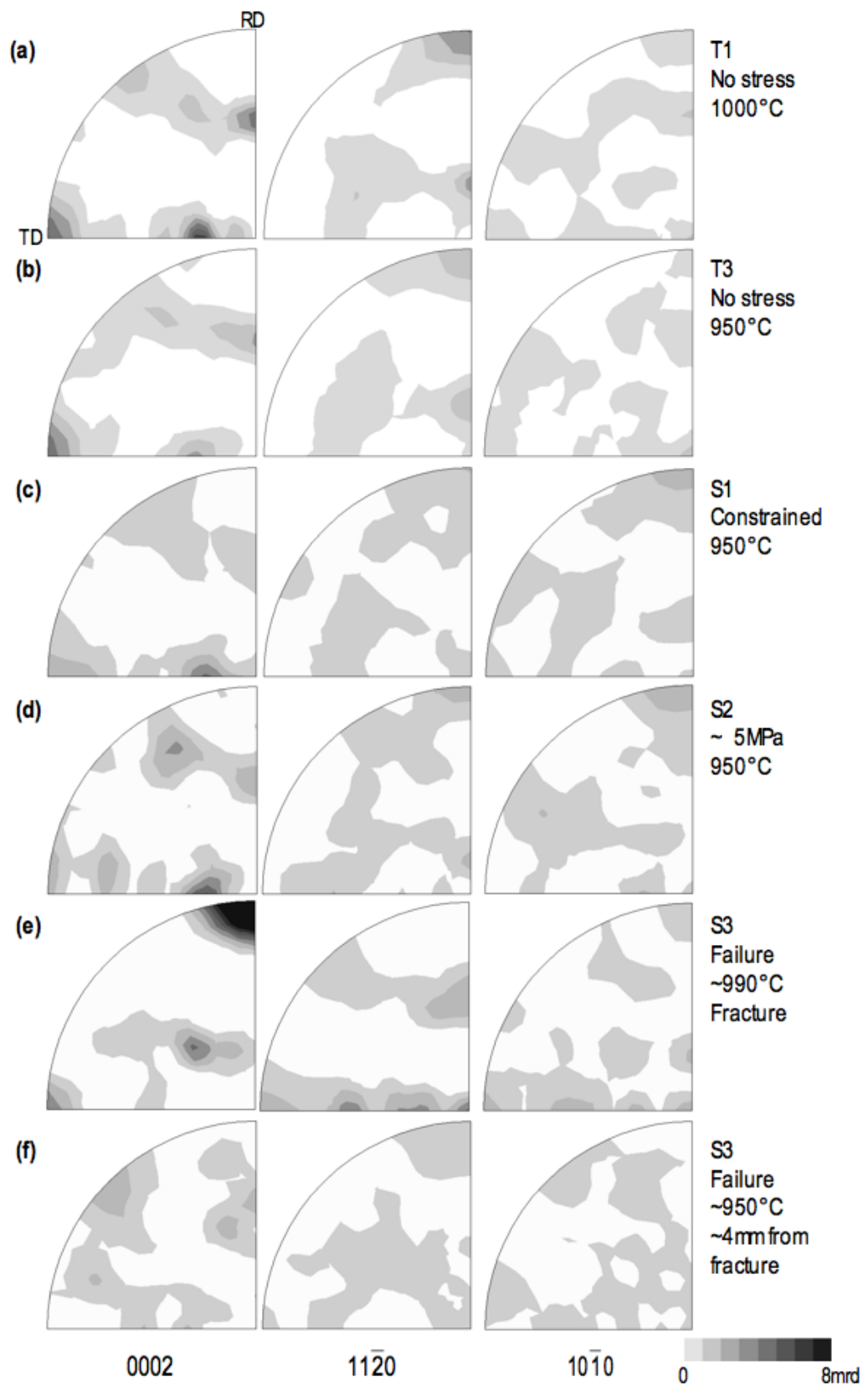
Figure 5.2 Pole figures corresponding to α EBSD maps of samples β-quenched in the SXRD experiment: (a) T1, (b) T3, (c) S1, (d) S2, (e) S3 at the fracture tip and (f) S3 ~4mm away from the fracture
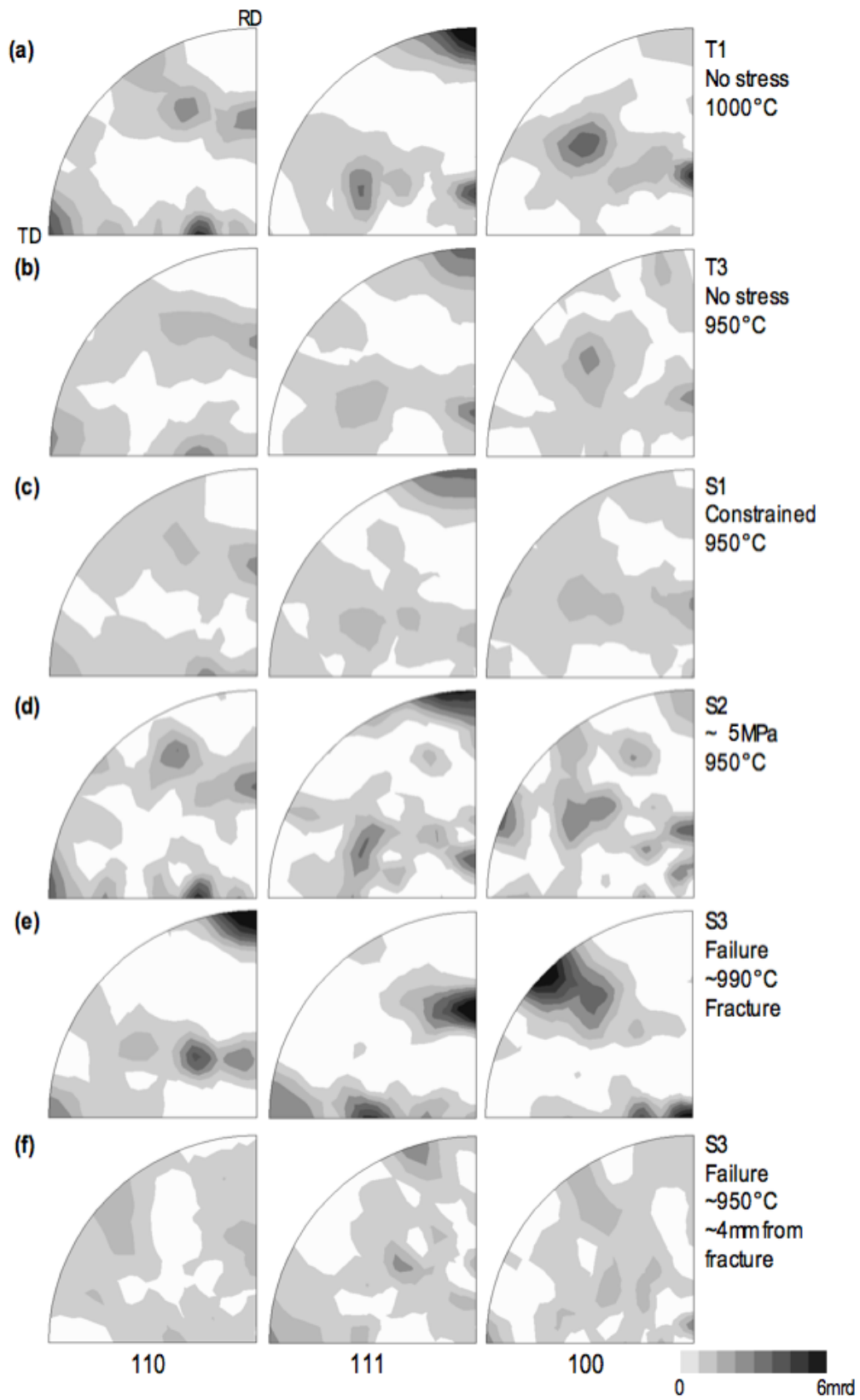
Figure 5.3 Pole figures corresponding to β reconstruction maps calculated from α EBSD data of samples β-quenched in the SXRD experiment: (a) T1, (b) T3, (c) S1, (d) S2, (e) S3 at the fracture tip and (f) S3 ~4mm away from the fracture

Despite the fact that the global texture has been weakened by β-quenching, in the EBSD maps there is evidence of variant selection and local texture memory. The regions encircled in white in Figure 5.4 show prior β/β grain boundaries that produced α variants with low misorientation between them ($<8°$), and with crystallographic orientations very close to that before β-quenching, i.e. with their (0002) poles near ND. The β grains corresponding to these boundaries share a common (110) pole, and the α variants produced have their (0002) pole parallel to that common (110) pole. This mechanism of variant selection has been observed previously (Stanford and Bate 2004, Bhattacharyya et al. 2007), and will be discussed in detail in Chapter 7.

The special β/β grain boundaries are related not only to the local replication of texture components present before β-quenching, but also to the local strengthening of others, as illustrated by the yellow circle towards the left hand side in the maps in Figure 5.4. In this particular example a new texture component (close to g_α^3), dominates the region. This evidence indicates that mechanisms of local variant selection at special β/β grain boundaries could, at least partially, explain the appearance and strength of the new texture components observed in the β-quenched condition.

The IPF colouring of the β-phase map in Figure 5.4(c) corresponds to RD, aiming to illustrate the strong alignment of the (111) poles parallel to RD by a predominant blue colour. RD is used as the reference direction for all of the β-phase EBSD maps presented in this chapter. The β reconstruction algorithm worked relatively well,

achieving just below 70% of area reconstructed. In order to produce the map shown in Figure 5.4(c) the missing areas could be extrapolated easily.

The band contrast map and the β reconstruction map of sample T1, shown in Figure 5.4(b-c), show a prior β grain size of ~150-160 μm, and in the area scanned there were approximately 140 β grains. According to the literature (Bozzolo *et al.* 2007) this would be enough to determine the features of the β texture with some uncertainty in the densities of the orientation distribution.

The results of EBSD mapping in sample T3, heat treated at 950°C for 3 seconds, are shown in Figure 5.5. The inherited α texture in this sample is weaker than that found in sample T1, evidenced by lower pole intensities in Figure 5.2(b) than in Figure 5.2(a). Due to the resolution of the maps, evidence of local variant selection at special β/β grain boundaries cannot be pointed as clearly as in sample T1.

In the maps obtained from sample T3 shown in Figure 5.5(b-c), the prior β grain size observed was approximately ~70-80 μm, and the β-reconstruction map does not appear as dominated by the blue colour as that from sample T1. All this evidence suggests that the limited β-grain growth in sample T3 is related to a weaker β-texture, confirmed by comparing the β pole figures in Figure 5.3(a) and Figure 5.3 (b), which in turn is related to a weaker inherited α texture. The differences in texture with respect to sample T1 lie in the intensity of the two pole maxima corresponding to texture components g_α^1 and g_α^2.

Figure 5.4 EBSD maps from sample T1: (a) IPF map of α-phase (ND), (b) band contrast map showing probable prior β grain boundaries, (c) IPF map of β-phase reconstruction (RD).

Figure 5.5 EBSD maps from sample T3: (a) IPF map of α-phase (ND), (b) band contrast map showing probable prior β grain boundaries, (c) IPF map of β-phase reconstruction (RD)

5.2.1   RECONSTRUCTED BETA TEXTURE IN LOAD-FREE SAMPLES

One of the limitations of texture measurement using SXRD was that, due to accelerated β grain growth after the α→β phase transformation is complete, it was not possible to follow the evolution of the β texture beyond this point, i.e. during β grain growth. In order to investigate the evolution of the β-phase texture once the α→β phase transformation is complete, the β texture just before the start of the β→α phase transformation was reconstructed using the variant-based β reconstruction technique (Davies *et al.* 2007) as explained in section 2.2.4, and compared to the texture obtained at the end of the α→β phase transformation.

Figure 5.6 shows three different sets of pole figures illustrating the evolution of the β texture in sample T1. Figure 5.6(a-b) were obtained in-situ using SXRD at the end of the α→β phase transformation, while Figure 5.6(c) was obtained reconstructing the β texture from the map shown in Figure 5.4. All the features are similar, but the intensities are significantly higher in the pole figures from reconstructed EBSD data. If one assumes that these changes in intensity are not caused by poor grain statistics, then this result suggests that the texture of the β phase changes after the α→β transformation is complete. This is probably due to some kind of preferential growth that strengthens the main β texture components.
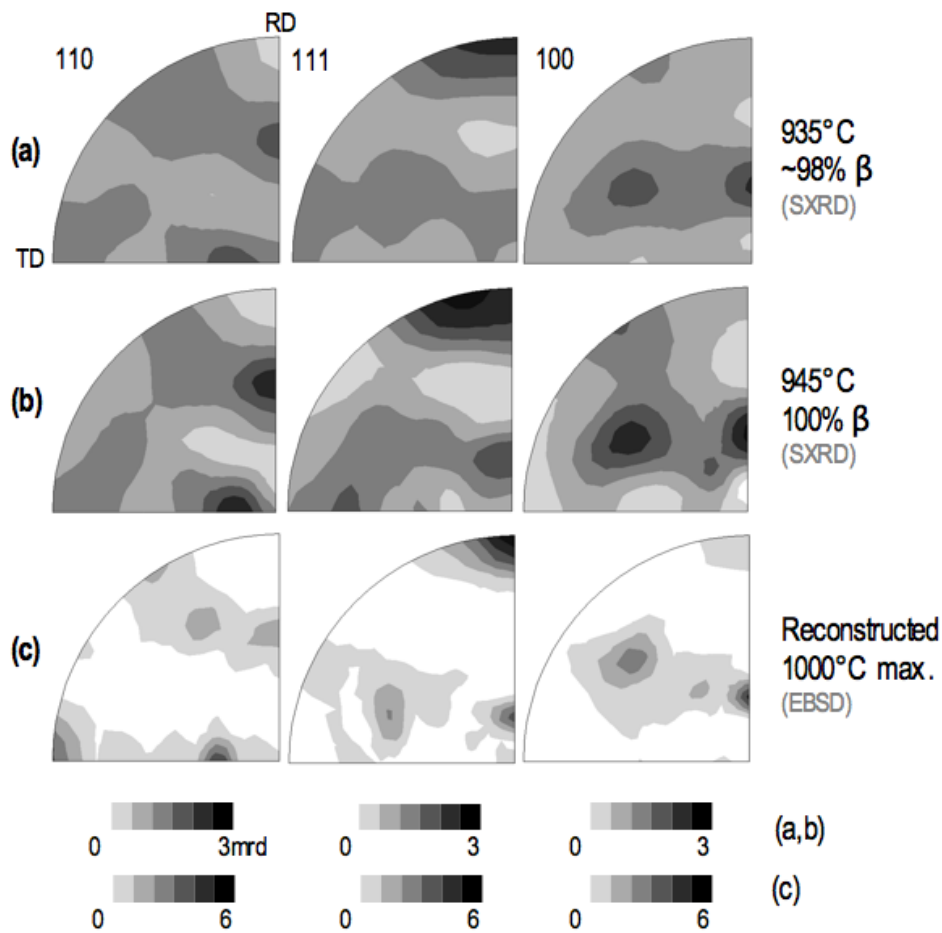
Figure 5.6 Comparison between β pole figures obtained using reconstructed EBSD maps and SXRD

5.3 THE EFFECT OF STRESS/DEFORMATION ON THE MICROTEXTURE

The second scenario studied during the in-situ experiment was β-quenching of samples with applied stress in three different schemes: under displacement constraint (sample S1), under moderate tensile stress (sample S2) and with large plastic deformation (sample S3). The aim was to investigate the effect of stress and strain in the texture development. EBSD mapping was used to evaluate the inherited microtexture in these three samples.

5.3.1   EFFECT OF DISPLACEMENT CONSTRAINT AND MODERATE TENSILE STRESS

Effect of Displacement Constraint

EBSD maps obtained from sample S1, which was β-quenched at 950°C without dwell time and under displacement constraint, are shown in Figure 5.7. It is important to note that in this sample the EBSD maps were acquired on the ND-RD plane, as opposed to the maps from samples T1 and T3, which were acquired on the TD-RD plane.

In the IPF map of the α phase in Figure 5.7(a), there is an increased presence of red colour in the regions at the top and bottom left, which is associated to accumulation of (0002) poles close to ND. This suggests that the maximum temperature in these regions is very close to the β-transus; hence the texture was not weakened as effectively as in the rest of the map. Sharp changes in texture when the peak temperature is close to the β-transus were found in the SXRD experiment and will be discussed in section 5.4.

The band contrast map in Figure 5.7(b) indicates a β grain size of ~60-70μm. However, it is interesting that in this sample the β reconstruction algorithm was not effective. The reconstruction failed in approximately 50% of the map, which is illustrated in Figure 5.7(c). This is explained by the fact that during the β→α phase transformation on cooling, stress is built up in the sample by the phase transformation and by thermal contraction, as illustrated previously in the curves obtained in the ETMT (see Figure 4.22). The α phase nucleating during cooling undergoes deformation while it is growing, thus its crystallographic orientation moves away from the ideal Burgers

relationship with the parent β. The β reconstruction algorithm is based on the Burgers orientation relationship, and it will fail if the orientation relationship does not lie within a narrow range from the ideal. The α and β pole figures shown in Figure 5.2(c) and Figure 5.3(c) respectively are similar to those obtained in sample T3, both in morphology and intensity. However, there is some evidence of a slightly weaker inherited α texture.   The intensity of the $\alpha\left(11\bar{2}0\right)$ component parallel to RD is somewhat reduced, and there is a slight increase of the $\alpha\left(10\bar{1}0\right)$ pole intensity parallel to RD. The $\left(0002\right)$ pole maximum parallel to TD (corresponding to component g_α^2) is lower in sample S1 than in sample T3, suggesting that the stress would have an effect on this component. This observation was missed in the SXRD results, because this component is considerably underestimated (see section 4.1.6).

The texture component g_α^2 has its $\left(0002\right)$ aligned with TD, while due to the displacement constraint in the sample a tensile load was developed along RD. It is known that the strains associated with the β→α phase transformation are maximum (±10%) in two perpendicular directions in the basal plane (Holt and Aldridge 1985), which would explain why g_α^2 is affected by the presence of a relatively low tensile stress applied, while other texture components are not affected as much. All this evidence indicates that with the level of stress present in sample S1 the global texture evolution was not significantly affected, but the presence of stress may influence the development of one particular texture component (g_α^2).

Effect of Moderate Tensile Stress

Sample S2 was β-quenched at 940°C and under a permanent tensile load of 7N (~5MPa stress). The EBSD maps obtained from this sample are shown in Figure 5.8. From these maps it can be seen that the prior β grain size is ~70-80μm. Although this map covers a smaller region compared to other samples, it can be seen that this level of stress does not cause significant changes in the global inherited texture or microstructure. However, the pole figures in Figure 5.2(d) show a lower (0002) maximum parallel to TD when compared with a stress-free sample, probably due to the same reason as sample S1, i.e. the presence of a tensile stress in the direction of maximum transformation strain for α grains corresponding to the texture component g_α^2.

One difference with respect to the load-free samples (T1 and T3) is that the algorithm for β reconstruction did not work effectively, for the same reasons as sample S1, i.e. the presence of stress during cooling moves the orientation relationship between the two phases away from the ideal Burgers. The α pole figures shown in Figure 5.2 (d) differ very little to those obtained in sample S1, despite the lower number of α colonies measured. The reconstructed β pole figures show higher pole intensities, but this is most likely caused by poor grain sampling, since in this map there were only ~50 β grains. The conclusion from these results is the same as sample S1, that is, that the level of stress applied does not affect the global texture evolution significantly, but the presence of stress probably lowers the pole maxima associated with component g_α^2.
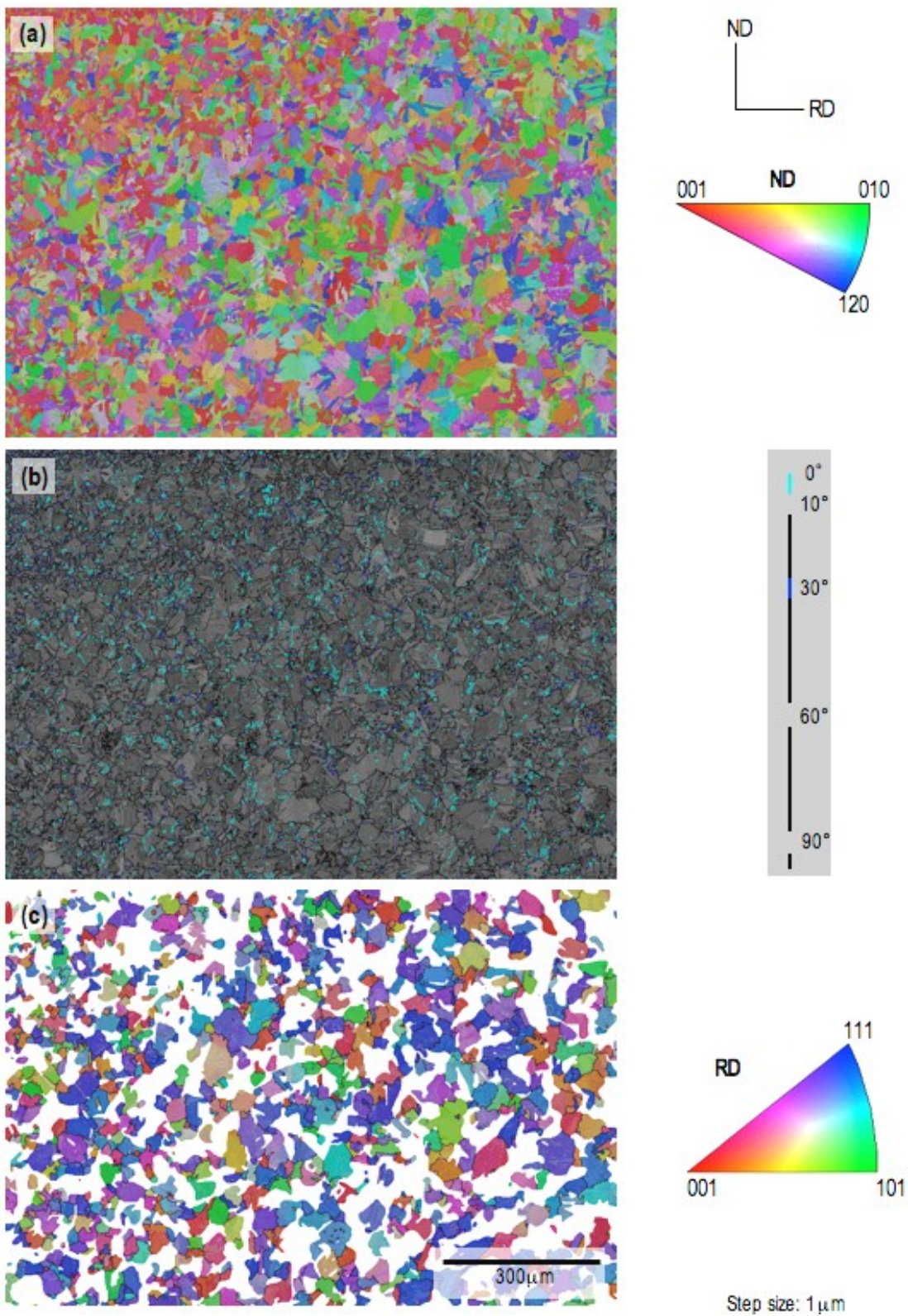
Figure 5.7 EBSD maps from sample S1: (a) IPF map of α-phase (ND), (b) band contrast map showing probable prior β grain boundaries, (c) IPF map of β-phase reconstruction (RD)
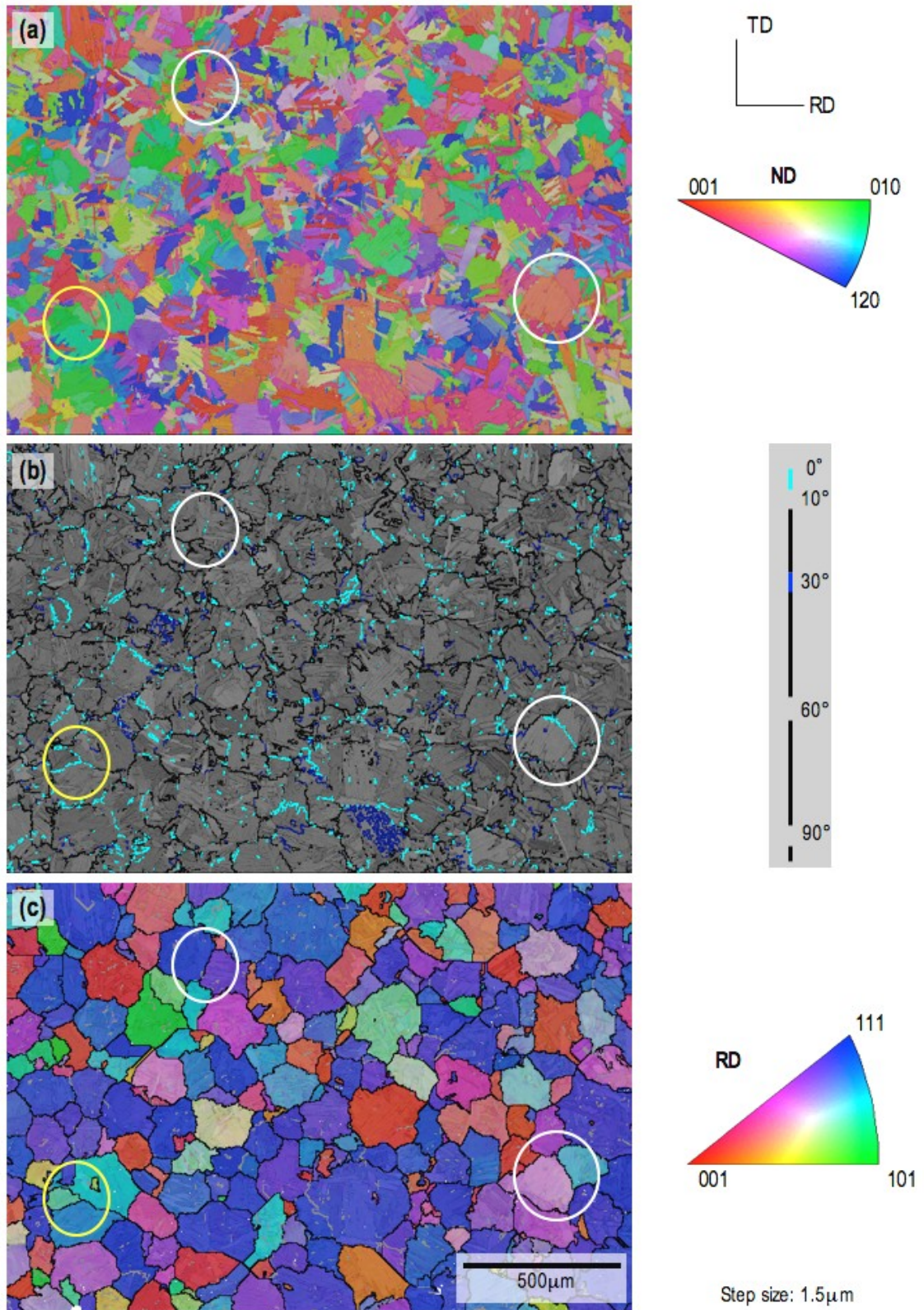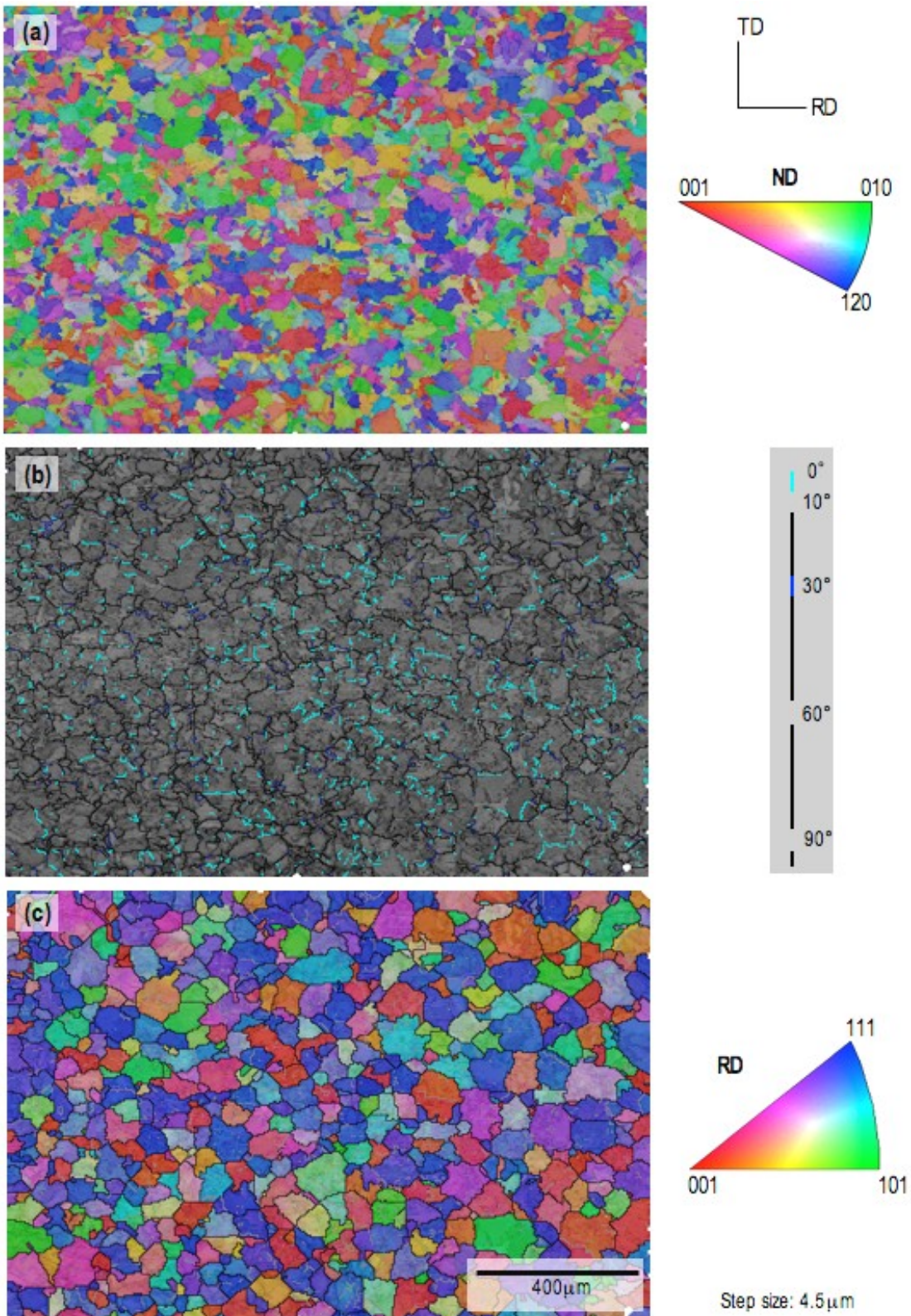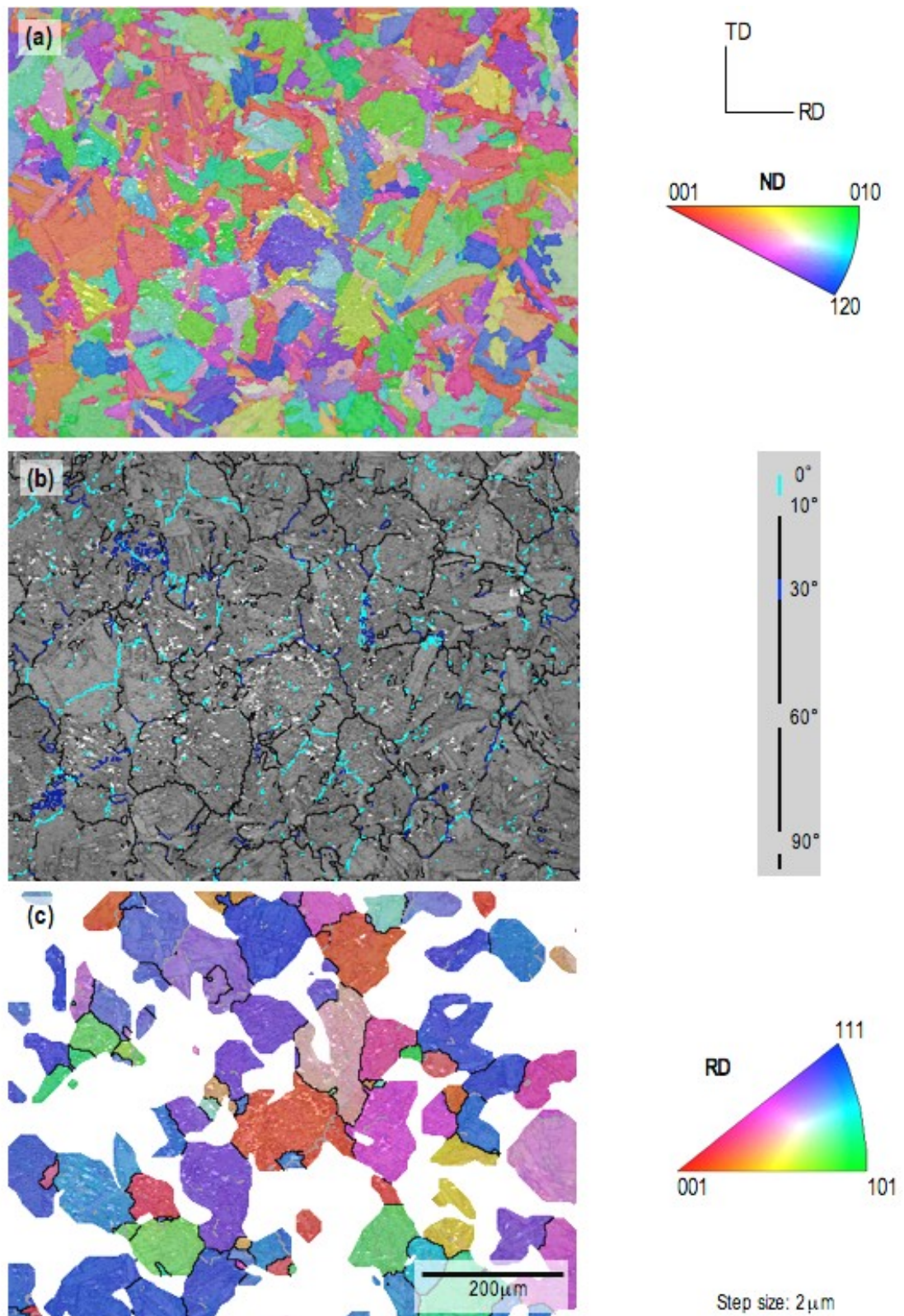
Figure 5.8 EBSD maps from sample S2: (a) IPF map of α-phase (ND), (b) band contrast map showing probable prior β grain boundaries, (c) IPF map of β-phase reconstruction (RD)

5.3.2 EFFECT OF PLASTIC DEFORMATION

In one of the samples of the SXRD experiment, sample S3 in Table 4.1, a relatively high tensile load was applied during the thermal cycle, to the point that the sample failed during cooling. Two post-mortem EBSD maps were made in this sample: one next to the fracture and another ~4mm away from the fracture, at the approximate location of the thermocouple. The location of the EBSD maps is indicated in Figure 5.9. According to area reduction calculations, the plastic strain at the fracture is above 2.5, while at ~4mm from the fracture is approximately 0.25.

Figure 5.10 and Figure 5.11 show the orientation maps obtained, while the pole figures from these two maps are shown in Figure 5.2(e-f) and Figure 5.3(e-f). The EBSD results from this sample are revealing, and similar to the synchrotron results shown in section 4.4. The inherited texture at the fracture, where the material suffered the largest plastic deformation, is extremely strong and completely different to the inherited texture observed in the absence of stress. The texture at this point (Figure 5.2(e)) becomes practically a fibre texture, exhibiting a dominating (0002) pole maximum parallel to RD, i.e. the loading direction. This is consistent with the results of the in-situ experiment. The reconstructed β texture illustrates clearly the Burgers orientation relationship: the strong (110) pole maximum parallel to RD observed in the β texture corresponds to the strong (0002) pole maximum in the inherited texture, while the $(11\bar{2}0)$ α pole figure resembles the (111) β pole figure. In this sample, the β reconstruction algorithm exhibited the best performance of all the samples, with more

than 90% of the map reconstructed successfully. This is explained by the fact that the Burgers orientation relationship between parent β and inherited α grains was not affected whatsoever, since the sample failed and cooled down free of constraint and therefore stress.

The prior β grain size is similar in the two maps in sample S3, although it looks slightly larger in the map taken away from the fracture region. The misorientation and β reconstruction maps show an approximate prior β grain size of ~150μm next to the fracture and ~170μm at the thermocouple. Interestingly, both the α and β pole figures at the point away from the fracture region, which underwent an elongation of ~0.25 look almost random with no discernible features (Figure 5.2(f) and Figure 5.3(f)). This suggests that different levels of plastic deformation in the β phase produce different inherited α textures. The region shown in Figure 5.11 underwent some plastic deformation in the β field, which moved the strong (110) β maxima from TD and ND towards RD, but without creating a strong β fibre texture. The moderate plastic deformation modified the prior β texture significantly, which led to a much more random α texture on cooling.
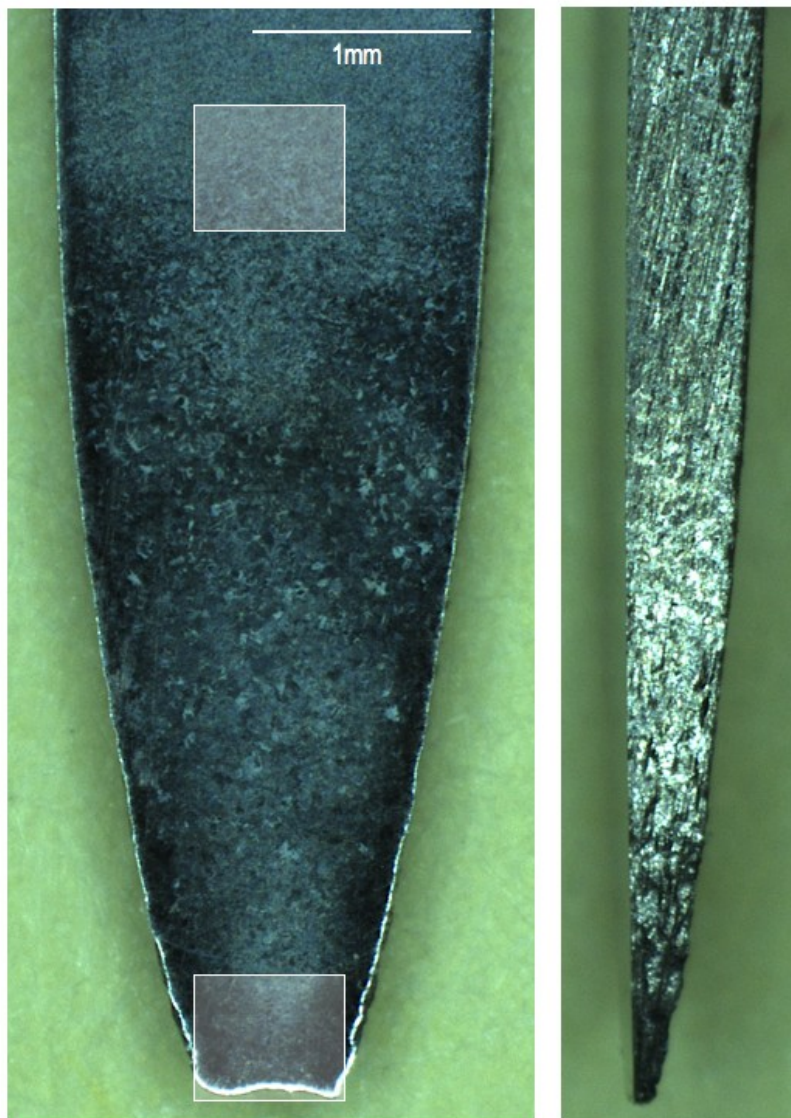
Figure 5.9 Sample S3 (as polished). The location of the two EBSD maps, at the fracture tip (strain>2.5) and ~4mm away from the fracture (strain ~0.25), is indicated.
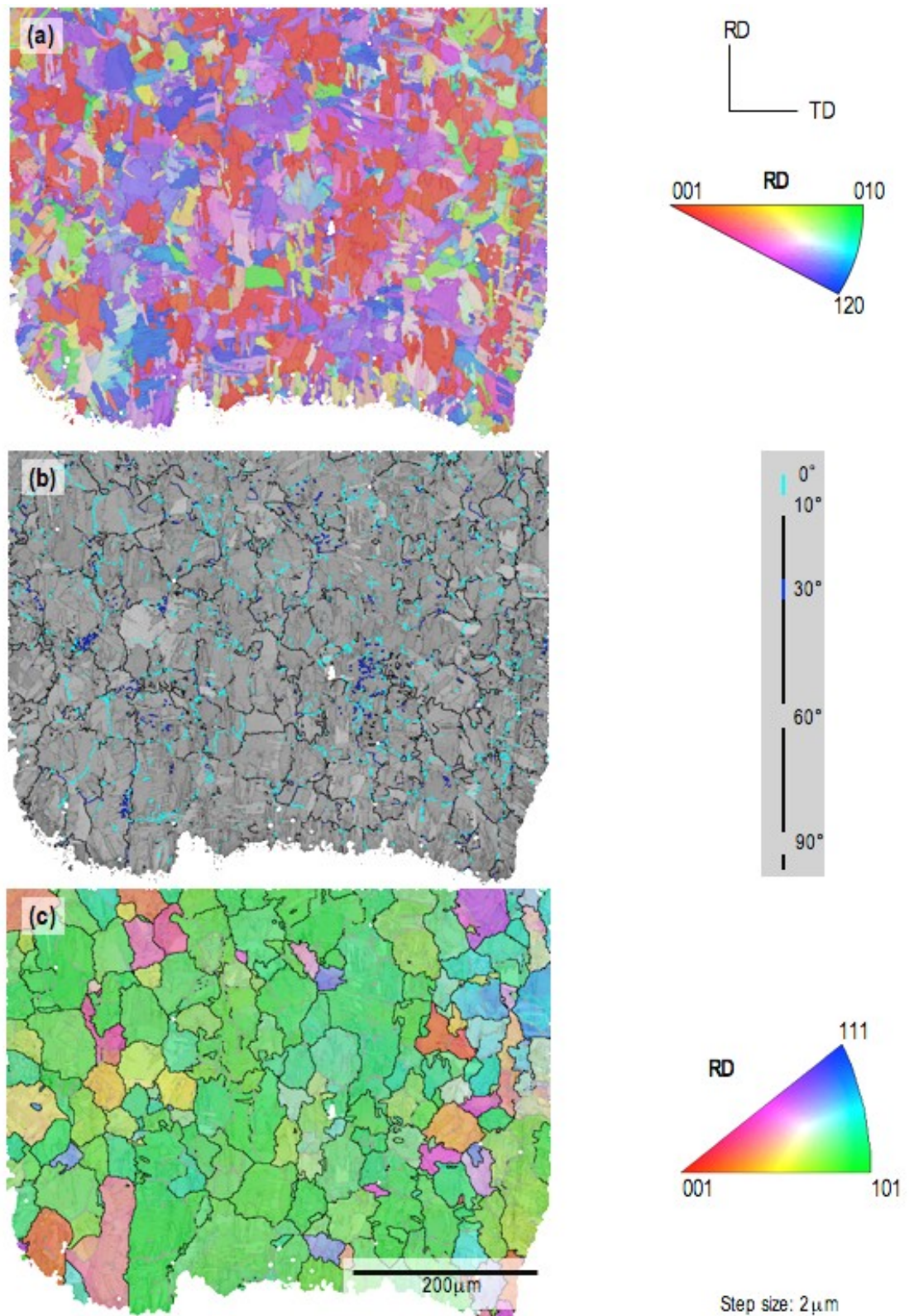
Figure 5.10 EBSD maps from sample S3 at the fracture tip: (a) IPF map of α-phase (RD), (b) band contrast map showing probable prior β grain boundaries, (c) IPF map of β-phase reconstruction (RD)
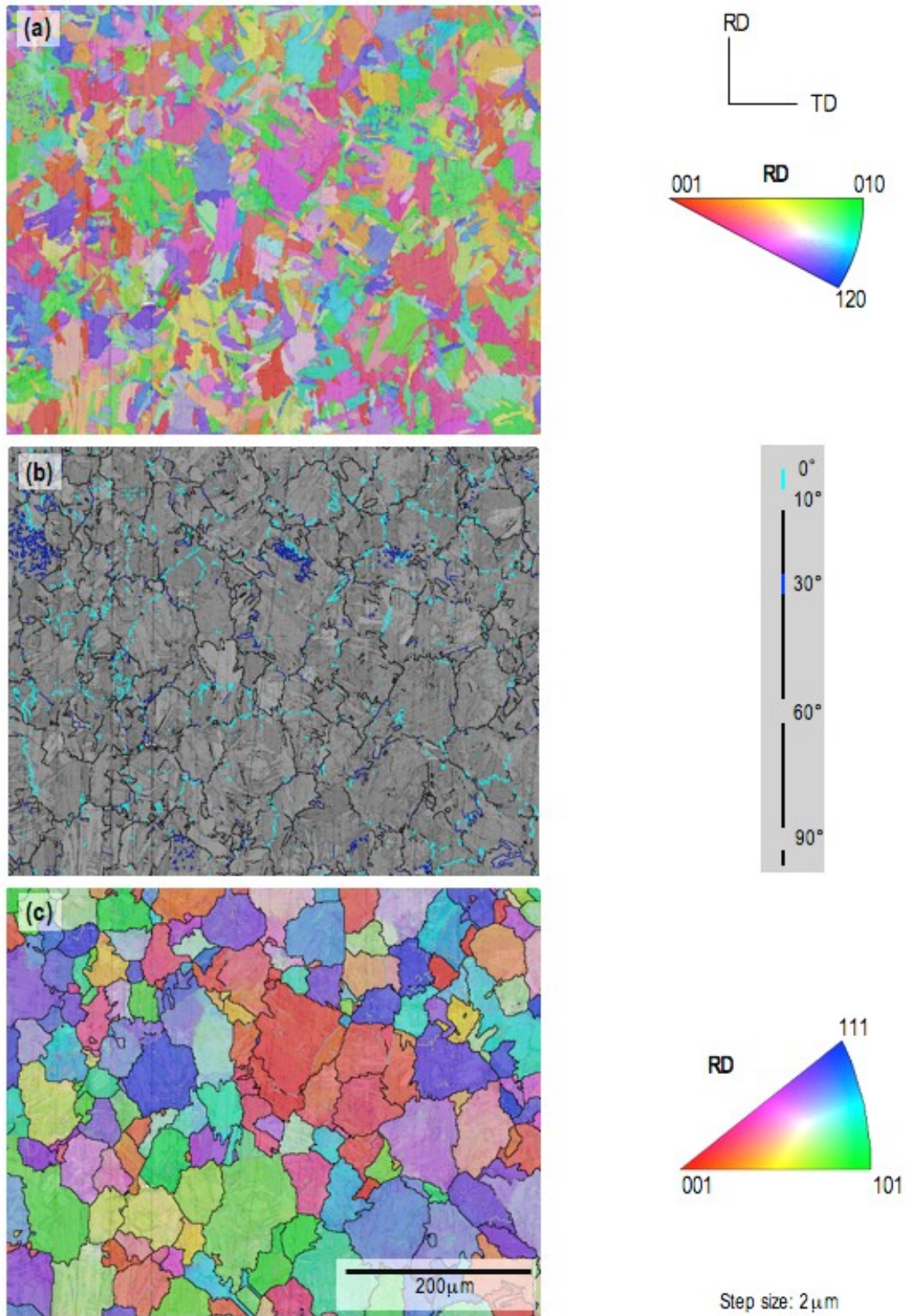
Figure 5.11 EBSD maps from sample S3 ~4mm away from the fracture: (a) IPF map of α-phase (RD), (b) band contrast map showing probable prior β grain boundaries, (c) IPF map of β-phase reconstruction (RD)

5.4   THE EFFECT ON THE MICROTEXTURE OF A TEMPERATURE GRADIENT NEAR THE β-TRANSUS

In samples heat treated in the ETMT, the maximum temperature reached by the material during the thermal cycle varies with position. In section 4.3, it was shown that the samples exhibit sharp changes in texture along their length. In order to investigate this in detail and to confirm the results obtained using SXRD, EBSD mapping was carried out in sample T3 in the region where the sample reached temperatures near the β-transus, and where a sudden change in texture was observed. The results are displayed in Figure 5.12. First, a large map (a) was made in this area, covering as much area as possible to improve sampling. Then a very high-resolution map (b) was acquired in the middle of this region to study the microstructure closely.

The plot in Figure 5.12(b) confirms that a significant texture change occurs within a very narrow region, which corresponds to a variation of only about 20°C in peak temperature. The Kearns factor changes from ~0.33 at the top of the figure, indicating a weak texture, to significantly different values associated to very strong textures at the bottom, e.g. $f_{0002}^{ND} > 0.6$. This confirms the results obtained using SXRD. The magnified area shown in Figure 5.12(c) has undergone significant morphological changes in the microstructure, evidenced by the presence of lamellar α, but still exhibits strong texture. This is evidenced not only by the evolution of the Kearns factors, but also by the colouring of the map. The map in Figure 5.12(b) shows random colouring towards the top, where the β transus was well exceeded, turning more and more red

downwards, indicating an accumulation of (0002) poles close to ND as the peak temperature decreases and the β-transus was not exceeded completely.

Figure 5.13 shows the probable prior β grain boundaries in this map, as well as the results of the β reconstruction algorithm. The reconstruction is poor in the region of the map where the β-transus was not exceeded, i.e. the region with strong basal normal texture and small prior β grains. The deficient reconstruction would be caused by the fact that in this region only one or maximum two variants per β grain could be identified. It is clear that the transition temperature occurs around the middle region of the map, where the size of the prior β grains increases sharply. The texture in the region that exceeded the transformation temperature in the map shown in Figure 5.12(a) (region A) is significantly weaker than that observed in regions of samples T1 and T3 that reached 1000°C and 950°C respectively. The pole intensities in the pole figures shown in Figure 5.14 are considerably lower than those observed in Figure 5.2(a-b), and even though the general morphology is similar, the (0002) pole intensity parallel to TD (g_α^2) is not as strong when compared to g_α^1. This illustrates again the correlation between peak temperature and the strength of the inherited α texture, probably due to very limited β grain growth. In the map shown in Figure 5.13, the prior β grain size of this region is between ~30-50μm.
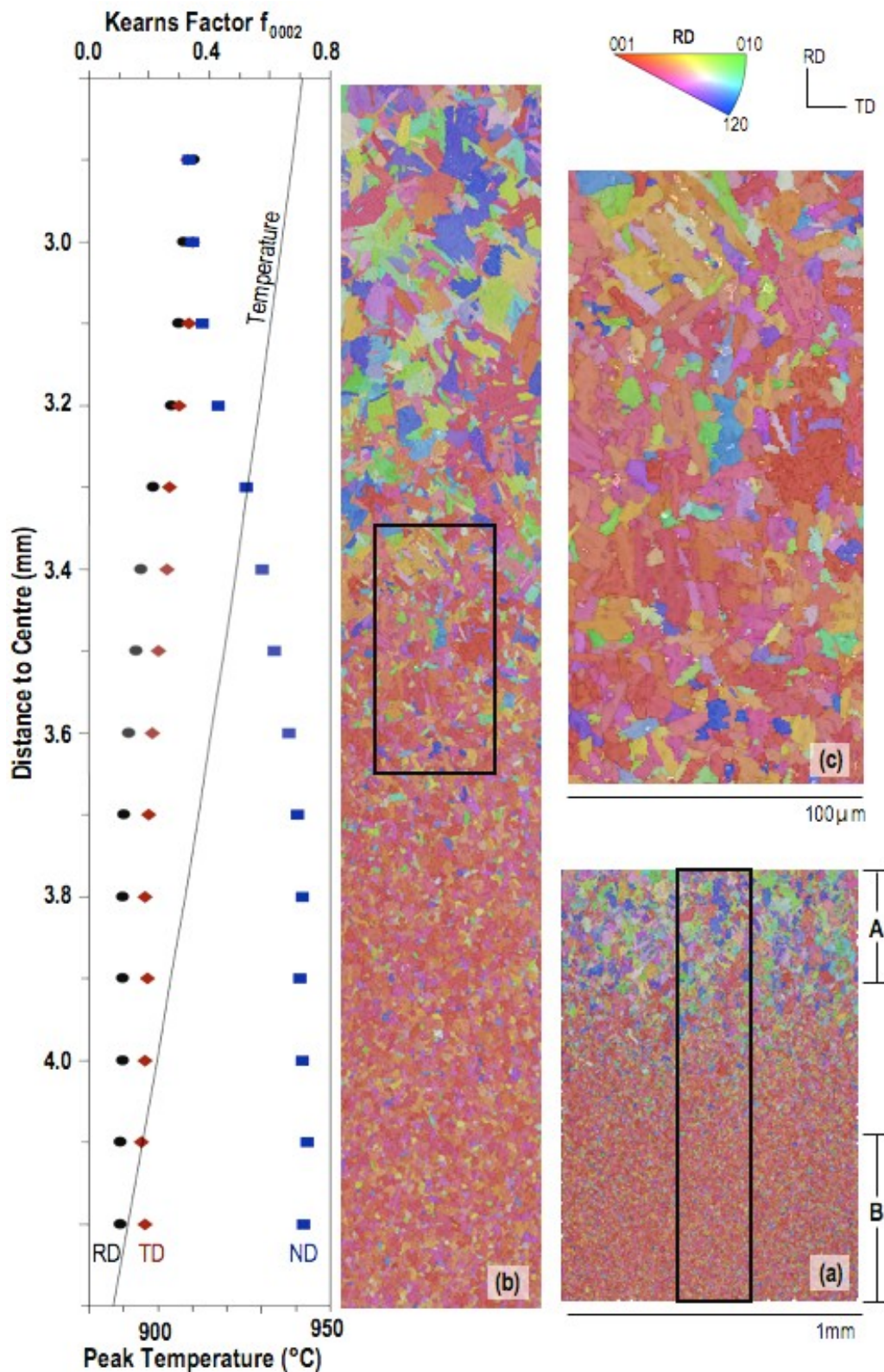
Figure 5.12 EBSD mapping illustrating the texture gradient in sample T3. (a) Low resolution map showing the location of the high resolution map and the regions whose pole figures are shown in Figure 5.14 (A and B). (b) High resolution map and corresponding Kearns factors. (c) Magnified area showing strong texture.
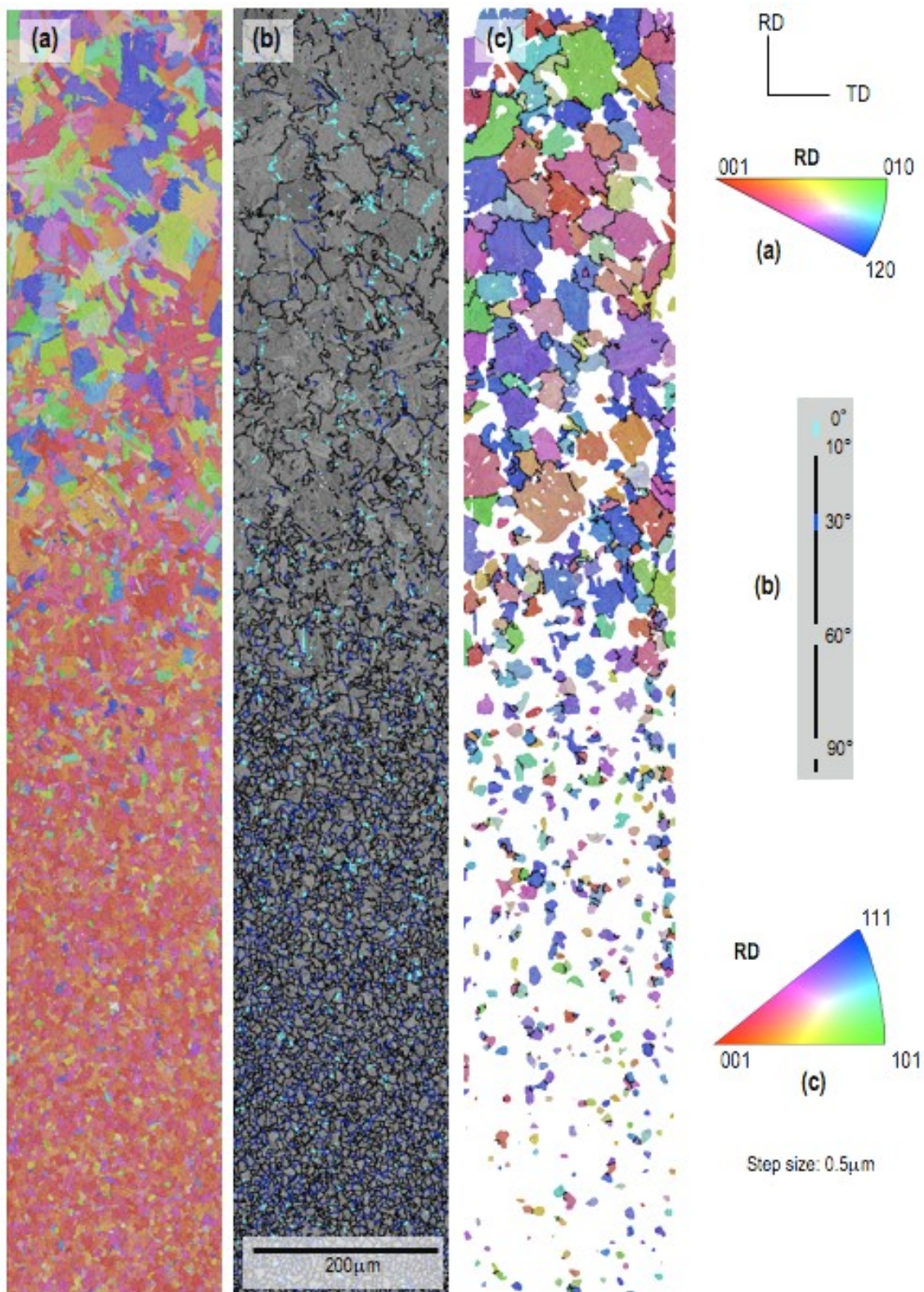
Figure 5.13 EBSD mapping illustrating the texture gradient in sample T3: (a) IPF map of α-phase (ND), (b) band contrast map showing probable prior β grain boundaries, (c) IPF map of β-phase reconstruction (RD).
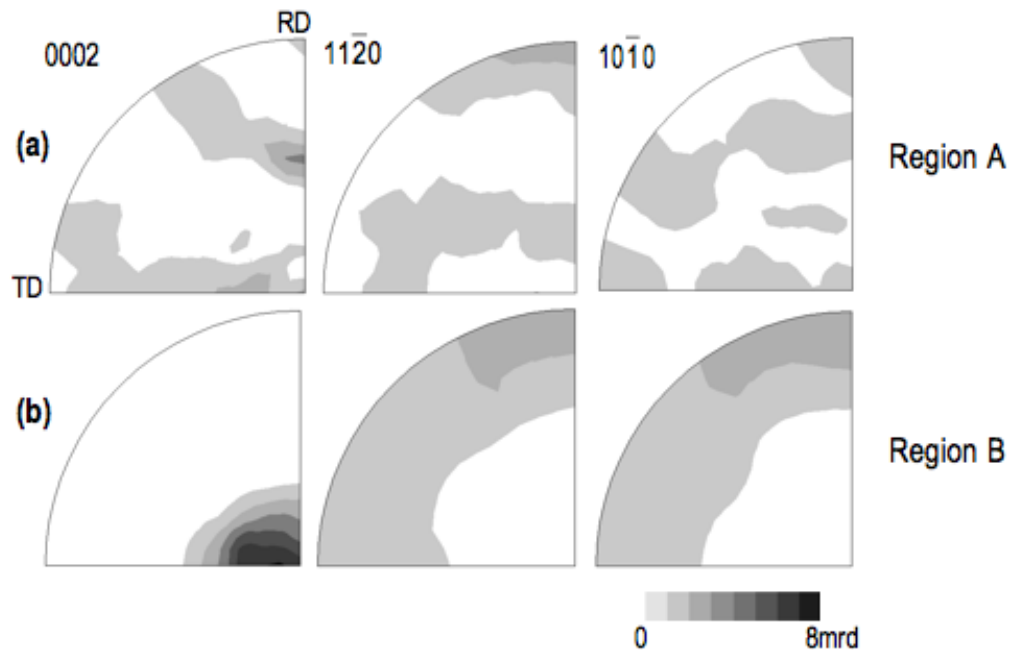
Figure 5.14 Pole figures obtained from regions A and B as illustrated Figure 5.12(a). Same colour scale as Figure 5.2. Region B exhibits texture memory, while region A has a weaker texture compared to those obtained in regions that reached higher temperatures.

5.5 SUMMARY

The microtexture of selected regions of some of the samples β-quenched in-situ has been characterised using EBSD. EBSD data from the α-phase was post-processed in order to minimise noise/misindexing, and also to determine the microstructure and orientation of the high-temperature β phase by using a reconstruction algorithm. The results confirmed that despite dramatic microstructural changes, regions of the samples that did not exceed the β-transus result in very strong textures. On the other hand, regions that just exceeded the β-transus exhibit very weak textures compared to regions reaching higher temperature. This has been related to β grain growth, since in the absence of stress, the higher the temperature above the β-transus, the larger the β grains

and the sharper the pole intensities observed. This suggests that the high temperature β texture changes after the end of the α→β phase transformation, probably involving preferential grain growth.

The presence of moderate tensile stress during the β→α phase transformation reduces the intensity of texture component g_α^2, probably due to the orientation of the maximum transformation strains with respect to the applied stress. This observation was made using EBSD but was missed in the SXRD results because this texture component is underestimated. However, the effect of stress is significant for the global texture only if it causes plastic deformation in the β-phase. Extreme plastic deformation in the β-phase completely modifies the β texture and the inherited α texture; while moderate levels of elongation along RD (~0.25) produce β and α textures very close to random.

CHAPTER 6
LABORATORY BETA-QUENCHING

In previous chapters, the texture of cold-rolled Zircaloy-2 sheets during the α→β→α phase transformation has been studied extensively using small ETMT samples in accurately controlled heating/cooling conditions. These investigations have provided some insight into the mechanisms involved in the development and evolution of crystallographic orientation under different conditions. This chapter presents the results of β-quenching trials carried out on laboratory furnaces. These experiments were aimed to confirm some of the findings reported above, and to expand the range of the variables used, more specifically the maximum β-quenching temperature, since it has been observed that changes in the high temperature β texture have a strong influence on the inherited α texture.

6.1   TUBE FURNACE BETA-QUENCHING

Specimens of Zircaloy-2 in as-rolled condition were heat treated in horizontal tube furnaces under argon atmosphere. An initial batch of specimens was heat treated in a small electric tube furnace using a basic temperature control. The maximum available

setting temperature in this furnace was 1150°C. In this first batch, the samples had a size of 14 x 16 mm^2, preserving the original thickness of the sheet (0.9 mm). The temperature control of the furnace used for the first batch was not optimum, evidenced by a temperature variation during the heat treatment of ±5°C with respect to the setting value.

As it was discussed in previous chapters, when the material exceeds the β-transus there is an accelerated grain growth, which can affect the statistics of global texture measurements. For this reason, a second batch of samples was prepared, this time with a size of 35 x 35 mm^2, also preserving the thickness of the sheet. These specimens were heat treated in a Vecstar tube furnace, with a more sophisticated temperature control and a maximum setting temperature of 1500°C. In the second batch of samples, the temperature was better controlled, with a maximum variation of ±1°C during the test.

The heat treatment procedure was the same for all the specimens and temperatures. First the temperature of the furnace was stabilised at the desired setting, then a calibration temperature measurement was carried out inserting a thermocouple in the tube as close as possible to the middle of the heating zone and maintaining the flow of argon. After that, each specimen was introduced in the tube and kept at the temperature for five (5) minutes, after which it was removed and cooled in air. The temperatures for the tests are listed in Table 6.1, including the setting temperature and the calibration temperature

taken with the thermocouple. The correction of the temperature will be discussed in the

following section.

Table 6.1 Temperatures for laboratory heat treatment

Sample	Treatment Temperature (°C)		
	Setting	Thermocouple	Corrected
A1	816	814	765
A2	838	829	780
A3	858	855	806
A4	875	871	822
A5	900	893	844
A6	910	902	853
A7	920	913	864
A8	930	921	872
A9	940	936	887
A10	950	947	898
A11	960	952	903
A12	970	966	917
A13	980	976	927
A14	1000	993	944
A15	1010	1002	953
A16	1030	1023	974
A17	1050	1041	992
A18	1070	1063	1014
A19	1090	1082	1033
A20	1100	1094	1045
A21	1160	1154	1105
B1	1000	916	861
B2	1020	952	882
B3	1040	960	905
B4	1060	975	920
B5	1080	995	940
B6	1100	1015	960
B7	1120	1033	978
B8	1150	1057	1002
B9	1200	1103	1048
B10	1250	1144	1089
B11	1300	1181	1126
B12	1350	1225	1170
B13	1400	1271	1216
B14	1450	1314	1259
B15	1500	1357	1302

6.2   MICROSTRUCTURE

Samples for optical microscopy were prepared and analysed following the procedures

described in section 3.3. From the analysis of the micrographs obtained, it was found

that in addition to the difference between the temperature setting in the furnace and the temperature measured with a thermocouple, there is an additional discrepancy with the actual temperature reached by the sample.

Figure 6.1 shows optical micrographs from selected samples of the first batch, illustrating the microstructural differences. The first observation is a significant microstructural change between samples A13 and A14 in Figure 6.1(b-c). Although the difference in setting temperature between these two specimens was only 20°C, they exhibit considerably different microstructures: in specimen A13 equiaxed grains are observed, whereas in sample A14 the microstructure appears almost completely composed by lamellas. This suggests that the β-transus (~940°C according to previous chapters) is between the peak temperatures of these two samples, which prompted an additional correction in the peak temperature, hence the corrected value in Table 6.1. Similar evidence was found in the samples of the second batch. Figure 6.2 illustrates the peak temperature correction for the second batch of samples. The difference between temperatures measured using a thermocouple and the corrected temperatures is ~50°C. This significant discrepancy could be explained by the presence of oxygen in the tube furnace, which would stabilise the α phase and increase the actual β-transus. The extent of this source of error is difficult to determine given that the discrepancy results as a combination of temperature measurement error and an unknown actual β-transus. Therefore, in order to compare the results obtained from these samples with those reported in previous chapters, a temperature offset of ~50°C was used.
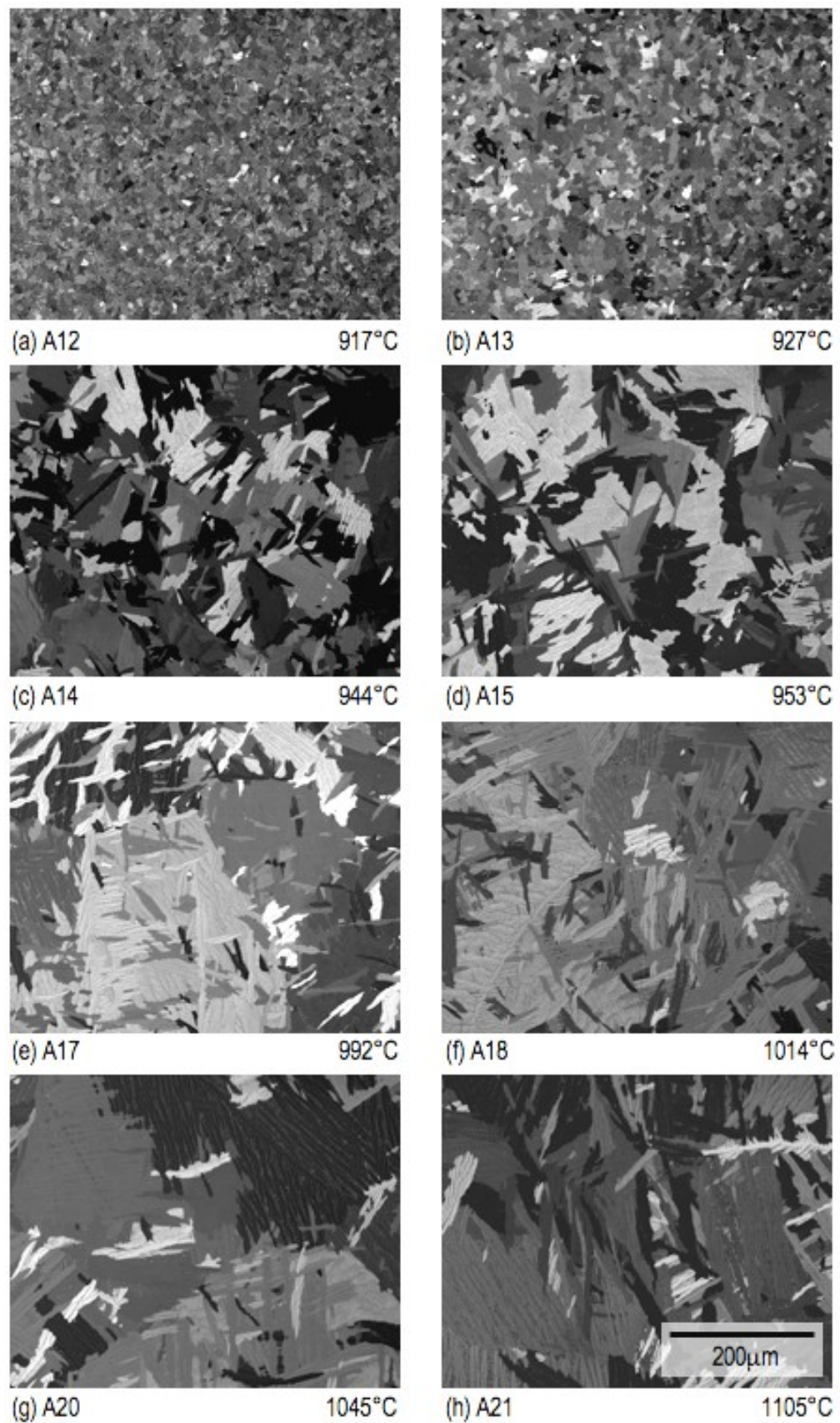
Figure 6.1 Optical micrographs of samples β-quenched in a tube furnace at different temperatures.
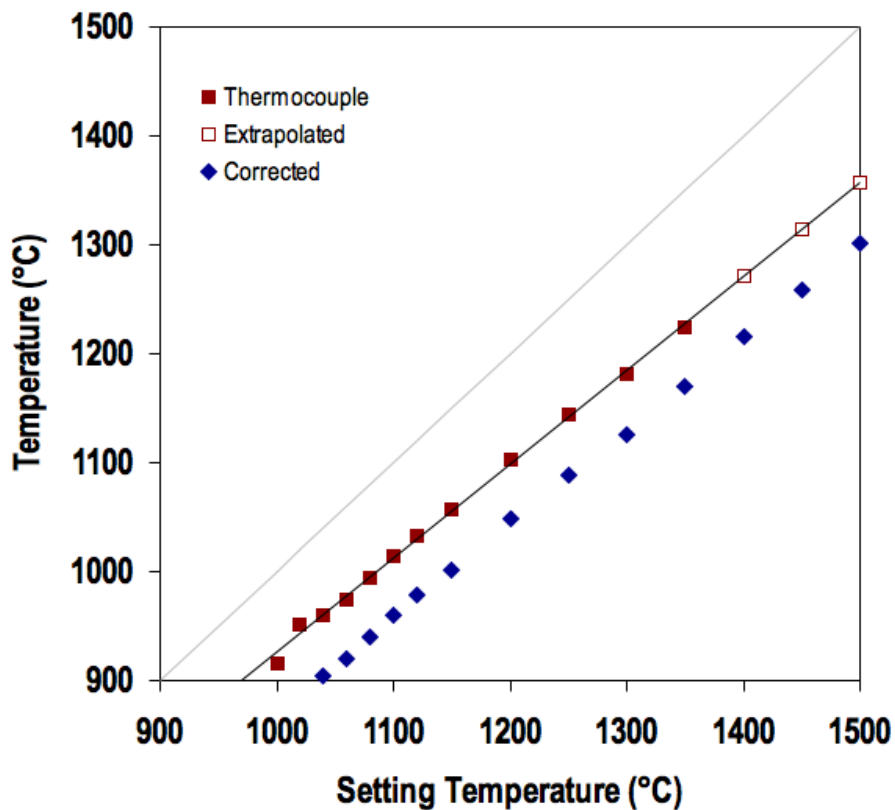
Figure 6.2 Temperature correction in the second batch of furnace samples

In samples with peak temperature above the β-transus, the prior β grain size was measured using the line intercept method in eight micrographs for each condition. For measuring prior β grains, the grain boundary α lamellae were considered as prior β grain boundaries. When the temperature of treatment neared the β-transus, the prior β grains were very difficult to recognise. As the peak temperature was increased, the prior β grains appear more polyhedral in shape, with increasingly more straight boundaries. The α lamellae thickness was measured in samples of the first batch (A), at ten different points in four micrographs, aiming to measure the thinnest observable lamellae.

The results of the measurements are shown in Figure 6.3 and Figure 6.4. Despite the increasing error with peak temperature, it is clear that the prior β grain size increases significantly for temperatures just above the β-transus, reaching certain stability at around ~400μm, and increasing further at very high temperatures. The temporary stability observed could be attributed to pinning of the β grain boundaries by the surface of the sheet, taking into account that the thickness is only 900μm. At extremely high temperature, there would be enough energy to overcome the pinning of the surface and stimulate further grain growth.

The α lamellae width exhibits an increasing trend with peak temperature, ranging between 3 and 6μm, which is a much smaller difference compared to that found in industrial samples in section 3.3 (~2 to 8μm). According to the literature (Massih et al. 2003), the α lamellae width can range between 1 and 7μm for cooling rates between 2 and 100Cs^{-1}. It can be said that the cooling rate in these samples ranges between 20 and 50Cs^{-1}, taking into account the resolution of an optical microscope and the error observed.
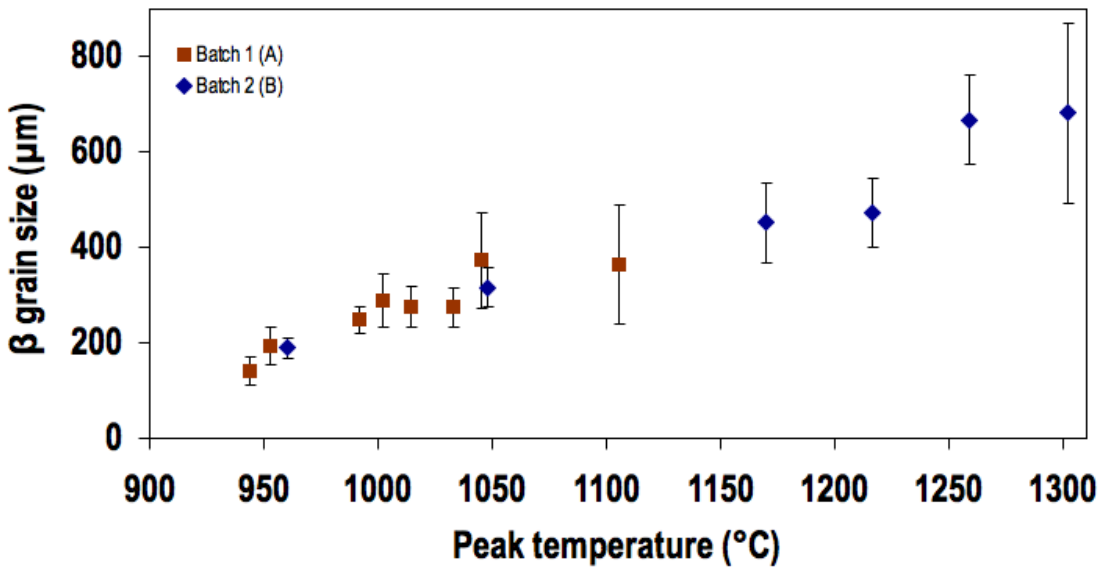
Figure 6.3 Prior β grain size as a function of peak temperature for laboratory β-quenched samples.
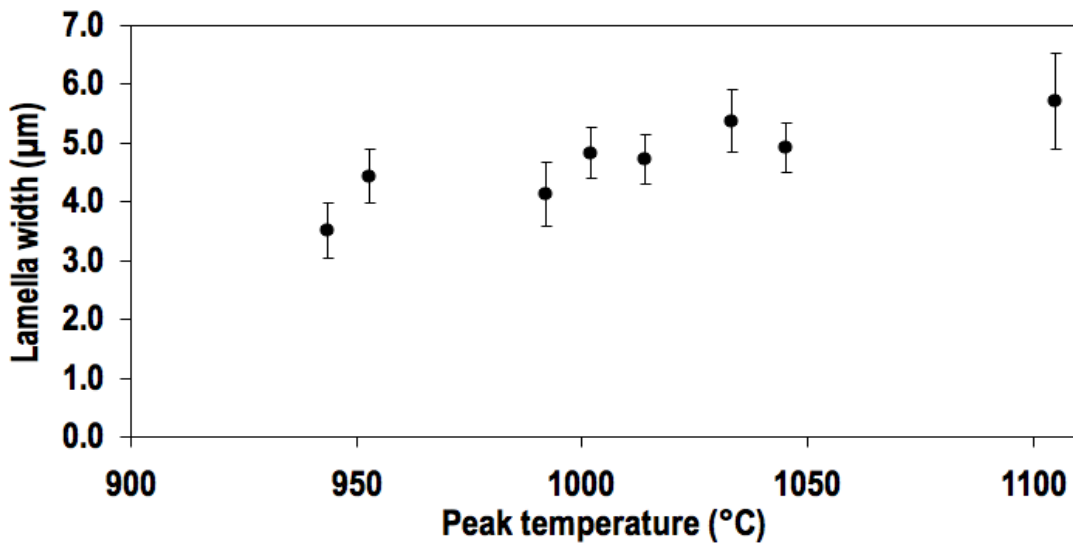
Figure 6.4 Lamella width as a function of peak temperature for laboratory β-quenched samples (batch 1).

6.3   MACROTEXTURE

LXRD texture measurements were carried out on all the samples following the procedure described in section 3.4. The specimens were ground down between 200 and 300μm to guarantee the removal of the oxide layer and the surface effects observed

previously in industrially β-quenched samples, since the interest here is to analyse the behaviour of the texture in the core of the sheet. After grinding, the samples were electropolished in the same way as the industrially treated samples.

Figure 6.5 to Figure 6.7 show a series of pole figures with increased β-quenching peak temperature. It is evident again that only the samples that exceeded the β-transus completely show texture weakening. The first set of pole figures evidencing texture weakening is shown in Figure 6.5(d). On the other hand, as the β-quenching peak temperature increases, the pole intensities evolve. The samples β-quenched at very high temperature, e.g. Figure 6.7(d-e), exhibit very sharp pole intensities, with the poles aligned in the directions representing the main texture components of the transformation texture.

This point is further illustrated in Figure 6.8 and Figure 6.9, where the evolution of the ODF components g_1^{α} and g_2^{α} is plotted as a function of the β-quenching peak temperature. From these plots, it is clear that these texture components change with maximum temperature. The main component present before the phase transformation (g_1^{α}), is initially weakened by β-quenching at temperatures close to the β transus, but its intensity grows again at higher peak temperatures.
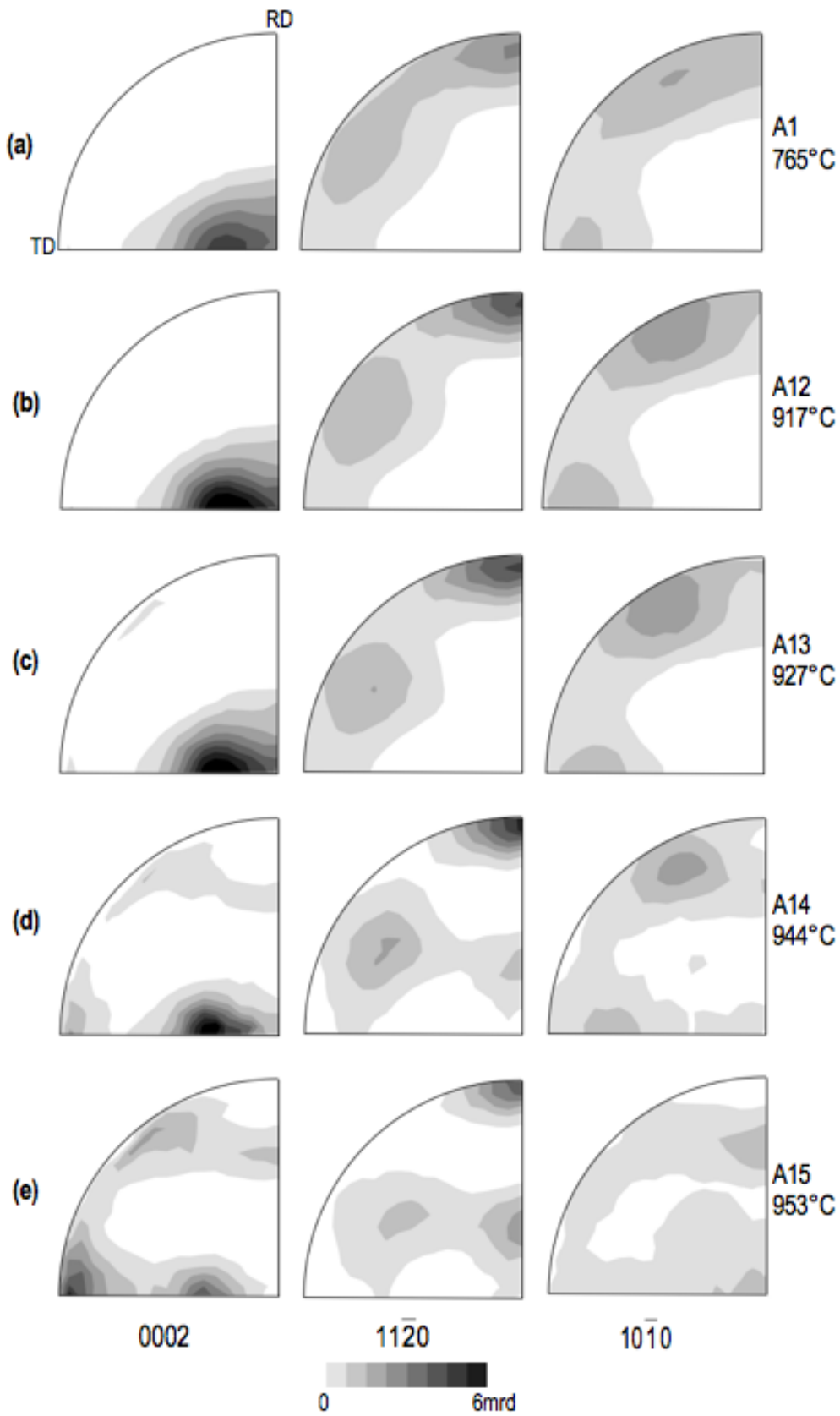
Figure 6.5 LXRD pole figures of samples β-quenched in a tube furnace at different temperatures, from 765°C to 953°C (batch 1).
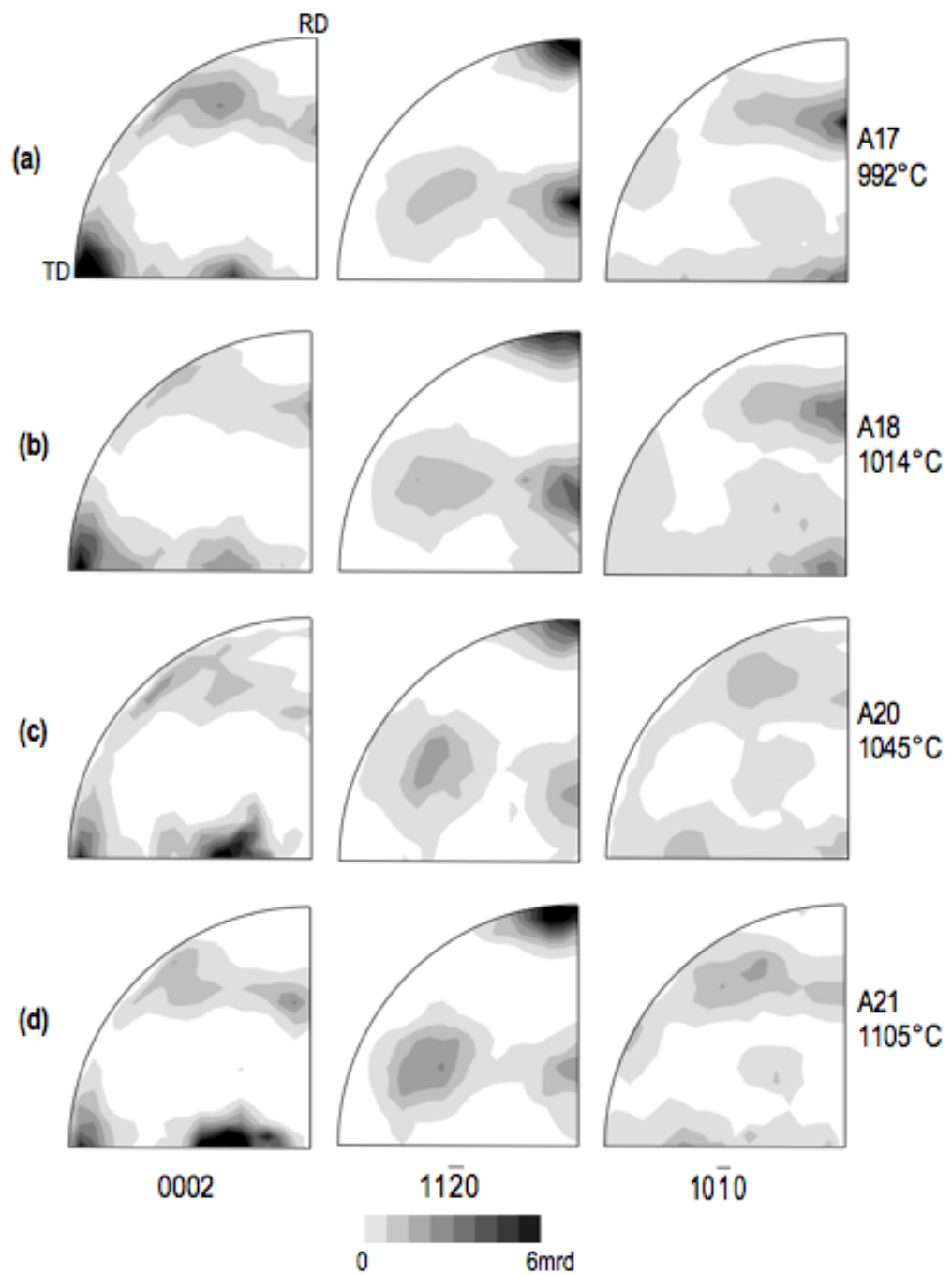
Figure 6.6 LXRD pole figures of samples β-quenched in a tube furnace at different temperatures, from 992°C to 1105°C (batch 1).
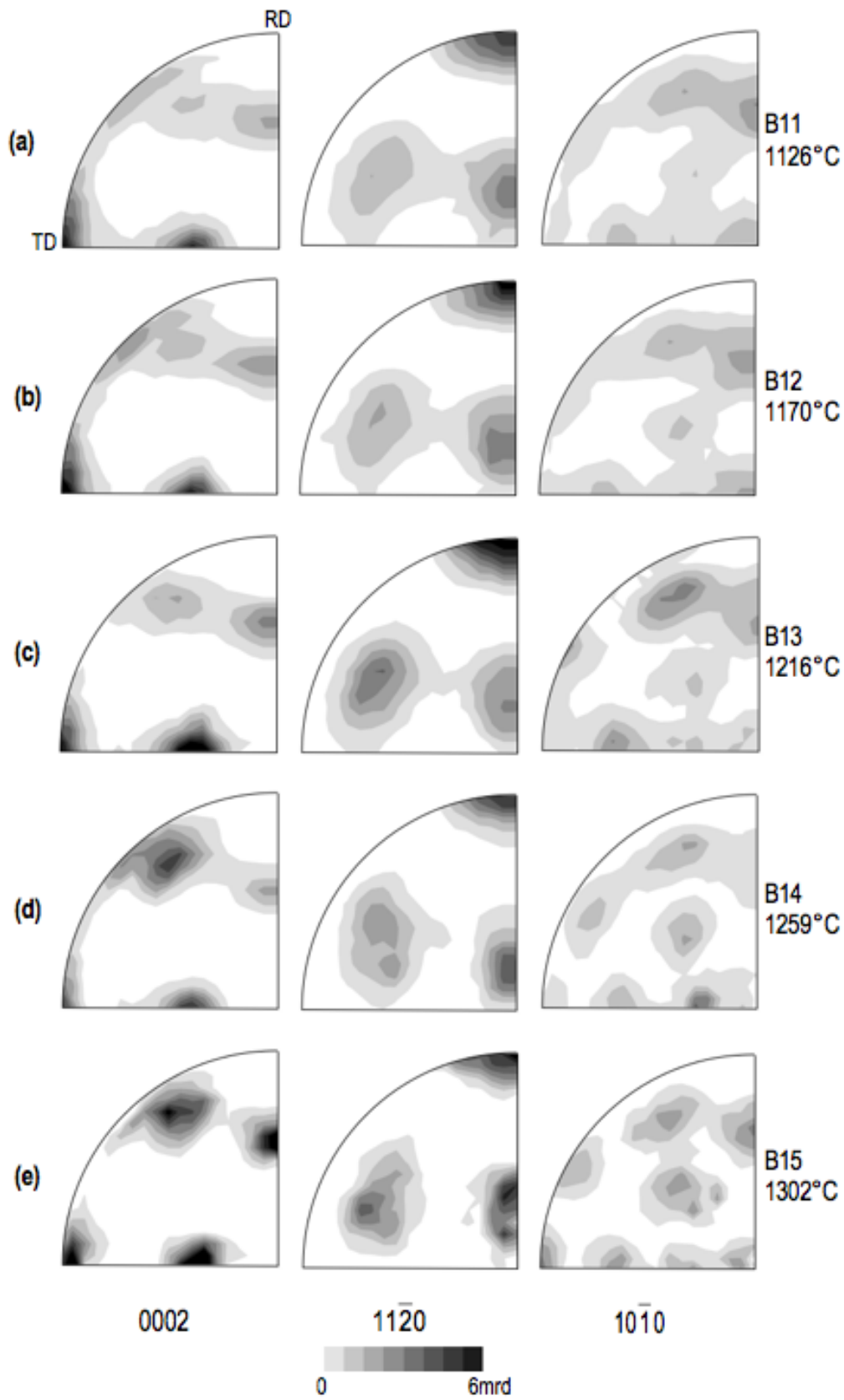
Figure 6.7 LXRD pole figures of samples β-quenched in a tube furnace at different temperatures, from 1126°C to 1302°C (batch 2).
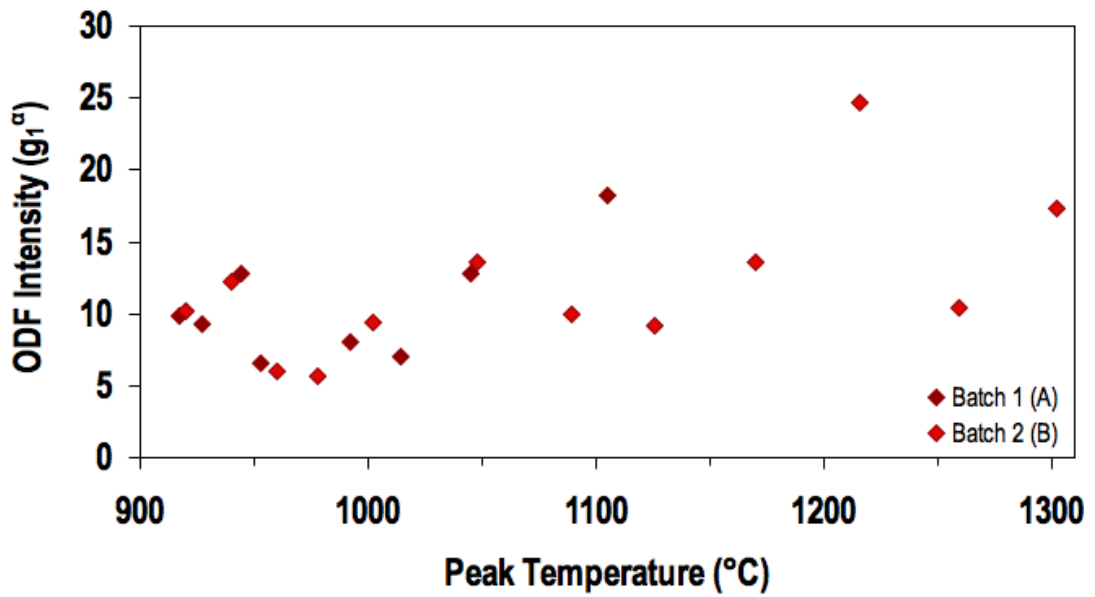
Figure 6.8 ODF component $g_1{}^\alpha$ as a function of the β-quenching peak temperature.
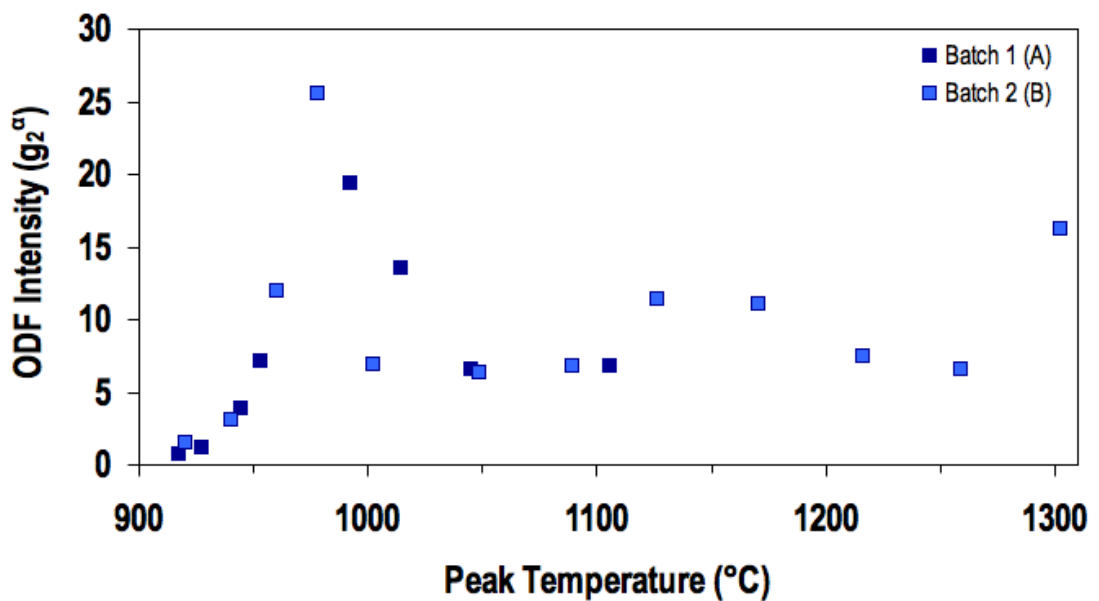
Figure 6.9 ODF component $g_2{}^\alpha$ as a function of the β-quenching peak temperature.

On the other hand, the main new component observed in the transformed textures (g_2^α) gradually increases as the β-transus is exceeded, peaking at temperatures between 950°C and 1000°C. At very high temperatures, this texture component gains intensity,

producing the very sharp pole figures shown in Figure 6.7(e). The weakest texture is obtained by β-quenching between 950°C and 1000°C, where the best balance between the two texture components is achieved. The strengthening of the two main texture components as the peak temperature is increased, suggests one more time that the evolution of the high temperature β-texture is determinant for the inherited α texture.

The trends of the main texture components were confirmed in two ways. The first was by the similar results obtained between the two batches of samples: despite being independent measurements, the ODF intensities observed are similar, illustrated by close points with different colour in Figure 6.8 and Figure 6.9. The second confirmation came from additional macrotexture measurements: using large EBSD scans with relatively large step size.

6.4   MICROTEXTURE AND BETA RECONSTRUCTION

In order to get some insight on the causes of the strengthening of the main texture components observed in samples β-quenched at very high temperatures, high-resolution EBSD mapping was carried out in two samples: B6 and B15, which were β-quenched at 960°C and 1302°C respectively. B6 is the first sample of the second batch that showed texture weakening after exceeding the β transus, while B15 was the sample β-quenched at the highest possible temperature. The α and β (reconstructed) orientation maps obtained are shown in Figure 6.10 and Figure 6.11, while the corresponding pole figures are shown in Figure 6.12 and Figure 6.13.
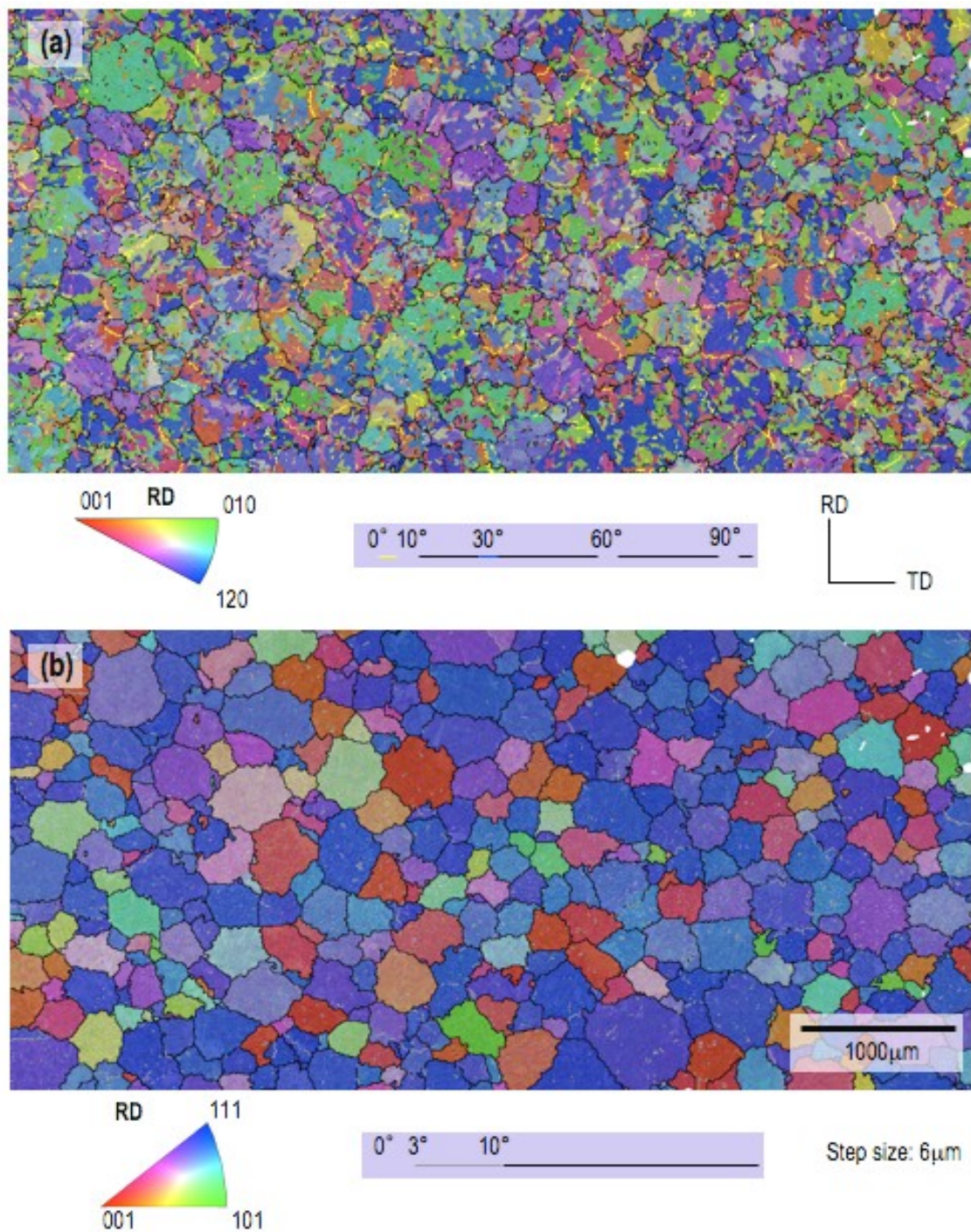
Figure 6.10 EBSD maps from sample B6, β-quenched at ~960°C, near the β-transus: (a) IPF map of α-phase showing probable prior β boundaries, (b) IPF map of β-phase reconstruction.
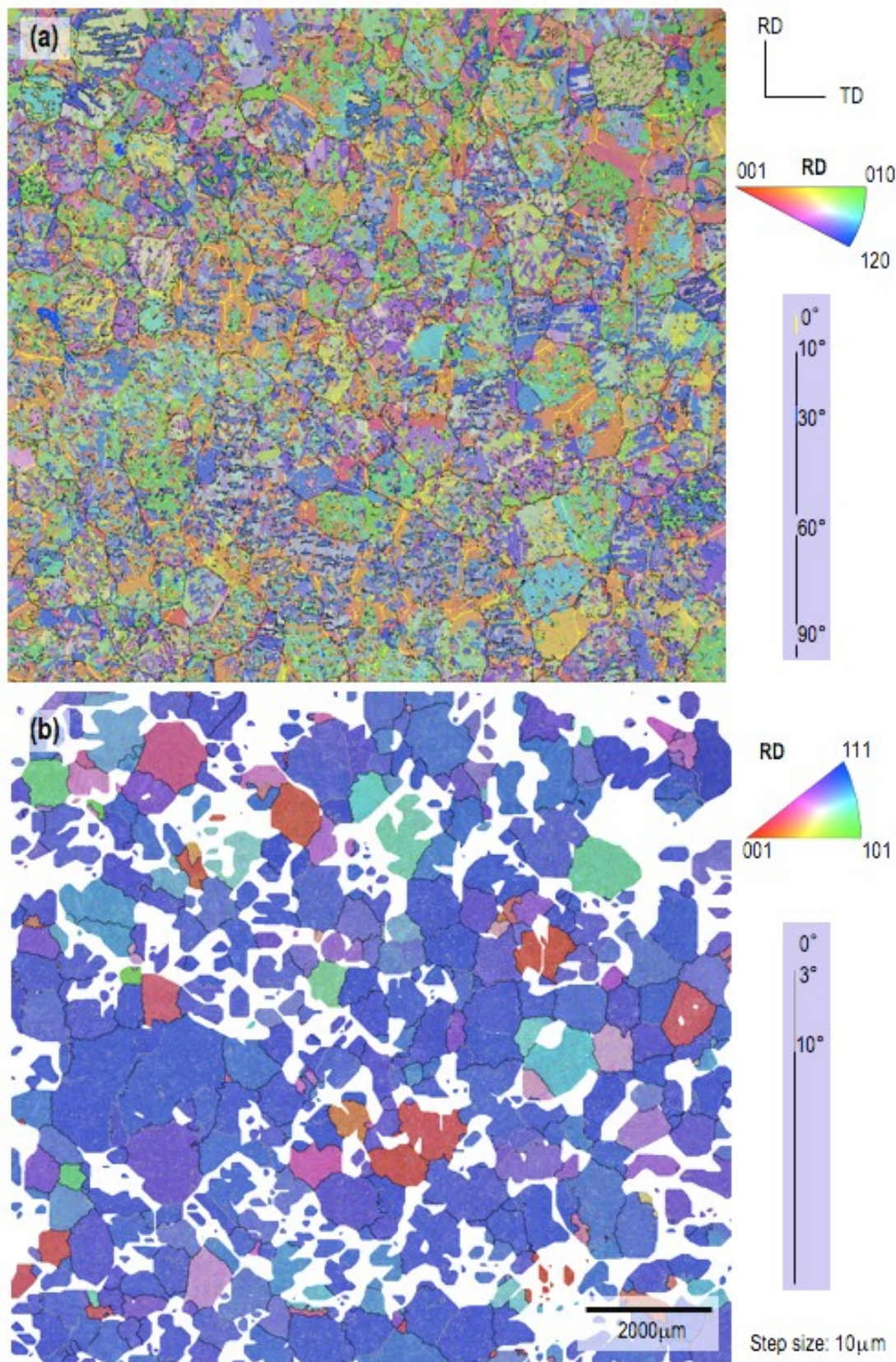
Figure 6.11 EBSD maps from sample B15, β-quenched at ~1302°C, far from the β-transus: (a) IPF map of α-phase showing probable prior β boundaries, (b) IPF map of β-phase reconstruction.
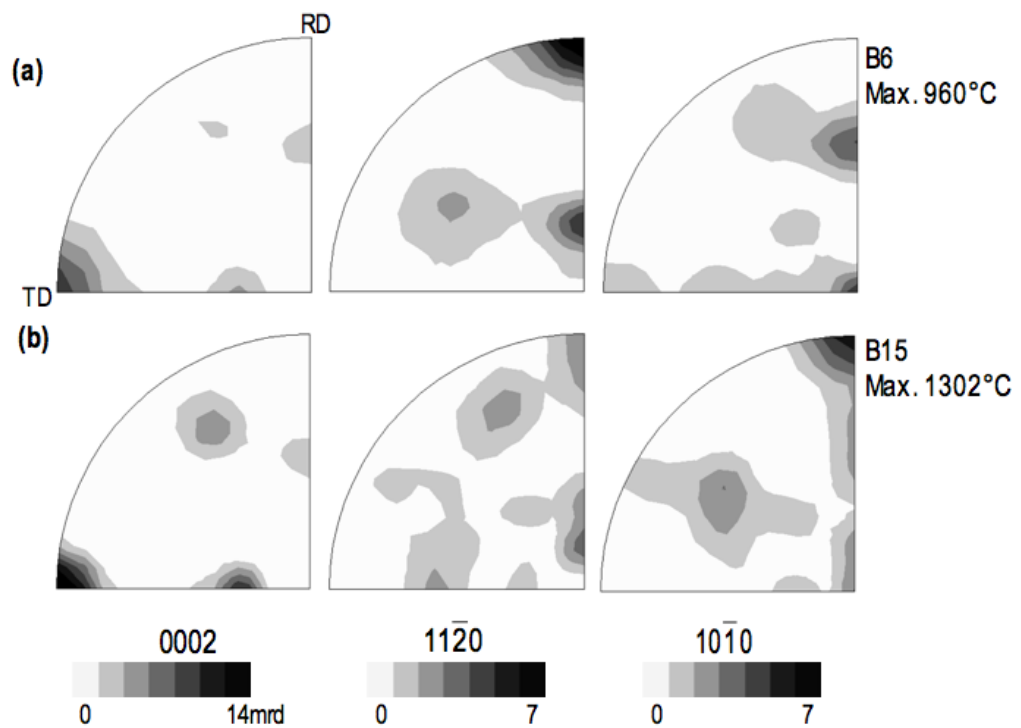
Figure 6.12 α pole figures of samples B6 (a) and B15 (b), obtained from EBSD data.
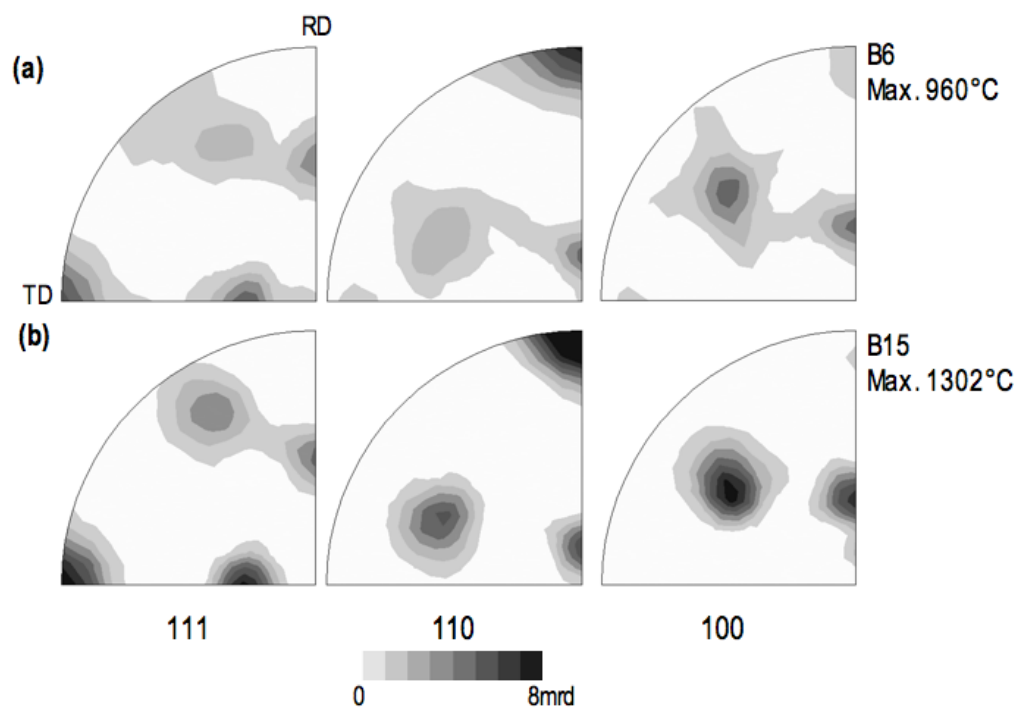
Figure 6.13 β pole figures of samples B6 (a) and B15 (b), obtained from β reconstruction.

The α prismatic pole figures of sample B15, shown in Figure 6.12(b), do not exhibit the normal behaviour observed so far, with absence of the strong $(11\bar{2}0)$ maximum parallel to RD. This is inconsistent with the LXRD results shown in Figure 6.7(e). One possible (but unproven) explanation for this would be misindexing that could not be detected/corrected. This also could be related to the deficient behaviour of the β-reconstruction algorithm in this sample, despite the absence of external stresses during the β→α phase transformation. For this reason, the discussion of EBSD results for this sample will be limited to the behaviour of the basal poles.

The α basal pole figures in Figure 6.12 confirm that the pole maxima associated with the main texture components (g_1^{α} and g_2^{α}) are dramatically stronger as the β-quenching peak temperature is increased. In other words, there are more grains with the basal (0002) poles aligned near ND and parallel to TD. This is related to the considerable sharper and stronger β texture components, illustrated by the pole figures in Figure 6.13.

The EBSD orientation maps of these two samples illustrate significant differences in β grain size and shape. In sample B15 the prior β grains are ~900-1000μm in size and exhibit predominant straight boundaries, whereas in sample B6 the grains are ~200-250μm in size and have slightly more equiaxed shape. The reconstructed β maps illustrate the very strong texture observed in the sample β-quenched at the highest temperature (B15), dominated by a (111) maximum parallel to RD. Figure 6.11(b) is

predominantly blue, while Figure 6.10(b), corresponding to the samples β-quenched close to the β-transus, indicates a much weaker β texture

The spatial distribution of the main α texture components for each map is illustrated in Figure 6.15 and Figure 6.16. In both maps, the component g_1^α is observed mainly at prior β grain boundaries and in many cases at boundaries where the neighbour parent β grains have very close orientation, or at least have alignment of one $\langle 110 \rangle$ pole. This corresponds the mechanism of orientation variant selection postulated by Stanford and Bate (Stanford and Bate 2004), which results from preferential nucleation of α orientation between β grains having nearly parallel $\langle 110 \rangle$. In these cases, the c-axis of the inherited α-phase takes the same direction. According to these results, this variant selection mechanism would be important for texture memory, since g_1^α is the dominant component before the phase transformation, having been developed during recrystallization.

The component g_2^α is observed mainly within the grains. In sample B6, it appears more dominant than in sample B15. In sample B15, g_2^α is also observed within the grains, but interestingly it appears in lamella colonies that propagated parallel to TD. This means that these lamellae propagated in the direction of their c axis. It is known that during an unconstrained β→α phase transformation there is anisotropy of transformation strains, Figure 6.14 (Holt and Aldridge 1985) illustrates the orientation relationship and the transformation strains associated with the β→α phase transformation. Due to the lower

transformation strain required, α nuclei oriented with their c-axis parallel to TD (g_2^α) propagate easily along this direction, which would explain the selection of this particular variant.
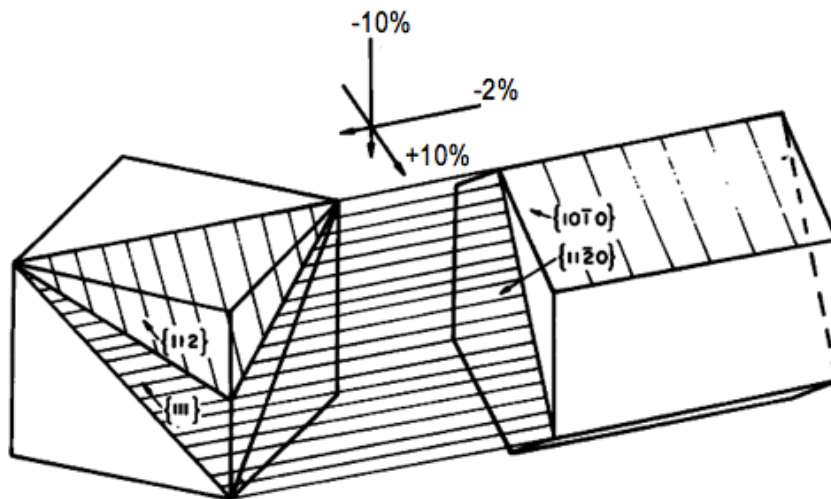
Figure 6.14 Crystallographic relationship and transformation strains during the $\beta \rightarrow \alpha$ phase transformation (Holt and Aldridge 1985)
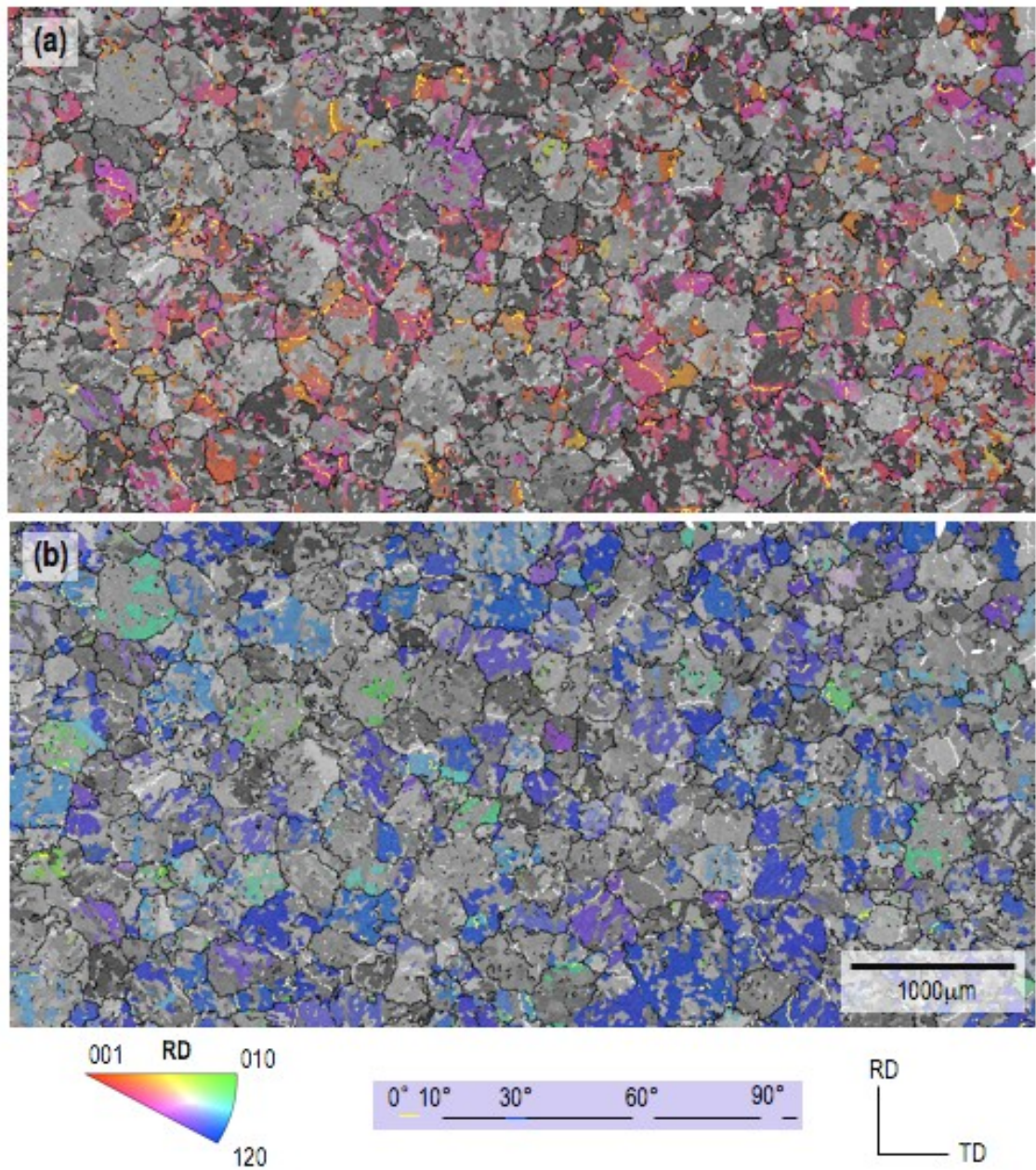
Figure 6.15 Components g_1^α (a) and g_2^α (b) in EBSD map from sample B6.
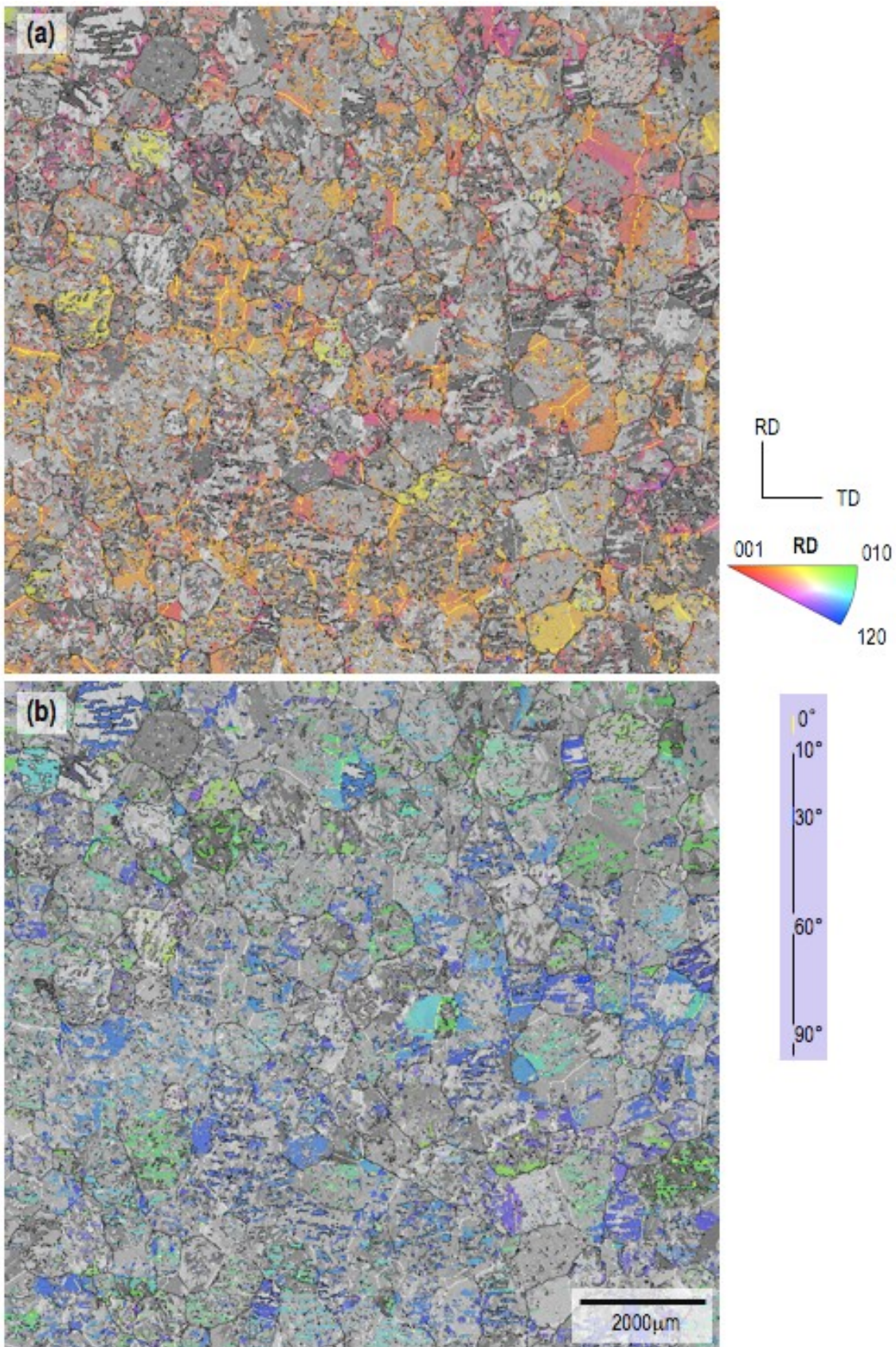
Figure 6.16 Components g_1^{α} (a) and g_2^{α} (b) in EBSD map from sample B15.

6.5   MODELLING ANISOTROPIC THERMAL EXPANSION AND IRRADIATION GROWTH

After studying the mechanisms involved in texture evolution during the $\alpha \rightarrow \beta \rightarrow \alpha$ transformation, the aim of this section is to explore the effect of the most representative α textures observed on the anisotropy of the material. This is ultimately the interest of almost all texture studies: the prediction of anisotropy in physical/mechanical properties of the polycrystal. For this purpose thermal expansion and irradiation growth strains were calculated using polycrystal averaging as implemented in the EPSC code (Tome 1998), which allowed to establish a relation between different α textures obtained in this project, the single crystal anisotropy, and the overall elastic and thermal properties on a polycrystalline aggregate.

The input for the EPSC code consists of the properties of the single crystal (in this case elastic constants and thermal expansion coefficients), a population of orientations corresponding to the texture of the material to be modelled, and the thermomechanical processing procedure desired. The single crystal elastic constants (GPa) and thermal expansion coefficients ($°C^{-1}$) used in the simulations are listed in Table 6.2. The coefficients of zirconium are compared to those of copper, a less anisotropic material in terms of thermal expansion (Tome 1998).

Table 6.2 Single crystal elastic constant and thermal expansion coefficients

	C_{11}	C_{22}	C_{33}	C_{12}	C_{13}	C_{23}	C_{44}	C_{55}	C_{66}	C_{14}	α_{11}	α_{22}	α_{33}
Zr	143.5	143.5	164.9	72.5	65.4	65.4	32.1	32.1	35.5	0.0	5.7	5.7	11.4
Cu	168.0	168.0	168.0	121.4	121.4	121.4	75.4	75.4	75.4	0.0	16.0	16.0	16.0

The sets of orientations used in the simulations were obtained from EBSD macrotexture data of selected samples β-quenched in tube furnaces. The EBSD data was used to calculate the harmonic expansion coefficients, and then sets of 5000 orientations were calculated using TEXTAN III (Bate 1990) for representative conditions:

1. Single grain oriented with the *c* axis parallel to ND (for reference)

2. Random texture (for reference)

3. As-rolled condition.

4. Recrystallized at ~765°C (sample A1)

5. β-quenched in the α+β field, just below the β-transus (sample A13).

6. β-quenched in the β field, just above the β-transus (sample A14).

7. β-quenched at 1300°C, the highest temperature available (sample B15).

The thermomechanical process applied to the polycrystal in the model consisted on heating from room temperature to 600°C with zero applied stress. These parameters were selected in order to represent pure thermal expansion without changes in the microstructure. Figure 6.17 summarises the strains obtained. It is evident that complete β-quenching has a significant impact on the anisotropy of the material, samples A14 and B15 show much more balanced components, while samples that were not β-quenched exhibit a large thermal expansion along ND. It is important to notice how the three strain components change between sample A14 and sample B15. In sample A14 the components are relatively balanced and close to those of the random texture,

whereas in sample B15 a maximum strain is observed in TD, which is the direction along which the c axis of the strong texture component g_2^α is aligned.
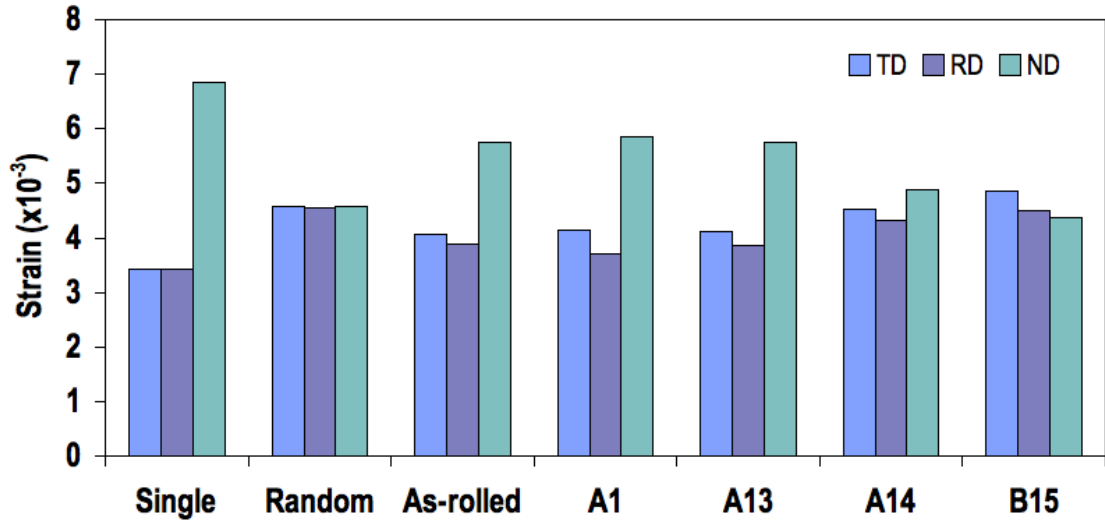
Figure 6.17 Thermal expansion strains calculated from EPSC modelling.

In order to approximate the behaviour of the polycrystals regarding irradiation growth, the thermal expansion coefficients were modified to represent an expansion along the a directions of the crystal and a contraction along the c axis. The growth tensor associated with preferential diffusion of defects to dislocations is of the form (Tome *et al.* 1996):

$$\gamma = \gamma_0 \begin{vmatrix} 1 & 0 & 0 \\ 0 & 1 & 0 \\ 0 & 0 & -2 \end{vmatrix} \qquad \text{Equation 6.1}$$

Therefore, for basic qualitative modelling of the behaviour of the polycrystal regarding irradiation growth, the thermal expansion coefficients can be given values of 1 (directions 1 and 2) and -2 (direction 3). The results of this exercise are shown in Figure

6.18, where they are compared with results of calculations of irradiation strain using just the fraction of poles aligned in a particular direction (i.e. the Kearns factor), as explained in section 2.3.1. From the figure it is clear that the anisotropy of irradiation growth is more dramatic than that seen in thermal expansion, and that the β-quenched samples have an acceptable behaviour. The Kearns factor approximations are very close to the values obtained using the EPSC code.
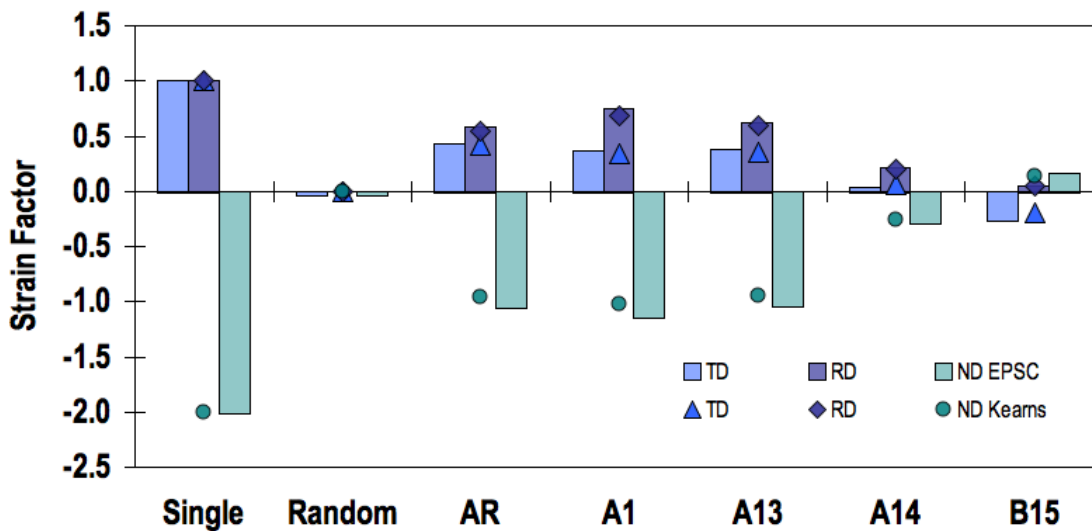
Figure 6.18 Irradiation growth strains obtained from EPSC modelling and Kearns factor calculations.

6.6   SUMMARY

This chapter has reported the characterisation of samples β-quenched in laboratory tube furnaces. Two sets of samples were produced using peak temperatures between 765°C and 1302°C. Optical microscopy, LXRD and EBSD have been used to characterise these samples. The main finding is that the strength of the main texture components observed in the transformed textures increase dramatically with the peak temperature,

which is related to strong texture components in the β-phase, probably caused by preferential growth. The ratio between the intensities of these texture components changes with the peak temperature. Evidence of β/β grain boundary variant selection was observed, as well as preferential growth of variants with favoured transformation strain in certain directions.

Models of polycrystal anisotropy have shown that β-quenching has a significant and positive impact on the anisotropy of the material. β-quenched textures are close to random distributions regarding anisotropy. When compared to EPSC calculations, Kearns factor calculations have been proven to give a good approximation of thermal expansion and irradiation growth.

CHAPTER 7
VARIANT SELECTION

Discussions and results in previous chapters have indicated that the phenomenon of selection of crystallographic orientations or variants, commonly called variant selection, plays an important role in the texture evolution during phase transformation of zirconium alloys. Experimental results presented have shown evidence of variant selection, and different degrees of texture memory associated with it. This final chapter is intended to gather the main findings of this project and discuss them in the context of the work in this area, on zirconium and on other systems such as titanium and steel.

The main findings can be summarised as follows:

· The initial strong rolling texture observed in cold-rolled Zircaloy-2 sheets is weakened by a complete β-quenching heat treatment. New texture components are observed, but there are indications of variant selection.

· β-quenching treatments with peak temperatures close to the β-transus (~940°C) are strongly associated with perfect texture memory. It is unlikely that this texture

memory is caused simply by nucleation of inherited α variants near to untransformed α clusters, so an alternative explanation is needed.

· The global texture evolution during a α→β→α phase transformation is not significantly sensitive to applied stress unless significant plastic deformation takes place in the β-phase.

· Plastic deformation and/or grain growth in the β-phase lead to changes in the β texture, which modifies the inherited α texture.

In order to follow the discussions below, it is important to revise some important concepts in texture development during a phase transformation (Banerjee and Mukhopadhyay 2007) :

· Phase transformations involve nucleation and growth. The orientations appearing in the new phase are generally established at the nucleation stage. However, variability in the growth rates will affect the contribution of each orientation in the final texture.

· In many cases, nucleation is dominated by processes occurring at the grain boundaries of the parent phase. Nuclei generally form low energy interfaces with at least one of the adjacent parent grains, typically following an orientation relationship. In some cases, the daughter phase forms within a parent grain in an intragranular nucleation, following the orientation relationship with the parent grain.

· Two different types of growth can be observed after the nucleation stage: diffusional and displacive. Nuclei exhibiting diffusional growth develop rapidly with disordered incoherent interfaces, and the orientation relationship is not very strict. Displacive mechanisms, on the other hand, are closely constrained by the orientation relationship. They result in shear deformations and can be influenced by residual or imposed stress. The difficulty is to identify the contribution of each of these mechanisms during a particular phase transformation.

The transition from a displacive to a diffusional transformation is a key factor when explaining the phenomenon of variant selection. However, it is sometimes difficult to distinguish the contribution of each mode if they happen simultaneously. The clear facts relevant for this project are that the morphology of the inherited α phase after a $\beta \rightarrow \alpha$ transformation depends strongly on the cooling rate, and that at very high cooling rates, above $500°Cs^{-1}$, the phase transformation in zirconium based alloys is predominantly martensitic (Banerjee and Mukhopadhyay 2007). For the cooling rates employed in this project, between 2 and $50°Cs^{-1}$, the transformation can be considered predominantly diffusional.

In this chapter, the phenomenon of crystallographic variant selection will be discussed in three stages: (1) variant selection on heating during the $\alpha \rightarrow \beta$ phase transformation, (2) variant selection during β grain growth (when present), and (3) variant selection on cooling during the reverse $\beta \rightarrow \alpha$ transformation.

7.1 VARIANT SELECTION DURING THE ALPHA TO BETA TRANSFORMATION

In order to evaluate the presence of variant selection during the α→β and β→α phase transformations, basic crystallographic modelling was carried out, making use of the Burgers orientation relationship. The relationship between the orientations of the α and β phases can be expressed as a matrix product as follows (Humbert 1995):

$$\mathbf{S}_j^\alpha \mathbf{G}_\alpha = \mathbf{D} \mathbf{S}_i^\beta \mathbf{G}_\beta \qquad \text{Equation 7.1}$$

Where $\mathbf{G}$ are the rotations that characterise the orientation of the crystals, and $\mathbf{S}$ are the rotations that characterise the symmetry groups for each phase. For cubic crystals there are 24 elements $\mathbf{S}_i^\beta$, while for hexagonal crystals there are 12 elements $\mathbf{S}_j^\alpha$. The rotation $\mathbf{D}$ describes the orientation relationship between the two phases (Burgers 1934), which can conveniently be expressed using Euler angles or an orientation matrix (Humbert 1995):

$$\mathbf{D} \equiv \left(135^\circ, 90^\circ, 354.74^\circ\right) \qquad \text{Equation 7.2}$$

$$\mathbf{D} = \begin{bmatrix} -\dfrac{1}{2}\left(1+\dfrac{1}{\sqrt{6}}\right) & \dfrac{1}{2}\left(\dfrac{1}{\sqrt{3}}-\dfrac{1}{\sqrt{2}}\right) & \dfrac{1}{\sqrt{2}} \\ \dfrac{1}{2}\left(1+\dfrac{1}{\sqrt{6}}\right) & -\dfrac{1}{2}\left(\dfrac{1}{\sqrt{3}}-\dfrac{1}{\sqrt{2}}\right) & \dfrac{1}{\sqrt{2}} \\ -\dfrac{1}{2}\left(1-\dfrac{1}{\sqrt{6}}\right) & \dfrac{1}{2}\left(\dfrac{1}{\sqrt{3}}+\dfrac{1}{\sqrt{2}}\right) & 0 \end{bmatrix} \qquad \text{Equation 7.3}$$

These expressions were used to calculate the expected orientation variants from the main texture components observed for the α→β and β→α phase transformations. In

addition to these individual orientation calculations, the expected textures assuming total absence of variant selection from experimental macrotexture data were calculated. The calculation was carried out by applying the Burgers orientation relationship as a rotation in the form of Euler angles, using the spherical harmonics method (Bunge 1982) as implemented in TEXTAN III (Bate 1990), calculating the coefficients of the new texture from those of the initial texture. A portion of these results was published in (Romero *et al.* 2009).

One of the key advantages of the SXRD experiment presented in Chapter 4 is that it provided information about the texture evolution *during* the $\alpha \rightarrow \beta$ phase transformation, and very importantly, it provided experimental data of the β texture immediately after this phase transformation is complete, i.e. before any significant β grain growth. Figure 7.1 compares sections of experimental β ODFs obtained from high temperature data, with those calculated from the α recrystallization texture assuming total absence of variant selection during the $\alpha \rightarrow \beta$ phase transformation. The sections shown ($\gamma=0°$ and $\gamma=45°$) contain most of the important orientations describing the complete ODF. Table 7.1 lists the main texture components observed. As mentioned before, the β texture is dominated by two components: g_A^β (~65%) and g_B^β (~35%). The similarities in texture components, distribution and intensity between the experimental and calculated ODFs suggest that during the $\alpha \rightarrow \beta$ phase transformation there is very little (almost negligible considering measurement errors) variant selection.
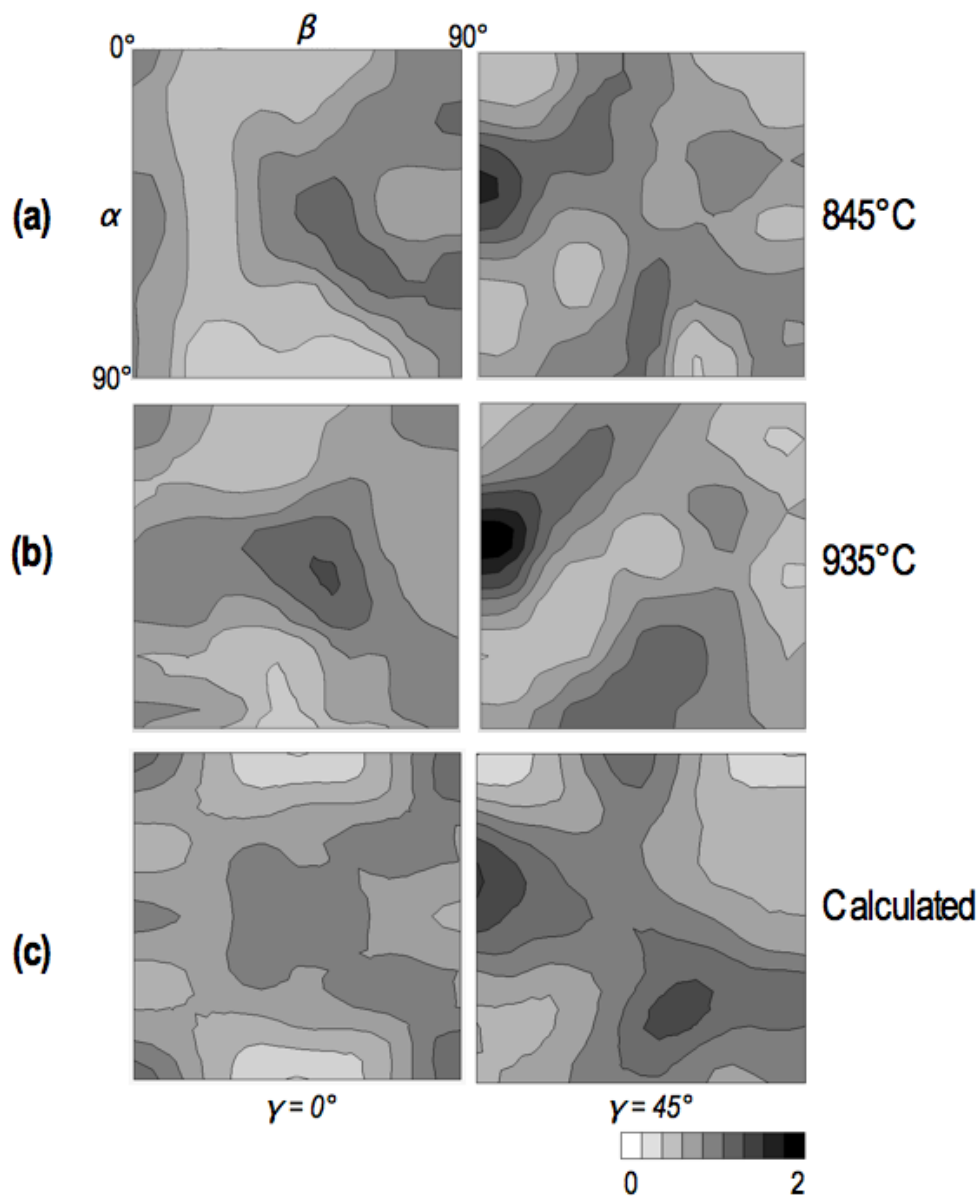
Figure 7.1 Comparison of ODF sections of the β-phase: experimental at (a) 845°C (~54% β) and (b) 935°C (~98% β), and (c) calculated without variant selection from α recrystallization texture at 795°C.

The apparent absence of variant selection during the α→β phase transformation was confirmed by means of individual orientation calculations. All the six β orientation variants that can be produced from the dominant texture component of the α recrystallization texture (g_1^α) were calculated using a strict Burgers orientation relationship. Due to the superposition caused by orthorhombic sample symmetry only

three independent β variants can be distinguished, two of these variants are close to g_A^β

and the other one is close to g_B^β. This explains why g_A^β dominates the high temperature β

phase with a ratio of ~2:1 with respect to g_B^β. The three independent β orientations

contribute equally to form a texture very similar to that observed experimentally at

935°C, when the α→β transformation is finishing.

Table 7.1 Main texture components observed during β-quenching of cold-rolled Zircaloy-2

Component	Euler Angles ($\square$)		
	α	β	γ
g_1^α	90	30	30
g_2^α	90	90	30
g_3^α	0	60	0
g_4^α	30	70	20
g_A^β	0	35	135
g_B^β	0	0	0

Although the texture measured at the end of the α→β phase transformation is not

particularly strong, during this transformation the β texture showed signs of

strengthening, suggesting preferential growth of variants that nucleated following the

orientation relationship. On the other hand, the α texture did not show significant

changes during the process, which contradicts the work of some authors (Wenk *et al.*

2004, Lonardelli *et al.* 2007), who claim that certain orientations in the α phase

transform preferentially.

The β texture obtained in this project at 935°C is very similar to that obtained by Wenk

et al. (Wenk *et al.* 2004) using neutron diffraction. The morphology and intensities of

the pole figures are similar (see section 4.2.3). They carried out in-situ texture measurements on cubes of Zircaloy-4 at various different temperatures. The maximum temperature reached in their experiment was 950°C. At that temperature, presence of residual α phase (5-10%) was observed, so although at this point the transformation was at an advanced stage, it was still incomplete. They fitted their experimental β texture by preferentially transforming one of the main texture components of their starting α texture, the recrystallization component, as well as applying some manual selection of variants. It was suggested that the observed β texture could be explained as preferential transformation of texture components that appear during recrystallization, combined with symmetry variant selection. The orientations that dominate the β texture due to preferential transformation are presumed to originate in α grains that are highly deformed, and exhibit heterogeneous microstructure. In this project, however, the experimental β texture at the end of the α→β phase transformation was obtained from the recrystallization texture without applying any modelled variant selection.

More recently Lonardelli et al. (Lonardelli *et al.* 2007) used neutron diffraction to carry out in-situ texture measurements in CP titanium. This time the texture was measured at two points during the α→β transformation: at 900°C when the volume fraction of the two phases was ~50%, and at 950°C when no diffraction from the α phase was detected and the transformation was complete. The first significant finding reported was a decrease in the α $\left(11\bar{2}0\right)$ pole intensity at the intermediate point with respect to that before the transformation. This was associated with the preferential transformation of

grains developed during recrystallization and grain growth, agreeing with the hypothesis of Wenk et al.. At this intermediate point the main components of the β texture are similar to g_A^β and g_B^β found here, but with g_A^β dominating. At 950°C when the transformation is complete, the relative volume fraction of these two β texture components was more even, the pole maxima look sharper, and the best simulation of the β texture was obtained from the α grain growth component (g_1^α), but with equal contribution of all the possible β variants (i.e. without variant selection). The β texture changes from 900 to 950°C were attributed to competitive growth between the β orientations.

The in-situ SXRD experiments presented in Chapter 4 provided the evolution of the texture components during the α→β phase transformation with several points during the process. There was no evidence of preferential transformation of α texture components, the recrystallization texture remained practically constant during the phase transformation, even to the point when the volume fraction of untransformed α phase was below 10%. On the other hand, the sharpening of the β texture components was indeed observed, which supports the mechanism of competitive growth between grain boundary and intragranular β observed by Seward et al. (Seward *et al.* 2004) during in-situ SEM on CP titanium, advocated as well by Lonardelli et al.. Figure 7.2 illustrates this mechanism schematically. At the beginning of the α→β transformation, the β nuclei are more or less random. Subsequently the grain boundary β allotriomorphs

dominate the growth process due to their faster moving interfaces, especially towards the end of the transformation.
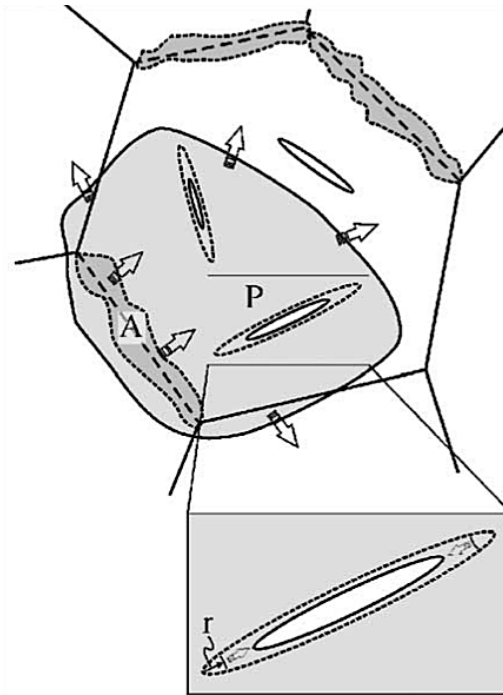
Figure 7.2 Competitive growth between β intragranular plates and grain boundary allotriomorphs
(Seward *et al.* 2004)

7.2   VARIANT SELECTION DURING BETA GRAIN GROWTH

The in-situ SXRD experiment showed evidence of fast grain growth of the β-phase once the α→β phase transformation is complete. Once the β-transus is exceeded, the diffraction patterns show only few spots after small increases in temperature and/or small dwell times. In CP titanium it has been reported that the β grain growth rate is at least an order of magnitude higher than that of the α phase for comparable grain size (Seward *et al.* 2004). This section will discuss the texture evolution in the β-phase during considerable β grain growth, which excludes heat treatments with peak

temperatures nearing the β-transus. These heat treatments exhibited texture memory associated with strong variant selection during cooling, which will be discussed in the next section.

Although during the in-situ SXRD experiment it was not possible to follow the evolution of the β texture during grain growth, the β maps reconstructed from inherited α EBSD data provided information of the β texture before the beginning of the β→α transformation, i.e. after the β grains have grown, either by increased temperature or dwell time above the β transus. All the reconstructed β maps showed stronger texture than that obtained in-situ at the end of the α→β transformation, which indicates that the mechanisms leading to variant selection in the β phase act after the α→β transformation is complete. Therefore, grain growth plays a significant role in modifying the β texture.

Although in-situ data of the evolution of the β texture after the β transus is exceeded could not be obtained, the results of the furnace heat treatments reported in Chapter 6 suggest that the β texture does change during grain growth. In the absence of an external stress, the β texture components g_A^β and g_B^β strengthen as the peak temperature is increased, and in general the β texture developed is extremely sharp. This suggests a phenomenon of preferential growth. Apparently, grains belonging to the main texture components grow faster at expense of those that had orientations far from these main orientation variants. In addition, not all of the Burgers orientation variants would grow at the same rate, resulting in selection during β grain growth.

7.3   VARIANT SELECTION DURING THE BETA TO ALPHA TRANSFORMATION

Figure 7.3 compares sections of α ODFs obtained from SXRD images with those calculated from the experimental β texture obtained at 945°C assuming absence of variant selection during the β→α phase transformation (similar type of calculation as in section 7.1, but using the inverse orientation relationship). After cooling, the experimentally measured α texture, shown in Figure 7.3(b), is substantially different from that calculated, which indicates that mechanisms responsible of variant selection do occur after the α→β transformation is finished, this is either during β grain growth and/or during cooling. In the in-situ SXRD experiment presented in Chapter 4, it was pointed out that upon cooling the initial fractions of α show all the features of the final texture, suggesting that any selection of α variants has occurred already at this point, probably during α nucleation.

The twelve α orientation variants that can be produced by each of the two dominant texture components of the β texture (g_A^β and g_B^β) were calculated using the Burgers orientation relationship. Due to the superposition of variants caused by orthorhombic sample symmetry, the number of independent ODF components is reduced. Table 7.2 lists the number of α orientation variants (calculated from the two main β texture components), which are close (within a radius of 5°) to the main α texture components. According this distribution, even in the absence of variant selection, it is clear that sample symmetry produces uneven intensities of α texture components. Components

g_1^α and g_2^α are respectively the most and least favoured during the β→α phase transformation. However, according to experimental results, components g_3^α and g_4^α are the ones exhibiting less intensity, indicating the presence of orientation variant selection.
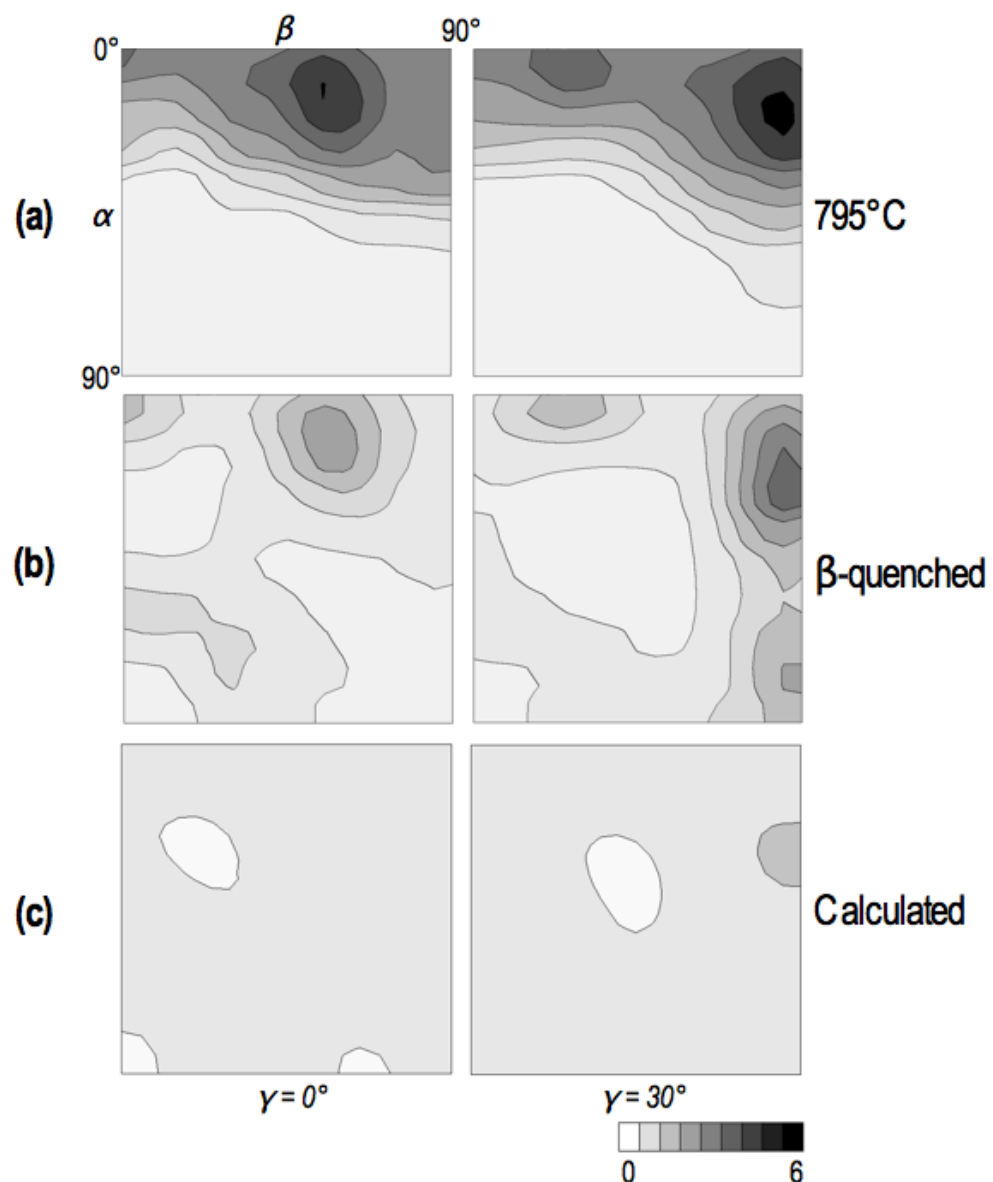
Figure 7.3 Comparison of ODF sections of the α-phase: (a) experimental at 795°C before the α→β phase transformation (for reference), (b) experimental at room temperature after β-quenching, and (c) calculated without variant selection from experimental β texture at 945°C.

Table 7.2 Distribution of calculated inherited α orientation variants without variant selection.

	g_A^β ~65%	g_B^β ~35%
g_1^α	4	4
g_2^α	2	0
g_3^α	2	4
g_4^α	2	4

Different degrees of variant selection have been observed in this project, leading to diverse changes in the texture:

·   Extremely strong variant selection in stress-free β-quenching with peak temperatures nearing the β-transus, leading to perfect texture memory despite dramatic changes in the microstructure.

·   Strong variant selection in stress-free β-quenching with very high peak temperatures (above 1100°C), leading to creation of new but very strong texture components.

·   Moderate variant selection in stress-free complete β-quenching with medium-range peak temperatures (950-1100°C), leading to texture weakening, i.e. creation of new texture components at expense of the intensities of those components present before the phase transformation.

The evidence presented in this project has demonstrated that the mechanisms leading to variant selection act mainly during grain growth in the β-phase, and/or during cooling. The phenomenon of orientation variant selection during the phase transformation on cooling has also been seen in other systems such as titanium alloys (β→α) and austenite to ferrite (γ→α) in steels. For example, strong variant selection leading to texture

memory or texture strengthening has been reported in manganese alloyed IF steel, while lower degrees of variant selection have been seen in plain low carbon of conventional IF steels (Yoshinaga *et al.* 2007, Wenk *et al.* 2007).

Several possible causes of variant selection have been suggested in the literature, which have been extensively reviewed in (Hutchinson *et al.* 2005, Hutchinson and Kestens 2008). The following paragraphs will try firstly to group and list the different principles proposed, and then confront them with the evidence presented so far. The mechanisms proposed to explain variant selection are diverse. However, according to the principles suggested, they can be classified as follows:

1. Stresses generated by volume contraction on heating, or other residual stresses, survive recovery in the high-temperature phase and are retained. These stresses bias the transformation behaviour on cooling (Yoshinaga et al. 1994).

2. Residual dislocations and other crystal defects in a deformed high-temperature phase determine the nucleation of certain variants (Furuhara and Maki 2001).

3. Specific grain boundaries are created in the high temperature phase, having characteristics that favour nucleation of certain orientation variants. A boundary between two adjacent parent grains with characteristics such that nucleation or growth is favourable into both, will strengthen that specific orientation variant (Stanford and Bate 2004, Bhattacharyya et al. 2007).

4. Precipitates retained at high temperature act as special nucleation sites. In steels it has been postulated that thin rims of ferrite might be stabilised around precipitates, acting as nuclei with the original orientations (Ryde et al. 1999).

5. The grain shape of the high temperature phase, for instance if it is deformed, favours the growth rate of certain variants (Butrón-Guillén et al. 1997).

6. Transformation-induced stresses modify the interaction between grains, leading to selection of variants. The effect of elastic anisotropy of the parent phase is accounted for in this group (Bate and Hutchinson 2000, Humbert and Gey 2003).

In steel, little evidence has been found for the first two mechanisms of the list above, related to stress and crystal defects in the high-temperature phase. They can be disregarded in zirconium and titanium alloys for similar reasons: any residual stresses, or other stresses generated during heating will be relieved by plastic deformation in the extremely soft and fully recrystallized β phase. One experiment here indicated that the β-phase flow stress was below 10MPa. The same would occur with residual dislocations or crystal defects. As for the remaining four mechanisms, some evidence supporting them has been observed in this project under specific conditions.

7.3.1   VARIANT SELECTION WHEN THE α→β TRANSFORMATION IS COMPLETE

The in-situ SXRD experiment presented in Chapter 4 provided evidence that, regardless of the maximum temperature, the initial fractions of α developed during cooling show already the main characteristics of the final texture. Although it was observed that one of the main α texture components (g_2^α) is underestimated in the SXRD measurements, the α texture appears not to change significantly during the β→α transformation. This indicates that the α orientation variants are probably selected during the nucleation stage.

During the β→α phase transformation there are two possible nucleation sites: within the β grains or at β/β grain boundaries. The transformation can occur with a combination of both, but it is known that for titanium and zirconium alloys the beginning of the β→α transformation is dominated by the formation of grain boundary α (Lütjering and Williams 2003, Banerjee and Mukhopadhyay 2007). Once the grain boundary α is formed, the interior of the grain is not significantly affected by adjacent β grains, thus one can assume that the dominating phenomenon in the selection of variants is the nucleation of α at the β/β grain boundaries.

The grain boundary α nuclei need a low energy interface with at least one of the adjacent β grains, meaning that the orientation relationship is fulfilled with at least one of them. The relationship is usually not very strict, and the orientation of the grain boundary α is normally a compromise between the orientation relationships with the two adjacent β grains. However, nucleation would be strongly favoured if the β/β grain boundary is such that the nucleus can meet the orientation relationship with both β grains, i.e. having a low energy interface on both sides. This favoured nucleus is prone to grow into the two β grains with minimal changes in orientation (see mechanism number 3 in the list above). In this project, when the α→β transformation is complete, numerous examples of this mechanism are seen in EBSD maps, where there is a clear β/β grain boundary but the α colonies at both sides have practically the same crystallographic orientation. This would, to certain extent, explain the moderate variant selection observed.

Variant selection in diffusional transformation in hcp metals has been attributed widely to a local mechanism: preferential α nucleation between β grains having a common (110) direction. Many researchers have noticed this coincidence and the subsequent nucleation of α variants with the $\vec{c}$ axis parallel to the common (110) direction, preferring it to the other five (Gey and Humbert 2003, Stanford and Bate 2004, Bhattacharyya *et al.* 2007). The evolution of these particular α variants in these special β/β grain boundaries has been attributed to local anisotropy imposed by the β grains (Humbert *et al.* 2006) and minimisation of interfacial energy (Bhattacharyya *et al.* 2007). Sometimes α variants sharing the $\vec{c}$ axis have only a misorientation of 10.5°, and are called 'twin sisters'. According to calculations based on minimisation of elastic energy in isotropic conditions (Barberis, 2005), these twin sisters are not energetically favoured, and the special β/β condition is necessary for them to exist. The maximum angle between (110) directions at which this mechanism develops is ~10°, no local variant selection has been observed when the alignment of the directions exceeds this angle (Stanford and Bate 2004).

The question is how do these particular β/β grain boundaries develop and how often. It has been proposed that they arise naturally during the $\alpha \rightarrow \beta$ phase transformation. By careful examination of EBSD β data published in the literature, Cayron (Cayron 2008) also established that in titanium the adjacent β grains sharing a (110) pole are actually β variants inherited from the $\alpha \rightarrow \beta$ transition, even despite the presence of retained β before the heat treatment. It has also been found that two special misorientations occur

frequently in adjacent β grains and lead to α variants with very close orientations and very different growing directions: a rotation of 10.5° around a $\langle 110 \rangle$ direction and a rotation of 60° around a $\langle 111 \rangle$ direction (Bhattacharyya *et al.* 2007). The schematic shown in Figure 7.4, adapted from work carried out on variant selection in steel (Hutchinson and Kestens 2008), illustrates a theory of how these special β grain boundaries can be created when two β grains fulfil the Burgers orientation relationship with the same initial α grain.
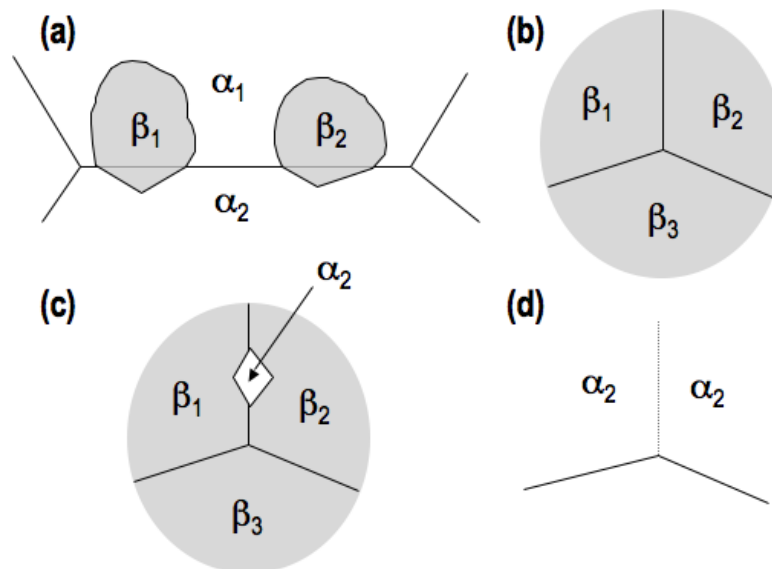
Figure 7.4 Schematic representation of the process of texture memory at β grain boundaries, adapted from (Hutchinson and Kestens 2008). (a) Two β grains nucleated in the same (or a similar) α grain boundary, meeting Burgers relationship with α_2. (b) β phase after transformation. (c) Favoured nucleation of α grain on cooling, meeting Burgers relationship with both β_1 and β_2. (d) Inherited structure after displacive growth, the orientation α_2 is restored.

Based on this hypothesis, the β grain boundary plane would be the dominant factor for the selection of variants during cooling. Here it has been shown that the orientation of the β grains is completely determined by the initial α texture, since variant selection during the α→β transformation is negligible. Therefore, it is very likely that the β grain

boundaries that are first created would subsequently nucleate α grains with similar orientations. That is to say, if the β grain boundary texture remains unchanged, the transformed texture will be identical or stronger than the original alpha texture. This is consistent with the effects of limited grain boundary mobility on the α→γ→α transformation in steel (Yoshinaga *et al.* 2007, Hutchinson and Kestens 2008). This would be one of the reasons why heat treatments with peak temperatures very close to the β-transus (even with absence of α reflections in the diffraction patterns) resulted in perfect texture memory.

When a strong β texture is developed, for example by deformation in the β field or preferential β grain growth, the grain boundary variant selection mechanism discussed here would be exacerbated. Small misorientation between β grains, caused by a strong β texture, increases the occurrence of special β/β grain boundaries, which in turn would stimulate selection of α variants. This would explain not only the very strong inherited α textures obtained when strong plastic strain was applied to one of the in-situ tested samples (section 5.3.2), but also the strong α textures observed in furnace β-quenched at very high temperature (section 6.3).

7.3.2   VARIANT SELECTION WHEN THE α→β TRANSFORMATION IS INCOMPLETE

From the results of the synchrotron experiment, it is evident that the α→β phase transformation must be complete in order to modify the texture. The presence of untransformed α, often referred to as primary α or α_p, becomes an important source of

variant selection for two reasons: (1) it can act as a nucleation site (related to mechanism 4 in the list above), and (2) it inhibits β grain growth.

Variant selection at α_p is a relatively simple mechanism. At low cooling rates, and if the untransformed α_p follows the Burgers relationship with its β vicinity, secondary α variants will grow from the untransformed α. This mechanism has been seen repeatedly in titanium billets, where large zones with very close crystallographic orientations are observed after treatment in the α+β field. Humbert et al. (Humbert *et al.* 2006) found that although only 10% of the α_p/β obey the Burgers relationship, in 80% of the cases the secondary α had an orientation very close to that of the untransformed α_p. This means that the large texture heterogeneities, so-called macrozones, are caused by closely aligned α_p grains, which are further strengthened by secondary α variants.

When cooling from the α+β field, the pre-existence of α modifies the transformation. Semiatin et al. (Semiatin *et al.* 2003) carried out work on Ti-6Al-4V, leaving 27% of volume of α remaining and used different cooling rates and undercooling temperatures. At very low cooling rates ($<0.5Cs^{-1}$), the new α phase grows epitaxially from the pre-existing α. At higher cooling rates ($>3.5Cs^{-1}$), the inherited microstructure changes dramatically. As the undercooling temperature is reduced, there is less epitaxial growth from the pre-existing α and more nucleation occurs in the β grain boundaries. These observations and diffusion-based modelling led to the conclusion that slow cooling initially leads to growth of the untransformed α grains, but a certain cooling rate there is

a transition towards the formation of Widmanstätten microstructure. In Zircaloy-2 the identification of α_p is difficult, but its presence and role in texture memory cannot be discarded. The second potential role of α_p as a source of variant selection, i.e. as inhibitor of β grain growth, will be discussed in the following section.

7.3.3 EFFECT OF β GRAIN GROWTH ON VARIANT SELECTION DURING THE $\beta \rightarrow \alpha$ PHASE TRANSFORMATION

The relatively fast cooling rates applied in the present project, in combination with the very low volume fractions of α just below the β transus, make it unlikely that retained α_p traces can solely explain the perfect memory effect at peak temperatures near the β-transus. Therefore, an additional mechanism is likely to be present, this is the restricted change of grain boundary texture, stimulating the β/β grain boundary variant selection. Once the β-transus is well exceeded, the transformation texture is weakened since the retained α nuclei are no longer available and the grain boundary texture has changed, reducing the probability of selection of variants at special β/β grain boundaries.

The β-grain boundary texture hypothesis is also consistent with the texture components observed following transformation. Although it is likely that some of the grain boundaries will change character during β grain growth, some will not. It is therefore unsurprising that the main texture components before the transformation are still present in the transformed texture, alongside the new components that have been developed. Some authors report texture memory without taking into consideration the new texture

components developed during a complete α→β→α transformation. For example Lonardelli et al. in CP titanium (Lonardelli *et al.* 2007).

As the peak temperature for β-quenching is increased above the β-transus, it has been observed here that the main β texture components are strengthened. This strengthening can be solely related to preferential growth of favourably oriented β grains. Stored energy created during the α→β phase transformation is a possible explanation for this preferential growth. With large β grains with selected orientation, variant selection on cooling during the α→β phase transformation is stimulated due to several reasons: reduced number of nucleation sites caused by less grain boundary area and the absence of high temperature precipitates (C and Si); increased variant selection at special β/β grain boundaries; and accelerated growth of α variants that are favourable oriented to minimise transformation stress in the parent β grain. The latter is the remaining variant selection mechanism that has not been discussed (number 6 in the list at the beginning of the chapter): transformation-induced stresses that modify the interaction between grains. Evidence of this variant selection mechanism has been found in other systems, and models have been proposed (Bate and Hutchinson 2000, Humbert *et al.* 2005, Barberis *et al.* 2005). These models are based in minimisation of energy as a criterion of selection of variants. The effect of elastic anisotropy of the parent phase is determinant in these calculations. This effect is likely to be responsible for the appearance and selection of the component g_2^α, as evidenced by the propagation of this variant parallel

to its *c* axis in samples β-quenched at very high temperature, as well as its reduced intensity in samples β-quenched under stress.

7.4 SUMMARY

This final chapter has discussed the main findings of this project, in the context of the work on crystallographic variant selection during phase transformations in zirconium, titanium and steel. The discussion was presented in three sections: variant selection on heating during the α→β phase transformation, variant selection during β grain growth (when present), and variant selection on cooling during the reverse β→α transformation.

During the α→β transformation there are indications of slight strengthening of the β texture due to competitive growth, dominated by β variants that follow the Burgers orientation relationship. No preferential transformation of α texture components was observed. Using crystallographic modelling it was demonstrated that during the α→β transformation the selection of β variants is almost negligible. Due to the orthorhombic sample symmetry present, the β texture observed experimentally results from the combination of few independent β variants, produced from selection-free transformation of the α recrystallization texture.

The β texture obtained in-situ at the end of the α→β phase transformation (using SXRD) is significantly weaker than the β texture obtained from reconstructed EBSD

maps of the inherited α-phase, i.e. before the β→α phase transformation. This indicates preferential growth of certain crystallographic orientations in the β-phase, dominated by grains that follow a strict Burgers orientation relationship. In addition, changes in the β texture caused by plastic deformation modify the inherited α texture. It was observed that strong β textures, caused by β grain growth or by plastic deformation, derived in strong inherited α textures.

Crystallographic modelling of the β→α phase transformation showed evidence of variant selection. Upon cooling, the initial fractions of α-phase show all the features of the final texture, and subsequently the α texture does not change significantly. This suggests that the mechanisms leading to variant selection act mainly during α nucleation, and most likely during α nucleation at α_p/β or β/β grain boundaries. If the α→β transformation is incomplete, α_p traces can act as nucleation sites and/or as inhibitors of β grain growth. Growth of α variants from α_p will produce secondary α with texture memory. Limited β grain growth will also produce texture memory, due to restricted change of the β grain boundary texture, which in turn leaves a number of special β/β grain boundaries where α variants similar to those present before the phase transformation will be nucleated (g_1^α). Transformation-induced stresses are an additional mechanism of variant selection likely to be present, evidenced by the selection of one α variant (g_2^α) that propagates parallel to its *c* axis. The occurrence and effect of these different variant selection mechanisms depend on the peak temperature,

and the texture of the β-phase. The combination of these mechanisms leads to the

different changes in texture observed in this project.

CONCLUSIONS

The development and evolution of crystallographic texture during β-quenching of cold-rolled sheets of a zirconium alloy has been studied. In this investigation, the aim was to gain understanding on the mechanisms involved on texture development and evolution during the α→β→α phase transformation undergone by the material during this process, as well as exploring optimum processing parameters towards a randomised crystallographic texture, minimising anisotropy and improving the performance of zirconium components in nuclear reactors. Some of the results can be transferred to other systems such as titanium alloys and steel.

An extensive and critical literature review summarised the theoretical basis necessary to understand the subsequent results. This review included basic concepts of texture and anisotropy, physical metallurgy of zirconium and its alloys, and an account of the behaviour of zirconium alloys during operation in a nuclear reactor. The investigation of texture evolution was carried out in different stages and with different strategies. Initially industrially β-quenched samples were characterised using laboratory X-ray

diffraction (LXRD), electron backscatter diffraction (EBSD) and optical microscopy. Subsequently the texture during the $\alpha \rightarrow \beta \rightarrow \alpha$ phase transformation was studied in-situ using synchrotron X-ray diffraction (SXRD), which was complemented by detailed post-mortem characterisation using EBSD. After that, samples β-quenched in laboratory furnaces using a wide range of peak temperatures were analysed. Finally, a comprehensive discussion on variant selection during β-quenching was presented.

The following sections will present the conclusions drawn from this study. The questions that need further investigation and insights on future research are outlined in the final section.

CHARACTERISATION TECHNIQUES

One of the most important contributions of this work is the step forward taken in the development of SXRD as a texture measurement technique. The experimental setup employed allowed measuring texture during fast structural changes, at high temperature and with the presence of multiple phases. Furthermore, the spatial resolution provided by SXRD allowed the detection of sharp texture changes across temperature gradients. It was demonstrated that the results obtained using SXRD are reliable compared to those obtained using well-established techniques such as LXRD and EBSD. However, when designing a synchrotron experiment, the geometry of the sample and the texture components must be taken into account, since certain orientations are significantly underestimated. To overcome this problem, it is recommended that the in-situ tests be

repeated for different sample orientations. The diffraction images acquired at the same temperature could be combined to obtain more complete texture information. The other limitation of the experimental setup employed in the in-situ SXRD experiment is the uncertainty of the temperature/stress associated to each diffraction image. For this reason, the values obtained must be treated carefully.

Despite the fact that in LXRD the tilting of the sample does not allow measuring the outer intensities in experimental pole figures, it was found that the results are practically identical to those obtained using EBSD. Numerous measurements of global texture were carried out in this work using both techniques, finding a significant agreement in the texture components observed both in morphology and in intensity. This leaves the possibility of using either of these techniques, making a decision based not on the reliability of the results, but on other aspects such as sample size, sample preparation, equipment availability, etc. In this work, the benefit of using more than one technique to characterise the same phenomenon has been proved, exploiting the advantages of each method.

TEXTURE EVOLUTION DURING β-QUENCHING

The most important difference between most zirconium alloys and other similar materials such as titanium alloys is the fact that no β phase is retained at room temperature. The evolution of texture without retention of the high-temperature β phase

appears to differ significantly with respect to that observed when β phase is present at the start of the process.

The initial rolling texture observed after cold rolling Zircaloy-2 sheets to the final thickness is modified by β-quenching. This occurs in two steps: first by recrystallization when the material exceeds 620°C, and subsequently by the phase transformation, above 940°C, which weakens the initial texture and creates new orientation components.

A possible mechanism of competitive growth between intragranular β and grain boundary β allotriomorphs, dominated by the latter, was indicated by slight strengthening of the β texture components during the α→β transformation. It was demonstrated that during the α→β transformation the selection of variants is practically negligible, and no signs of α preferential transformation were observed. This means that the mechanisms leading to variant selection occur after this point. Upon cooling, the initial α grains show the features of the final texture, meaning that the mechanisms leading to variant selection occur mainly during β grain growth and/or during early stages on cooling.

The final texture is strongly influenced by the peak temperature, which is one of the most critical parameters during β-quenching. Incomplete transformations, those were the β-transus was not completely exceeded, exhibit perfect texture memory. The inherited texture is identical to the texture observed before the transformation, i.e. the recrystallization texture. This is attributed to the presence of untransformed α, which

stimulates two mechanisms of variant selection: (1) variant selection at the boundaries of untransformed α, and (2) variant selection at the β/β grain boundaries probably caused by insufficient β grain growth.

As the peak temperature is increased beyond the β-transus, the risk of texture memory is eliminated, but other effects may be detrimental for the final texture. The total dissolution of surviving precipitates and the growth of the β grains reduces significantly the availability of nucleation sites, which statistically diminishes the probability of precipitating diverse orientation variants. Additionally, the growth of β orientations above the β transus is preferential, which results in strong β texture components at very high temperature. The combination of these phenomena results in an inherited α texture exhibiting extremely strong components.

The effect of stress and plastic deformation was also studied. The presence of moderate tensile stress during the β→α phase transformation reduces the intensity of a particular texture component, probably due to the orientation of the transformation strains with respect to the applied stress. The effect of stress is significant for the global texture only if it causes plastic deformation in the β-phase. Extreme plastic deformation in the β-phase completely modifies the β texture and the inherited α texture; while moderate levels of plastic deformation can produce β and α textures very close to random.

TEXTURE MEMORY AND VARIANT SELECTION

In this work, different degrees of the phenomenon referred to in the literature as 'texture memory' have been observed, thus it is necessary to define this concept more precisely. In this project, this term has been applied only to cases where the texture after the heat treatment is identical to the starting texture, both in morphology and in intensity, within the margin of error of the technique employed. In this work, this was observed only when the peak temperature of the β heat treatment was below the β transus. There are other types of texture change that can occur during thermomechanical processing, which can be listed as follows:

1. Texture randomisation: the initial texture is eliminated and the inherited texture is random, i.e. there are no discernible texture components. This was observed if the β-transus was exceeded in combination with moderate plastic deformation in the β-phase.

2. Texture weakening: the texture components observed before the transformation are observed with diminished intensity and new orientations appear. This was observed in most of the fully β-quenched samples.

3. Texture strengthening: this type of texture change can be observed in two cases. The first when the initial texture components are replicated in the transformed textures but exhibit increased intensity, and the second where there are new texture components but the texture is stronger than the initial one. The latter was observed in samples β-quenched at very high temperature.

The results demonstrate that the phenomenon of selection of crystallographic orientation variants must be analysed globally and locally, because local relationships between β grains play a key role for nucleation and growth of α variants. Statistical

analysis of macrotexture evolution requires evaluation of the local variant selection mechanisms by measuring microtexture.

From the number of mechanisms proposed in the literature, variant selection at β/β grain boundaries sharing a common (110) pole is one that explains some of the results presented in this work. This mechanism is strongly related to the grain boundary texture, thus it is affected by changes in β grain size and shape. There were also indications of the influence of transformation-induced strain during the β→α transformation. The inherited α textures observed are probably influenced by a combination of these mechanisms.

INDUSTRIAL SHEET BETA-QUENCHING

Considering the industrial application of the β-quenching process, this work has demonstrated that one critical aspect during the heat treatment of the sheet material for channels of BWR fuel assemblies is the peak temperature. In order to weaken the rolling texture obtained after cold rolling, it is essential to exceed the β-transus. On the other hand, excessive peak temperature results in undesirable β grain growth and strong α texture components. This is also detrimental for the desired isotropy of the material. The range of temperature recommended for β-quenching of channel sheet material is narrow, between 950 and 1050°C. Plastic deformation in the β-phase contributes to further randomization of the texture. Plastic deformation in the range of 20 to 30% along the rolling direction was demonstrated to produce practically random α texture.

FURTHER WORK

During this research, many questions in need of further investigation have arisen Therefore, it is recommended that further research be undertaken in the following areas:

- In-situ characterisation of texture evolution of the β phase above the β transus. The evolution of the β texture at temperatures above the β transus will complete the results presented in this work. Neutron diffraction is the only technique capable of carrying out this kind of study with statistical reliability. An upcoming experiment at the general materials diffractometer (GEM) at the ISIS facility pulsed neutron source will cover these tests.

- In order to evaluate the effect of stresses during the phase transformation more systematically, additional in-situ and ex-situ experiments should be carried out. Accurate measurements of stress/strain are required, and stress can be applied at different stages of the $\alpha \rightarrow \beta \rightarrow \alpha$ phase transformation. Detailed study of the mechanical properties of the β-phase is required for this purpose. Modelling of the necessary plastic deformation in the β-phase to randomize the texture would complement this work.

- In-situ EBSD should be tried in zirconium alloys. Current devices can take small samples up to 1000°C, which would be enough to study the nucleation and growth during the $\alpha \rightarrow \beta$ and $\beta \rightarrow \alpha$ transformations. In-situ confocal microscopy is a possibility to study the evolution of the microstructure.

· The effect of different levels of prior cold working has not been studied in this project. In CP titanium it has been reported that increased cold work strengthens the β texture (Gey and Humbert 2002), which in turn influences the inherited α texture. Therefore, a systematic study on the effect of stored energy on the texture evolution of zirconium alloys is worthwhile.

· A detailed quantitative analysis of the effect of the observed mechanisms of variant selection is required. A strategy to quantify the extent of β/β grain boundary variant selection is a natural step forward from the results obtained here. Automatic mapping and quantification of special β/β grain boundaries would be of great interest for all the researchers interested in variant selection.

· The nucleation of orientation variants in the α→β and β→α phase transformations may depend on the thermal rates applied. Therefore, a systematic study of the effect of heating/cooling rates on the texture evolution is desirable. This can be complemented with a study on the effect of multiple β-quenching cycles

· The amount of information that can be extracted from 2D diffraction images is vast. In this work, only the main findings regarding texture were reported. Analyses of thermal expansion, deformation mechanisms and volume fraction can be carried out with the data acquired.

· The difference in texture between the surface and the middle of cold-rolled and β-quenched Zircaloy-2 sheets was not investigated further. Progressive

EBSD/LXRD removing layers of material would be an alternative to study this phenomenon.

· Extensive crystallographic modelling of variant selection with the experimental data acquired here should be carried out. The effect of individual orientation variants should be assessed in order to probe the different criteria/mechanisms of variant selection.

· A systematic study of the reliability and error of texture measurements using SXRD is important to develop the technique. This should include the effect of geometry, grain size and texture strength.

Apart from the fundamental work suggested above, investigations could be carried out in order to optimise engineering processing parameters:

· During this work, it was clear that an accurate measurement of the temperature reached by the material during heat treatment is critical. The temperature measurement devices employed here can be improved. A study of the temperature distribution along Zircaloy-2 samples heat-treated in an ETMT is recommended, perhaps using multiple thermocouples or thermal imaging.

· Trials of β-quenching under stress in the continuous furnace. Different coiling speeds can be tried in the continuous furnace, coupled with systematic measurements of strain and texture in the sheets. This can provide optimum parameters for texture randomisation.

REFERENCES

Altmann, S. L. (1986) *Rotations, Quaternions and Double Groups,* Oxford, Clarendon Press.

Anderson, A. J., Thompson, R. B. and Cook, C. S. (1999) Ultrasonic Measurement of the Kearns Texture Factors in Zircaloy, Zirconium and Titanium. *Metallurgical and Materials Transactions A,* 30A, 1981-1988.

Balasubrahmanyam, V. V. and Prasad, Y. V. R. K. (2002) Deformation behaviour of beta titanium alloy Ti-10V-4.5Fe-1.5Al in hot upset forging. *Materials Science and Engineering,* A336, 150-158.

Banerjee, S. (2001) Nuclear Applications: Zirconium Alloys. In Jürgen-Buschow, K. H., Cahn, R. W., Flemings, M. C., Ilschner, B., Kramer, E. J., Mahajan, S. & Veyssière, P. (Eds.) *Encyclopedia of Materials: Science and Technology.* Elsevier Science Ltd.

Banerjee, S. and Mukhopadhyay, P. (2007) *Phase Transformations: Examples from Titanium and Zirconium Alloys,* Oxford, Elsevier.

Barberis, P., Montheillet, F. and Chauvy, C. (2005) Variant selection in Zr alloys: how many variants generated from one beta grain? *Solid State Phenomena,* 105, 133-138.

Bate, P. (1990) *TEXTAN III - A program for the analysis of crystallographic texture using harmonic series expansion.* Version 3.3.

Bate, P. and Hutchinson, B. (2000) The effect of elastic interaction between displacive transformation on textures in steels. *Acta Materialia,* 48, 3183-3192.

Bhattacharyya, D., Viswanathan, G. B., Denkenberger, R., Furrer, D. and Fraser, H. L. (2003) The role of crystallographic and geometrical relationships between α and β phases in an α/β titanium alloy. *Acta Materialia,* 51, 4679-4691.

Bhattacharyya, D., Viswanathan, G. B. and Fraser, H. L. (2007) Crystallographic and morphological relationships between β phase and the Widmanstätten and allotriomorphic α phase at special β grain boundaries in an α/β titanium alloy. *Acta Materialia,* 55, 6765-6778.

Bhattacharyya, D., Viswanathan, G. B., Vogel, S., Williams, D. J., Venkatesh, V. and Fraser, H. L. (2006) A study of the mechanism of α to β phase transformation by tracking texture evolution with temperature in Ti-6Al-4V using neutron diffraction. *Scripta Materialia,* 54, 231-236.

Bolz, R. E. and Tuve, G. L. (1973) *CRC Handbook of Tables for Applied Engineering Science,* Boca Raton, CRC Press.

Bozzolo, N., Gerspach, F., Sawina, G. and Wagner, F. (2007) Accuracy of orientation distribution function determination based on EBSD data - A case study of a recrystallized low alloy Zr sheet. *Journal of Microscopy,* 227, 275-283.

Bunge, H. J. (1982) *Texture Analysis in Materials Science,* London, Butterworths.

Burgers, W. G. (1934) On the Process of Transition of the Cubic-Body-Centered Modification into the Hexagonal-Close-Packed Modification of Zirconium. *Physica,* 1, 561-586.

Butrón-Guillén, M. P., da Costa Viana, C. S. and Jonas, J. J. (1997) A variant selection model for predicting the transformation texture of deformed austenite. *Metallurgical and Materials Transactions A,* 28A, 1755-1768.

Carpenter, G. J., Zee, R. H. and Rogerson, A. (1988) Irradiation Growth of Zirconium Single Crystals: A Review. *Journal of Nuclear Materials,* 159, 86-100.

Cayron, C. (2007) ARGPE: a computer program to automatically reconstruct the parent grains from electron backscatter diffraction data. *Journal of Applied Crystallography,* 40, 1183-1188.

Cayron, C. (2008) Importance of the α→β transformation in the variant selection mechanisms of thermomechanically processed titanium alloys. *Scripta Materialia,* 59, 570-573.

Cayron, C., Artaud, B. and Briottet, L. (2006) Recostruction of parent grains from EBSD data. *Materials Characterization,* 57, 386-401.

Ciurchea, D., Pop, A. V., Gheorghiu, C., Furtuna, I., Todica, M., Dinu, A. and Roth, M. (1996) Texture, morphology and deformation mechanisms in β-transformed Zircaloy-4. *Journal of Nuclear Materials,* 231, 83-91.

Comstock, R. J. (2006) ZIRLO Properties. (Personal Communication)

Dahlbäck, M. (2007) Qualification Report. (Personal Communication)

Dahlbäck, M., Limbäck, M., Hallstadius, L., Barberis, P., Bunel, G., Simonot, C., Andersson, T., Askeljung, P., Flygare, J., Lehtinen, B. and Massih, A. R. (2005) The Effect of Beta-Quenching in Final Dimension on the Irradiation Growth of Tubes and Channels. *Journal of ASTM International,* 2, 1-28.

Davies, P. S., Wynne, B. P. and Rainforth, W. M. (2007) Investigating microstructural evolution in the near-α alloy Timetal R834 using electron backscatter diffraction (EBSD). In Niinomi, M., Akiyama, S., Hagiwara, M., Ikeda, M. & Maruyama, K. (Eds.) *11th World Conference on Titanium (Ti-2007).* Kyoto, Japan, Japan Institute of Metals.

Davis, J. R. (1998) Zirconium and Hafnium. In Davis, J. R. (Ed.) *Metals Handbook - Desk Edition.* Materials Park, ASM International.

Donachie, M. J. (2000) *Titanium: a technical guide,* Materials Park, ASM International.

Fidleris, V. (1988) The Irradiation Creep and Growth Phenomena. *Journal of Nuclear Materials,* 159, 22-42.

Frank, F. C. (1988) Orientation Mapping. *Metallurgical and Materials Transactions A,* 19, 403-408.

Furuhara, T. and Maki, T. (2001) Variant selection in heterogenous nucleation on defects in diffusional phase transformation and precipitation. *Materials Science and Engineering,* A312, 145-154.

Garde, A. M. (2010) Mechanical Properties of Zircaloy-2 at High Temperature. (Personal Communication)

Garde, A. M., Chung, H. M. and Kassner, T. F. (1978) Micrograin superplasticity in Zircaloy at 850°C. *Acta Metallurgica,* 26, 153-166.

Gaunt, P. and Christian, J. W. (1959) The Crystallography of the Beta-Alpha Transformation in zirconium and in Two Titanium-Molybdenum Alloys. *Acta Metallurgica,* 7, 534-543.

Germain, L., Gey, N. and Humbert, M. (2007) Reliability of reconstructed β-orientation maps in titanium alloys. *Ultramicroscopy,* 107, 1129-1135.

Gey, N., Gautier, E., Humbert, M., Cerqueira, A., Bechade, J. L. and Archambault, P. (2002a) Study of the α/β phase transformation of Zy-4 in presence of applied stress at heating: analysis of the inherited microstructures and textures. *Journal of Nuclear Materials,* 302, 175-184.

Gey, N. and Humbert, M. (2002) Characterization of the variant selection occuring during the α→β→α phase transformations of a cold rolled titanium sheet. *Acta Materialia,* 50, 277-287.

Gey, N. and Humbert, M. (2003) Specific Analysis of EBSD Data to Study the Texture Inheritance due to the Beta-Alpha Phase Transformation. *Journal of Materials Science,* 38, 1289-1294.

Gey, N., Humbert, M., Gautier, E. and Bechade, J. L. (2002b) Analysis of the Beta-Alpha Variant Selection in a Zy-4 Rod by Means of Specific Crystal Orientation Maps. *Matrials Science Forum,* 408-412.

Glavicic, M. G., Kobryn, P. A., Bieler, T. R. and Semiatin, S. L. (2003a) A method to determine the orientation of the high-temperature beta phase from measured EBSD data for the low-temperature alpha phase in Ti-6Al-4V. *Materials Science and Engineering,* A346, 50-59.

Glavicic, M. G., Kobryn, P. A., Bieler, T. R. and Semiatin, S. L. (2003b) An Automated Method to Determine the Orientation of the High Temperature Beta Phase from Measured EBSD Data for the Low-Temperature Alpha-Phase in Ti-6Al-4V. *Materials Science and Engineering,* A351, 258-264.

Glavicic, M. G., Kobryn, P. A. and Semiatin, S. L. (2004) Validation of an automated EBSD method to deduce the β-phase texture in Ti-6Al-4V with a colony-α microstructure. *Materials Science and Engineering,* A385, 372-376.

Hammersley, A. P. (1998) FIT2D V9.129 Reference Manual V3.1. Grenoble, European Synchrotron Radiation Facility (ESRF).

Heidelbach, F., Riekel, C. and Wenk, H. R. (1999) Quantitative analysis of small domains with synchrotron radiation X-rays. *Journal of Applied Crystallography,* 32, 841-849.

Heinz, B. and Neumann, P. (1991) Representation of Orientation and Disorientation Data for Cubic, Hexagonal, Tetragonal and Orthorombic Crystals. *Acta Crystallographica,* A47, 780-789.

HKL Technology (2006) *Channel 5*. Version 5.0.9.0.

Holt, R. A. (1970) The beta to alpha phase transformation in Zircaloy-4. *Journal of Nuclear Materials,* 35, 322-334.

Holt, R. A. (1973) Comments on the beta to alpha phase transformation in Zircaloy-4. *Journal of Nuclear Materials,* 47, 262-264.

Holt, R. A. and Aldridge, S. A. (1985) Effect of Extrusion Variables on Crystallographic Texture of Zr-2.5 wt% Nb. *Journal of Nuclear Materials,* 135.

Holt, R. A. and Causey, A. R. (2004) Volume conservation during irradiation growth of Zr-2.5Nb. *Journal of Nuclear Materials,* 335, 529-533.

Hull, D. and Bacon, D. J. (2001) *Introduction to Dislocations,* Oxford, Butterworth-Heinemann.

Humbert, M. (1995) Determination of the Orientation of a Parent Beta Grain from the Orientations of the Inherited Alpha Plates in the Phase Transformation from Body-Centred Cubic to Hexagonal Close Packed. *Journal of Applied Crystallography,* 28, 571-576.

Humbert, M., Germain, L., Gey, N., Bocher, P. and Jahazi, M. (2006) Study of the variant selection in sharp textured regions of bimodal IMI 834 billet. *Materials Science and Engineering A,* 430, 157-164.

Humbert, M. and Gey, N. (2002) The Calculation of a Parent Grain Orientation from Inherited Variants for Approximate (BCC-HCP) Orientation Relations. *Journal of Applied Crystallography,* 35, 401-405.

Humbert, M. and Gey, N. (2003) Elasticity-Based Model of the Variant Selection Observed in the Beta to Alpha Phase Transformation of a Zircaloy-4 Sample. *Acta Materialia,* 51, 4783-4790.

Humbert, M., Gey, N. and Germain, L. (2005) Study and modelling of some variant selections in BCC to HCP phase transformations. *Materials Science Forum,* 495-497, 1111-1120.

Humbert, M., Gey, N., Muller, J. and Esling, C. (1996) Determination of a Mean Orientation from a Cloud of Orientations. Application to Electron Back-Scattering Pattern Measurements. *Journal of Applied Crystallography,* 29, 662-666.

Humbert, M., Moustahfid, H., Wagner, F. and Philippe, M. J. (1994) Evaluation of the High Temperature Texture of the Beta Phase of a TA6V Sample from the Individual Orientations of Grains of the Low Temperature Alpha Phase. *Scripta Metallurgica et Materialia,* 30, 377-382.

Humphreys, F. J. (2001) Grain and subgrain characterisation by electron backscatter diffraction. *Journal of Materials Science,* 36, 3833-3854.

Hutchinson, B. and Kestens, L. (2008) Origins of Texture Memory in Steels. In Rollett, A. D. (Ed.) *Applications of Texture Analysis, Ceramic Transactions.* New Jersey, John Wiley & Sons Inc.

Hutchinson, B., Ryde, L. and Bate, P. (2005) Transformation Textures in Steels. *Materials Science Forum,* 495-497, 1141-1150.

Instron Corporation (2007) ETMT8800 Electrothermal Mechanical Test System.

Ischia, G., Wenk, H. R., Lutterotti, L. and Berberich, F. (2005) Quantitative Rietveld texture analysis of zirconium from single synchrotron diffraction images. *Journal of Applied Crystallography,* 38, 377-380.

Jourdan, C., Gastaldi, J., Marzo, P. and Grange, G. (1991) In situ statistical study of the nucleation, the variant selection and the orientation memory effect during the α-β titanium martensitic transformation. *Journal of Materials Science,* 26, 4355-4360.

Kallend, J. S. (1998) Determination of the Orientation Distribution from Pole Figure Data. In Kocks, U. F., Tome, C. N. & Wenk, H. R. (Eds.) *Texture and Anisotropy.* Cambridge, Cambridge University Press.

Kallend, J. S., Kocks, U. F., Rollett, A. D. and Wenk, H. R. (1991) Operation Texture Analysis. *Materials Science and Engineering,* A132, 1-11.

Kaschner, G. C., Tome, C. N., Beyerlein, I. J., Vogel, S. C., Brown, D. W. and McCabe, R. J. (2006) Role of twinning in the hardening response of zirconium during temperature reloads. *Acta Materialia,* 54, 2887-2896.

Kaschner, G. C., Tome, C. N., McCabe, R. J., Misra, A., Vogel, S. C. and Brown, D. W. (2007) Exploring the dislocation/twin interactions in zirconium. *Materials Science and Engineering A,* 463, 122-127.

Kearns, J. J. (2001) On the Relationship among 'f' Texture Factors for the Principal Planes of Zirconium, Hafnium and Titanium Alloys. *Journal of Nuclear Materials,* 299, 171-174.

Kelly, A., Groves, G. W. and Kidd, P. (2000) *Crystallography and Crystal Defects,* Chichester, John Wiley & Sons Ltd.

Kocks, U. F. (1998) The Representation of Orientations and Textures. In Kocks, U. F., Tome, C. N. & Wenk, H. R. (Eds.) *Texture and Anisotropy.* Cambridge, Cambridge University Press.

Le Bail, A., Duroy, H. and Fourquet, J. L. (1988) Ab Initio Structure Determination of LiSbWO6 by X-ray Powder Diffraction. *Materials Research Bulletin,* 23, 447-452.

Linga-Murty, K. and Charit, I. (2006) Texture Development and Anisotropic Deformation of Zircaloys. *Progress in Nuclear Energy,* 48, 325-359.

Lonardelli, I., Gey, N., Wenk, H. R., Humbert, M., Vogel, S. and Lutterotti, L. (2007) In situ observation of texture evolution during α→β and β→α phase transformations in titanium alloys investigated by neutron diffraction. *Acta Materialia,* 55, 5718-5727.

Lonardelli, I., Wenk, H. R., Lutterotti, L. and Goodwin, M. (2005) Texture analysis from synchrotron diffraction images with the Rietveld method: dinosaur tendon and salmon scale. *Journal of Synchrotron Radiation,* 12, 354-360.

Lütjering, G. and Williams, J. (2003) *Titanium,* Berlin, Springer.

Lutterotti, L., Matthies, S., Wenk, H. R., Schultz, A. J. and Richardson, J. (1997) Combined Texture and Structure Analysis of Deformed Limestone from Time-of Flight Neutron Diffraction Spectra. *Journal of Applied Physics,* 81, 594-600.

Massih, A. R., Andersson, T., Witt, P., Dahlbäck, M. and Limbäck, M. (2003) Effect of quenching rate on the β-to-α phase transformation structure in zirconium alloy. *Journal of Nuclear Materials,* 322, 138-151.

Matthies, S., Pehl, J., Wenk, H. R., Lutterotti, L. and Vogel, S. (2005) Quantitative texture analysis with the HIPPO neutron TOF diffractometer. *Journal of Applied Crystallography,* 38, 462-475.

Matthies, S. and Vinel, G. W. (1982) On the Reproduction of the Orientation Distribution Function of Texturized Samples from Reduced Pole Figures Using the Conception of a Conditional Ghost Correction. *Physica Status Solidi (b),* 112, K111-K114.

Moustahfid, H., Humbert, M. and Philippe, M. J. (1997) Modeling of the texture transformation in a Ti-64 sheet after hot compression. *Acta Materialia,* 45, 3785-3790.

Northwood, D. (1985) The Development and Applications of Zirconium Alloys. *Materials & Design,* 6, 58-70.

O'Haver, T. (2009) An Introduction to Signal Processing in Chemical Analysis.

Ökvist, G. and Källström, K. (1970) The effect of zirconium carbide on the β→α transformation structure in Zircaloy. *Journal of Nuclear Materials,* 35, 316-321.

PANalytical (2005) *X'Pert Texture*. Version 1.0.

Randle, V. (2001) Texture. In Jürgen-Buschow, K. H., Cahn, R. W., Flemings, M. C., Ilschner, B., Kramer, E. J., Mahajan, S. & Veyssière, P. (Eds.) *Encyclopedia of Materials: Science and Technology.* Elsevier Science Ltd.

Randle, V. (2003) *Microtexture determination and its applications,* London, Maney.

Randle, V. and Engler, O. (2000) *Introduction to Texture Analysis: Macrotexture, Microtexture and Orientation Mapping,* Amsterdam, Overseas Publishers Association.

Rietveld, H. M. (1969) A Profile Refinement Method for Nuclear and Magnetic Structures. *Journal of Applied Crystallography,* 2, 65-71.

Rodriguez, P. (2001) Nuclear Reactor Materials: Irradiation Effects. In Jürgen-Buschow, K. H., Cahn, R. W., Flemings, M. C., Ilschner, B., Kramer, E. J., Mahajan, S. & Veyssière, P. (Eds.) *Encyclopedia of Materials: Science and Technology.* Elsevier Science Ltd.

Roe, R. J. (1965) Description of Crystallite Orientation in Polycristalline Materials. III. General Solution to Pole Figure Inversion. *Journal of Applied Physics,* 36, 2024-2031.

Rollett, A. D. and Wright, A. D. (1998) Typical Textures in Metals. In Kocks, U. F., Tome, C. N. & Wenk, H. R. (Eds.) *Texture and Anisotropy.* Cambridge, Cambridge University Press.

Romero, J., Preuss, M. and Quinta da Fonseca, J. (2009) Texture memory and variant selection during phase transformation of a zirconium alloy. *Acta Materialia,* 57, 5501-5511.

Rosinger, H. E., Bera, P. C. and Clendening, W. R. (1979) Steady-state creep of Zircaloy-4 fuel cladding from 940 to 1873 K. *Journal of Nuclear materials,* 82, 286-297.

Ryde, L., Artymowicz, D. and Hutchinson, W. B. (1999) Transformation textures and texture memory in low carbon steels. In Szpunar, J. A. (Ed.) *12th International Conference on Textures of Materials.* Montreal, Canada.

Sabol, G. P. (2005) ZIRLO - An Alloy Development Success. *Journal of ASTM International,* 2, 3-24.

Semiatin, S. L., Knisley, S. L., Fagin, P. N., Zhang, F. and Barker, D. R. (2003) Microstructure Evolution during Alpha-Beta Heat Treatment of Ti-6Al-4V. *Metallurgical and Materials Transactions A,* 34A, 2377-2386.

Seward, G. G. E., Celotto, S., Prior, D. J., Wheeler, J. and Pond, R. C. (2004) In situ SEM-EBSD observations of the hcp to bcc phase transformation in commercially pure titanium. *Acta Materialia,* 52, 821-832.

Stanford, N. and Bate, P. (2004) Crystallographic variant selection in Ti-6Al-4V. *Acta Materialia,* 52, 5215-5224.

Tenckhoff, E. (1970) Annealing Textures in Zircaloy Tubing. *Journal of Nuclear Materials,* 35, 14-23.

Tenckhoff, E. (1988) *Deformation Mechanisms, Texture and Anisotropy in Zirconium and Zircaloy,* Philadelphia, ASTM.

Tenckhoff, E. (2005) Review on Deformation Mechanisms, Texture and Mechanical Anisotropy in ZIrconium and Zirconium Base Alloys. *Journal of ASTM International,* 2.

Tome, C. N. (1998) Tensor properties of textured polycrystals. In Kocks, U. F., Tome, C. N. & Wenk, H. R. (Eds.) *Texture and Anisotropy.* Cambridge, Cambridge University Press.

Tome, C. N., Christodoulou, N., Turner, P. A., Miller, M. A., Woo, C. H., Root, J. and Holden, T. M. (1996) Role of internal stresses in the transient of irradiation growth of Zircaloy-2. *Journal of Nuclear Materials,* 227, 237-250.

Tome, C. N., So, C. B. and Woo, C. H. (1993) Self-consistent calculations of steady-state creep and growth in textured zirconium. *Philosophical Magazine A,* 67, 917-930.

Trixell (2007) Pixium 4700. Digital detector for real-time X-ray imaging.

Urbanic, V. F. (1977) Oxidation of Zirconium Alloys in Steam at 1000 to 1850°C. In Parry, G. W. & Lowe, A. L. (Eds.) *Zirconium in the Nuclear Industry: Proceedings of the 5th International Symposium.* Baltimore, American Society for Testing and Materials.

Vander Voort, G. (1999) *Metallography. Principles and Practice,* Materials Park, ASM International.

Vander Voort, G. F. and Van Geertruyden, W. (2006) Metallographic Preparation for Electron Backscatter Diffraction. *Microscopy and Microanalysis,* 12, 1610-1643.

Von Dreele, R. B. (1997) Quantitative Texture Analysis by Rietveld Refinement. *Journal of Applied Crystallography,* 30, 517-525.

Wagner, F., Bozzolo, N., Van Landuyt, O. and Grosdidier, T. (2002) Evolution of recrystallisation texture and microstructure in low alloyed titanium sheets. *Acta Materialia,* 50, 1245-1259.

Wenk, H. R. (1998) Pole Figure Measurements with Diffraction Techniques. In Kocks, U. F., Tome, C. N. & Wenk, H. R. (Eds.) *Texture and Anisotropy.* Cambridge, Cambridge University Press.

Wenk, H. R. and Grigull, S. (2003) Synchrotron texture analysis with area detectors. *Journal of Applied Crystallography,* 36, 1040-1049.

Wenk, H. R., Huensche, I. and Kestens, L. (2007) In-Situ Observation of Texture Changes during Phase Transformation in Ultra-Low-Carbon Steel. *Metallurgical and Materials Transactions A,* 38, 261-267.

Wenk, H. R. and Kocks, U. F. (1987) The Representation of Orientation Distributions. *Metallurgical and Materials Transactions A,* 18A.

Wenk, H. R., Lonardelli, I. and Williams, D. (2004) Texture changes in the hcp→bcc→hcp transformation of zirconium studied in-situ by neutron diffraction. Acta Materialia, 52, 1899-1907.

Wenk, H. R., Matthies, S., Donovan, J. and Chateigner, D. (1998) BEARTEX: a Windows-Based Program System for Quantitative Texture Analysis. *Journal of Applied Crystallography,* 31, 262-269.

Wenk, H. R. and Van Houtte, P. (2004) Texture and Anisotropy. *Reports on Progress in Physics,* 67, 1367-1428.

Wright, S. I. (2000) Fundamentals of automated EBSD. In Schwartz, A. J., Kumar, M. & Adams, B. (Eds.) *Electron Backscatter Diffraction in Materials Science.* London, Kluwer Academic.

Yoo, M. H. (1981) Slip, twinning and fracture in hexagonal close-packed metals. *Metallurgical Transactions A,* 12, 409-418.

Yoshinaga, N., Inoue, H., Kawasaki, K., Kestens, L. and De Coorman, B. C. (2007) Factors Affecting Texture Memory Appearing through $\alpha\rightarrow\gamma\rightarrow\alpha$ Transformation in IF Steels. *Materials Transactions,* 48, 2036-2042.

Yoshinaga, N., Ushioda, K., Itami, A. and Akisue, O. (1994) $\alpha+\gamma$ and γ Phases Annealing in Ultra Low-carbon Sheet Steels. *ISIJ International,* 34, 33-42.